

UNIVERSITY OF LIVERPOOL



Characterising the Optical Response of the SNO+ Detector

Author:

Robert STAINFORTH

Supervisor:

Dr. Neil McCUALEY

Thesis submitted in accordance with the requirements of the
University of Liverpool for the degree of Doctor in Philosophy

in the

Faculty of Science and Engineering

Department of High Energy Particle Physics

March 2016

UNIVERSITY OF LIVERPOOL

Abstract

Faculty of Science and Engineering
Department of High Energy Particle Physics

Characterising the Optical Response of the SNO+ Detector

by Robert STAINFORTH

SNO+ is a liquid scintillator based neutrino experiment located 2039 m underground in VALE's Creighton mine, Lively, Ontario, CA. It is a re-purposing of the original Cherenkov detector used in the SNO experiment to study neutrino oscillations. The advent of neutrino oscillations has revealed that neutrinos have a small yet non-zero mass. However, the nature of this mass has yet to be determined. It is possible that the neutrino is its own anti-particle, a *Majorana* fermion. If so, such particles necessitate lepton number violating processes such as neutrinoless double beta decay. SNO+ intends to search for the neutrinoless double beta decay of ^{130}Te . Other physics objectives include the study of low-energy solar neutrinos, reactor anti-neutrinos, geo-neutrinos and sensitivity to nucleon decay and supernova neutrinos. To fulfil these objectives, SNO+ will operate over three detector phases; water, scintillator and tellurium (loading of the scintillator with tellurium). Prior to each phase, the experiment will undergo a full detector calibration. This includes an optical calibration that seeks to characterise the optical response of the detector using two types of in-situ light sources; one of these is called the *laserball*. The laserball provides a pulsed, near-isotropic light distribution throughout the detector. Laserball data is used in conjunction with a parameterised model that characterises the optical response; the parameters are determined using a statistical fit. This thesis presents an implementation of said model to all three phases of the SNO+ experiment. A characterisation of the optical response in water is presented using a combination of original laserball data from SNO and MC data of the SNO+ detector. Thereafter, the two scintillator based phases are considered, wherein the increased attenuation of light due to absorption and reemission introduced by the scintillator is addressed alongside a model of the scintillation time profile.

Acknowledgements

There are numerous people I would like to thank for their help throughout my time as a PhD student. Indeed, the words herein are my own, but only through the insight of others have they been conceived. Firstly, I would like to thank my supervisor Neil McCauley for his continual support, enthusiasm and time. He has always made time for me, and will never cease to impress me with his knowledge of neutrino physics and experimental practices. As my time at Liverpool ends, I attribute a lot of my understanding to him for which I will always be thankful. I hope we are able to work again sometime in the future. For now though I am glad to be rid of his weekly reminders concerning the status of my football team, Aston Villa relative to the *mighty* West Bromwich Albion.

I would also like to extend many thanks to José Maneira at LIP. Since joining the SNO+ optics group, José has provided invaluable knowledge concerning the laserball and the optical model discussed in this work. He has been an excellent mentor and friend. I would also like to thank other members of the optics group; Gersende Prior, Nuno Baros and Phil Jones for their help.

I feel very fortunate to have worked on SNO+ at Liverpool alongside my colleague, and fellow PhD student John Walker. Seemingly in tandem¹, John and I began and concluded our work on SNO+ side by side. From summer schools and conferences to a thoroughly enjoyable eight months living together in Sudbury, there is no one I would have rather shared these memories with.

I have made many good friends without whom my time on SNO+ would have been less enjoyable. I would like to thank fellow SNO+ UK students; Evelina Arushanova, Ashley Back, Jack Dunger, Chris Jones, Stefanie Langrock and James Waterfield and Sudbury locales Aleksandra Bialek, Caitlyn Darrach, Janet Rumleskie and Andy Stripay. I would also like to thank those all important non-physicists in my life; Maike Pötschulat, Emily Hole and Jenna Hinds as well as Linda Fielding and Angie Reid at Liverpool for their help in assisting with my travel arrangements.

Finally, thanks to my parents and sister for their support and love throughout both this and all moments in my life; you couldn't have given more.

¹We did in fact once ride a tandem bike over the golden gate bridge...

Statement of Originality

All the work, analysis and discussion presented in this thesis is that of the author unless otherwise stated.

The SNO+ collaboration is composed of approximately 100 members from various institutions in Europe and North America. As such, the individual tasks required to run the experiment are split between working groups of 10-15 people. Calculations or features of the SNO+ MC, RAT are therefore the result of iterative improvements authored by several people from different groups. Relevant to this work is the implementation of the different scintillator mixtures into RAT by L. Segui of Oxford and spectrometer measurements of the laser-dye profiles by J. Maneira of LIP. Past characterisations of the laserball light distribution obtained from several optical calibrations in SNO were provided by N. Baros, after which the author implemented these into RAT for use in the MC laserball data sets. The laserball generator used to produce MC data was co-authored by the author and J. Maneira. The calculation of refracted light paths discussed here originally featured in the optical calibration software used in SNO, LOCAS. This calculation has been revised and as such the mathematical derivation of this calculation has been re-performed by the author and implemented into RAT. Similarly, the optical model and occupancy ratio method have previously been applied to laserball data in SNO through LOCAS. LOCAS has now been replaced by a completely new software utility for SNO+, OCA. OCA intends to serve the same purpose and as such shares similarities to LOCAS. OCA was written entirely by the author in C++. The time profile model presented as part of the discussion of laserball simulations in scintillator was conceived by the author.

Contents

1	Searching for a Neutrino Mass	1
1.1	The Neutrino	1
1.2	Neutrino Oscillations	3
1.2.1	The Solar Neutrino Problem	4
1.2.1.1	Cherenkov Detectors	8
1.2.1.2	The Kamiokande Experiment	10
1.2.1.3	The Sudbury Neutrino Observatory	12
1.2.1.4	KamLAND	16
1.2.2	Atmospheric Neutrino Anomaly	17
1.2.3	Neutrino Mixing and Oscillations	18
1.2.4	Neutrino Oscillations in Matter	21
1.2.5	Neutrino Oscillation Experiments	23
1.3	Nature of the Neutrino Mass	27
1.3.1	Dirac Neutrino Masses	27
1.3.2	Majorana Neutrino Masses	28
1.3.3	Lepton Number Violation	30
1.4	Detection of the Neutrino Mass	31
1.4.1	Neutrinoless Double β -Decay	33
1.4.2	Neutrinoless Double β -Decay Experiments	36
1.4.2.1	Detector Technologies	37
2	The SNO+ Experiment	45
2.1	Detector Components and Materials	45
2.1.1	PMTs & Electronics	47
2.2	Operating Phases & Backgrounds	50
2.3	Detector Calibration	53
2.3.1	Optical Sources	54
2.3.2	LED/Laser Light Injection System	55
2.3.3	The Laser System and Laserball	56
2.4	SNO+ Monte-Carlo: RAT	60
3	Scintillators in SNO+	61
3.1	Scintillator Structure	63

3.2	The SNO+ Scintillator	66
3.3	Excitation & Attenuation	68
3.4	De-Excitation & Luminescence	72
3.4.1	Fluorescence	72
3.4.2	Phosphorescence & Delayed-Fluorescence	73
3.4.3	Energy Migration	74
3.4.4	Wavelength Shifters	74
3.4.5	Scintillation Time Profile	77
3.5	Quenching	79
3.6	The SNO+ Scintillator Plant	81
3.7	A Deep Rooted Plant	82
3.7.1	Transportation & Storage of LAB	83
3.7.2	Construction of the Plant	84
3.7.3	Helium Leak Checking	86
4	Characterising Optical Response	91
4.1	Optical Response	92
4.1.1	Energy & Physics Sensitivty to Optical Effects	93
4.2	Optical Response Model	95
4.2.1	Calculation of a Light Path	97
4.2.1.1	Mathematical Description of a Path	97
4.2.2	Time Residuals & Group Velocity	101
4.2.3	Prompt Peak Count Calculation	102
4.2.4	PMT Angular Response	105
4.2.5	Laserball Light Distribution	108
4.2.6	Solid Angle	112
4.2.7	Fresnel Transmission Coefficient	112
4.3	Implementation of the Optical Model	113
4.3.1	Occupancy Ratio Method	117
4.3.2	PMT Variability	117
4.4	Data Selection	119
4.4.1	PMT Shadowing	120
4.4.2	Chi-Square Selection Cuts	122
4.5	Scintillator Response	127
4.5.1	In-situ Scintillator Time Profile	127
4.5.2	Scintillator Time Profile Model	128
4.5.3	Scintillator Time Profile Model Log-Likelihood	132
4.6	Conclusion on Optical Response	133
5	Production and Processing of Data	136
5.1	Monte-Carlo Production	136
5.1.1	Selection of Laser Intensity & Wavelength	139
5.1.1.1	Average Reemitted Wavelengths	142
5.1.2	Laserball Scan Positions	145

5.2	Processing	147
5.2.1	The SOC-run File	148
5.2.2	RAT's SOCFitter Processor	151
5.2.3	OCA Processors	153
5.2.3.1	soc2oca	154
5.2.3.2	oca2fit	155
5.2.3.3	rdt2soc	156
5.3	Summary of Data Production	156
6	Optical Fit in Water	158
6.1	Data Selection	159
6.1.1	Chi-Square Cuts	162
6.2	Optical Fit Results: Data & Monte-Carlo	164
6.2.1	Attenuation Coefficients	167
6.2.2	PMT Angular Response	176
6.2.2.1	Discrepancies between Data & Monte-Carlo	180
6.2.3	PMT Variability	181
6.2.4	Laserball Light Distribution	183
6.2.4.1	Laserball Mask Function	184
6.2.4.2	Laserball Angular Distribution	186
6.2.5	Covariance Matrix & Parameter Correlations	191
6.2.5.1	Correlation Matrices	192
6.2.6	Systematic Errors	196
6.2.6.1	Systematic Variations	199
6.3	Laserball Water Phase Prospects	204
7	Optical Fit in Scintillator	206
7.1	Optical Fit Results: LABPPO(+0.3%Te+Bis-MSB/Perylene)	207
7.1.1	Attenuation Coefficients	208
7.1.2	PMT Angular Response	217
7.1.3	Laserball Light Distribution	219
7.1.4	Covariance Matrix & Parameter Correlations	225
7.1.5	Systematic Errors	226
7.1.6	Conclusion on Optical Fit in Scintillator	231
7.2	Scintillator Timing	232
7.2.1	Scintillator Time Model Results	234
7.2.2	Shape Comparison	240
7.2.3	Statistical and Systematic Uncertainties	242
7.2.4	Conclusion on Scintillator Time Profile Model	245
8	Conclusions	247

A Optical Response Calculations	252
A.1 Light Path Derivation	252
A.2 PMT Bucket Time	255
A.3 Fresnel Transmission Coefficient Calculation	256
A.4 Scintillator Time Profile Model Timings	257
B Monte-Carlo Data Production:	
Extended	259
B.1 KITON-RED Laser-Dye for Monte-Carlo Production	259
C Optical Model Fits:	
Extended Results	261
C.1 Attenuation Coefficient Systematics: Water & D ₂ O	261
C.2 Attenuation Coefficient Systematics: Scintillator	268
Bibliography	278

For my sister, Liz, my father, Mel, and my mother, Lindsey.

1

Searching for a Neutrino Mass

I'm not quite sure what my son does, I think he chases neutrinos down a hole...

Melvin Stainforth

1.1 The Neutrino

The neutrino was postulated by W. Pauli, who in 1930 predicted the existence of a *light*, neutrally charged elementary particle as a means to retain the conservation of momentum, energy and spin in β -decay; Pauli believed that such a particle could not be experimentally observed [1]. However, in 1956 the neutrino was indeed detected after C. Cowan and F. Reines observed anti-neutrinos from a nuclear reactor through β -capture [2]. This later became known as the Reines-Cowan experiment for which F. Reines was awarded the 1995 Nobel prize [3] ¹.

Within the same year as the Reines-Cowan result, work by T. Lee, C. Yang and C. Wu [4, 5] respectively predicted and experimentally confirmed parity violation in weak interactions, noting that all observed neutrinos and anti-neutrinos have respectively, left- and right-handed helicity states. This motivated a phenomenological description of the neutrino, whereby it is considered the electro-weak partner of the charged lepton, $\ell_{\alpha L}$. Collectively, both particles form components of

¹By this time C. Cowan had unfortunately passed away (dec. 1974).

the $SU(2)_L$ lepton doublet, $L_{\alpha L}$ of the Standard Model (SM). Alongside the right-handed charged lepton field, $\ell_{\alpha R}$ the SM picture of leptons is as follows;

$$L_{\alpha L} = \begin{pmatrix} \nu_{\alpha L} \\ \ell_{\alpha L} \end{pmatrix}, \quad \ell_{\alpha R}, \quad \alpha = e, \mu, \tau. \quad (1.1)$$

Here, the $\ell_{\alpha R}$ field is considered a *singlet* due to the absence of right-handed neutrinos in the SM. The neutrino is a spin-half particle and carries zero electrical or coloured charge. There are three flavours of neutrino, ν_{α} , $\alpha = e, \mu, \tau$. A constraint on the number of light neutrino flavours was found to be $N_{\alpha, \nu} = 2.981 \pm 0.012$ following precision electro-weak measurements of the Z^0 boson decay width at LEP [6]. More recently, cosmological studies from recent Planck data have provided a result consistent with LEP, $N_{\alpha, \nu} = 3.36^{+0.68}_{-0.64}$ [7].

Neutrinos interact through charged-current (CC) and neutral-current (NC) electro-weak interactions, coupling to charged and neutral leptons of the same flavour as well as W^{\pm} and Z^0 bosons. At the tree level, there exist no flavour changing neutral currents in the SM.

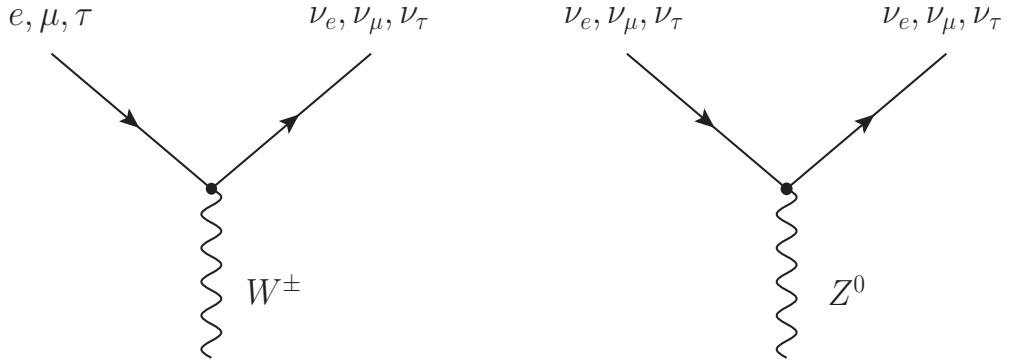


FIGURE 1.1: Left: The charged-current interaction vertex involving a neutrino, a charged lepton and a W^{\pm} boson. Right: The neutral current interaction vertex involving a neutrino with a Z^0 boson.

The neutrino is described as a massless particle in the SM. However, this has been disproved following various neutrino experiments conducted within the last half-century. These experiments have highlighted and confirmed the existence of a phenomena known as *neutrino oscillations*. This arises from neutrinos having a small but non-zero mass; a mass unaccounted for by the SM. At present, the

origin of the neutrino mass is unknown - it is a *known-unknown*, prompting three important questions:

- Q1.** *What is the absolute mass scale of the neutrino?*
- Q2.** *What is the nature of the neutrino mass?*
- Q3.** *Through what mechanism does the neutrino mass arise?*

The answers to these questions could be intrinsically linked, and any one solution to these questions has implications in answering the questions which remain. For example, neutrino masses under a Dirac formalism - like other SM particle masses - could possibly be obtained through the Higgs mechanism. This assumption is problematic, and as will be discussed, motivates an alternative consideration that the neutrino is a Majorana particle; its *own* anti-particle which necessitates new physics. However, the mechanisms through which Dirac and Majorana neutrino masses are produced may be constrained by different symmetries that produce masses on different scales.

In order to solve all three of these questions, it is arguably best to answer the second question first. A verification of the Majorana nature of neutrinos would point to new mechanisms beyond the standard model (BSM) (question 3) which would be constrained by some new energy scale (question 1). Therefore, two further questions should be considered;

- QA.** *How does the physics associated with Majorana particles manifest?*
- QB.** *Through what experimental study could this physics be probed?*

These two questions, and the pursuit of their answers, provide the phenomenological motivation for the experimental method and objectives discussed henceforth.

1.2 Neutrino Oscillations

Neutrino oscillations exhibit lepton flavour violation. Phenomenologically, neutrinos oscillate between flavour eigenstates as they propagate. The first, albeit then unbeknownst evidence of this phenomena followed investigations of the solar neutrino flux which began in the 1960s by R. Davis and J. Bachall. At the

time, Bachall was interested in the underlying reactions that drive the production of thermonuclear energy inside the Sun. The Sun produces energy through a series of nuclear fusion reactions and decays, converting protons (hydrogen) into α -particles (helium ions), positrons and neutrinos. The overall reaction can be written as follows;

$$4p \rightarrow {}^4\text{He}^{2+} + 2e^+ + 2\nu_e + Q \text{ [26.731 MeV]}, \quad (1.2)$$

where Q is the release of thermal energy which escapes the Sun as light, attributing to its luminosity. Positrons annihilate with nearby electrons producing photons which are subject to intense scattering. The neutrinos escape the Sun quickly with an energy spectrum reflective of the reaction that produced them. The objective for Davis was to build a detector that could detect these neutrinos and to confirm whether, at the time, the assumption in Equation 1.2 was correct. The detector Davis built became known as the Homestake experiment [8]. However, upon measuring the solar neutrino flux, Davis measured a deficit when compared to Bachall's predictions. As far as neutrinos were understood at the time, neutrinos from the Sun appeared to be *missing* when they arrived at Earth. This anomaly became known as the *Solar Neutrino Problem* and marked the epoch of neutrino spectroscopy in the decades and experiments that followed.

1.2.1 The Solar Neutrino Problem

The Homestake experiment was built by Davis in the period 1965-67. The name Homestake derives from the location of the experiment in the Homestake gold mine 1478 m below the surface of Lead, South Dakota, USA [9]. Homestake collected initial data in 1968-70 and thereafter ran continuously until 1994 [8]. The detector consisted of a single large cylindrical tank filled with 615 tonnes of tetrachloroethylene, C_2Cl_4 . The experiment was designed to be sensitive to the inverse β -decay process;

$$\nu_e + {}^{37}\text{Cl} \rightarrow {}^{37}\text{Ar} + e^-, \quad E_\nu \geq 0.814 \text{ MeV}, \quad (1.3)$$

where E_ν is the neutrino energy threshold for the capture of the neutrino on the chlorine nucleus. Davis was able to count the number of argon atoms produced and subsequently make a calculation of the solar neutrino flux. The neutrino

capture rate was measured in solar neutrino units (SNU) which is equivalent to the number of neutrino interactions on 10^{36} ^{37}Cl atoms s $^{-1}$. Initial findings of the solar-neutrino induced capture rate set an upper limit that was less than a third of that predicted by Bachall and collaborators [10, 11]. With 25 subsequent years worth of data and reduced uncertainties the final Homestake measurement supported the deficit originally reported [9];

$$\text{Homestake [1968]: } R_{^{37}\text{Cl}} \leq 3.0 \text{ SNU}, \quad (1.4)$$

$$\text{Bachall et al. [1968]: } R_{^{37}\text{Cl}} = 7.5_{-3.0}^{+3.0} \text{ SNU}, \quad (1.5)$$

$$\text{Homestake}^{25\text{yr}.}: R_{^{37}\text{Cl}} = 2.56 \pm 0.16 \text{ (stat.)} \pm 0.16 \text{ (sys.) SNU}, \quad (1.6)$$

$$\text{Bachall et al. [1995]: } R_{^{37}\text{Cl}} = 9.3_{-1.3}^{+1.3} \text{ SNU.} \quad (1.7)$$

Bachall's prediction was based on a mathematical treatment of the Sun that was parameterised to fit measurements of the Sun's luminosity, radius and the ratio of heavy-elements to hydrogen, known as the *metallicity*, on its surface. This is now commonly known as the standard solar model (SSM). The SSM describes the evolution of a star as its composition changes over time. Beginning with a high abundance of hydrogen, larger elements are created through fusion reactions. The increase in the abundance of these heavier elements causes the core to contract under gravity. As part of this contraction, gravitational potential energy is released in the form of radiation to the outer layer of the star, increasing the pressure and hence the temperature. Consequently, this increase in temperature increases the rate of further nuclear reactions and the overall luminosity. The outer layer compensates for this increase in pressure and temperature by expanding, increasing the radius of the star. This repeated process of core-contraction and energy release continues to keep the star in a near-steady equilibrium state until the hydrogen is ultimately consumed. The SSM is updated as relevant measurements and theories of the Sun's composition and mechanisms develop.

In reality, the process of nuclear fusion outlined in Equation 1.2 is driven by a chain and cycle of several intermediate reactions that contribute to the overall neutrino output of the Sun. The dominant series is known as the *pp*-chain which begins as the fusion of two protons. There is also the *pep*-chain, but this is less common. Figure 1.2 illustrates the steps involved in the *pp*- and *pep*-chains.

In addition to the *pp*- and *pep*-chains is the CNO-cycle, a cycle of fusion reactions between carbon, nitrogen, oxygen and protons as shown in Figure 1.3. These

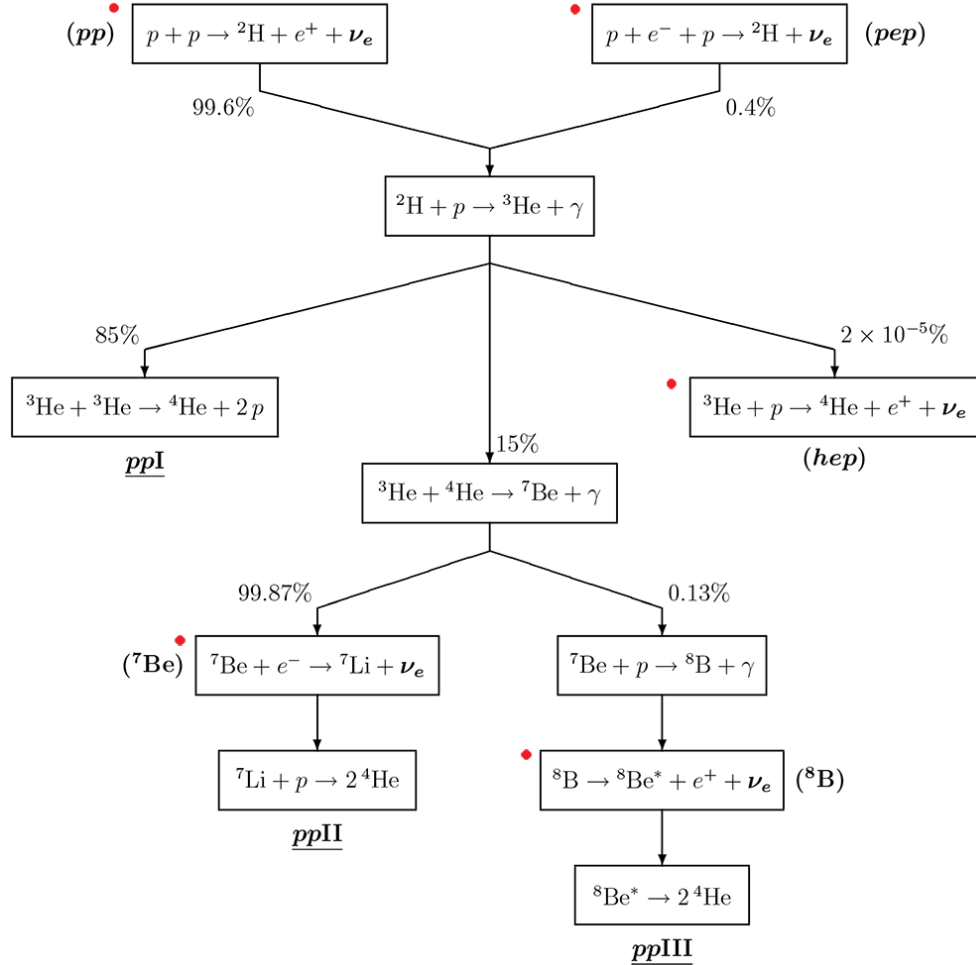


FIGURE 1.2: [12] The *pp*- and *pep*-chains. Reactions marked with red denote those which emit neutrinos. The majority of neutrinos emitted by the Sun are from the initial *pp*-reaction.

reactions also produce neutrinos. A complete table of the solar neutrino types and their respective energies is shown in Table 1.1.

It is of note that all solar neutrinos emitted as part of the reactions outlined here are electron-neutrinos. This removed at least some of the uncertainty as to what Homestake had actually measured, but further enforced the anomalous result. Due to the 0.814 MeV energy threshold on the chlorine nucleus, Homestake was limited to neutrino capture from primarily ${}^8\text{B}$ -neutrinos. These constitute only a small fraction of neutrinos emitted by the Sun. This prompted further measurements by similar radiochemical experiments such as SAGE [14], GALLEX [15] and GNO [16] in the period 1970-90s. These experiments used gallium instead of chlorine to

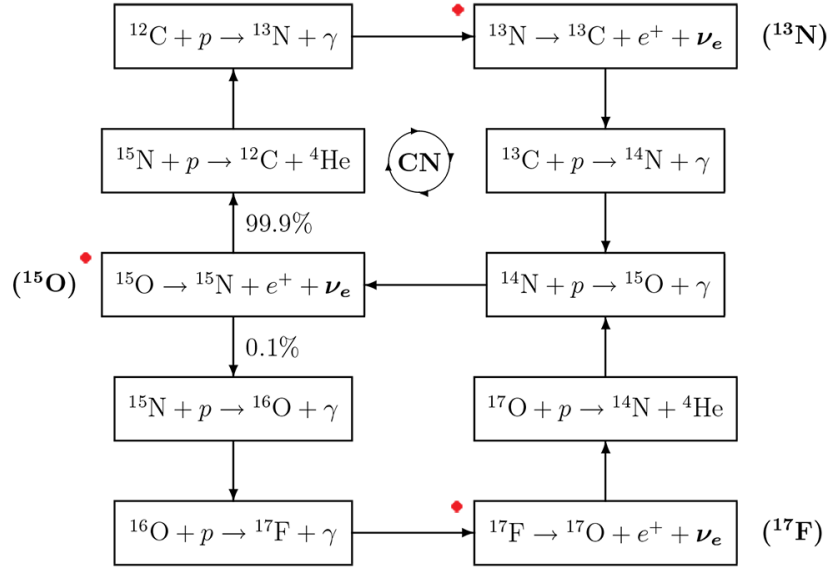


FIGURE 1.3: [12] The series of fusion reactions between carbon, nitrogen and oxygen in the CNO-cycle. Reactions marked with red denote those which emit neutrinos.

Solar Neutrino Types

Source	Process	$\langle E_\nu \rangle$ [MeV]	E_ν^{\max} [MeV]	$\langle Q_\nu \rangle$ [MeV]
<i>pp</i>	$p + p \rightarrow {}^2\text{H} + e^+ + \nu_e$	0.2668	0.423 ± 0.03	13.0987
<i>pep</i>	$p + e^- + p \rightarrow {}^2\text{H} + \nu_e$	1.445	1.445	11.9193
<i>hep</i>	${}^3\text{He} + p \rightarrow {}^4\text{He} + e^+ + \nu_e$	9.628	18.778	3.7370
${}^7\text{Be}$	${}^7\text{Be} + e^- \rightarrow {}^7\text{Li} + \nu_e$	0.3855 (10%) 0.8631 (90%)	0.3855 0.8631	12.6008 12.6008
${}^8\text{B}$	${}^8\text{B} \rightarrow {}^8\text{B}^* + e^+ + \nu_e$	6.735 ± 0.036	15 ± 0.090	6.6305
${}^{13}\text{N}$	${}^{13}\text{N} \rightarrow {}^{13}\text{C} + e^+ + \nu_e$	0.7063	1.1982 ± 0.0003	3.4577
${}^{15}\text{O}$	${}^{15}\text{O} \rightarrow {}^{15}\text{N} + e^+ + \nu_e$	0.9964	1.7317 ± 0.0005	21.5706
${}^{17}\text{F}$	${}^{17}\text{F} \rightarrow {}^{17}\text{O} + e^+ + \nu_e$	0.9977	1.7364 ± 0.0003	2.363

TABLE 1.1: Solar neutrino types as produced by the *pp*- and *pep*-chains. Shown also are the neutrinos produced as part of the CNO-cycle. $\langle E_\nu \rangle$ denotes the mean neutrino energy, E_ν^{\max} denotes the maximum and $\langle Q_\nu \rangle$ denotes the average thermal energy released alongside a neutrino. Values of the ${}^8\text{B}$ -neutrino energies are from [13], all others are from [12].

observe the following inverse β -decay reaction;

$$\nu_e + {}^{71}\text{Ga} \rightarrow {}^{71}\text{Ge} + e^-, \quad E_\nu \geq 0.233 \text{ MeV}. \quad (1.8)$$

The lower energy threshold of 0.233 MeV made these experiments sensitive to the

more abundant pp -neutrinos, $\langle E_\nu \rangle = 0.2668$ MeV. A combined analysis of the SAGE, GALLEX and GNO results [17] further confirmed the Homestake result reporting a deficit around one half of that theoretically predicted [12];

$$\text{SAGE+GALLEX+GNO: } R_{71\text{Ge}} = 66.1 \pm 3.1 \text{ (stat.+sys.) SNU}, \quad (1.9)$$

$$\text{SSM [2004]: } R_{71\text{Ge}} = 131^{+12}_{-10} \text{ SNU}. \quad (1.10)$$

The main disadvantage of Homestake and the gallium experiments was that they could only count neutrino interactions; they did not provide information on the neutrino energy or direction; one interaction was indistinguishable from another. In order to observe the real-time information of neutrinos on a per-interaction basis, a different type of detector technology known as *Cherenkov* detectors would need to be used. It would be through measurements made by Cherenkov detector experiments that the observed solar neutrino deficit would be explained alongside the first measurements of their energy spectra.

1.2.1.1 Cherenkov Detectors

Cherenkov detectors are designed to detect *Cherenkov radiation*; the emission of photons when a charged particle travels faster than the local phase velocity of light through a medium. This phenomena was first observed by P. Cherenkov in 1934 for which he later received the Nobel prize in 1958 [18]. Cherenkov radiation is produced inside detectors by the tracks of relativistically charged particles arising from some interaction. In the context of neutrino studies, one such example is the elastic scattering of a neutrino off of an electron;

$$\nu_\alpha + e^- \rightarrow \nu_\alpha + e^-, \quad \alpha = e, \mu, \tau. \quad (1.11)$$

For all three flavours this process can be mediated by a neutral-current interaction (Z^0 -boson exchange). However, the $\nu_e + e^- \rightarrow \nu_e + e^-$ cross-section also receives contributions from charged-current interactions (W^\pm -boson exchange). From electro-weak calculations, the cross-section for this process is therefore 6.43 times larger for electron-neutrinos, ν_e than for non-electron type neutrinos, $\nu_{\mu,\tau}$ [12].

As the neutrino scatters, it transfers a fraction of its momentum to the electron. For a sufficiently energetic neutrino, the recoiled electron will begin to travel relativistically; emitting Cherenkov radiation along its path (often referred to as a *track*). The electron is scattered through an angle θ_ν with respect to the original direction of the neutrino. The kinetic energy of the recoiled electron, T_e is related to θ_ν through the following expression [19];

$$T_e = E_\nu - E'_\nu = E_\nu \left(1 - \frac{1}{1 + \frac{E_\nu}{m_e c^2} (1 - \cos \theta_\nu)} \right), \quad (1.12)$$

where E_ν and E'_ν are the respective initial and recoiled neutrino energies and m_e is the electron mass. The electron *target* in Cherenkov detectors is typically water. The number of Cherenkov photons emitted is given by the following expression [20];

$$\frac{d^2N}{dx d\lambda} = \frac{2\pi\alpha Z^2}{\lambda^2} \left(1 - \frac{1}{(n\beta)^2} \right), \quad (1.13)$$

where x is the distance travelled by the charged particle, λ is the wavelength of the photon, Z is the charge of the particle, α the fine structure constant ($= 1/137$), $\beta = v/c$ and n is the refractive index of the medium. In water, approximately 340 photons cm $^{-1}$ are emitted within a wavelength range between 300 and 600 nm [12]. The photons are emitted at a characteristic angle about the axis defined by the track of the charged particle, forming a cone of light [18];

$$\cos \theta_C = \frac{1}{n\beta}, \quad (1.14)$$

$$\theta_C \sim 41^\circ \text{ for } n = 1.33 \text{ [Water].}$$

The above expression can be used to derive the energy threshold, E_c for Cherenkov radiation to be produced [21];

$$E_c \geq m \left(\frac{1}{\sqrt{1 - \frac{1}{n^2}}} - 1 \right), \quad (1.15)$$

where m is the mass of the charged particle. The energy threshold for electrons in water is $E_c^e = 260$ keV.

In order to observe Cherenkov radiation, detectors make use of highly sensitive photo-detectors called photo-multiplier tubes (PMTs). PMTs provide information on the amount of light produced within the detector, as well as its arrival time at the PMT itself. PMTs therefore make detectors sensitive not only to the particle momentum, type and direction, but also the location of the original interaction point from where the charged track began. In the case of elastic scattering, momentum information of the charged track is related to the original neutrino momentum through the expression in Equation 1.12.

1.2.1.2 The Kamiokande Experiment

One of the first Cherenkov detectors to study neutrinos was the Kamiokande experiment. Kamiokande started running in 1983 and was originally built to search for proton decay. The detector consisted of approximately 3000 tonnes of water surrounded by ~ 1000 PMTs in a cylindrical cavity 1 km underground in the Kamioka mine, Japan. After several years the detector was upgraded to study solar neutrinos through the elastic scattering process outlined in Expression 1.11. Despite an energy threshold of 260 keV for electron recoils in water, Kamiokande was limited to energies $T_e \geq 6.6$ (8.8) MeV at 50% (90%) efficiency [22]. This was because of radioactive nuclei - predominantly radon, which emanated from the rock that surrounded the detector - which decayed to produce backgrounds. Kamiokande was therefore particularly sensitive to the solar ^8B -neutrino spectrum, $\langle E_\nu \rangle = 6.735$ MeV. A comparison of the sensitivity of Cherenkov detectors to solar neutrinos compared to Homestake and the gallium experiments is shown in Figure 1.4.

Kamiokande published its first measurements of the solar ^8B -neutrino flux in 1989 after collecting data for 450 live days [22]. Again, the same anomalous deficit as originally reported by Homestake was observed. Kamiokande measured less than one half of the flux that Bachall had predicted a year before [24];

$$\frac{\phi(\text{Kamiokande}^{450 \text{ d.}})}{\phi(\text{SSM [1988]})} = 0.46 \pm 0.13 \text{ (stat.)} \pm 0.08 \text{ (syst.)}. \quad (1.16)$$

Although Kamiokande was unable to account for the missing solar electron-neutrinos, it was able to provide important energy and directional information, see Figure 1.5. Kamiokande provided the first real-time detection of neutrino interactions and

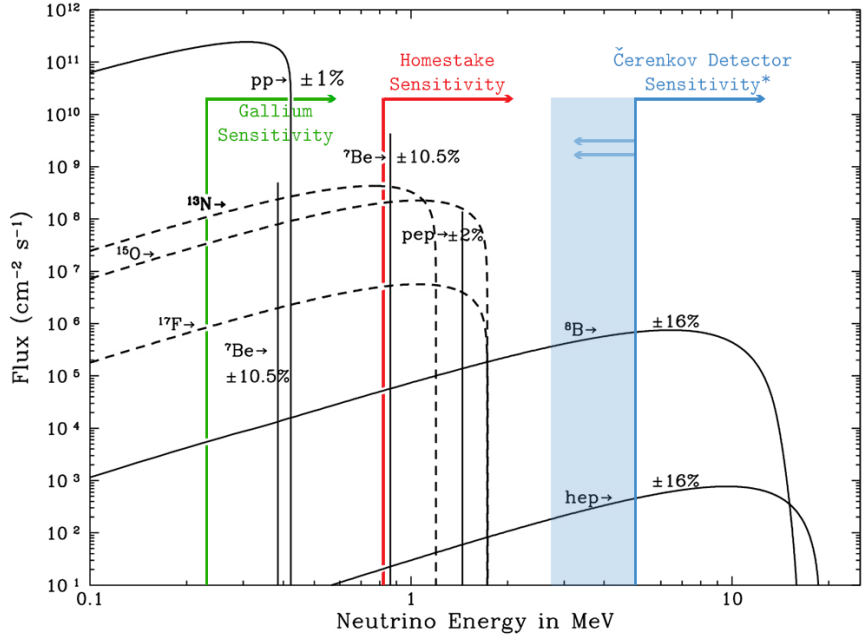


FIGURE 1.4: Shown are the different types of solar neutrino flux as detailed in Table 1.1. Dashed lines for the ^{13}N , ^{15}O and ^{17}F fluxes represent model predictions [23]. Overlaid are the sensitivities of the Homestake experiment, $^{37}\text{Cl}:E_\nu \geq 0.814$ MeV, the gallium experiments, $^{71}\text{Ga}:E_\nu \geq 0.233$ MeV and water Cherenkov detectors, $E_\nu \gtrsim 5$ MeV; the sensitivity of which is subject to background rejection.

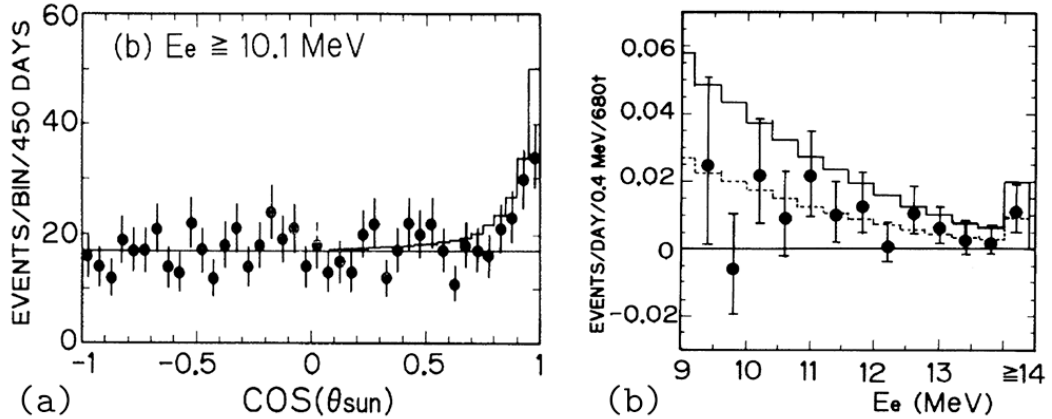


FIGURE 1.5: [22] Kamiokande solar ^8B -neutrino results. (a) The recorded directions of recoiled electrons with a kinetic energy ≥ 10.1 MeV. (b) The recorded number of solar ^8B -neutrino induced electron recoils with energies ≥ 9.3 MeV. The dotted line is the best fit to the data which lies at 46% of the theoretically predicted value (based on solar models).

continued to have a central role in an era of neutrino spectroscopy; providing measurements of neutrinos from sources aside from the Sun. These included neutrinos produced in the Earth’s atmosphere and supernova 1987A. Kamiokande left a lasting legacy of neutrino studies in Japan which continues today through its successor, the Super-Kamiokande (SK) experiment. An order of magnitude larger than Kamiokande (50,000 tonnes of water and over 11,000 PMTs) the experiment began in 1996 and provided precision measurements on the solar ${}^8\text{B}$ -neutrino flux [25].

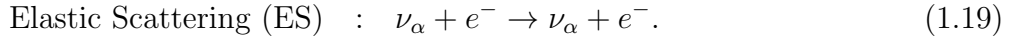
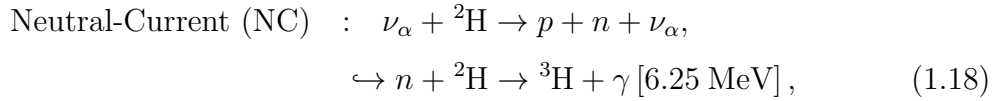
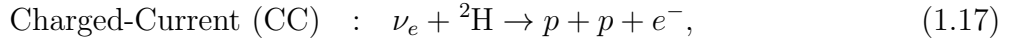
By 1999, the anomalous solar electron-neutrino deficit had been reinforced by a series of experiments spanning three decades since the original Homestake result. Despite using several detector technologies across different experiments, the solar neutrino problem remained unsolved. The strongest hypothesis at the time was that neutrinos were subject to some type of time or energy variation. This meant that a fraction of electron-neutrinos were not *missing*, but had reached detectors as a different type, *oscillating* to different flavour eigenstates such as muon- or tau-neutrinos. Measurements of elastic scattering up until this point had been flavour independent. Consequently, to test the theory of neutrino oscillations, an experiment was required that could distinguish between electron and non-electron type neutrino interactions. The experiment to do this was called the Sudbury Neutrino Observatory. By accounting for these *missing* neutrinos this experiment would provide conclusive evidence that supported neutrino oscillations as a solution to the solar neutrino problem.

1.2.1.3 The Sudbury Neutrino Observatory

The Sudbury Neutrino Observatory (SNO) was a second generation Cherenkov detector experiment located 2039 m underground in the Creighton mine in Lively near Sudbury, Ontario, CA. It was built in the 1990s and began collecting data in 1999. The detector was spherically shaped, featuring a 12 m diameter acrylic vessel surrounded by \sim 9000 inward looking PMTs. The PMTs were held in place by a steel geodesic sphere 17.8 m in diameter [26]. Many of these original detector components are to be reused for SNO+. A detailed description of the original SNO detector and the upgrades made for SNO+ are outlined in Chapter 2.

A unique feature of SNO was that it used D₂O, *heavy* water, as the target material to study Cherenkov radiation. Heavy water features a deuterium atom (${}^2\text{H}$)

on each water molecule. This is in contrast to the conventional water which had previously been used in Cherenkov detectors (featuring the naturally abundant ^1H atom). By using D_2O , SNO was able to measure the following neutrino interactions;



SNO resolved measurements into contributions from CC, ES and NC interactions using probability distribution functions (PDFs) parameterised by the kinetic energy of the electron, T_e , the electron deflection angle, θ_ν and a fiducial volume cut. An energy threshold of $T_e \geq 5.0 \text{ MeV}$ meant that SNO was sensitive primarily to solar ^8B -neutrinos.

It is the inclusion of the CC and NC interactions for the disintegration of deuterium that is important to note. The CC interaction is sensitive only to electron-neutrinos, whereas the NC interaction is sensitive to all three neutrino flavours. Measuring the rate of CC and NC interactions therefore allows flux contributions from electron and non-electron neutrino types to be separated. Assuming appropriate normalisation, the NC contributions to the flux can thus be considered to be a measure of the effective total flux of all neutrino types; electron and non-electron types;

$$\phi_{\text{NC}} = \phi_e + \phi_{\mu,\tau}, \quad \text{where } \phi_e = \phi_{\text{CC}}. \quad (1.20)$$

The contributions to the ES flux follow the ratio of 6.43 : 1 for electron to non-electron neutrino types;

$$\phi_{\text{ES}} = \phi_e + \frac{1}{6.43} \phi_{\mu,\tau}. \quad (1.21)$$

Assuming no distortions of the solar ^8B -neutrino energy spectrum, SNO tested a no-oscillation hypothesis of the ^8B -neutrino flux, publishing its first combined measurements of the flux contributions to all three CC, NC and ES interactions

in 2002 [27];

$$\phi_{CC} = 1.76^{+0.06}_{-0.05} \text{ (stat.)}^{+0.09}_{-0.09} \text{ (syst.) } 10^6 \text{ cm}^{-2} \text{ s}^{-1}, \quad (1.22)$$

$$\phi_{NC} = 5.09^{+0.44}_{-0.43} \text{ (stat.)}^{+0.46}_{-0.43} \text{ (syst.) } 10^6 \text{ cm}^{-2} \text{ s}^{-1}, \quad (1.23)$$

$$\phi_{ES} = 2.39^{+0.24}_{-0.23} \text{ (stat.)}^{+0.12}_{-0.12} \text{ (syst.) } 10^6 \text{ cm}^{-2} \text{ s}^{-1}. \quad (1.24)$$

As an example, the NC measurement can be expressed in terms of the electron and non-electron neutrino components by use of Equation 1.20;

$$\phi_e = 1.76^{+0.05}_{-0.05} \text{ (stat.)}^{+0.09}_{-0.09} \text{ (syst.) } 10^6 \text{ cm}^{-2} \text{ s}^{-1}, \quad (1.25)$$

$$\phi_{\mu,\tau}^{NC} = 3.41^{+0.45}_{-0.45} \text{ (stat.)}^{+0.48}_{-0.45} \text{ (syst.) } 10^6 \text{ cm}^{-2} \text{ s}^{-1}. \quad (1.26)$$

The measured rate for the NC reaction is shown to be in good agreement with the SSM, see Figure 1.6.

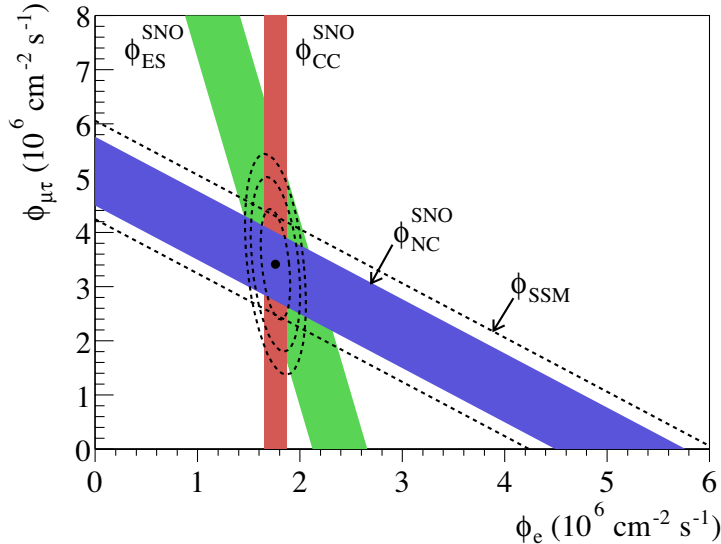
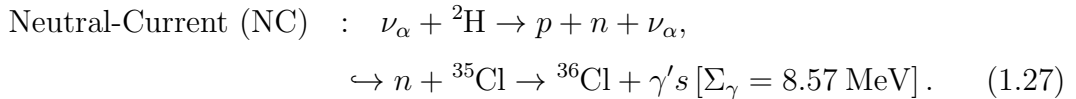


FIGURE 1.6: [27] The flux of solar ${}^8\text{B}$ -neutrinos detected as electron, ϕ_e or non-electron, $\phi_{\mu,\tau}$ types. The width of the coloured bands represent $\pm 1\sigma$ errors in the measured flux. The measured values of ϕ_e and $\phi_{\mu,\tau}$ intersect at the point shown. The dashed line represents the SSM predicted value of which the ϕ_{NC} flux is consistent.

This was a pioneering result. The ratio $\phi_e/\phi_{\mu,\tau} = 0.52$ strongly refutes the no-oscillation hypothesis at 5.3σ with close to 50% of the total flux being contributions from non-electron neutrino types [27]. SNO had provided conclusive evidence

supporting the theory of neutrino oscillations as a solution to the solar neutrino problem.

SNO continued to run until 2006, operating over three phases. The first was the deuterium phase as described, ending in June 2001. The second involved adding 2 tonnes of NaCl to the D₂O. The idea being to use chlorine to capture the thermal neutrons produced by deuterium disintegration through the NC interaction;



The thermal neutron capture cross-section on chlorine is larger than deuterium ($\sigma({}^{35}\text{Cl}) \simeq 44 \text{ b}$, $\sigma({}^2\text{H}) \simeq 0.5 \text{ b}$) [28]. This subsequently gave improved statistics for the measurements of the NC interaction. The capture on chlorine also emits several gammas with a distinctive isotropy. When compared to the distribution of Cherenkov light, this allows for better discrimination between the NC and CC interactions. The salt phase ran for 391 live days, ending in October 2003.

The third and final phase of SNO saw the deployment of 36 vertical strings of ³He counters; an array of neutral current detectors (NCDs) into the detector. Each string was 9-11 m in length. The NCD phase ran for 385 live days between November 2004 and November 2006. By this time neutrino studies were concerned with precision measurements in order to obtain values of the parameters which characterised neutrino oscillations, see Section 1.2.3. The use of NCDs allowed SNO to make measurements of the NC interactions using a method independent to that from the previous two phases. Neutrons from the NC interactions were detected in an NCD as follows [29];



The wire in each ³He counter was kept at a high voltage meaning the energetic proton and tritium pair induced an avalanche of secondary ionisation whose current could be read out as a signal.

Support for neutrino oscillations as a solution to the solar neutrino problem was strong. However, several other theories to explain it remained in contention [30]. As will be discussed, the theory of oscillations is parameterised by mixing *angles*,

θ that characterise the amplitude of the oscillation between neutrino flavours, and *phases*, Δm^2 that control the rate at which this oscillation occurs. In addition, neutrinos travelling through matter, such as the Sun, are subject to resonant oscillation effects (discussed in Section 1.2.4). At the time, one hypothesis was that solar neutrinos underwent matter effects in the Sun that were subject to a large mixing angle (LMA). To test the LMA-matter solution, information about the phase, Δm^2 was required. Given the naturally large distance over which solar studies had detected neutrinos, they were only sensitive to the mixing angle; the phase was effectively averaged over. It was therefore desirable to design an experiment that was sensitive to this phase in order to test the LMA-matter solution to the solar neutrino problem.

1.2.1.4 KamLAND

KamLAND was designed to specifically test the LMA-matter solution using a terrestrial source of neutrinos. Located in the Kamioka mine, the detector consisted of a 6.5 m radius vinyl balloon filled with 1000 tonnes of liquid scintillator surrounded by \sim 1900 PMTs in an 18 m diameter steel spherical support sphere [31]. KamLAND studied anti-neutrinos produced in a variety of nuclear reactors in Japan over an average distance of 180 km from the detector. By using scintillator as its target material, the energy of the analysis threshold was lower than that of water Cherenkov experiments, $T_e \geq 2.6$ MeV. KamLAND observed anti-neutrino interactions through the inverse β -decay process;

$$\begin{aligned} \bar{\nu}_e + p &\rightarrow n + e^+, \\ &\hookrightarrow n + p \rightarrow {}^2\text{H} + \gamma \text{ [2.22 MeV]}. \end{aligned} \tag{1.29}$$

Coincidence detection of both the e^+ and the 2.22 MeV γ allowed KamLAND to significantly reduce background contributions. Given the energy of the reactor anti-neutrinos, \sim 3-5 MeV and the shorter distance from which the detector was situated to the source, KamLAND was sensitive to the cyclic nature of the oscillation as determined by the phase, Δm^2 , see Figure 1.7. After 145.1 live days between March and October 2002, KamLAND observed a deficit in electron

anti-neutrinos above 3.4 MeV, refuting a no-oscillation hypothesis [32];

$$\frac{\phi_{\bar{\nu}_e} [\text{Measured}]}{\phi_{\bar{\nu}_e} [\text{No Oscillation}]} = 0.611 \pm 0.085 \text{ (stat.)} \pm 0.041 \text{ (sys.)}. \quad (1.30)$$

As KamLAND collected further data, the uncertainties on the spectral information of the oscillation were reduced, and hence values of Δm^2 were determined with better precision.

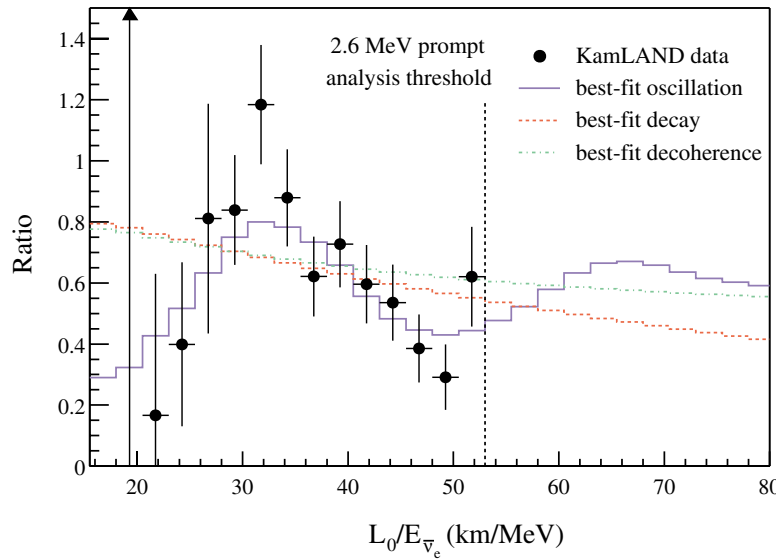


FIGURE 1.7: [33] The oscillation spectra of electron anti-neutrinos in KamLAND. The data (black) is in agreement with an oscillation spectrum generated, at the time, using the best-fit parameters available.

1.2.2 Atmospheric Neutrino Anomaly

Another early indicator of neutrino oscillations came from the Kamiokande experiment in 1988. When studying the flux of atmospheric neutrinos produced in the Earth's atmosphere (discussed in Section 1.2.5) Kamiokande observed electron-like events consistent with predictions, but a deficit in muon-like events, detecting only $59 \pm 7\%$ of what was expected [34]; this became known as the *atmospheric neutrino anomaly*. Further studies by Kamiokande suggested that such an anomaly could not be described by oscillation between electron and muon neutrinos ($\nu_e \leftrightarrow \nu_\mu$), and so an alternative channel, $\nu_\mu \leftrightarrow \nu_{\tau,x}$ was investigated [35, 36]. The larger scale of the Super-Kamiokande experiment increased the statistical significance of this

original result, demonstrating that the deficit in the atmospheric muon neutrino flux was consistent with neutrino oscillations, see Figure 1.8.

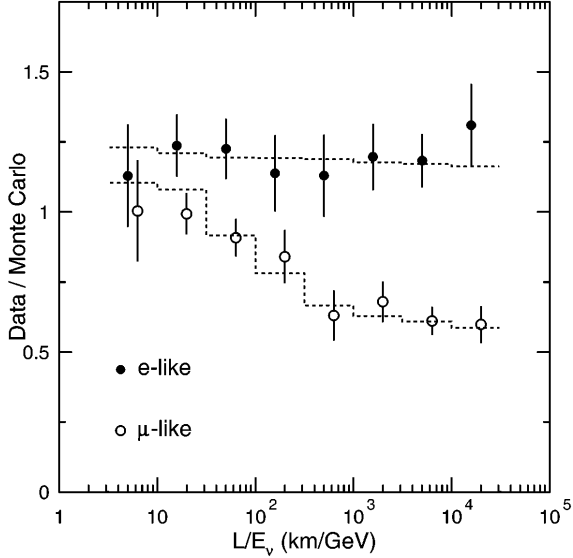


FIGURE 1.8: [37] Results from Super-Kamiokande: The points shown denote the ratio of observed electron- and muon-like events to the MC prediction assuming no oscillations. The dashed line denotes the value from a two-neutrino mixing scenario, $\nu_\mu \leftrightarrow \nu_{\tau,x}$, to which the data agrees well.

1.2.3 Neutrino Mixing and Oscillations

B. Pontecorvo first discussed the possibility of neutrino oscillations in 1957 [38]. Pontecorvo proposed that each neutrino flavour state is a linear superposition of three light neutrino mass states, each with a different mass (eigenvalue);

$$|\nu_\alpha\rangle = \sum_{k=1}^3 U_{\alpha k}^* |\nu_k\rangle, \quad \alpha = e, \mu, \tau. \quad (1.31)$$

The coefficients $U_{\alpha k}$ are elements of a unitary matrix, U known as the *Pontecorvo-Maki-Nakagawa-Sakata* (PMNS) mixing matrix, the structure of which is analogous to the CKM mixing matrix between the three quark generations. U is parameterised by three mixing angles, $\theta_{12}, \theta_{23}, \theta_{13}$ and a *charge-parity* (CP) phase,

δ_{CP} ;

$$U = \begin{pmatrix} c_{12}c_{13} & s_{12}c_{13} & s_{13}e^{-i\delta_{\text{CP}}} \\ -s_{12}c_{23} - c_{12}s_{23}s_{13}e^{i\delta_{\text{CP}}} & c_{12}c_{23} - s_{12}s_{23}s_{13}e^{i\delta_{\text{CP}}} & s_{23}c_{13} \\ s_{12}s_{23} - c_{12}c_{23}s_{13}e^{i\delta_{\text{CP}}} & -c_{12}s_{23} - s_{12}c_{23}s_{13}e^{i\delta_{\text{CP}}} & c_{23}c_{13} \end{pmatrix}, \quad (1.32)$$

where $c_{ij} \equiv \cos \theta_{ij}$ and $s_{ij} \equiv \sin \theta_{ij}$ [39]. In vacuum, the temporal evolution of the mass states is governed by the time-dependent Shrödinger equation;

$$\mathcal{H}_0|\nu_k\rangle \equiv i\frac{d}{dt}|\nu_k\rangle = E_k|\nu_k\rangle. \quad (1.33)$$

As each mass is different, these states evolve in time with varying phases, leading to transitions between flavour states with a non-zero probability. The general form of the neutrino oscillation probability can be written as follows;

$$P_{\nu_\alpha \rightarrow \nu_\beta}(L, E_\nu) = \sum_{k,j=1}^3 U_{\alpha k}^* U_{\beta k} U_{\alpha j} U_{\beta j}^* \exp\left(-i\frac{\Delta m_{kj}^2 L}{2E_\nu}\right), \quad (1.34)$$

where E_ν is the neutrino energy and L is the propagation distance, often referred to as the *baseline*. The probability depends on $\theta_{12}, \theta_{23}, \theta_{13}, \delta_{\text{CP}}$ and two linearly independent mass-squared differences;

$$\Delta m_{21}^2 = m_2^2 - m_1^2, \quad (1.35)$$

$$\Delta m_{31}^2 = m_3^2 - m_1^2. \quad (1.36)$$

In the context of neutrino oscillation experiments, the phenomena is best illustrated by considering mixing between just two neutrino generations. In such a scenario, the flavour eigenstates are related to the mass eigenstates by the following unitary transformation;

$$\begin{pmatrix} |\nu_\alpha\rangle \\ |\nu_\beta\rangle \end{pmatrix} = \begin{pmatrix} \cos \theta & \sin \theta \\ -\sin \theta & \cos \theta \end{pmatrix} \begin{pmatrix} |\nu_i\rangle \\ |\nu_j\rangle \end{pmatrix}. \quad (1.37)$$

By use of Equation 1.34, an expression for the neutrino *disappearance* probability, $P_{\nu_\alpha \rightarrow \nu_\beta}$ in vacuum can be obtained;

$$P_{\nu_\alpha \rightarrow \nu_\beta}(L, E_\nu) = \sin^2(2\theta) \sin^2\left(\frac{\Delta m^2 L}{4E_\nu}\right), \quad (1.38)$$

where the complementary *survival* probability is simply $P_{\nu_\alpha \rightarrow \nu_\alpha} = 1 - P_{\nu_\alpha \rightarrow \nu_\beta}$. The disappearance probability therefore has a maximum amplitude of $\sin^2(2\theta)$ which completes one full oscillation over a length;

$$L^{\text{osc}} = \frac{4\pi E_\nu}{\Delta m^2}. \quad (1.39)$$

This implies that for an appropriate neutrino energy, experiments observing neutrino oscillations over different baselines will be sensitive to different values of Δm^2 . In general, long baseline experiments are sensitive to small values of Δm^2 , and short baselines are sensitive to larger values of Δm^2 . If the baseline of an experiment is much greater than the oscillation length, the total probability will be averaged over the oscillating phase characterised by Δm^2 , see Figure 1.9.

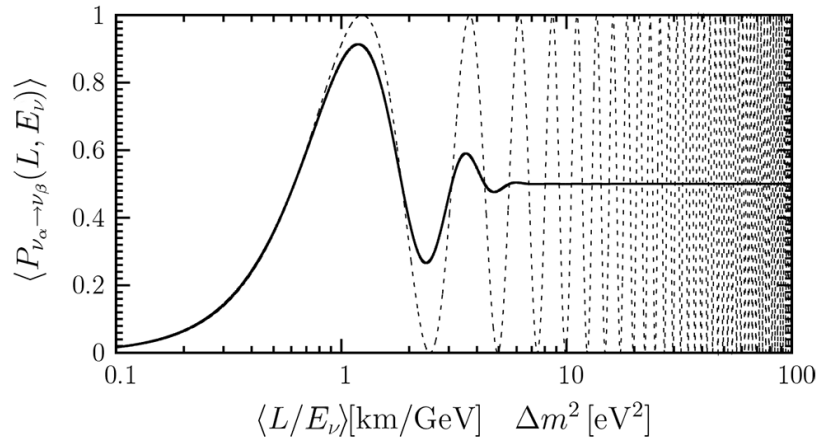


FIGURE 1.9: [12] The averaging of the neutrino oscillation probability, $P_{\alpha \rightarrow \beta}$ (solid line) over the Δm^2 phase (dashed line) with L/E_ν .

From the above formalism it is clear that neutrino oscillations in vacuum are sensitive to only the mass squared differences, and hence do not reveal an absolute mass scale of the three neutrino masses, m_1, m_2 and m_3 . As determined by the solar experiments, Δm_{21}^2 is positive definite through confirmation of the matter effects in the sun. The sign of Δm_{31}^2 has not yet been determined to a sufficient

level of significance, so far only the relative sizes of the two parameters has been deduced; $|\Delta m_{31}^2| \gg |\Delta m_{21}^2|$. This means that two mass hierarchies are possible;

$$\text{Normal Hierarchy (NH): } \Delta m_{31}^2 > 0 : m_3 \gg m_2, m_1, \quad (1.40)$$

$$\text{Inverted Hierarchy (IH): } \Delta m_{31}^2 < 0 : m_3 \ll m_2, m_1. \quad (1.41)$$

The values of all six parameters $\theta_{12}, \theta_{23}, \theta_{13}, \Delta m_{21}^2, \Delta m_{31}^2$ and δ_{CP} are determined by experiment. Experiments are designed with the ratio L/E_ν in mind, strategically situating their sensitivities to oscillation maxima and minima in order to probe the parameter space.

1.2.4 Neutrino Oscillations in Matter

Within ten years of the Homestake result a theory of neutrino oscillations in matter had been developed, later known as the *Mikheyev-Smirnov-Wolfenstein* (MSW) effect. First introduced by L. Wolfenstein in 1978, the MSW effect describes the resonance enhancement of neutrino oscillations involving electron-neutrino states in matter [40]. This arises because matter is composed of atoms; nuclei and electrons, rather than nuclei and muon or tau particles. As a result, electron-neutrinos are subject to both charged- as well as neutral-current interactions when propagating through matter; muon- and tau-neutrinos are restricted to only the neutral-current interaction. The charged-current interaction therefore subjects the electron-neutrino to an additional non-zero potential, A_{CC} which contributes to the Hamiltonian as expressed in Equation 1.33;

$$A_{\text{CC}} = \pm 2\sqrt{2}E_\nu G_F N_e, \quad (1.42)$$

where G_F is the Fermi constant and N_e is the electron density of the matter. The value of A_{CC} is positive for electron-neutrinos and negative for electron-anti-neutrinos. This potential term manifests as a new mass-squared difference, Δm_M^2 and mixing angle, θ_M , different to those in vacuum, which control the evolution of the oscillating neutrino state in matter. For the case of two-neutrino mixing as

previously discussed, these can be written as follows;

$$\Delta m_{21,M}^2 = \sqrt{(\Delta m_{21}^2 \cos(2\theta_{12} - A_{CC}))^2 + (\Delta m_{21}^2 \sin(2\theta_{12}))^2}, \quad (1.43)$$

$$\tan(2\theta_{12,M}) = \frac{\tan(2\theta_{12})}{1 - (A_{CC}/\Delta m_{21}^2 \cos(2\theta_{12}))}. \quad (1.44)$$

An interesting scenario is when,

$$A_{CC} \rightarrow \Delta m_{21}^2 \cos(2\theta_{12}) \Rightarrow \tan(2\theta_{12,M}) \rightarrow \infty, \quad (1.45)$$

giving rise to a resonance in the mixing which corresponds to complete transitions of the initial flavour states ². This is equivalent to the following electron number density of the matter;

$$N_e = \frac{\Delta m_{21}^2 \cos(2\theta_{12})}{2\sqrt{2}E_\nu G_F}. \quad (1.46)$$

It is of experimental interest that the potential is reversed for electron anti-neutrinos ($A_{CC} \rightarrow -A_{CC}$), leading to different values of $\Delta m_{21,M}^2$ and $\theta_{12,M}$. In a full three-flavour mixing paradigm, the transition probability between any two flavour states is dependent on all six of the neutrino oscillation parameters: θ_{12} , θ_{23} , θ_{13} , Δm_{21}^2 , Δm_{31}^2 and δ_{CP} . Two outstanding issues which have yet to be experimentally determined are the mass hierarchy i.e. the sign of Δm_{31}^2 as previously mentioned, and the value of δ_{CP} . By studying the neutrino oscillation channels $\nu_\mu \rightarrow \nu_e$ and $\bar{\nu}_\mu \rightarrow \bar{\nu}_e$ at the Δm_{31}^2 baseline, experiments are sensitive to a residual probability difference between these two channels which is attributed to sub-leading matter effects and CP-violation. This residual term being proportional to Δm_{31}^2 and δ_{CP} [41, 42];

$$\begin{aligned} P_{\nu_\mu \rightarrow \nu_e} - P_{\bar{\nu}_\mu \rightarrow \bar{\nu}_e} = & \frac{16 |A_{CC}|}{\Delta m_{31}^2} \sin^2 \left(\frac{\Delta m_{31}^2 L}{4E_\nu} \right) c_{13}^2 s_{13}^2 s_{23}^2 (1 - 2s_{13}^2) \\ & - \frac{2 |A_{CC}| L}{E_\nu} \sin \left(\frac{\Delta m_{31}^2 L}{4E_\nu} \right) c_{13}^2 s_{13}^2 s_{23}^2 (1 - 2s_{13}^2) \\ & - \frac{4\Delta m_{21}^2 L}{E_\nu} \sin^2 \left(\frac{\Delta m_{31}^2 L}{4E_\nu} \right) \sin \delta_{CP} s_{13} c_{13}^2 c_{23} s_{23} c_{12} s_{12}. \end{aligned} \quad (1.47)$$

²This is effectively what happens to neutrinos produced in the Sun.

As the complexity of the above expression suggests, resolving the sign of Δm_{31}^2 and the value of δ_{CP} is difficult. However, for a sufficiently long baseline, L the above expression becomes more sensitive to the value of δ_{CP} . Next generation experiments such as DUNE/LBNF [43] and Hyper-Kamiokande [44] have been proposed to make this measurement.

1.2.5 Neutrino Oscillation Experiments

As mentioned, neutrino oscillation experiments are attuned to the ratio L/E_ν in order to probe the oscillation parameter space which controls the rate of neutrino appearance and disappearance. This is done either by controlling the baseline, L , the neutrino energy, E_ν or both. For studies of natural neutrino sources e.g. solar and atmospheric neutrinos, this ratio is effectively fixed and the measured flux is relatively small. Instead, by using an artificially intense neutrino source e.g. nuclear reactors or an accelerator based neutrino beam, a category of experiments known as *baseline* experiments are able to situate their detectors at a fixed short- or long-baseline from the source. Through a combination of solar, atmospheric, short- and long-baseline experiments, a complete determination of the neutrino oscillation parameters is possible.

Determination of θ_{12} and Δm_{21}^2

Solar and short-baseline reactor neutrino studies ($E_\nu \sim O(\text{MeV})$) are sensitive to the mass squared difference Δm_{21}^2 and the mixing angle θ_{12} . Studies of electron-neutrino disappearance of the solar ${}^8\text{B}$ -neutrino flux by SK and SNO provide accurate measurements for θ_{12} . In addition, KamLAND has contributed to this *solar* parameter space with precision measurements of Δm_{21}^2 by looking at electron anti-neutrino disappearance.

Determination of θ_{23} and Δm_{31}^2

Early values of Δm_{31}^2 and θ_{23} originally came from measurements of ν_μ -disappearance in atmospheric data by SK [37]. This was itself prompted by the earlier indication of a missing atmospheric neutrino flux by Kamiokande as discussed in Section 1.2.2. Neutrinos are produced in the atmosphere as the result of hadronic interactions

of cosmic rays (mostly protons) with nuclei in the Earth's atmosphere e.g.

$$\begin{aligned} p + X &\rightarrow Y + \pi^\pm, \\ \hookrightarrow \pi^\pm &\rightarrow \mu + \nu_\mu, \end{aligned} \tag{1.48}$$

$$\hookrightarrow \mu \rightarrow e + \nu_e + \nu_\mu, \tag{1.49}$$

where X and Y are nuclei. The charge conjugated versions of the above interactions occur with equal frequency, providing an atmospheric flux ratio of $(\phi_{\nu_\mu} + \phi_{\bar{\nu}_\mu}) / (\phi_{\nu_e} + \phi_{\bar{\nu}_e}) \simeq 2$. These atmospheric neutrinos are produced over a broad energy spectrum between 0.1-100 GeV, that peaks around 1 GeV. To leading order, the *atmospheric* parameters Δm_{31}^2 and θ_{23} characterise the probability of ν_μ -disappearance. The SK result was obtained by observing ν_μ and ν_e quasi-elastic scattering off of nuclei (e.g. oxygen) through charged-current interactions, categorising events as either muon-like or electron-like. By demonstrating that a two neutrino mixing hypothesis for the $\nu_\mu \leftrightarrow \nu_e$ channel was incompatible with data, SK inferred the $\nu_\mu \leftrightarrow \nu_\tau$ channel as the cause for the observed ν_μ -disappearance.

Currently, the most precise measurements of the atmospheric parameters are from accelerator based long-baseline experiments. These experiments use accelerator facilities to artificially create an intense beam of ν_μ or $\bar{\nu}_\mu$. The accelerator collides protons into a target (e.g. graphite or beryllium), producing many mesons, mostly pions (and some kaons). The pions are focussed into a beam directed at the far detector using strong magnets, and proceed to decay as in expressions 1.48 and 1.49. By using magnets to focus either particles or anti-particles, accelerator baseline experiments can be ran in neutrino or anti-neutrino modes. The leading measurements of Δm_{31}^2 come from two recent accelerator long-baseline experiments, MINOS and T2K [45, 46]. The latter of these two has also provided the current best measurement of θ_{23} [47].

An outstanding issue with the measurement of θ_{23} is which octant its value is in. In a two-neutrino mixing picture, the measurement of the $\nu_\mu \leftrightarrow \nu_\tau$ channel is actually sensitive to $\sin^2(2\theta_{23})$; it is surjective in θ_{23} . Consequently there are two qualifying values of θ_{23} , see Figure 1.10. Current data favours different octant values based on the nature of the neutrino mass hierarchy.

Determination of θ_{13}

Until relatively recently, the value of θ_{13} was the least well known of the mixing angles, some theories even considered it to be zero ($\theta_{13}, \delta_{\text{CP}} = 0$, see *tri-bimaximal* mixing [48]). This changed however in the years 2010-11 as the T2K experiment reported six events in the $\nu_\mu \rightarrow \nu_e$ channel after its first two runs of collecting physics data. The electron-neutrino appearance was an indication of $\theta_{13} \neq 0$ and as such T2K provided an early indication to the value of θ_{13} at a 90% confidence level; $0.03(0.04) < \sin^2(2\theta_{13}) < 0.28(0.34)$ for normal (inverted) hierarchies [49]. A statistically more significant result followed with the advent of the Daya-Bay experiment; a short baseline experiment studying reactor anti-neutrinos. Daya-Bay provided evidence for $\theta_{13} \neq 0$ at 5.2σ after collecting 55 live days worth of data between the end of 2011 and early 2012. Daya-Bay probed the $\bar{\nu}_e$ survival probability which for short baselines can be approximated as follows;

$$P_{\bar{\nu}_e \rightarrow \bar{\nu}_e} \simeq 1 - \sin^2(2\theta_{13}) \sin^2\left(\frac{\Delta m_{13}^2 L}{4E_\nu}\right). \quad (1.50)$$

Note that the structure of this expression is simply the complement of the oscillation probability in Equation 1.38. Further to the Daya-Bay result, not only was θ_{13} non-zero, but it was also larger than originally anticipated, $\theta_{13} \sim 9^\circ$. Given the relationship between θ_{13} and δ_{CP} in the PMNS matrix, the size of θ_{13} provides a good opportunity to probe δ_{CP} in future long-baseline experiments. Current values for the neutrino oscillation parameters (including primitive esitmates for δ_{CP}) from a combined global analysis are shown in Figure 1.10.

Three decades after the original Homestake result, experiments have ultimately confirmed flavour transmutation in the neutrino sector. Through various technique, and by studying neutrino fluxes from different sources, a more complete understanding of neutrino oscillations as well as the eponymous particle itself has been revealed. Most prominently, these studies have led to the conclusion that the neutrino has a small but non-zero mass i.e. $m_\nu \neq 0$. Neutrino oscillations therefore provide evidence of physics beyond the standard model. This is a pioneering discovery that has led to the recognition of the original work done by R. Davis at Homestake and M. Koshiba at Kamiokande. In 2002, they were awarded the Nobel prize for the detection of cosmic neutrinos; those from the Sun and supernova 1987A [52]. More recently, A. McDonald and T. Kajita received the

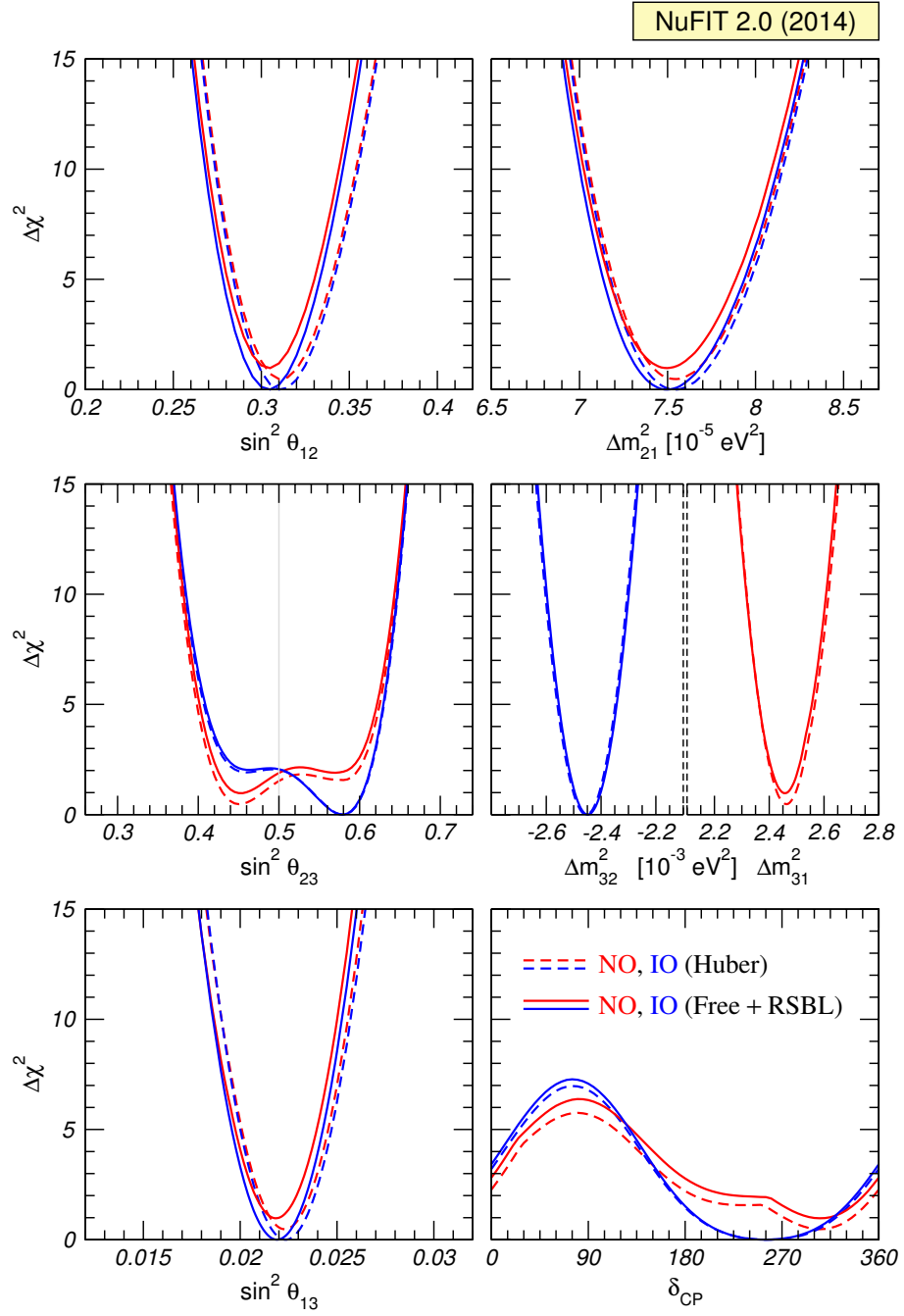


FIGURE 1.10: [50] Current estimates for the neutrino mixing oscillation parameters. Values are taken from [51]. The estimates include those with, and without short baseline reactor (RSBL) neutrino data. Values are shown for both currently possible mass hierarchies; normal (red) and inverted (blue).

same accolade in 2015 for their respective work on the SNO and T2K experiments which contributed to the discovery of neutrino oscillations.

1.3 Nature of the Neutrino Mass

The existence of a neutrino mass provides ample motivation to conjecture the mechanism by which this mass arises, and to search for any inherent new physics that manifest. However, before such searches begin, determining the nature of the neutrino itself is essential. *Nature* being the phenomenological description of the neutrino, either as a Dirac or Majorana particle.

1.3.1 Dirac Neutrino Masses

SM neutrinos are members of an $SU(2)_L$ doublet, $L_{\alpha L}$ (as in Expression 1.1), whose massless states are described by single left-handed chiral fields, $\nu_{\alpha L}$. These fields satisfy the Weyl equation;

$$i\gamma^\mu \partial_\mu \nu_{\alpha L} = 0. \quad (1.51)$$

In order to obtain a mass one can treat neutrinos as Dirac particles alongside the other SM fermions whose masses are obtained through the Higgs mechanism. These Dirac masses require couplings of both left- and right-handed fields in the Lagrangian mass term, \mathcal{L}_ν^{DM} of the form;

$$-\mathcal{L}_\nu^{DM} = m\overline{\nu_{\alpha L}}\nu_{\alpha R}, \quad \alpha = e, \mu, \tau \quad \overline{\nu_{\alpha L}} = \nu_{\alpha L}^\dagger \gamma^0. \quad (1.52)$$

Consequently, for such field couplings to be possible for neutrinos, an extension to the SM is required in the form of additional right handed neutrino fields, $\nu_{\alpha R}$. These fields are singlets under $SU(2)_L \times U(1)_Y$ and are often referred to as *sterile* as they do not participate in weak interactions and have zero isospin ($I = 0$) and hypercharge ($Y = 0$). The SM can be arbitrarily extended by any number of sterile fields. In the natural extension with three additional right-handed fields, $\nu_{\alpha R}$ ($\alpha = e, \mu, \tau$) the diagonalised Higgs-lepton Lagrangian reads;

$$-\mathcal{L}_{\text{Higgs-lepton}}^{DM} = \left(\frac{v + H}{\sqrt{2}} \right) \left[\sum_{\alpha=e,\mu,\tau} y_\alpha^\ell \overline{\ell_{\alpha L}} \ell_{\alpha R} + \sum_{k=1}^3 y_k^\nu \overline{\nu_{k L}} \nu_{k R} \right] + \text{H.c.} , \quad (1.53)$$

where H is the Higgs field, v is the Higgs *vacuum expectation value* (VEV), ~ 246 GeV and H.c. is the hermitian conjugate term. The y_α^ℓ and y_k^ν terms are real and positive elements of two separate diagonalised matrices of *Yukawa* couplings. Here, ν_k are the massive neutrino fields which are related to ν_α by the unitary transformation in Equation 1.31. The following neutrino masses arise from the Higgs mechanism following electro-weak symmetry breaking;

$$m_k = \frac{y_k^\nu v}{\sqrt{2}}, \quad k = 1, 2, 3. \quad (1.54)$$

These masses are proportional to the Higgs VEV, as are the charged lepton masses. However, limits on the neutrino mass bound its size to no more than 2 eV [53]. Given the size of the Higgs VEV, y_k^ν is thus required to be $O(10^{-12})$ GeV. This is problematic since the SM does not account for the size of the Yukawa couplings. Other than convenience, there is no just cause for including such small values of y_k^ν . The Higgs mechanism then is unsatisfactory in explaining the source of the neutrino mass. If instead the neutrino is assumed to behave as a Majorana particle, then the origin of its mass may become closer to being understood.

1.3.2 Majorana Neutrino Masses

The motivation behind Majorana particles lies in considering the following question:

Q. *What is the smallest component formalism required to describe a massive fermion?*

In 1937, E. Majorana looked to answer this question in response to P. Dirac's four component spinor theory of electrons and positrons [54]. Majorana devised that massive fermions could in fact be described by two-component spinors, alleviating the constraint of two additional *negative* energy states present in Dirac's theory. This is achieved provided the fermion field, $\psi = \psi_L + \psi_R$ satisfies the *Majorana condition*;

$$\psi = \psi^c \quad \text{with} \quad \psi^c = C \bar{\psi}^T, \quad C = i\gamma_0\gamma_2, \quad (1.55)$$

where ψ^c is the *charge conjugated* field and C is the charge conjugate operator. The reduction of four component Dirac spinors into the two component theory proposed by Majorana requires that the left- and right-handed fields, ψ_L and ψ_R , be somehow related. In fact, it can be shown that ψ_L^c is right handed and ψ_R^c is left handed, i.e.

$$P_L \psi_L^c = 0, \quad P_R \psi_R^c = 0, \quad P_{\frac{R}{L}} = \frac{1}{2} (1 \pm \gamma_5). \quad (1.56)$$

Equation 1.55 manifestly imposes equality between particles and anti-particles, meaning physically, Majorana particles must be neutrally charged. With a non-zero mass inferred by neutrino oscillations, and being the only known neutral fermion, the neutrino is the best current candidate for being a Majorana particle and provides reason to consider Majorana mass terms.

Similarly to Dirac mass terms, Majorana masses arise from the coupling of left- and right-handed fields,

$$\begin{aligned} -\mathcal{L}_\nu^{MM} &= \frac{1}{2} m (\overline{\nu_{\alpha L}} \nu_{\alpha L}^c + \overline{\nu_{\alpha L}^c} \nu_{\alpha L}) \\ &= \frac{1}{2} m (\overline{\nu_{\alpha L}} C \overline{\nu_{\alpha L}}^T - \nu_{\alpha L}^T C^\dagger \nu_{\alpha L}), \end{aligned} \quad (1.57)$$

where the factor of $1/2$ is to avoid double counting, as the left- and right-handed fields are related. However, these $\nu_{\alpha L}$ fields are members of an SM doublet, $L_{\alpha L}$. Hence, each mass term behaves as an isospin triplet ($I_3 = 1$) with hypercharge $Y = -2$. Consequently, the above mass term does not leave the Lagrangian invariant. In fact, construction of a Majorana mass using only SM fields requires two Higgs doublets, Φ forming the non-renormalisable dimension-5 operator, $(LH)^2$ [55];

$$(LH)^2 = \frac{g}{\mathcal{M}} (L_{\alpha L}^T \tau_2 \Phi) C^\dagger (\Phi^T \tau_2 L_{\alpha L}) + \text{H.c.} . \quad (1.58)$$

Here, τ_2 is the Pauli matrix and g/\mathcal{M} is a new coupling of dimension E^{-1} which is required to maintain the correct dimensions of the Lagrangian. The following Majorana mass is generated,

$$m_\nu = \frac{gv^2}{\mathcal{M}}. \quad (1.59)$$

To be in agreement with the current bounds on the neutrino mass, the coupling g/\mathcal{M} must be $O(10^{-15})$ GeV), suppressed by some large mass, \mathcal{M} existing near the energy scale of *Grand Unification Theories* (GUT), $\sim 10^{15}$ GeV. However, it should also be acknowledged that this is the only Majorana mass which can be constructed using the low-energy theory that the Standard Model outlines. Therefore, there is no reason to exclude similar masses from a possible BSM source existing at higher energies. In many phenomenological models, Majorana contributions to the neutrino mass of the form in Equation 1.57 come from sterile fields, $\nu_{\alpha R}$ whose Majorana mass terms behave as singlets of the SM symmetries, leaving the Lagrangian invariant. These Majorana contributions feature in what are known as type-I see-saw mechanisms, in which the smallness of the neutrino mass is resolved through the existence of heavy sterile neutrinos [56]. This is of particular interest to phenomenologists, as these heavy neutrinos can be used propagate leptogenesis and subsequently CP violation in cool-down models of the early universe [57].

1.3.3 Lepton Number Violation

A Majorana neutrino will interact differently than a Dirac neutrino. Specifically, a particle being its own anti-particle will mediate new physics such as lepton number violation (LNV). The concept of lepton number is illustrated by considering the following local U(1) gauge transformations of the lepton fields [12];

$$\nu_{kL} \rightarrow e^{i\phi} \nu_{kL}, \quad \nu_{kR} \rightarrow e^{i\phi} \nu_{kR}, \quad k = 1, 2, 3, \quad (1.60)$$

$$\ell_{\alpha L} \rightarrow e^{i\phi} \ell_{\alpha L}, \quad \ell_{\alpha R} \rightarrow e^{i\phi} \ell_{\alpha R}, \quad \alpha = e, \mu, \tau. \quad (1.61)$$

Invariance of the Lagrangian under these transformations conserves lepton number. Leptons have a lepton number of $L = +1$ and anti-leptons have a lepton number of $L = -1$. By considering the behaviour of the left-right field couplings in the Dirac and Majorana mass terms of equations 1.52 and 1.57 under these transformations, it is observed that Dirac neutrinos conserve lepton number whereas Majorana neutrinos do not;

$$\text{Dirac : } \overline{\nu_{kL}} \nu_{kR} \longrightarrow \overline{\nu_{kL}} e^{-i\phi} \nu_{kR} e^{i\phi} = \overline{\nu_{kL}} \nu_{kR}, \quad (1.62)$$

$$\text{Majorana : } \overline{\nu_{\alpha R}^c} \nu_{\alpha R} = -\nu_{\alpha R}^T C^\dagger \nu_{\alpha R} \longrightarrow -e^{i2\phi} \nu_{\alpha R}^T C^\dagger \nu_{\alpha R}. \quad (1.63)$$

Phenomenologically, Majorana masses would modify the PMNS matrix. Mathematically, an $n \times n$ unitary matrix (such as the PMNS matrix) is parameterised by $n(n - 1)/2$ mixing angles and $n(n + 1)/2$ complex phases. For $n = 3$ this leads to three mixing angles and six phases. However, in the case of Dirac particles five of these phases can be eliminated through a rephasing of the lepton fields, and thus reduce the parameterisation to three mixing angles and just one phase, δ_{CP} . However, it is clear that a rephasing of the Majorana fields as above cannot be performed to the same extent. Consequently, if neutrinos are Majorana particles there can exist additional Majorana CP-violating phases in the mixing matrix. These are associated with the neutrino masses, modifying the PMNS by multiplying it with a diagonal matrix of Majorana phases, $D = \text{diag}(1, e^{i\alpha_1}, e^{i\alpha_2})$ i.e. $U \rightarrow UD$.

All SM interactions conserve lepton number, however, it is only an accidental symmetry of the theory. Due to the construction of the Majorana fields presented here, wherein the left- and right-handed fields are related to one another, the field transformations leave an overall residual phase. Majorana particles then mediate lepton number violation. One LNV process is called neutrinoless double β -decay ($0\nu\beta\beta$ -decay). Yet to be experimentally observed, verification of such a process would further elucidate the nature of the neutrino and its mass. This is discussed in Section 1.4.1.

1.4 Detection of the Neutrino Mass

The study of atmospheric, solar, reactor and accelerator based neutrino sources has provided sufficient evidence of at least three neutrino mass eigenstates. However, the study of oscillations does not discern the nature, Dirac or Majorana or the absolute scale at which these eigenstates exist. In general, there are three methods through which the neutrino mass scale can be inferred; cosmological studies, direct detection and $0\nu\beta\beta$ -decay.

The neutrino mass scale is of interest in cosmological models in the form of the neutrino eigenstate mass sum, $\sum_i^\nu m_i$. The sum is often used as a parameter which drives structure formation in the early universe from which a large abundance of *relic* neutrinos were left over. Current models combined with recent Planck data constrain $\sum_i^\nu m_i \leq 0.23 \text{ eV}$ [7]. Similar to the relic photons of the cosmic microwave

background, relic neutrinos are expected to constitute a similar *cosmic neutrino background* (CNB). The CNB has yet to be experimentally verified, although its existence has been inferred through several other cosmological observables [58]. The PTOLEMY experiment, currently in a prototype phase intends to search for relic neutrinos through neutrino capture on tritium [59].

Interpretation of a neutrino mass through cosmological data is highly analysis and model dependent, and ultimately only provides an upper-bound on the sum of the masses. An alternative route is through direct mass detection by studying weak decays of the form;

$$X \rightarrow Y + e^- + \bar{\nu}_e. \quad (1.64)$$

Here, the determination of the mass is purely kinematic and model independent. Relative to the recoiling nucleus, the electron and neutrino share the majority of the energy released; the Q -value. The energy is distributed between the two particles statistically, characterised by the distribution of emitted electron energies known as the β -spectrum. Even if the electron takes all of the available energy, some residual energy must remain for the rest mass of the neutrino and hence the end-point of the β -spectrum should have a well defined cut-off. This was originally noted by Fermi [60]. Naturally, the frequency of electrons with such high energies is small, and hence detection through this method requires exquisite energy resolution. From end-point measurements, the average squared neutrino mass is determined [53];

$$m^2(\bar{\nu}_e) = \sum_{i=1}^3 |U_{ei}|^2 m_i^2. \quad (1.65)$$

As the particles are released in their flavour eigenstates (i.e. electron), the observed mass is the coherent sum of the electron anti-neutrino mass eigenstates. Figure 1.11 illustrates the differences in the β -spectrum endpoint region between a massive and massless neutrino scenario. It is important to note that for massive neutrinos, there is both an end-point cut-off and a distortion in the overall spectrum itself. The KATRIN experiment plans to perform an end-point study of tritium. Tritium is ideal for such studies because of its small Q -value = 18.58 keV, meaning that distortions from massive neutrinos are a larger fraction of the

total spectrum. KATRIN is expected to have a sensitivity to a neutrino mass of 200 meV (90% C.L.) [61].

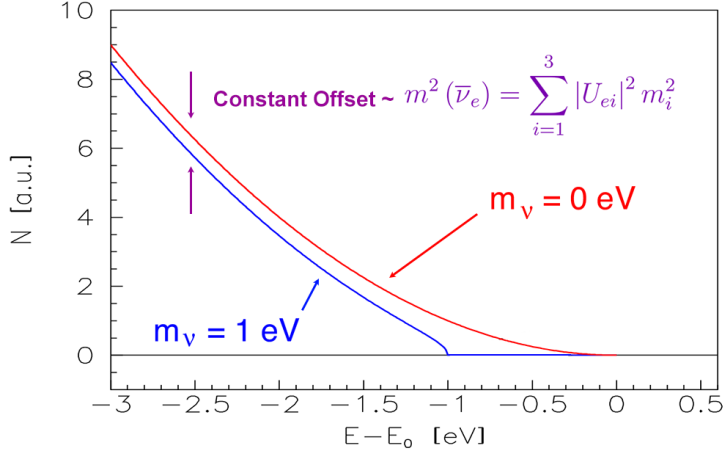
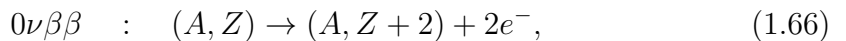


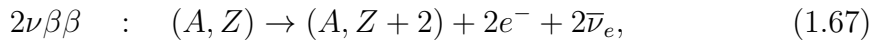
FIGURE 1.11: Illustrative diagram of the β -spectrum for electron energies, E relative to the Q -value, E_0 in two neutrino mass scenarios; massless (red) and massive (blue). In the massive regime there is a well defined cut-off 1eV from E_0 . In the massless case the spectrum is continuous up to E_0 . Plot is a modified version of that originally appearing in [62].

1.4.1 Neutrinoless Double β -Decay

Neutrinoless double beta decay is a hypothesised lepton number violating process mediated by BSM physics; this includes Majorana neutrinos. $0\nu\beta\beta$ -decay involves the emission of two electrons following the decay of a parent nuclei;



with atomic mass, A and proton number, Z . This process violates lepton number, $\Delta L = +2$. This is in contrast to conventional double β -decay ($2\nu\beta\beta$ -decay) in which two electron anti-neutrinos and two electrons are emitted;



for which lepton number is conserved, $\Delta L = 0$. $2\nu\beta\beta$ -decay occurs in isotopes where it is energetically more favourable for two nucleons within the nuclei to decay rather than one (standard β -decay). If neutrinos are indeed Majorana in

nature, a small branching fraction of the decays of these isotopes should be through $0\nu\beta\beta$ -decay. The tree-level Feynman diagrams for $2\nu\beta\beta$ -decay and $0\nu\beta\beta$ -decay are shown in Figure 1.12. In $0\nu\beta\beta$ -decay the neutrino acts as a fermionic propagator between the two electron vertices. This is only possible if the neutrino is a Majorana fermion; the two anti-neutrino vertices of the $2\nu\beta\beta$ -decay process are joined, where an anti-neutrino emitted from one vertex is absorbed as a neutrino with matching helicity by the other i.e. $\nu_e = \bar{\nu}_e$. This is prohibited by the massless description of neutrinos in the SM, $\nu_e \neq \bar{\nu}_e$ whose purely left- and right-handed fields result in a mismatch between positive and negative helicities. Both these issues are resolved by a massive Majorana neutrino, $m_\nu \neq 0$, $\nu_e = \bar{\nu}_e$. The helicity matching is made possible only through suppression of the state by a factor of m_ν/E at one of the vertices. This description of $0\nu\beta\beta$ -decay, mediated by a light Majorana neutrino, is known as the *light* neutrino exchange model. Ultimately, $0\nu\beta\beta$ -decay is a process in which only two electrons are emitted; a different, perhaps more exotic, BSM theory could similarly mediate the process. Hence $0\nu\beta\beta$ -decay studies are not technically a neutrino mass experiment in the same vein as experiments such as KATRIN are.

The $0\nu\beta\beta$ -decay rate is as follows [56]:

$$\Gamma^{0\nu\beta\beta} = G^{0\nu\beta\beta}(Q, Z) \left| \mathcal{M}_{A,Z}^{0\nu\beta\beta} \right| \langle m_{\beta\beta} \rangle^2, \quad (1.68)$$

where $G^{0\nu\beta\beta}(Q, Z)$ is the phase space factor which describes the physics of the final emitted states; it is proportional to Q^5 . $\left| \mathcal{M}_{A,Z}^{0\nu\beta\beta} \right|$ is the nuclear matrix element (NME), describing the energetic transition of the nuclei between its initial and final state, and $\langle m_{ee} \rangle$ is the *effective* neutrino mass;

$$\langle m_{\beta\beta} \rangle = \sum_{i=1}^3 |U_{ei}|^2 m_i = \left| |U_{e1}|^2 m_1 + |U_{e2}|^2 m_2 e^{i2\alpha_1} + |U_{e3}|^2 m_3 e^{i2\alpha_2} \right|, \quad (1.69)$$

where the above assumes the light neutrino exchange model as described. In this scenario the effective mass is dependent on the parameters of neutrino oscillation physics, where α_1 and α_2 are the additional Majorana phases. Note the additional dependency on α_1 and α_2 in comparison to Equation 1.65. Whilst end-point studies are not sensitive to a Majorana phase, they provide constraints on measurements of the effective Majorana neutrino mass from $0\nu\beta\beta$ -decay experiments. As illustrated in Figure 1.13 the $\langle m_{\beta\beta} \rangle$ parameter space is different for either normal or inverted

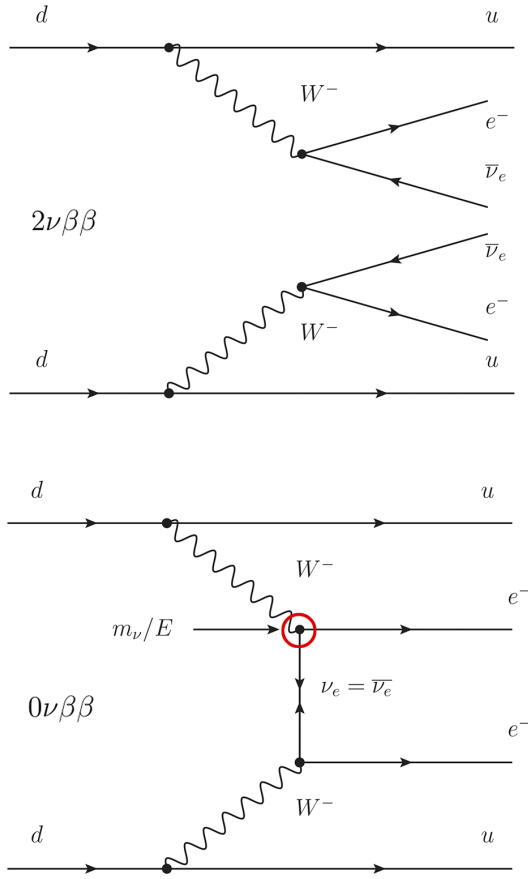


FIGURE 1.12: Top: tree level Feynman diagram of $2\nu\beta\beta$ -decay allowed within the SM framework. Bottom: lepton number violating, $0\nu\beta\beta$ -decay permitted by the Majorana neutrino acting as a propagator between the two leptonic vertices.

hierarchies. Furthermore, from Equation 1.68 it is evident that the half-life of the process is also related to the effective mass of the neutrino, $t_{1/2}^{0\nu\beta\beta} \propto 1/\Gamma^{0\nu\beta\beta} \propto \langle m_{\beta\beta} \rangle^{-2}$. Therefore an experimental observation of $0\nu\beta\beta$ -decay probes both the nature and (effective) mass scale of the neutrino. Depending on the true state of the mass hierarchy, and assuming a lightest neutrino mass of 0.01-0.05 eV, the half-life can range from 10^{26-27} years for IH, and 10^{28-29} years for NH based on the isotope [63].

It is important to emphasise the uncertainty inherent to the expression in Equation 1.68. The NME is obtained from nuclear physics calculations. These are many body calculations in which the wavefunctions of the decaying nucleons can be configured into one of many states. The NME is calculated by solving the Dirac equation for these wavefunctions in a mean background field (the local potential

within the nuclei). The small overlapping of these wavefunctions induce large changes in the Hamiltonian and hence the NME. Subsequently, the uncertainties on the NME can have a factor 2-3 uncertainty, which is itself different depending on the nuclear model assumed [56].

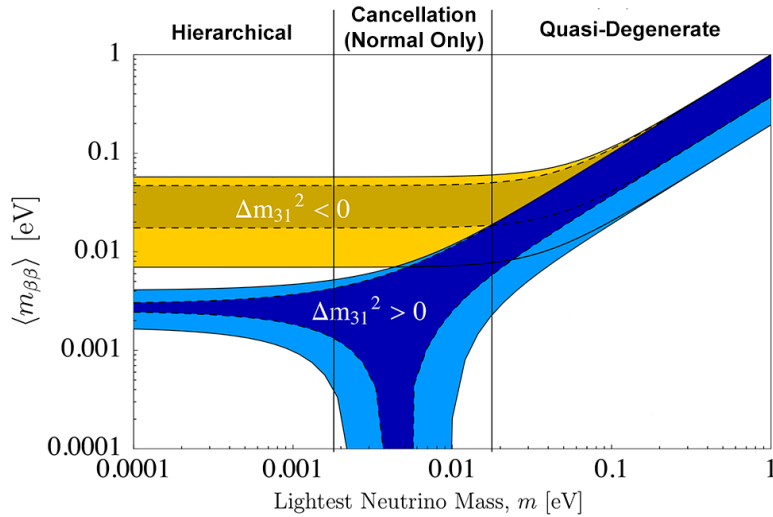


FIGURE 1.13: The $\langle m_{\beta\beta} \rangle$ parameter space with lightest neutrino mass. Plot is a modified version of that originally appearing in [56].

As with standard β -decay, the electrons emitted in $2\nu\beta\beta$ decay are similarly distributed according to a $\beta\beta$ -spectrum, where some of the energy is taken by the two neutrinos. Experimentally then, the signature of $0\nu\beta\beta$ -decay is the reconstructed sum of the emitted electrons being close to the Q -value of the decay i.e. $(T_1 + T_2)/Q \simeq 1$, this is shown illustratively in Figure 1.14.

1.4.2 Neutrinoless Double β -Decay Experiments

Previous searches for $0\nu\beta\beta$ -decay have provided no tangible evidence for it, although some claims have been made [64]. Currently, the best results are based on putting limits on the isotope $0\nu\beta\beta$ -decay half-life, $t_{1/2}^{0\nu\beta\beta}$ and the effective Majorana neutrino mass, $\langle m_{\beta\beta} \rangle$. A summary of the most recent limits are given in Table 1.3. The large uncertainties associated with the values of $\langle m_{\beta\beta} \rangle$ shown are related to the discrepancies between the NME assumed. The current generation of experiments make use of a variety of detector technologies using different candidate isotopes; a summary is provided in Table 1.2. There is no single ideal isotope

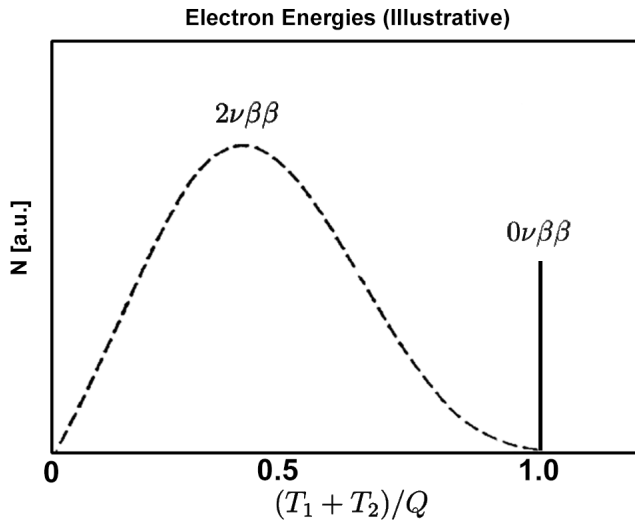


FIGURE 1.14: The distribution of electron energies in $2\nu\beta\beta$ - and $0\nu\beta\beta$ -decay. In $0\nu\beta\beta$ -decay the electrons share the total available phase space energy (Q -value). The size of the $0\nu\beta\beta$ peak is exaggerated for illustrative purposes.

for $0\nu\beta\beta$ -decay experiments. Rather, the choice of isotope is informed by the experimental set-up³. Ideally, an experiment seeks to maximise the sensitivity, $S^{0\nu\beta\beta}$ through a combination of source mass M , exposure time, $t_{\text{exp.}}$, detector efficiency, ϵ and energy resolution, σ_E whilst minimising possible backgrounds, B [65, 66];

$$S^{0\nu\beta\beta} \propto \epsilon \frac{N_{\text{atoms}}}{A} \left(\frac{Mt_{\text{exp.}}}{B\sigma_E} \right)^{1/2}, \quad (1.70)$$

where N_{atoms} is the number of atoms of the isotope and A is the atomic number.

1.4.2.1 Detector Technologies

A variety of experimental methods have been, or are currently considered, to search for $0\nu\beta\beta$ -decay. A brief overview of recent experiments that have either finished, continue to run, or are to begin shortly is now given alongside the experimental method they employ. The current generation of experiments have used an isotope mass on the order of $10\text{-}10^2$ kg, demonstrating a technique that could potentially be scaled to a larger version as part of a next-generation of $0\nu\beta\beta$ -decay experiments using $10^2\text{-}10^3$ kg mass. The sensitivities of such future experiments

³... and financial resources available i.e. cost of isotope enrichment.

$0\nu\beta\beta$ -decay Isotope Candidates and Experiments

Isotope	Nat. Abd. %	Q-Value [MeV]	Experiment
^{48}Ca	0.187	4.27	CANDLES [67], SuperNEMO [68]
^{76}Ge	7.8	2.04	GERDA [69], MAJORANA [70]
^{82}Se	9.2	2.99	NEMO-3 [71], SuperNEMO [68]
^{96}Zr	2.8	3.35	NEMO-3 [72]
^{100}Mo	9.6	3.04	NEMO-3 [73]
^{116}Cd	7.6	2.81	NEMO-3 [71]
^{130}Te	34.5	2.53	SNO+ [74], CUORE [75]
^{136}Xe	8.9	2.46	EXO-200 [76], KamLAND-Zen [77]
^{150}Nd	5.6	3.37	NEMO-3 [78], SuperNEMO [68]

TABLE 1.2: [56] Summary of candidate $0\nu\beta\beta$ -decay isotopes with corresponding natural abundances and Q -values. Shown also are recent experiments which have either previously, intend to, or are currently studying these isotopes for evidence of $0\nu\beta\beta$ -decay.

Current Limits on $t_{1/2}^{0\nu\beta\beta}$ and $\langle m_{\beta\beta} \rangle$

Isotope	Experiment	$t_{1/2}^{0\nu\beta\beta}$ [yr]	$\langle m_{\beta\beta} \rangle$ [meV]
^{76}Ge	GERDA	$> 2.1 \times 10^{25}$	<200-400 [79]
^{82}Se	NEMO-3	$> 3.2 \times 10^{23}$	<940-2500 [80]
^{100}Mo	NEMO-3	$> 1.0 \times 10^{24}$	<470-960 [80]
^{130}Te	CUORICINO	$> 2.8 \times 10^{24}$	<300-710 [81]
^{136}Xe	EXO-200	$> 1.1 \times 10^{25}$	<190-450 [76]
^{136}Xe	KamLAND-Zen	$> 1.3 \times 10^{25}$	<140-280 [77]

TABLE 1.3: The current respective lower and upper limits on isotope half-lives, $t_{1/2}^{0\nu\beta\beta}$ and the effective Majorana neutrino mass, $\langle m_{\beta\beta} \rangle$ from recent $0\nu\beta\beta$ -decay experiments.

is also discussed, and illustrated in Figure 1.15 in terms of the effective Majorana neutrino mass $\langle m_{\beta\beta} \rangle$.

High Purity Germanium Detectors - GERDA & MAJORANA

The principle behind high purity germanium (HPGe) detector based experiments is that the isotope (^{76}Ge) is both the source and detection medium. A conventional Ge-detector consists of a cylindrical configuration of germanium crystals that are coaxial (i.e. annular in cross-section) to electrical readouts on the inner and outer surfaces. Germanium is a semi-conductor with an electron-band structure such that excited electrons can induce a current. Doping of the germanium accordingly allows for the formation of n-p junctions; an interface between electron-rich and electron-deficient forms of germanium in which the transport of charge takes place.

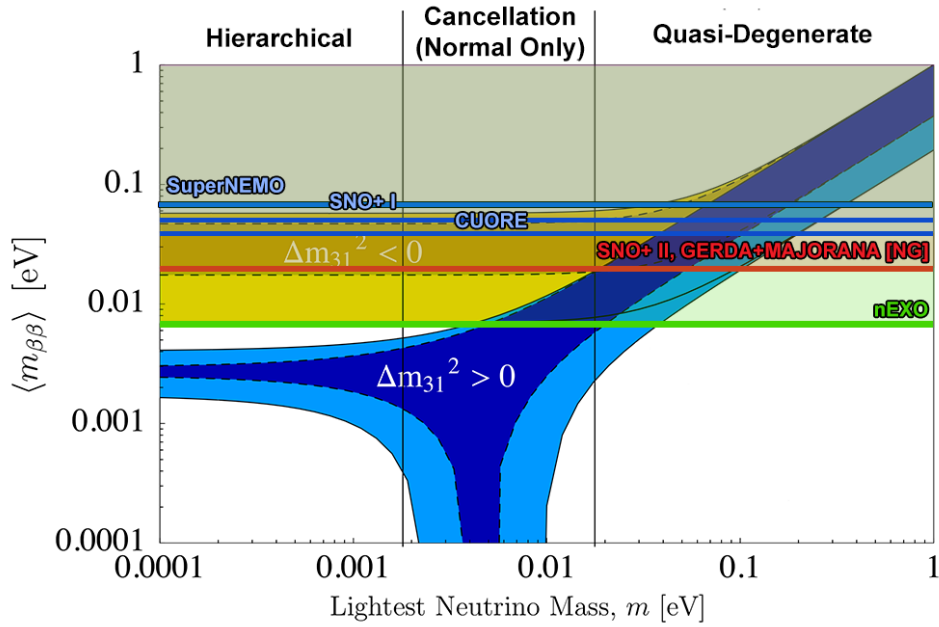


FIGURE 1.15: Current and future sensitivities of experiments to $0\nu\beta\beta$ -decay. Values are based on 5 years worth of running with the respective experiment isotope. Sensitivities are subject to change based on the detector efficiency and the nuclear model assumed.

The nature of this transportation - and hence the detector read-out - varies based on the type incident ionising radiation which excited the electrons e.g. light/heavy charged particles or photons. Given this, pulse-shape discrimination of the read-out can be performed for particle identification [82].

HPGe detectors are suited to $0\nu\beta\beta$ -decay experiments for a variety of reasons; the germanium source is intrinsically low in backgrounds, the detector construction allows for excellent energy resolution (\sim 2-5 keV) and the industrial production of Ge-detectors is well established. Indeed, some of the current most stringent limits on $0\nu\beta\beta$ -decay are from ^{76}Ge experiments that have, or continue to make use of HPGe detectors. The most recent being from the GERDA experiment [83], located at Laboratori Nazionali del Gran Sasso (LNGS). During its first phase, GERDA reused a combination of enriched and natural HPGe detectors from the Heidelberg-Moscow, ANG and IGEX collaborations, totalling a source mass of 17.7 kg of ^{76}Ge . The GERDA HPGe detectors were bathed in a cryostat of liquid argon. The first phase lasted for an exposure time of 21.6 kg yr. GERDA is currently being refurbished for a second phase, which aims to run at an exposure time of 100 kg yr with a source mass of 20.8 kg [83].

The upcoming MAJORANA experiment also plans to use HPGe detectors to study $0\nu\beta\beta$ -decay. It is currently at the demonstrator stage, using 29 kg of enriched $\sim 87\%$ ^{76}Ge and 15 kg of natural germanium [84]. It plans to run for an exposure time of 100 kg yr. A novel feature of MAJORANA over GERDA is that the HPGe detectors are stored in a vacuum in order to reduce the background rate. The MAJORANA and GERDA collaboration intend to work cooperatively in a future tonne scale ^{76}Ge experiment with an expected sensitivity to an effective Majorana neutrino mass of $\langle m_{\beta\beta} \rangle \simeq 20 \text{ meV}$ [70].

Cryostat Bolometers - CUORICINO & CUORE(-0)

Bolometers are used to measure the change in temperature of a material. Under ideal conditions, a bolometer can in principle be made such that it is sensitive to the small changes in temperature arising from the radioactive decay of nuclei in a material. This was the principle of the CUORICINO experiment, located at LNGS.

CUORICINO ran from 2003-08, and studied the decay of ^{130}Te . The CUORICINO bolometers consisted of TeO_2 crystals cooled in a cryostat to 8-10 mK; at this temperature, the Debye law predicts a specific heat capacity in the crystals of $c_Q = 2.3 \times 10^{-9} \text{ J K}^{-1}$. Given this, an energy deposition of a few keV results in a measurable temperature difference. Such a measurement requires excellent resolution; CUORICINO was able to achieve a resolution of 7 keV at the ^{130}Te Q -value. The detector consisted of a stacked tower of 44 125 cm^3 and 18 54 cm^3 crystals arranged in arrays over 13 planes. Most of these crystals contained natural tellurium except four; two enriched at 75% ^{130}Te and another two at 82.3% ^{130}Te [81]. CUORICINO collected data over an exposure time of 19.6 kg yr with 40.7 kg of tellurium equivalent to 11.6 kg ^{130}Te .

CUORICINO was a prototype for a larger scale experiment, CUORE. CUORE intends to use 988 TeO_2 crystal bolometers arranged into 19 CUORICINO-type towers with a total source mass of 750 kg of tellurium which is equivalent to ~ 200 kg of ^{130}Te . One of the largest challenges is to keep ~ 1000 bolometers at a temperature of 10 mK, for which a cryostat has been specially constructed. Assuming optimal background rejection, CUORE is sensitive to an effective Majorana neutrino mass of $\langle m_{\beta\beta} \rangle = 26\text{-}40 \text{ meV}$ [75]. Prior to CUORE, between 2013-2015, a single CUORE-style tower, CUORE-0 collected data in order to test

the background reduction techniques envisioned for CUORE [85]. CUORE-0 had a comparable source mass as CUORICINO.

Time Projection Chamber - EXO-200

Time projection chambers (TPC) are particle detectors that make use of electric and magnetic fields in order to drift charge induced by ionising radiation passing through a liquid or gas. TPCs allow for a fully three-dimensional reconstruction of a particle track, and have been used in previous neutrino experiments, such as ICARUS [86] and the T2K near-detector, ND280 [87].

The EXO-200 experiment is an example of a liquid xenon TPC used to search for the $0\nu\beta\beta$ -decay of ^{136}Xe , located at the waste isolation pilot plant in New Mexico. EXO-200 makes use of 110 kg of liquid xenon enriched to 80.6% ^{136}Xe inside of a 40 cm diameter, 44 cm long cylindrical TPC separated into two drift regions by a cathode at the centre. The TPC provides good trajectory information, collecting both charge and scintillation light simultaneously [88]. In doing so, the detector is able to distinguish tracks separated by more than ~ 1 cm, with an individual position resolution of ~ 1 mm. At the ^{136}Xe Q -value the energy resolution is 1.53% [76]. The experiment recently published results after an exposure time of 100 kg yr in the period 2011-13 providing the most stringent limits on the $0\nu\beta\beta$ -decay half-life of ^{136}Xe , see Table 1.3.

EXO-200 is itself a proof of concept for a larger liquid xenon based experiment, nEXO. The current proposal for nEXO is to use 5000 kg of 90% enriched liquid Xe^{136} in a large single-drift region TPC. After five years at optimal running, nEXO's sensitivity to an effective Majorana neutrino mass would be in the region $\langle m_{\beta\beta} \rangle \simeq 7\text{-}18$ meV [89].

Tracking & Calorimetry - NEMO-3 & SuperNEMO

A unique approach to a $0\nu\beta\beta$ -decay search came in the form of the NEMO-3 experiment. NEMO-3 ran between 2003-10 and was located in the Modane underground laboratory in France. The detector consisted of a cylindrical configuration of gaseous drift cells and plastic scintillator blocks interlaced with foils of the candidate isotope. Surrounding this were PMTs connected to the scintillator blocks by light guides [90]. The foils were distinctly modular to the surrounding detection medium. This allowed for simple installation and replacement of the foils meaning multiple isotopes could be deployed. The combination of tracking and calorimetry

enabled NEMO-3 not only to measure the energy deposits of radioactive decays in the detector, but also the event topology by measuring the angular distribution of the emitted particles. NEMO-3 deployed multiple isotopes including; ^{48}Ca , ^{82}Se , ^{96}Zr , ^{100}Mo , ^{116}Cd , ^{130}Te , and ^{150}Nd . The majority of these were for $2\nu\beta\beta$ -decay measurements. The most used for a $0\nu\beta\beta$ -decay search was ^{100}Mo at 6.92 kg, running for a live time of 4.96 yr to an exposure time of 34.3 kg yr [73].

The next generation version of NEMO-3, superNEMO is currently being constructed and intends to make use of the same tracking and calorimetry principles used by its predecessor. SuperNEMO plans to deploy multiple isotopes as 20 5 kg foils. As an example, with ^{150}Nd , SuperNEMO will be sensitive to an effective Majorana neutrino mass of $\langle m_{\beta\beta} \rangle \simeq 70$ meV after an exposure time of 500 kg yr (5 years live time). Assuming a successful $0\nu\beta\beta$ -decay signature, the event topology information of the events can be studied to test for exotic physics beyond the standard light neutrino exchange interpretation of $0\nu\beta\beta$ -decay [68].

Liquid Scintillator - KamLAND-Zen & SNO+

Liquid scintillator has previously been used as a detection medium for neutrino oscillation studies, examples include; KamLAND [32], Borexino [91], LSND [92], MiniBooNE [93] and Daya-Bay [94]. Given its relatively cheap availability and high light yield, it is also suited for use in $0\nu\beta\beta$ -decay searches.

Prior to EXO-200, the best limits on the $0\nu\beta\beta$ -decay half-life using ^{136}Xe came from KamLAND-Zen. KamLAND-Zen was a re-purposing of the short-baseline reactor anti-neutrino detector used in KamLAND (see Section 1.2.1.4). Inside of KamLAND's liquid scintillator filled vinyl balloon, a smaller 1.54 m radius balloon containing 320 kg of enriched Xe^{136} gas dissolved in scintillator was deployed [77]. KamLAND-Zen ran for a live time 114.8 days between December 2013 and May 2014, equivalent to an exposure time of 108.8 kg yr of ^{136}Xe . To date, KamLAND-Zen is the largest $0\nu\beta\beta$ -decay search (by source mass) to have been conducted.

SNO+ is another liquid scintillator based $0\nu\beta\beta$ -decay experiment. It intends to take advantage of the naturally high abundance of ^{130}Te and exploit the large pre-existing SNO Cherenkov detector. SNO+ plans to load 780 tonnes of liquid scintillator with 0.3% natural tellurium, corresponding to ~ 800 kg of ^{130}Te . One disadvantage of ^{130}Te is that the Q -value coincides with several backgrounds (see Section 2.2). However, through characterisation of the scintillator emission profile,

most of this background can be rejected. The hypothetical sensitivity to the $0\nu\beta\beta$ -decay of ^{130}Te for an effective Majorana neutrino mass of $\langle m_{\beta\beta} \rangle = 200$ meV is shown in Figure 1.16 with a region of interest (ROI) of 2.47-2.70 MeV.

One advantage of the loading technique employed by SNO+ is that it can be scaled to a higher loading-%. A second phase of SNO+ with upgraded high quantum-efficiency PMTs and a 3% loading of natural tellurium would increase sensitivity to an effective Majorana neutrino mass in the region $\langle m_{\beta\beta} \rangle \simeq 19\text{-}46$ meV [74].

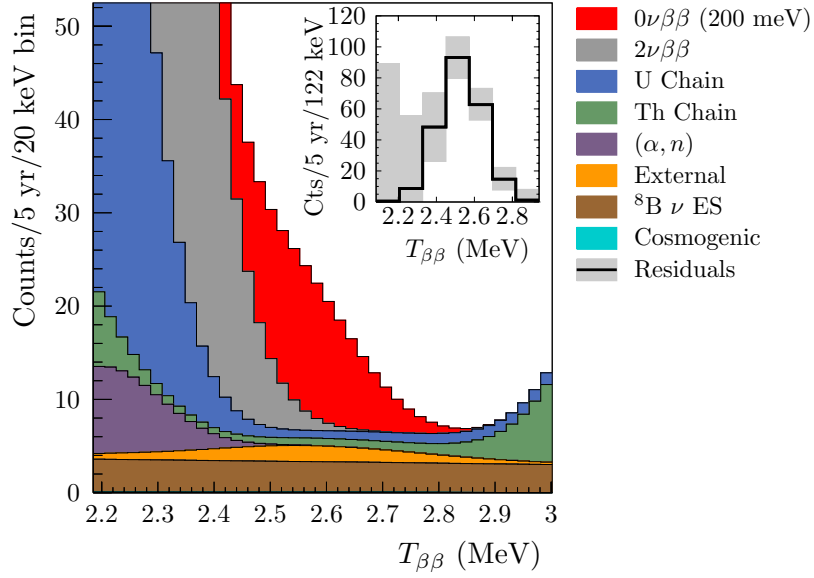


FIGURE 1.16: [74] SNO+ sensitivity for a hypothetical $0\nu\beta\beta$ -decay signal (red) at $\langle m_{\beta\beta} \rangle = 200$ meV for five years worth of data taking with 0.3% loading of natural tellurium in liquid scintillator. $T_{\beta\beta}$ is the sum of the reconstructed electron energies. Shown also are a variety of backgrounds which SNO+ must address, including the tail of the $2\nu\beta\beta$ spectrum (grey).

As is evident in Figure 1.16, the $0\nu\beta\beta$ -decay ROI is populated by a number of background processes, including the tail of the $2\nu\beta\beta$ -decay spectrum. The $0\nu\beta\beta$ -decay is less of a well defined peak (as in Figure 1.14) and is smeared due to the anticipated energy resolution of the detector. Given the sensitivity required to detect a positive signal, which could possibly be smaller than that in Figure 1.16, an accurate understanding of the detector and its materials is required; a full detector calibration. One component of the calibration is determining the optical response of the detector. This is the focus of the work discussed here. Chapter 2 provides a summary of the SNO+ detector and experimental objectives, introducing a calibration hardware system called the *laserball*. Chapter 3 discusses the

use of scintillator in SNO+; its intrinsic, chemical and optical properties. Using laserball data, a model which characterises the optical response of the detector and the scintillator timing profile is introduced in Chapter 4. Chapter 5 follows with an outline of the production and processing of SNO and simulated SNO+ laserball data discussed under the context of RAT; the SNO+ Monte-Carlo, and OCA; the software implementation of the optical response model written by the author. Chapters 6 and 7 discuss the results of a statistical fit of the optical model to data in water (Chapter 6) and scintillator (Chapter 7). This body of work concludes in Chapter 8 with a summary of the work presented.

2

The SNO+ Experiment

The scientist begins by carrying out experiments whose aim is to make carefully controlled and meticulously measured observations at some point on the frontier between our knowledge and our ignorance.

Popper, Bryan Magee

2.1 Detector Components and Materials

The SNO+ detector is a re-purposing of the original Cherenkov detector used in the SNO experiment, and is located 2039 m underground in VALE’s Creighton mine, Lively, Ontario, CA. A cross-sectional diagram of the original SNO detector is shown in Figure 2.1. The detector is comprised of the following features:

- **Cavity:** The cavity is a barrel shaped 22 m wide by 34 m high recess in the mine rock in which the SNO+ detector is contained [95]. The cavity walls and floor consist of shotcrete coated with nine layers of a urylon liner with a total thickness of 8 mm [96]. The cavity is filled with \sim 7000 tonnes of ultra-pure water.
- **PMT support sphere (PSUP):** The PMT support sphere is a geodesic steel sphere approximately 17.8 m in diameter. It is designed to hold \sim 9000 PMTs and encapsulate all the other detector components. The PSUP is supported by cables connected to bolts on the ceiling and walls of the cavity.

- **Acrylic vessel (AV):** The acrylic vessel is a thin, 55 mm thick, 12 m diameter spherical volume. In SNO, the AV contained D₂O, in SNO+ it will be filled with liquid scintillator. The vessel is constructed out of a series of acrylic tiles/panels bonded together as shown in Figure 2.3. The AV is positioned concentrically inside the PSUP. At the top of the vessel is a cylindrical *neck* that reaches a deck level above the cavity containing a clean room area.
- **Support ropes:** The AV is suspended inside the PSUP with the use of support ropes. These consist of 10 U-shaped loops of 3/4" tensylon rope that are threaded through the equator of the AV to the outside the PSUP where they are connected to the cavity ceiling.
- **Belly plates:** The support ropes are threaded through 10 square acrylic layers that are located around the equator, the ‘*belly*’ of the AV. The plates are bevelled, and curved to match the spherical shape of the AV.

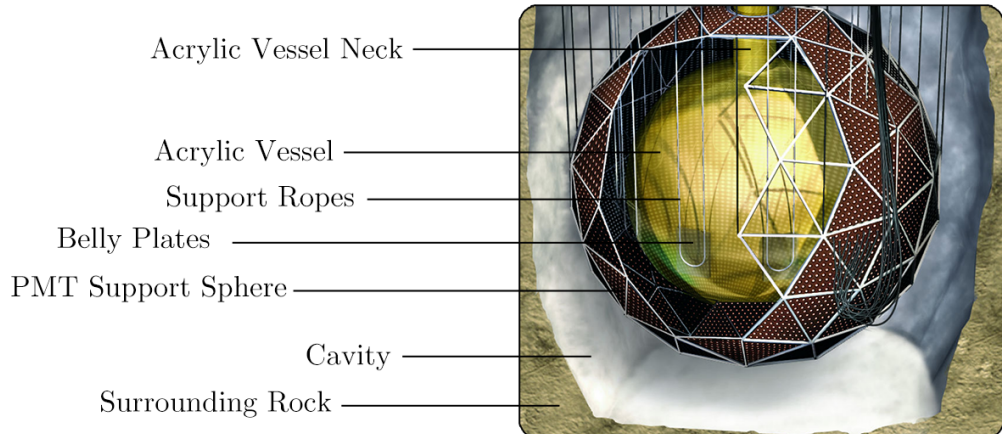


FIGURE 2.1: Cross sectional diagram of the original SNO detector. Shown is the PSUP inside the cavity. Inside the PSUP is the acrylic vessel.

Not shown in Figure 2.1 is a recently installed AV hold-down rope net. The main difference between SNO+ and SNO is the deployment of liquid scintillator instead of D₂O inside the AV. Liquid scintillator is less dense than water with a density of 0.865 g cm⁻³ [97]. As a consequence, once filled with scintillator the AV will have a buoyant tendency against the surrounding water in the outer AV region. The AV hold-down rope net is an interwoven basket of 20 1¹/₄" tensylon ropes laid across the top of the AV and anchored to the floor of the cavity to keep the AV in position [98]. A schematic diagram of the rope net is shown in Figure 2.2.

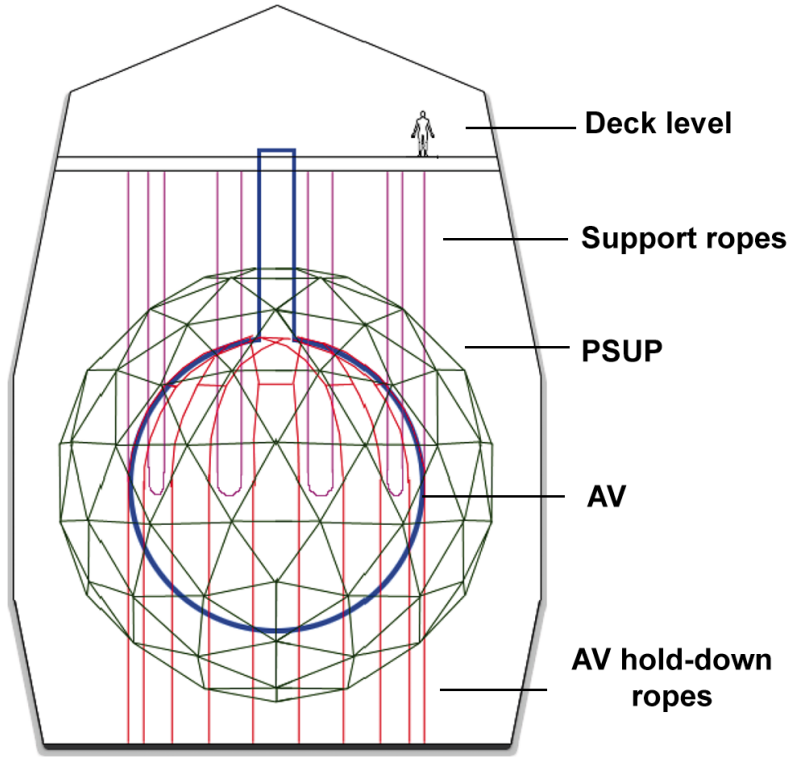


FIGURE 2.2: Wireframe diagram of the SNO+ detector. Shown is the location of the AV hold-down rope net (red) relative to the AV (blue) and PSUP (green). Figure is a modified version of that originally appearing in [74].

In addition to several detector upgrades, the original D₂O purification facility from SNO has been replaced with a scintillator plant for SNO+. The construction of the scintillator plant is discussed in Section 3.6.

2.1.1 PMTs & Electronics

SNO+ contains approximately 9000 inward looking, 8" diameter Hamamatsu R1408 PMTs. These are the same PMTs as used in SNO. SNO+ has repaired or replaced those which have since broken. The original choice for this model of PMT was based primarily on the fast rise and fall time of the PMT pulse with a single photoelectron timing resolution of ~ 1.70 ns [26]. The PMTs are held within the PSUP and centred towards the middle of the AV. These PMTs measure the resultant light from particle interactions of interest inside the detector. In addition, there are PMTs about the neck of the AV and 91 outward looking PMTs (OWLs) located on the outer surface of the PSUP; these are used to detect light from exterior sources such as cosmogenic muons travelling through the cavity.

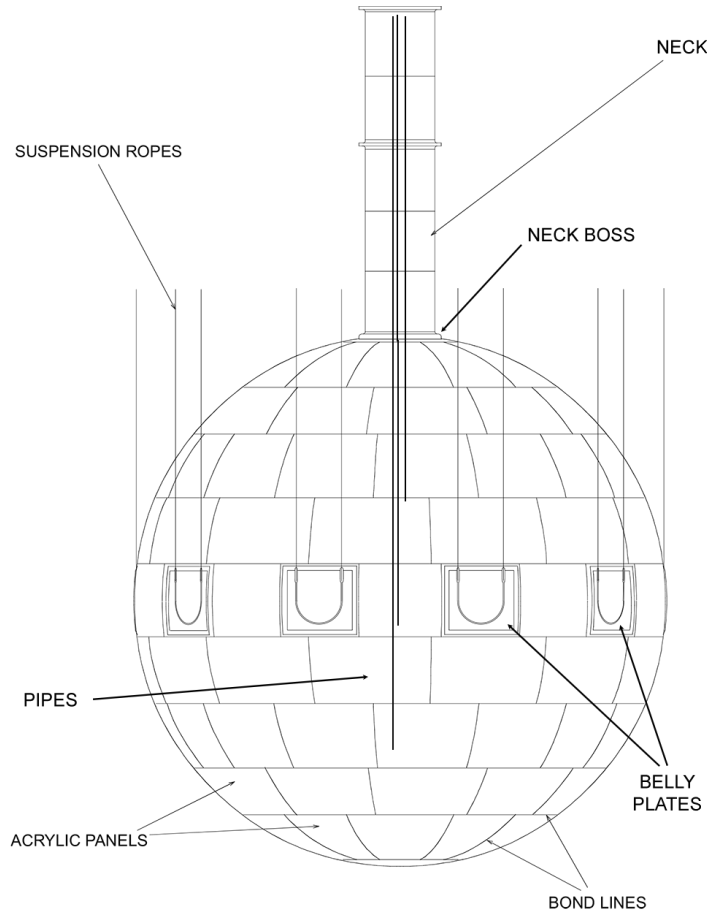


FIGURE 2.3: Technical drawing of the AV. Shown are the support ropes and belly plates about the equator. The spherical vessel is constructed out of acrylic panels that are bonded together. In reality there exist seven pipes which terminate at different heights along the vessel, only three are shown for illustrative purposes. Figure is a modified version of that originally appearing here [26].

The inward looking PMTs are surrounded by a series of concave petal-like reflectors formed into a Winston cone. These reflectors act to *collect* light, redirecting it onto the PMT face. A technical drawing of a PMT and its surrounding reflector assembly is shown in Figure 2.4. The reflector assembly is an important component which is the subject of an investigation and characterisation that is discussed in Chapter 4.

The PMTs read out time and charge values that are used to identify physics events in SNO+. Each individual PMT is connected to a *channel* with 16 12-bit analog-to-digital converter (ADC) cells. Each channel is connected to a PMT interface card (PMTIC). Each PMTIC contains eight channels which are connected to a daughter board (DB). Each set of four DBs are connected to a mother board,

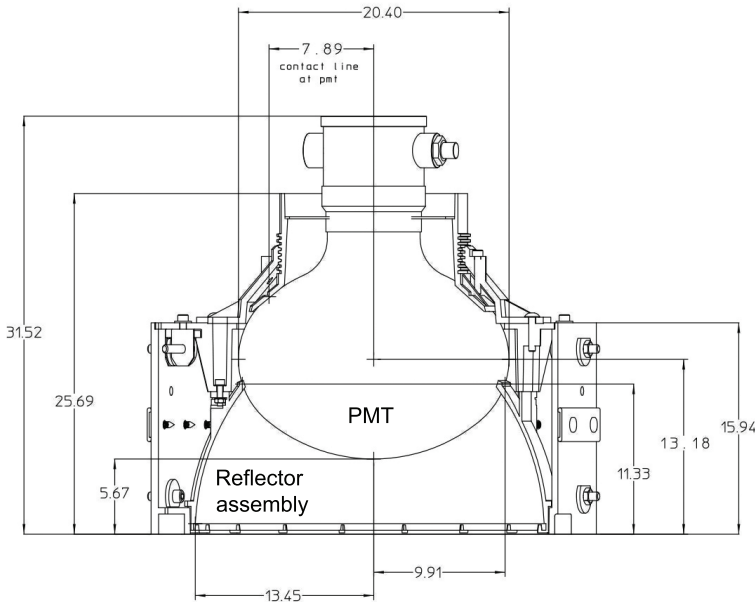


FIGURE 2.4: [26] Technical drawing of a PMT and its surrounding reflector assembly. Measurement units are in cm.

known as a front end card (FEC). Therefore each FEC interfaces with $8 \times 4 = 32$ PMTs. There are approximately 300 FECs. Physically, the FECs are stacked into 19 crates on the deck level. Each crate interfaces with a centralised master trigger card (MTC) via a crate trigger card (CTC) [99].

Light incident at a PMT will create a photoelectron at the PMT cathode. Under a strong electric field this electron is accelerated through a stack of nine anodes creating an electron shower that accumulates as charge, interpreted as a pulse. As charge accumulates, the time-to-amplitude (TAC) slope of the pulse is used to convert the ADC counts into a time value. If the pulse passes a discriminator threshold value, it is known as a PMT *hit*. The accumulated charge (Q) values under high-gain (H) over short (S) and long (L) integration times are known as QHS and QHL respectively. Another value is also calculated over the long integration time using low-gain (X) known as QLX.

Each DB performs an initial sum of the number of PMTs that pass their discriminator threshold. The information from all DBs in a crate is sent to the CTC where it is summed and subsequently sent to the analogue MTC (MTCA). The MTCA performs a total sum of the number of hit PMTs across all crates. The MTCA interfaces with a digital MTC (MTCD) that compares the total sum with the trigger requirements for a *global* trigger (GT) e.g. N_{hit} threshold in a 100 ns

window. If a GT is declared then the hit information of each PMT contributes to the event. If no GT is declared within a nominal window (~ 400 ns) then the PMT time and charge information is reset.

The use of scintillator not only requires physical modifications to the detector, but due to the increased light output of scintillation light compared to Cherenkov light (factor of ~ 50), the electronics have also been upgraded to handle the expected increased event rate.

2.2 Operating Phases & Backgrounds

The SNO+ experiment will operate throughout three planned *phases*:

- **Water phase:** In this phase, water will fill both the inner and outer AV regions. This phase allows for a first complete calibration of the detector since the end of SNO in 2006. In addition, it also provides an opportunity to search for nucleon decay through *invisible* decay modes [100].
- **Scintillator phase:** The water in the inner AV region will be replaced with liquid scintillator. Once scintillator is in the detector, the energy threshold is reduced. At this stage, SNO+ becomes a multi-purpose experiment, sensitive to the following types of low-energy neutrinos;
 - Solar neutrinos:
 - * *pep*-chain neutrinos, $E_\nu = 1.44$ MeV
 - * CNO-cycle neutrinos, $E_\nu \sim 0.7\text{-}1.7$ MeV
 - Geo-neutrinos: $E_{\bar{\nu}} \sim 1.8\text{-}3.5$ MeV
 - Reactor anti-neutrinos: $E_{\bar{\nu}} \geq 1.8$ MeV
 - Supernova neutrinos: $E_\nu \geq 0.2$ MeV
- **Tellurium phase:** The tellurium phase is the primary phase of the SNO+ experiment. Natural tellurium ($\sim 34\%$ ^{130}Te) will be loaded into the scintillator in order to search for $0\nu\beta\beta$ -decay with a 2.47-2.70 MeV ROI. The tellurium phase will begin with an initial loading of 0.3%, ~ 800 kg of ^{130}Te , with the possibility to increase the loading-% in the future.

The use of scintillator not only increases the detector sensitivity to physics of interest, but also a sensitivity to a variety of background processes. In SNO, the analysis threshold of Cherenkov events was greater than 4.5 MeV largely due to an irreducible background *wall* of β - and γ -particles (α -particles also arose from background processes, but did not directly produce Cherenkov light). This was sufficient for the study of solar ^8B -neutrinos, $E_\nu \geq 6$ MeV. However, given that the physics of interest in SNO+ is within the 1-3 MeV range, the processes that contribute to this background wall need to be identified and removed. Unwanted physics interactions that produce these β -, α - and γ -particles in the ROI are mostly due to the decay of radioactive isotopes. They can be found within the materials from which the detector was constructed e.g. PMTs, PSUP, cavity rock and the acrylic vessel. These are known as *external* backgrounds. Alternatively they can also be found within the detector media itself e.g. water and scintillator. These types are known as *internal* backgrounds. The isotopes are predominantly the daughter nuclei of the uranium-238 (^{238}U) and thorium-232 (^{232}Th) chains. ^{238}U and ^{232}Th are long lived isotopes that occur naturally in almost all materials.

The decay chains of ^{238}U and ^{232}Th are shown in Figure 2.5. In both cases the background problem arises once the chain reaches radon-222/210 ($^{222/210}\text{Rn}$) which is a gas at 12° (the expected water temperature inside the cavity). Radon therefore emanates into the detector; it is short-lived ($t_{1/2}^{\text{Rn-220}} = 55.6$ sec, $t_{1/2}^{\text{Rn-222}} = 3.82$ days) and proceeds to decay further through a series of β , γ and α emissions until terminating at lead-206/208 ($^{206/208}\text{Pb}$). Of primary concern is bismuth-212 (^{212}Bi), which has a half-life of $t_{1/2}^{\text{Bi-212}} = 60.6$ mins, decaying 36% of the time into thallium-208 (^{208}Tl) by α emission. ^{208}Tl proceeds to decay to ^{208}Pb through the emission of a 2.61 MeV γ that falls within the $0\nu\beta\beta$ -decay ROI. The other 64% of the time, ^{212}Bi decays to polonium-212 (^{212}Po) through β emission. Background events of this type can be rejected through tagging of the subsequent ^{212}Po decay to ^{208}Pb by α emission using particle identification of the scintillator timing profile. This is discussed in Section 3.4.5.

Other radioactive backgrounds not part of the ^{238}U and ^{232}Th chains include ^{40}K , ^{85}Kr and ^{14}C . In addition, the 2039 m rock overburden provides a shielding of 6010 metres of water equivalent (m.w.e), reducing the through going rate of cosmogenic muons to about three per hour ($0.27 \mu \text{ m}^{-2}$ [95]). Ultimately, for SNO+ to be sensitive to any of the objective physics events, it needs to operate in a sufficiently background free environment. For ^{238}U and ^{232}Th chains the target purity levels of

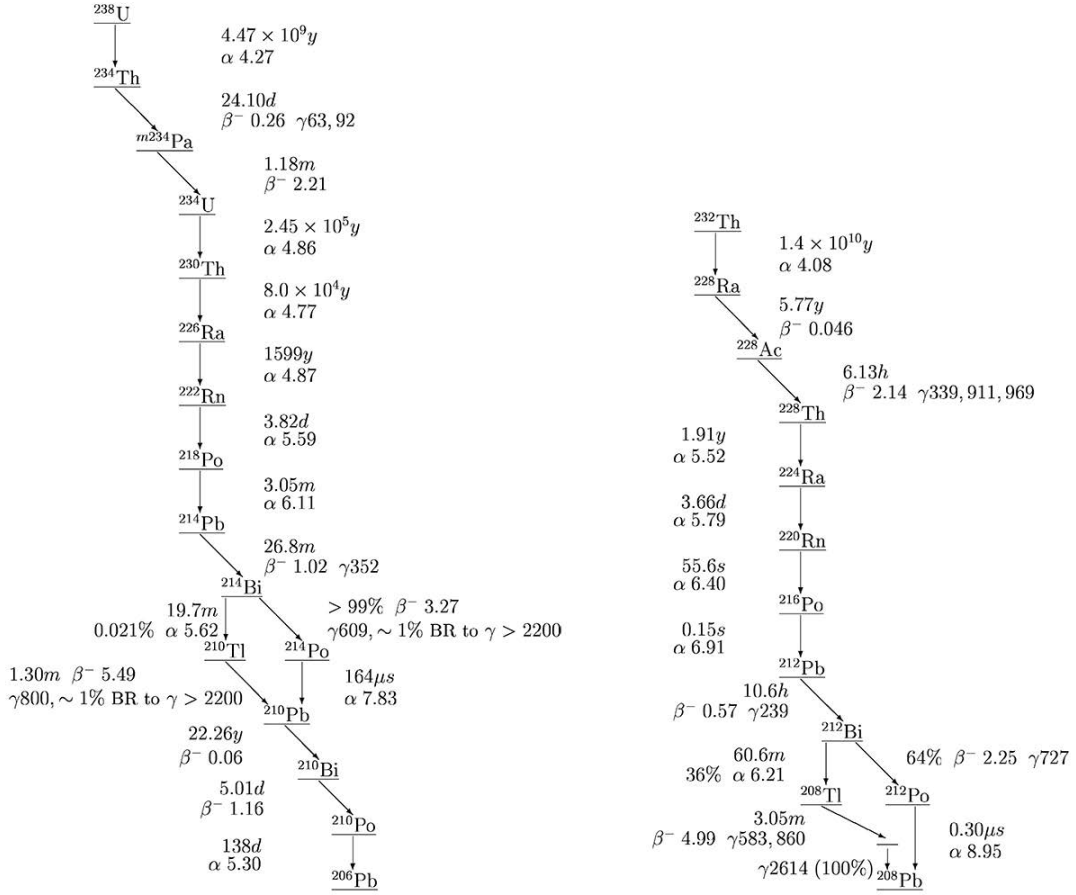


FIGURE 2.5: [101] The decay chains of ^{238}U (left) and ^{232}Th (right). Once each of the chains reaches $^{222}/^{210}\text{Rn}$ it decays through a series of β , γ and α emissions into daughter nuclei, terminating at $^{206}/^{208}\text{Pb}$ which is stable. Energies are shown in MeV for β - and α -particles and in keV for γ -particles. The emission of β -, α - and γ -particles contribute towards the background event rate in SNO+.

the scintillator are $1.6 \times 10^{-17} \text{ g/g}$ and $6.8 \times 10^{-18} \text{ g/g}$ respectively [102]. To ensure these targets are met, a strict procedure to all commissioning work associated with the scintillator circulation and purification has been enforced. This includes the construction of the scintillator plant which is discussed in Section 3.6.

Outside of radioactive backgrounds, another type of background are *instrumental* backgrounds. Instrumental backgrounds are interferences or characteristics of the detector electronics that reduce the efficiency of interpreting event information; they are non-physics related. There are a variety of instrumental backgrounds, but static discharge and breakdowns in the electronics are most common [103].

2.3 Detector Calibration

Prior to collecting physics data a full calibration of the detector is required. The calibration is divided into four main procedures that collectively calculate the necessary offsets associated with the detector electronics and PMTs, as well as characterise the response of the detector to different energy and light sources;

- **Electronics calibration (ECA):** The ECA is the first necessary calibration step in order to convert PMT information into physics information. When a PMT is not hit, the ADC information can be read out to provide the *zero-hit* value for the channel. In general the ADC read-out will vary from PMT to PMT. The ECA therefore calculates the *pedestal* values of the ADC counts for each of the charge integrations; QHS, QHL and QLX for when the PMT is not hit. PMTs whose pedestal values vary frequently between calibrations can subsequently be flagged as unreliable. The ECA also determines the TAC which is used to convert the pulse shape into a time value [104].
- **PMT calibration (PCA):** The PCA calibrates the *walk* and gain at each PMT;
 - Walk calibration: The PMT walk is the rise time of the leading edge of the pulse between the creation of the photoelectron at the photocathode and the time at which the pulse passes the discriminator threshold. The walk is unique to each PMT.
 - Gain calibration: The purpose of the gain calibration is to characterise each PMT's single photoelectron charge spectrum in units of ADC counts above the pedestal values determined by the ECA [105]. This standardises the charge read out across all PMTs.
- **Optical calibration:** SNO+ will make use of scintillator which will emit over a broad wavelength spectra. As this light is produced it becomes subject to a number of optical effects such as absorption, scattering, reflection and refraction as it propagates through the detector to the PMTs. The optical calibration therefore characterises the response of the detector to light produced in different locations inside the detector and across different wavelengths. Optical calibration is sought using two systems; the *laserball* and a light injection system consisting of several optical fibres installed on the PSUP.

- **Energy calibration:** A variety of radioactive sources are deployed into the detector to probe its energy response between 0.1-10 MeV. The energy calibration also characterises the response to different types of particle interactions based on the source. This can be used to inform the reconstruction of physics events and the rejection of unwanted backgrounds. Of particular interest in SNO+ is the response to β -particles in the energy region of the $2\nu\beta\beta$ end-point spectrum of ^{130}Te $E_{\beta\beta}^{2\nu} \simeq 2.5$ MeV. A summary of the planned radioactive sources to be deployed in SNO+ is shown in Table 2.1.

SNO+ Radioactive Sources	
Source	Particle & Energy [MeV]
AmBe	$n, \gamma = 2.2, 4.4$ MeV
^8Li	$\beta = 10.0$ MeV
^{16}N	$\gamma = 6.1$ MeV
^{24}Na	γ (sum) = 4.1 MeV
^{48}Sc	γ (sum) = 3.3 MeV
^{57}Co	$\gamma = 0.122$ MeV
^{60}Co	γ (sum) = 2.5 MeV
^{65}Zn	$\gamma = 1.1$ MeV
^{90}Y	$\beta = 2.2$ MeV
Cherenkov	γ Spectrum

TABLE 2.1: [106] Radioactive sources planned for deployment in SNO+.

2.3.1 Optical Sources

Two calibration systems are used to characterise the optical response of the detector; the laserball, which is the focus of the work presented here, and a fibre based light injection system. Collectively, these quantify various optical effects such as scattering, attenuation and reflections. Using these systems the timing uncertainty of the PMTs is reduced such that the sensitivity to the temporal distribution of physics events is increased. This is important as the timing information of the PMTs is the most precise source of information in SNO+ and is used for the reconstruction of both physics and background events.

2.3.2 LED/Laser Light Injection System

The stringent radiopurity requirements in SNO+ make it undesirable to regularly deploy calibration sources stored externally. The idea of the light injection system is to mount optical fibres onto the PSUP which are connected to an LED or laser source in the clean room on the deck level above the cavity. The fibres are installed as part of the detector construction, and hence do not need to be adjusted once the experiment begins. Furthermore, the fibres are installed in the water region of the detector, and hence the sensitive scintillator region in the inner AV can remain sealed. A diagram of the fibre injection system is shown in Figure 2.6.

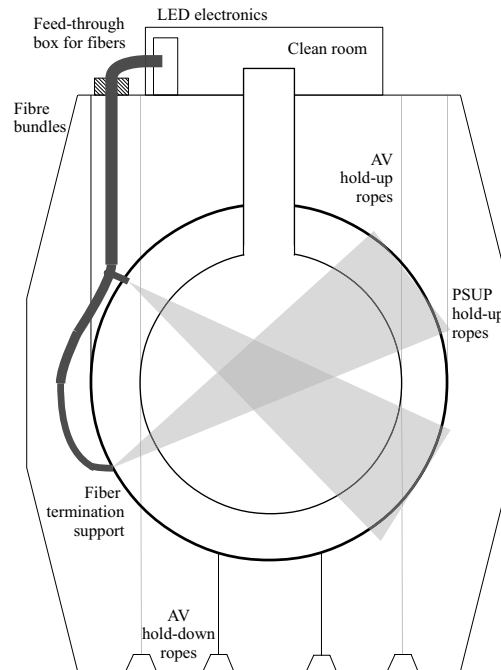


FIGURE 2.6: [107] Cross-sectional diagram of the SNO+ detector. The fibres installed on the PSUP pulse light across the detector.

The fibres pulse light across the detector that scatters or reflects based on the fibre position and beam direction. In using many fibres installed on the PSUP, the overlapping beam profiles of neighbouring fibres ensure a sufficient coverage of light to all the PMTs. A full description of the light injection system is given in [107].

2.3.3 The Laser System and Laserball

The laserball is designed to produce an isotropic, point-like source of laser light throughout the detector. The laserball was originally designed by R. Ford whilst working on the SNO experiment [108], and was deployed into the detector during several calibration phases of the SNO experiment between September 2000 and August 2006. SNO+ will make use of the original laserball used in SNO during the water phase. For the scintillator phase, a new laserball has been made by the University of Sussex that is designed to be compatible with scintillator, using materials with a low background emanation rate [109].

The principle of the laserball is to connect a laser source to a light diffusing sphere inside the detector. This diffusing sphere is a quartz flask 10.9 cm in diameter that is filled with 2 g of small air-filled glass beads 50 μm in diameter [110]. The beads are suspended in 0.5 kg of silicone gel and scatter light injected into the flask through a fibre guide inserted in through its neck. The flask is held from above by stainless steel mounting hardware that contains the connection between the fibre guide to the flask, and the end of a bundle of 20 optical fibres connected to the laser. The mounting hardware is connected to the manipulator rope guide system through a mating flange. Shown in Figure 2.7 is a technical drawing of the laserball flask and the mounting hardware of the SNO laserball to be deployed in the water phase. Also shown is the redesigned SNO+ laserball flask and neck intended for use in the scintillator phase. A significant improvement of this redesign is the reduced shadowing about the neck, $\sim 7.3^\circ$. This improves on the larger shadowing $\sim 30^\circ$ of the original SNO laserball design. The shadowing of upward light from the flask by the mounting hardware is the main cause of light anisotropy. For this reason the laserball is only *near-isotropic*. As will be discussed in Section 4.2.5, the overall anisotropy of the laserball is important to consider when interpreting laserball data.

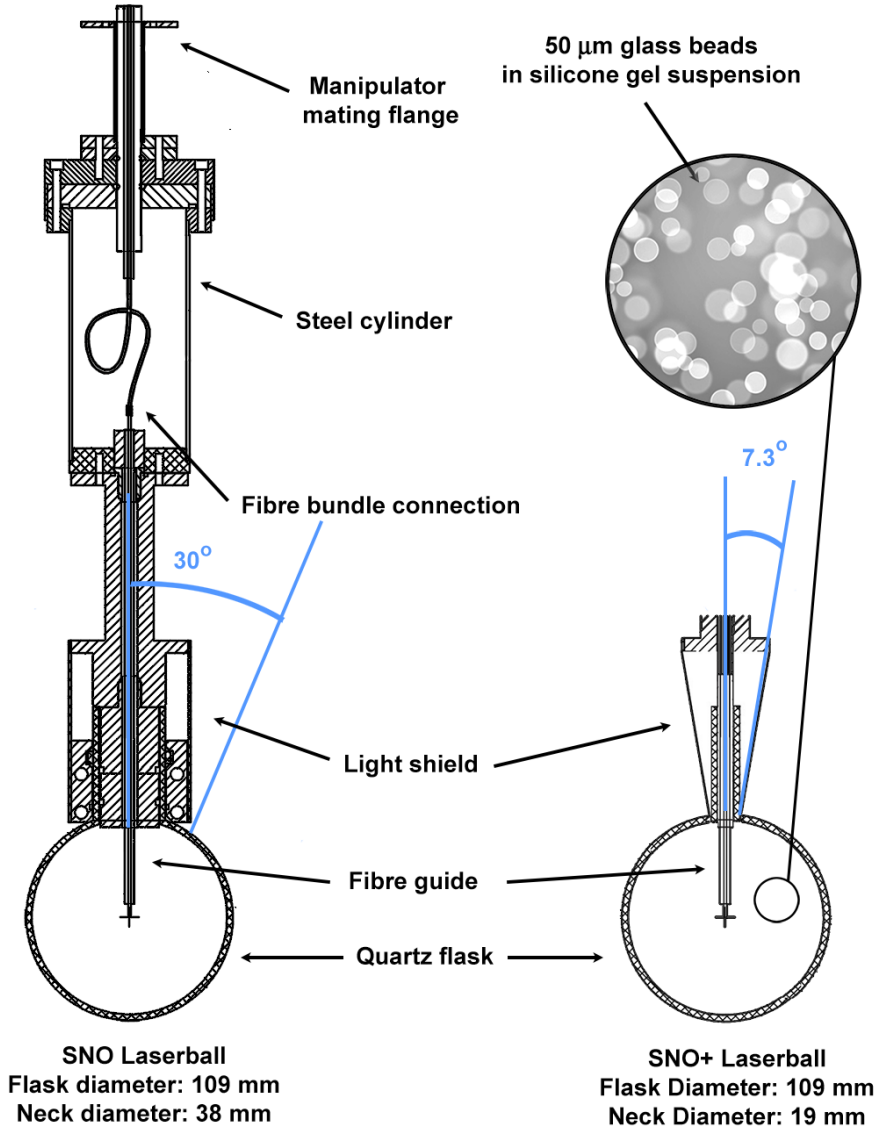


FIGURE 2.7: The SNO and SNO+ laserball flask and light shield designs. Diagram is a combination of modified versions originally appearing in [109, 110].

The laser system is located inside a clean room on the deck level. It consists of a nitrogen based laser, $\lambda = 337.1$ nm with a 1-45 Hz pulse rate of $100 \mu\text{J}$ per pulse. The laser is mounted to a table. Down the beam-line of the laser is a movable mirror that moves along the table parallel to the beam-line, redirecting the beam into one of four dye resonators. Within these resonators are cell cuvettes containing dyes. These dyes change the wavelength of the incident laser light, resulting in an outgoing beam with an approximate energy of $10\text{-}30 \mu\text{J}$ per pulse [110]. The original wavelengths and dyes used in SNO are as follows:

- Nitrogen laser, $\lambda_{LB} = 337$ nm, $\sigma_{\lambda_{LB}} = 0.1$ nm

- PBD dye, $\lambda_{LB} = 369$ nm, $\sigma_{\lambda_{LB}} = 10.0$ nm
- BBQ dye, $\lambda_{LB} = 385$ nm, $\sigma_{\lambda_{LB}} = 8.0$ nm
- Bis-MSB dye, $\lambda_{LB} = 420$ nm, $\sigma_{\lambda_{LB}} = 8.0$ nm
- COUMARIN-500 dye, $\lambda_{LB} = 505$ nm, $\sigma_{\lambda_{LB}} = 14.0$ nm
- KITON-RED Dye, $\lambda_{LB} = 620$ nm, $\sigma_{\lambda_{LB}} = 10.0$ nm

These dyes were chosen to probe the Cherenkov wavelength profile which was relevant to the solar neutrino studies of SNO. For SNO+, scintillation light will provide the relevant wavelength profile; therefore a selection of different dyes may be considered, this will be discussed in Section 5.1.1. Finally, before leaving the deck level, and entering the optical fibres connected to the laserball, the resulting laser beam intensity is controlled by the use of two successive attenuator wheels; the first containing six course adjustment neutral density (ND) filters, and a second with six fine adjustment filters. For a full description of the laser system see [110].

The optical fibres which transport light from the laser system on the deck level to the laserball flask inside the detector are protected inside a triple membraned cable known as the *umbilical*. The umbilical is ~ 30 m long and is stored and deployed using a pulley system inside what is known as an umbilical retrieval mechanism (URM). The deployment of the laserball with the umbilical and URM is shown in Figure 2.8. In SNO, the umbilical consisted of an inner Teflon tube in which the 20 optical fibres were located. The Teflon tube was protected by an outer polyethylene tube which itself was surrounded by an outer silicone tube. This triple membraned design was both impermeable to water once deployed and had a low background count, with an emanation rate less than 10% of the D₂O used in SNO [110]. For SNO+ the use of scintillator introduces three key points of concern. Once the umbilical is deployed and retracted, it will be drenched in scintillator; the stringent low background requirements of the scintillator and tellurium phases mean the umbilical will need to be made from materials with a low background count. Second, the storage of the umbilical in the URM when not in use needs to be in a low background environment; the pulley motors need to use little oil and operate under a nitrogen bath to avoid contaminating the scintillator with oxygen. Finally, scintillator has a small coefficient of friction, and therefore the pulley system of the URM needs to be robust against slippage of the umbilical

when deploying and retracting it. A new URM and umbilical is being designed by LIP and Queen's University for use with scintillator [111, 112].

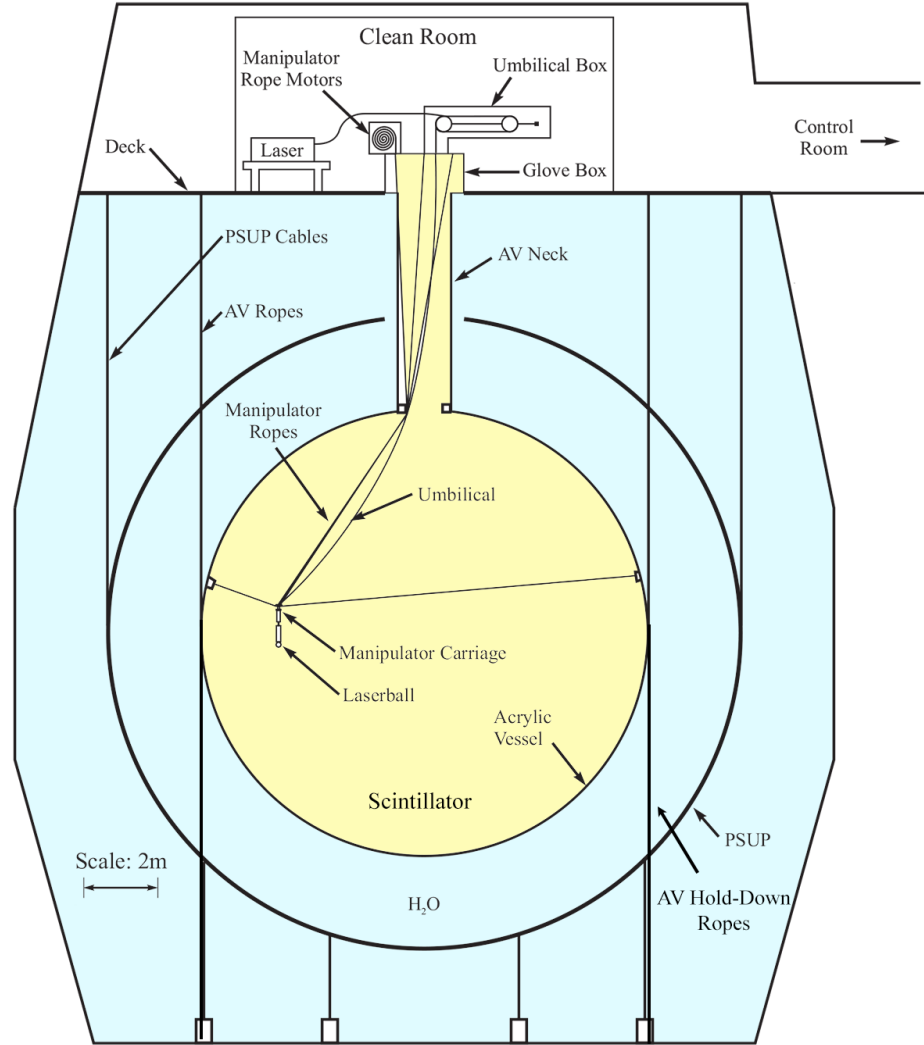


FIGURE 2.8: Deployment of the laserball inside the SNO+ detector. The laserball is attached to a motor-driven rope guide system via a manipulator assembly which holds the laserball flask. Diagram is a modification to that originally found in [110].

For the purposes of the work presented here, it is useful to define two sets of coordinate systems. One is the detector coordinate system whose origin is at the centre of the AV, with the z -axis pointing along the vertical, from the top of the cavity to the bottom through the neck of the AV. The (x, y) -plane points in four compass directions north ($+y$), east ($+x$), south ($-y$) and west ($-x$). The laserball flask and mounting hardware share a similar spherical symmetry with the AV, the local angular coordinate frame, $(\cos \theta_{LB}, \phi_{LB})$ of the laserball is thus

chosen to share a 1:1 mapping with the PSUP coordinates, north ($\phi_{LB} = \pi/2$), east ($\phi_{LB} = 0$), south ($\phi_{LB} = -\pi/2$) and west ($\phi_{LB} = \pi$). The PSUP and laserball coordinate systems are illustrated in Figure 2.9.

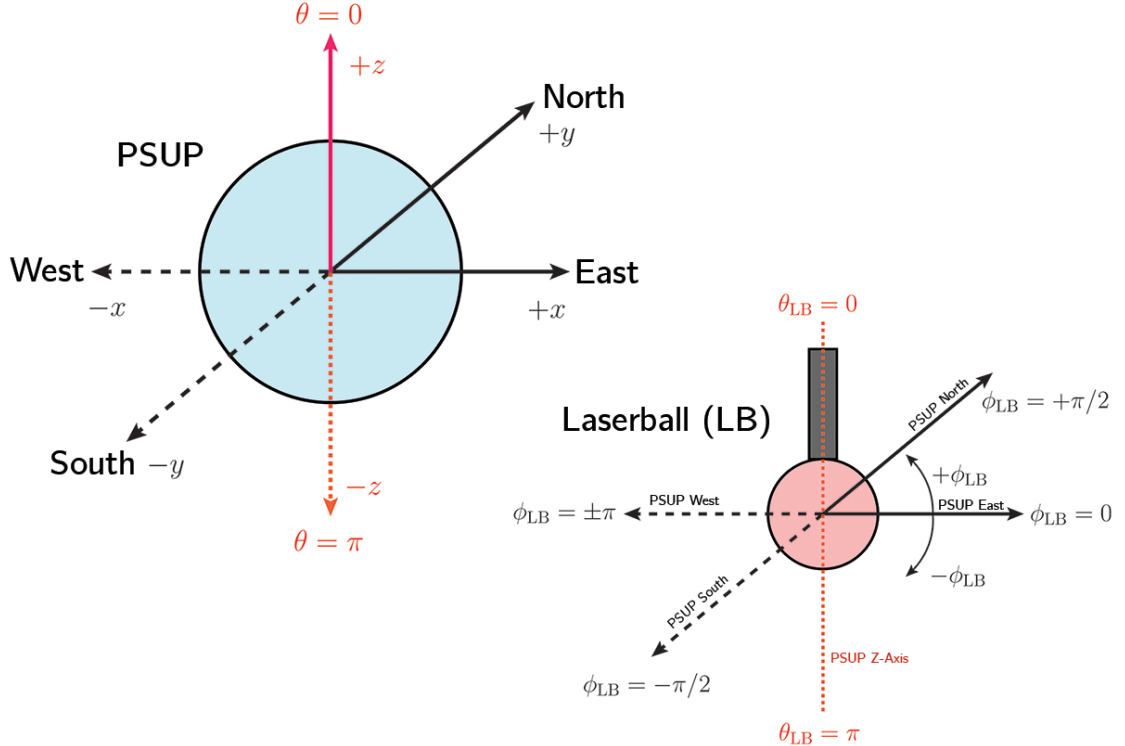


FIGURE 2.9: Illustrative diagram of the laserball coordinate system with reference to the detector coordinate system of the PSUP. The origin of the detector coordinates is located at the centre of the AV. Both the laserball and PSUP share a spherical symmetry, therefore the local $(\cos \theta_{LB}, \phi_{LB})$ coordinates of the laserball share a 1:1 mapping with the detector $(\cos \theta, \phi)$ coordinates.

2.4 SNO+ Monte-Carlo: RAT

Monte-Carlo simulations of the SNO+ detector are produced using reactor analysis tools (RAT) [113]. Originally developed by the Braidwood collaboration, versions of RAT have been adopted by other experiments in addition to SNO+, including MINI-CLEAN and DEAP-3600. RAT uses both Geant4 [114] and GLG4Scint [115] libraries to simulate scintillator properties. The MC data produced by RAT uses a data structure based on ROOT [116] libraries written in C++.

3

Scintillators in SNO+

Life seems to me like a long, weary night that would be intolerable if there were not occasionally flashes of light, the sudden brightness of which is so comforting and wonderful, that the moments of their appearance cancel out and justify the years of darkness.

Gertrude, Hermann Hesse

The use of liquid scintillator is common-place in large scale neutrino experiments such as SNO+. Recent examples of other scintillator based neutrino experiments include; KamLAND, Borexino, Double-Chooz and Daya-Bay [91, 94, 117, 118]. Scintillator is used because it produces luminescence in response to ionising radiation (IR) propagating through it. This luminescence is also known as *scintillation* light. Types of IR which induce scintillation light include;

- Electrons and positrons (β -particles); e^\pm
- Heavy charged particles such as protons, α -particles, muons, charged mesons and heavy ions; $p, \alpha, \mu^\pm, \bar{q}q, {}_Z^AX^\pm$.

In SNO+, these types of IR will originate from a combination of interesting and unwanted physics events inside the detector, produced over a broad range of energies, 0.1-10 MeV. Along their path, these ionising particles deposit energy in the scintillator, exciting and ionising atoms in the scintillator molecules. The rates at which an IR induces excitation and ionisation in the scintillator are known as

the excitation and ionisation *densities*, which vary based on the energy and IR type. As will be discussed in sections 3.4.5 and 3.5, the excitation and ionisation densities affect the time profile of the scintillation light, as well as the intensity of the light itself. Based on the physics objectives and backgrounds in SNO+, the most frequent types of IR are expected to be β -, α - and γ -particles. Using PMT information, the objective is to reconstruct scintillation light from processes of interest e.g. $0\nu\beta\beta$ -decay (β -particles), and distinguish it from that associated with background processes such as the daughter nuclei of the ^{238}U and ^{232}Th chains (β -, α - and γ -particles).

In comparison to SNO, scintillator provides an increased sensitivity to low-energy neutrino interactions over D_2O , for which the intensity of the Cherenkov light is indistinguishable to that from backgrounds at energies ≤ 4.5 MeV [103]. Types of low-energy neutrinos include solar neutrinos produced via the CNO-cycle, *pp*- and *pep*-chains, geo-neutrinos produced within the Earth's mantle, reactor anti-neutrinos and supernova neutrinos [19, 119]. Unlike Cherenkov radiation, scintillation light is produced isotropically, and is not correlated with the direction of the ionising radiation which induced it. Therefore, direction reconstruction is more challenging in scintillator than in water.

The energy sensitivity of SNO+ with respect to scintillator is dependent on three factors;

- **Scintillator light yield, L :** The light yield is a measure of the number of produced photons per quanta of energy absorbed by the scintillator; it is the effective intensity of the scintillation light. Here, the empirical unit of Hits MeV^{-1} is used to quantify the expected amount of scintillation light in terms of the number of PMTs registering a hit in response to its production per MeV of the incident IR. As will be discussed in Section 3.5, the light yield is non-linear at higher energies due to a phenomena known as *quenching*.
- **Scintillator emission profile:** Scintillation light is produced with a characteristic time and wavelength profile. Depending on the wavelength of the produced scintillation light, there is an associated likelihood of light being *lost* in the scintillator due to absorption or scattering; the effects of which are collectively known as *attenuation*.

- **Detector optical response:** In addition to attenuation, the PMTs themselves are more efficient at different wavelengths. The optical response of the detector is then a characterisation of the combined effect of both the attenuating processes and the PMT efficiencies.

The ideal scintillator for SNO+ should therefore produce a high light yield (especially in the $0\nu\beta\beta$ -decay ROI ~ 2.5 MeV) over an emission spectrum whose light is subject to minimal attenuation, but that also coincides with the optimal efficiency of the PMTs. The physics of scintillation light and its attenuating properties is to be discussed here. Aspects concerning the detector optical response are discussed in Chapter 4.

Finally, the use of liquid scintillator in SNO+ requires not only changes to the original SNO detector design, but also the associated infrastructure and systems which neighbour the SNO+ cavity. In particular, the D₂O purification facility used in SNO has been removed and replaced with a scintillator plant for use in SNO+. A brief description of the scintillator plant, its construction and commissioning at SNOLAB is presented in Section 3.6.

3.1 Scintillator Structure

A variety of scintillator types exist, including; organic crystals and liquids, inorganic crystals, plastics, gases and glasses. In particular, organic liquid compounds are ideal candidates for use as scintillators as they contain carbon ¹²C atoms. It is the electron configuration of carbon which gives rise to luminescence; the emission of light associated with these types of scintillators.

$$\begin{aligned} {}^{12}\text{C} [Z = 6] : & \quad 1s^2 2s^2 2p^2 \quad \text{Ground State}, \\ & \quad 1s^2 2s^1 2p^3 \quad \text{Binding State}. \end{aligned}$$

FIGURE 3.1: The electronic configuration of orbitals in a carbon ¹²C atom for the ground and binding states.

When a carbon atom features in a compound the electronic structure of the ground state is re-ordered into a *binding state* wherein one of the 2s electrons is excited to

the $2p$ orbital, see Figure 3.1. The four electrons in the valence orbitals ($2s^12p^3$) can orientate themselves in one of three ways [120];

- **Tetrahedral, sp^3 :** All four of the valence electrons align to form a tetrahedral shape with a separation angle of $\sim 109^\circ$, each electron contributing to a bond. This is the configuration exhibited by carbon in saturated hydrocarbons such as methane, CH_4 and crystal lattice structures such as diamond.
- **Trigonal, sp^2 :** Three of the valence electrons separate in a two-dimensional plane about, and perpendicular to a common axis forming a triangular shape with a separation angle of 120° . These three electrons contribute to bonds leaving a remaining valence electron in the $2p$ orbital, along the common axis. This is the configuration exhibited by carbon in aromatic compounds containing one or more ring-like benzene or toluene structures.
- **Digonal, sp :** Two of the valence electrons separate linearly back-to-back with a separation angle of 180° along a common axis. These two electrons contribute to bonds leaving two remaining valence electrons in the $2p$ orbital. This is the configuration exhibited by linear compounds such as acetylene, C_2H_2 and carbon dioxide, CO_2 .

The electrons that contribute towards bonds are called σ -electrons, the bonds being σ -bonds. The orientation of σ -electrons in benzene, C_6H_6 is shown in Figure 3.2. In both trigonal and digonal configurations, one or more electrons remain valent within the $2p$ orbital. These valent electrons are less tightly bound to their parent carbon nuclei and are known as π -electrons. These π -electrons may also form similar π -bonds in certain compounds depending on the orientation of their respective orbitals. In ring-like structures such as benzene, the π -electrons form a cloud of delocalised charge in parallel planes above and below the plane of the ring, see Figure 3.3. In general, a molecule containing n benzene rings will contribute $2(2n + 1)$ π -electrons, one from each carbon atom. The delocalisation of the π -electrons means they require less energy than σ -electrons to be excited. It is the excitation and subsequent de-excitation of π -electrons that is responsible for the production of luminescence, scintillation light, in organic liquid scintillators.

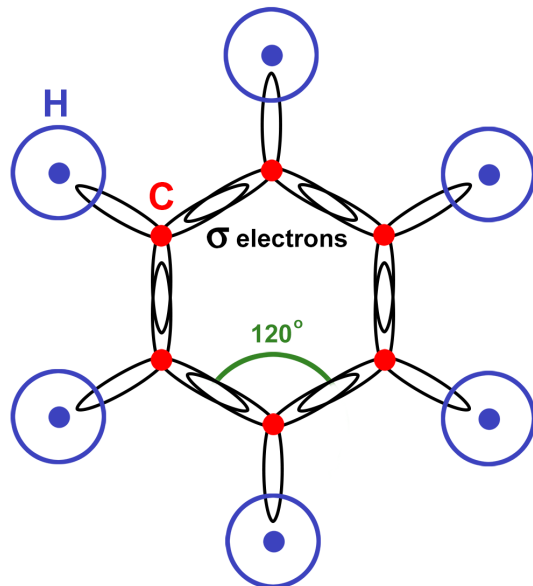


FIGURE 3.2: Two-dimensional plane perspective of the electron orbitals in benzene (C_6H_6). Shown are six carbon atoms (red) with trigonal orbital orientations (black). The σ -electrons form bonds with adjacent carbon and hydrogen atoms (blue).

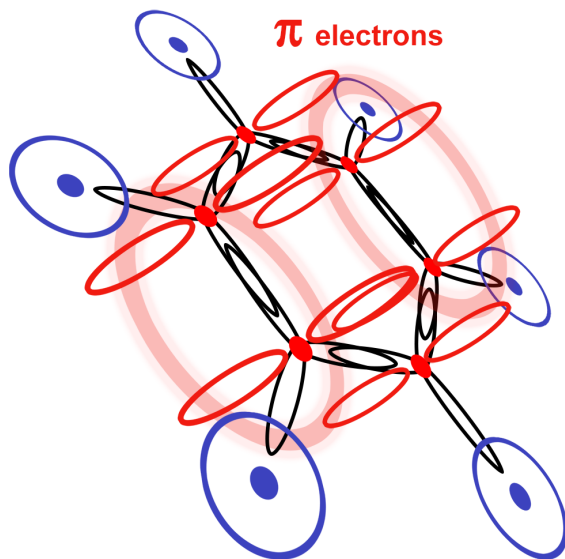


FIGURE 3.3: Three-dimensional perspective of the electron orbitals in benzene (C_6H_6). Shown are the six valent π -electron orbitals which are directed out of the plane of the ring structure. Collectively these form rings of positive and negative delocalised charge above and below the plane of the ring.

3.2 The SNO+ Scintillator

The primary scintillator used in SNO+ is LABPPO; a combination of an aromatic compound called linear alkyl-benzene (LAB) at a concentration of 825.0 g L^{-1} and 2,5-diphenyloxazole (PPO) at a concentration of 2.0 g L^{-1} . LABPPO is an example of a *binary* liquid scintillator; a two component mixture containing a *solvent* (LAB) and a *fluor* (PPO). The role of the solvent is to absorb energy deposited by ionising radiation and transfer it to the fluor molecules, thus exciting them. Whilst LAB will naturally scintillate, it is preferable to use a secondary component which has a higher quantum efficiency (photons emitted per quanta of energy absorbed). The fluor should also have an absorption spectrum coincident with the emission profile of the solvent. The absorption of scintillation light from the solvent by the fluor is known as *radiative* transfer. The fluor is often referred to as being a wavelength shifter (WLS). As will be discussed in Section 3.4.3, the mechanism for energy migration between the solvent and the WLS can be radiative or *non-radiative*. Primarily, it is the emission of light following excitation and de-excitation of the WLS which is associated with the scintillation light of a binary liquid scintillator. LABPPO is to be used during the scintillator phase of SNO+. At time of writing there are also two candidate *ternary* mixtures, containing two fluors, for use in the tellurium phase; LABPPO+0.3%Te+bis-MSB and LABPPO+0.3%Te+perylene. The chemical structures of LAB, PPO, bis-MSB and perylene are shown in Figure 3.4.

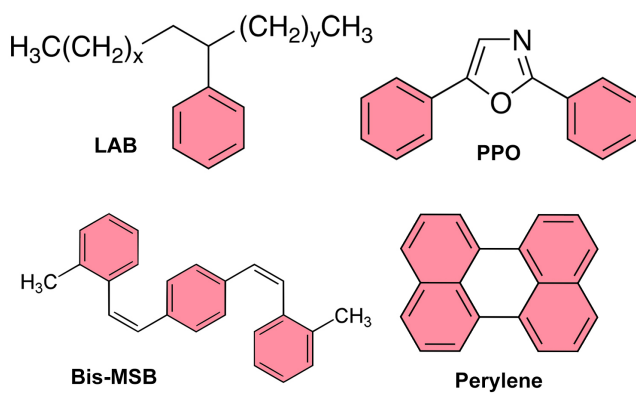


FIGURE 3.4: Chemical structures of LAB, PPO, bis-MSB and perylene. All four of these molecules contain benzene rings (red) which contribute valent π -electrons. It is within these regions that scintillation light is produced.

Tellurium is prone to precipitating in liquids [121]. Subsequently, an LAB based surfactant, PRS is used to maintain suspension of the tellurium in the scintillator. Unfortunately, the PPO emission spectrum coincides where the PRS is highly absorbing. As will be discussed, to avoid this problem, either bis-MSB or perylene can be added as a secondary WLS to *catch* the PPO emission and *shift* the wavelength away from the PRS absorption peaks. The concentrations of LAB, PPO, PRS, bis-MSB and perylene are shown in Table 3.1. The side-effect of adding PRS is that the light yield of the base mixture, LABPPO is decreased. The light yields of the three different scintillator mixtures are shown in Table 3.2. For comparison, the light yield of Cherenkov radiation in water is included also. It is the increased light yield with scintillator that allows SNO+ to probe low-energy neutrino interactions, 1-3 MeV.

SNO+ Scintillator Component Concentrations

Scintillator	Component	Conc. [g L ⁻¹]
LABPPO	LAB	825.0
	PPO	2.0
LABPPO+0.3%Te+Bis-MSB	LAB	825.0
	PPO	2.0
	PRS+0.3%Te	43.43
	Bis-MSB	0.015
LABPPO+0.3%Te+Perylene	LAB	825.0
	PPO	2.0
	PRS+0.3%Te	43.43
	Perylene	0.015

TABLE 3.1: Concentrations of LAB, PPO, PRS+0.3%Te, bis-MSB and perylene in different scintillator mixtures for use in the scintillator and tellurium phases of SNO+. There are currently two candidates for the tellurium phase; LABPPO+0.3%Te+bis-MSB and LABPPO+0.3%Te+perylene.

Light Yields, L

Material	L [Hits MeV ⁻¹]
LABPPO	520
LABPPO+0.3%Te+Bis-MSB	240
LABPPO+0.3%Te+Perylene	312
H ₂ O/D ₂ O (Cherenkov)	8-9

TABLE 3.2: The light yield of the three scintillator mixtures considered here. The light yield of water from Cherenkov radiation is included for comparison.

3.3 Excitation & Attenuation

The excitation and subsequent de-excitation of π -electrons in the fluor give rise to absorption and luminescence. Ionising radiation loses energy as it passes through a scintillator, depositing it in the material. A fraction of this energy is absorbed by the material, thus exciting the molecules in it. Because of the low concentration of the fluor, the solvent molecules typically absorb the energy and migrate it to the fluor either radiatively and non-radiatively. Once energy is absorbed by the fluor, excitation occurs rapidly 1-10 ps. Excitation of π -electrons occurs between the singlet ground state, S_0 and higher singlet states; $S_1, S_2, S_3\dots$ etc. The electrons will also couple to the different vibrational modes of the molecule, dividing each singlet state into further sub-levels.

The π -electrons may also exist in triplet states, $T_1, T_2, T_3 \dots$ etc. which exist at a slightly lower energy than the equivalent singlet state. Direct excitation from $S_0 \rightarrow T_1$ is spin-forbidden. However, excited singlet states can transition to their equivalent triplet state via spin-orbit coupling, often referred to as *inter-system crossing*. As will be discussed in Section 3.4, this leads to different types of luminescence. An example of the energy levels for π -electron singlet and triplet states is shown in Figure 3.5.

The transitions between singlet states, $S_0 \rightarrow S_1, S_0 \rightarrow S_2, S_0 \rightarrow S_3\dots$ etc give rise to the observed absorption of light in organic compounds across different wavelengths. The absorption of a component can be measured in terms of the *molar extinction coefficient*, ϵ a measure of the transition probability. This governs the *transmittance*; the fraction of energy transmitted, as light, through a material as defined by the Beer-Lambert law:

$$\text{Transmittance} = 10^{-A}, \quad A = \epsilon cd, \quad (3.1)$$

where c is the concentration of the component in the medium and d is the path length travelled by the light. The molar extinction coefficients for LAB, PPO, PRS, bis-MSB and perylene from measurements made by L. Segui at Brookhaven National Laboratory (BNL) are shown in Figure 3.6. The fluors; PPO, bis-MSB and perylene all have much larger extinction coefficients than LAB. This is indicative of the fluors higher quantum efficiency over the solvent to absorb energy and emit light. PRS also has a larger extinction coefficient than LAB; although

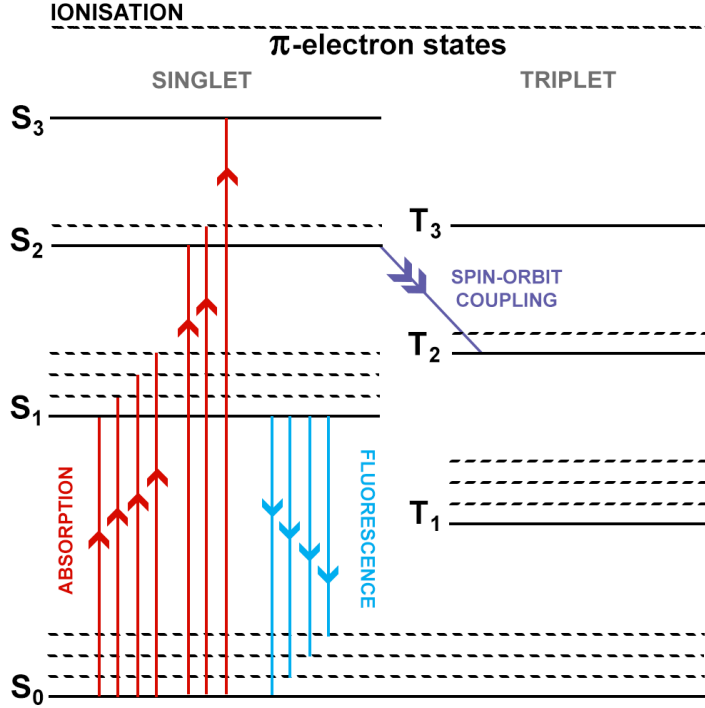


FIGURE 3.5: Energy level diagram for π -electrons. Shown are the singlet, S_i and triplet, T_i states. Dashed lines represent vibrational sub-levels of each state.

it is not a fluor, it only absorbs light. It is then important to note that PRS absorbs more than PPO in the $\sim 370\text{-}500$ nm region. This leads to absorption of the PPO emission by PRS. It is for this reason that mixtures containing PRS also contain bis-MSB or perylene as a secondary WLS. This is because they are more absorbing than PRS in this region, and therefore are more likely to absorb light and subsequently emit it at higher wavelengths away from the regions where the PRS is strongly absorbing.

In addition to absorption, light travelling through the detector will be subject to a variety of scattering effects; Mie, Compton and Rayleigh scattering. Rayleigh scattering is the most prominent because the wavelength of optical photons $O(10^2)$ nm is larger than the water or scintillator molecules (for comparison, the diameter of a benzene ring is ~ 0.28 nm [123]). In scintillator specifically, it is the solvent molecules (LAB) which provide the scattering media because of their large concentration; scattering from the WLS and PRS is negligible. Therefore, for all three scintillator mixtures considered here, the scattering lengths are similar. Measurements of the scattering lengths for each of the scintillator mixtures were combined; the average scattering length of LABPPO, LABPPO+0.3%Te+bis-MSB

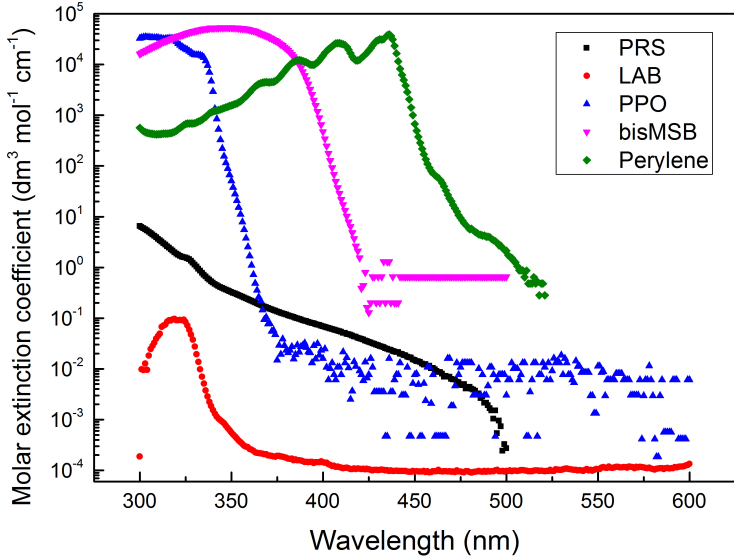


FIGURE 3.6: Molar extinction coefficients for LAB, PPO, PRS, bis-MSB and perylene. Measurements made at BNL by L. Segui [122].

and LABPPO+0.3%Te+perylene is shown in Figure 3.7. The Rayleigh scattering length increases quartically with wavelength $\propto \lambda^4$.

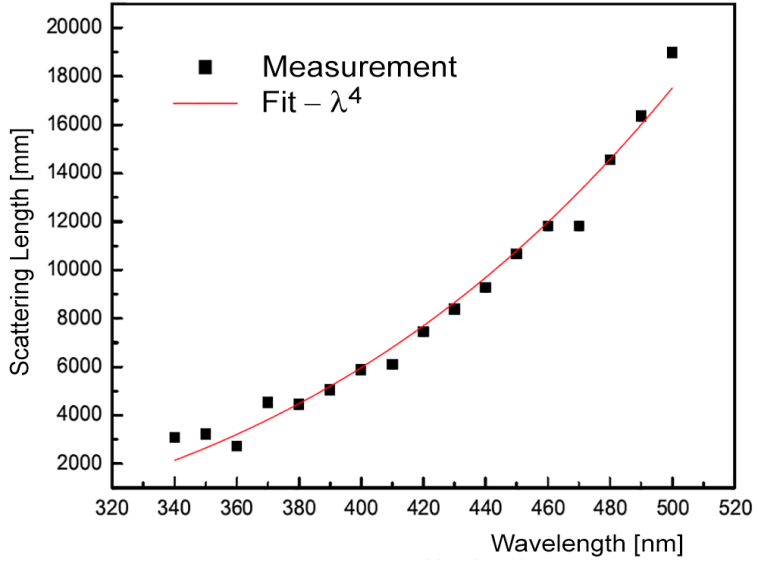


FIGURE 3.7: Average scattering length for LABPPO(+0.3%Te+bis-MSB/perylene). Measurements are fitted to a quartic function in wavelength. Measurements made at BNL by L. Segui [122].

The quantity A in Equation 3.1 is the *absorbance*, a decadic quantity that is related to the naperian attenuation coefficient of the component, α as follows:

$$\begin{aligned} \text{Transmittance} &= 10^{-A} = e^{-\alpha d}, \\ \Rightarrow \alpha &= \frac{A}{d} \ln(10) = \epsilon c \ln(10). \end{aligned} \quad (3.2)$$

Attenuation is the measure of the total extinction of light as it passes through a medium due to absorption and scattering. The attenuation coefficient is the sum of the absorption and scattering coefficients;

$$\alpha = \alpha_{\text{abs}} + \alpha_{\text{scat}} = \frac{1}{L_{\text{abs}}} + \frac{1}{L_{\text{scat}}} = \frac{1}{L_{\text{attn}}}, \quad (3.3)$$

where L_{abs} , L_{scat} and L_{attn} are the respective absorption, scattering and attenuation lengths. Using equations 3.2 and 3.3, measurements of the molar extinction coefficient can be related to the attenuation lengths, see Figure 3.8.

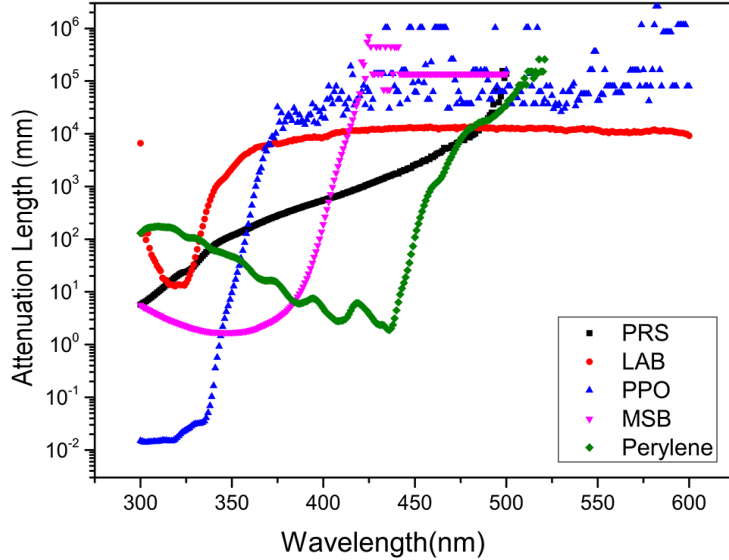


FIGURE 3.8: [122] Attenuation lengths for LAB, PPO, PRS, bis-MSB and perylene.

For a multi-component material such as the SNO+ scintillator the total attenuation coefficient is given as the sum of the individual coefficients:

$$\alpha = \sum_i \alpha_i = \ln(10) \sum_i \epsilon_i c_i. \quad (3.4)$$

Based on the scintillator mixture, the attenuation in scintillator will be dominated by either scattering or absorption. For example, in the 375-450 nm region in LABPPO, both the LAB and PPO molar extinction coefficients are small, $\leq 10^{-2} \text{ dm}^3 \text{ mol}^{-1} \text{ cm}^{-1}$ (weakly absorbing). Therefore, the majority of the attenuation will be due to Rayleigh scattering. However, in the same wavelength region for LABPPO+0.3%Te+perylene, the molar extinction coefficient of perylene is large, and hence the majority of the light will be absorbed and reemitted to longer wavelengths. The same applies for LABPPO+0.3%Te+bis-MSB in the 375-400 nm region. In all three of the mixtures light < 400 nm is subject to both high levels of absorption and scattering; the scattering length is shorter than the AV radius, $L_{\text{scat}} < 6$ m. Light in this region is therefore strongly attenuated. Consequently, it is preferable to select a scintillation emission profile which emits at longer wavelengths where there is less attenuation.

3.4 De-Excitation & Luminescence

The de-excitation of π -electrons to the S_0 state gives rise to luminescence. Depending on the transition between states, the luminescence will be produced with both a different emission and timing profile. There are three types of luminescence; fluorescence, phosphorescence and delayed-fluorescence.

3.4.1 Fluorescence

Fluorescence is the emission of light associated with the transition of π -electrons between $S_1 \rightarrow S_0$. The majority of light produced by scintillators is through fluorescence. The lifetime, τ_s of the S_1 states is typically 1-10 ns. Fluorescence is therefore considered a fast process. The intensity of the fluorescence decays exponentially in time;

$$I = I_0 \exp(-t/\tau_s), \quad (3.5)$$

where I_0 is the initial fluorescence intensity and I is the intensity at a time t following population of the excited states. The π -electrons which are initially excited into higher states, $S_2, S_3 \dots$ etc. quickly (~ 0.01 ns) thermalise into S_1 via non-radiative internal conversion, thereafter transitioning via $S_1 \rightarrow S_0$.

It is important to note that there is also a finite time associated with the population of excited singlet states. The length of this time depends on the nature of the incident ionising radiation. In the case of electromagnetic radiation, the fluor can be directly excited based on the absorption length at a particular wavelength, whereas with charged particles the fluor is excited by the energy transfer from the solvent molecules. The cumulative effect of these different energy transfers is a time spread for the population of excited states. This is often referred to as the *rise-time*, τ_r the mean time taken to populate excited states of the fluor, either radiatively or non-radiatively. Equation 3.5 can be modified to account for the rise time;

$$I = I_0 (\exp(-t/\tau_s) - \exp(-t/\tau_r)). \quad (3.6)$$

The rise time is typically no greater than 1 ns but can increase as additional components are added to the scintillator, increasing variations in energy migrations prior to excitation and emission [124]. The rise time can therefore be alternatively characterised as the *photon-walk* length, α_w ; the average displacement (not time) of energy migration between components prior to emission of the final scintillation light. This is discussed in Section 4.5.2.

3.4.2 Phosphorescence & Delayed-Fluorescence

Excited singlet states may transition to a triplet state, and vice-versa through inter-system crossing. Inter-system crossing arises from the spin-orbit coupling of excited π -electrons to their parent nuclei. Inter-system crossing is more favourable when the vibrational sub-levels of the singlet and triplet states overlap. Once in a triplet state, the molecule may acquire further energy allowing for the electron to return to the singlet state and decay radiatively via fluorescence. Due to inter-system crossing, this process is slower than standard fluorescence $\sim 10^{-4}$ s, it is *delayed* and decays non-exponentially in time. Alternatively, the triplet state may return to S_0 radiatively with a similarly long life-time; this is known as *phosphorescence*. The energy level transitions for fluorescence and phosphorescence are illustrated in Figure 3.9.

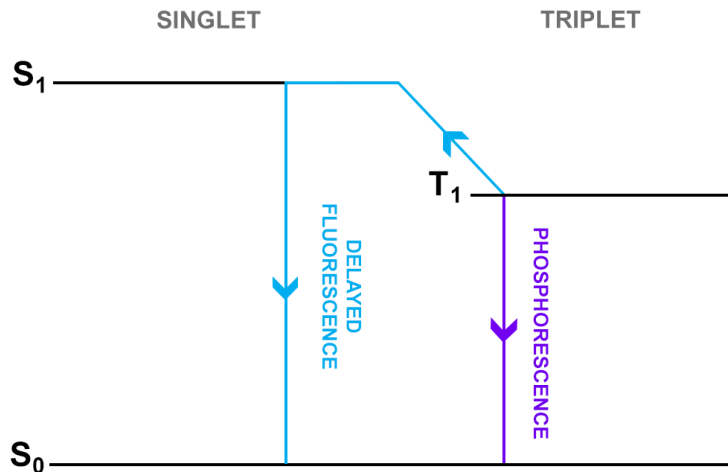


FIGURE 3.9: Energy level diagram for the required transitions between singlet and triplet states for phosphorescence and delayed fluorescence.

3.4.3 Energy Migration

Due to small concentrations of the fluor, the majority of the energy deposited by the IR is absorbed by the solvent molecules. Once this occurs, there are several mechanisms between the scintillator components that compete for this energy. For example, the energy could be transferred to the fluor, or another solvent molecule either radiatively, e.g. emission followed by absorption, or non-radiatively e.g. vibrational collisions. Alternatively, energy may be lost within the molecule itself through internal conversion. Figure 3.10 outlines the different mechanisms in a binary system such as LABPPO. The complexity of the competing processes is compounded for ternary systems, e.g. LABPPO+0.3%Te+bis-MSB and LABPPO+0.3%Te+perylene, which contain two types of fluor in addition to PRS.

3.4.4 Wavelength Shifters

As outlined in Section 3.3, the use of a secondary WLS is necessary during the tellurium phase to avoid absorption of the PPO emission by the surfactant, PRS. The current candidates for this secondary WLS are bis-MSB and perylene. As shown in Figure 3.11, both absorb relatively strongly in the primary PPO emission region 350-370 nm. Bis-MSB emits in a region of 390-450 nm whilst perylene emits at longer wavelengths, 450-500 nm.

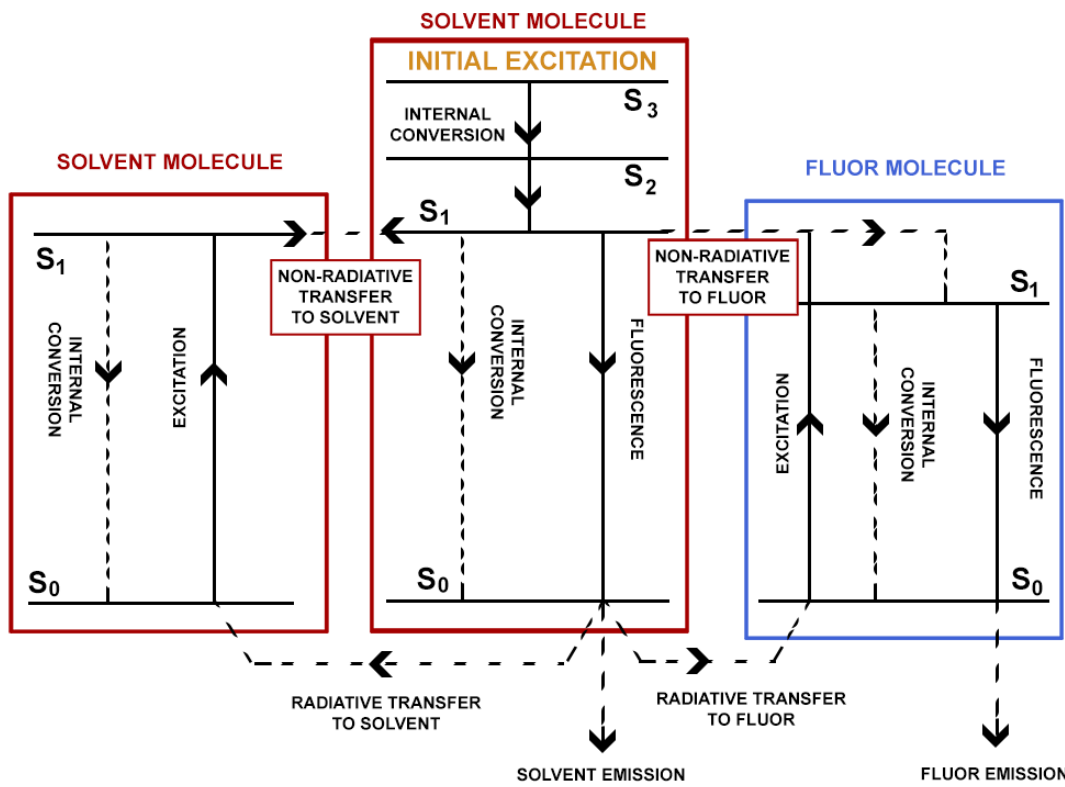


FIGURE 3.10: Flow diagram of the processes competing for energy in a binary scintillator. Energy can be transferred from the initially excited molecule to the solvent or fluor either radiatively or non-radiatively. It is also possible for the energy of the excited molecule to be lost through internal conversion.

Emission followed by immediate absorption is known as *reabsorption*. When the molecules emitting and absorbing are of the same type, it is called *self-absorption*. Reabsorption and self-absorption arise from overlaps in the absorption and emission spectra. As will be discussed in Section 7.1.1, the level of reabsorption or self-absorption is geometrically constrained by the size of the bulk liquid. As governed by the absorption lengths of the individual components, the longer light must travel through the scintillator, the more likely it is to be reabsorbed.

It is important to note that at wavelengths $\lesssim 400$ nm and $\lesssim 450$ nm in the bis-MSB and perylene scenarios respectively, regardless of the type of incident IR, the emission spectra of the scintillator will closely match that of the secondary wavelength shifter. An example using 400 nm photons in LABPPO+0.3%+perylene is shown in Figure 3.12, in which none of the original 400 nm is detected at the PMTs; it is absorbed and reemitted at longer wavelengths. For this reason, the emission spectra of the secondary WLS must also coincide with the quantum efficiency of the PMTs to detect light of a particular wavelength. In addition, scintillation

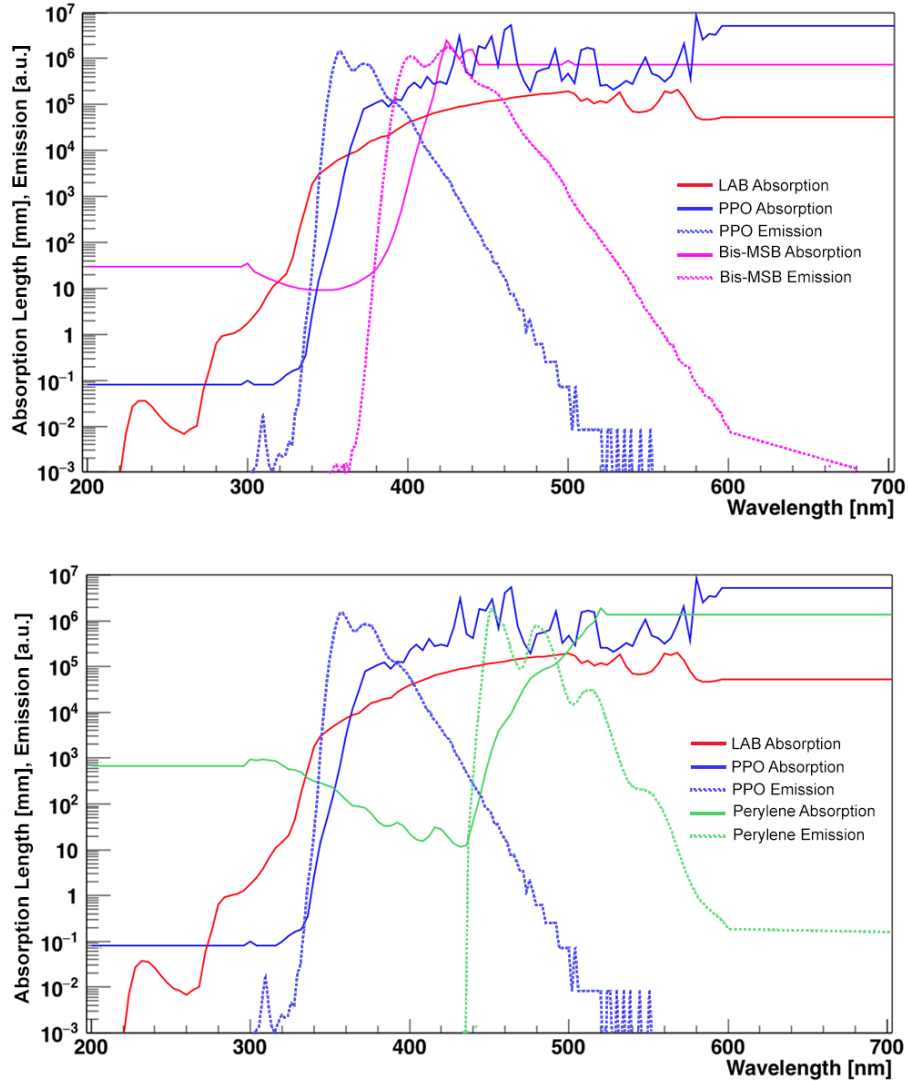


FIGURE 3.11: The absorption lengths of LAB, PPO and (top) bis-MSB and (bottom) perylene. Shown also are the respective emission spectra for PPO, bis-MSB and perylene. Bis-MSB and perylene absorbs the PPO emission 350-370 nm, reemitting at longer wavelengths; predominantly 390-450 nm (bis-MSB) and 450-500 (perylene).

light produced in the inner AV region will also need to pass through the acrylic of the AV itself, which is absorbing at shorter wavelengths. Figure 3.13 illustrates how the emission of the different wavelength shifters relates to the efficiency of the PMTs and the absorption length of the acrylic across different wavelengths.

The final choice of the secondary WLS to be used needs to account for the above factors. For example, the higher wavelengths of the perylene emission favours less scattering, less overall attenuation and higher transparency in the acrylic. However, the shorter wavelengths of the bis-MSB spectrum favour a higher PMT

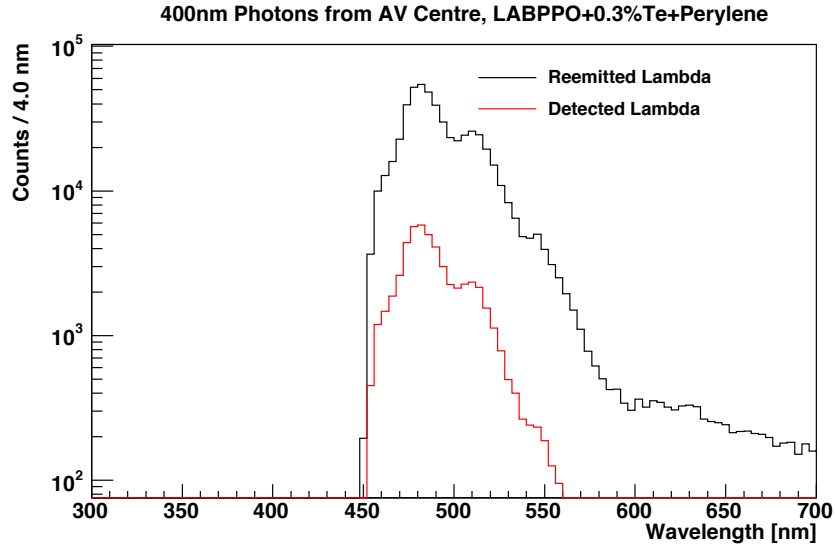


FIGURE 3.12: The emitted (black) and detected (red) emission profile from simulations of 400 nm photons at the centre of the detector in LABPPO+0.3%Te+perylene. At its maximum, the detected spectrum is $\sim 22\%$ of the emitted spectrum at ~ 475 nm. This corresponds to the approximate PMT efficiency of 21-22% in this region, see Figure 3.13. Above 550 nm the PMT efficiency is very small, this is reflected in the suppressed tail of the detected spectrum.

efficiency. Alongside the optical properties of the WLS, other factors include; compatibility with expected reconstruction techniques, cost, chemical compatibility with the other detector materials and the techniques used to purify the scintillator.

3.4.5 Scintillation Time Profile

Depending on the nature of the incident radiation, the timing of the scintillation profile will be different. This is particularly important when discriminating between β - and α -particles passing through the scintillator. α -particles have a greater excitation density than β -particles, meaning that excitations of the singlet states become saturated, increasing the likelihood of populating additional triplet states. The saturation of excited states increases the overall light yield of the scintillation process. However, the triplet states lead to a longer effective lifetime of the scintillation intensity due to delayed fluorescence. Reconstruction exploits this phenomena in order to identify different particles based on the scintillation

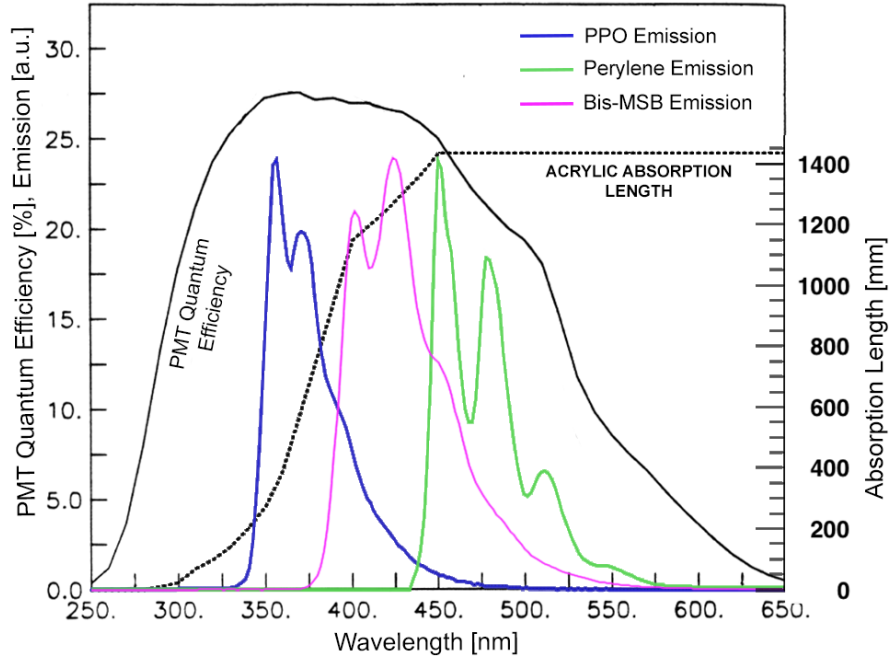


FIGURE 3.13: The quantum efficiency of the SNO+ PMTs alongside the emission spectra of PPO, bis-MSB and perylene. Shown also is the absorption length of the acrylic of the AV itself which absorbs light at shorter wavelengths. The PMT efficiency curves comes from measurements originally made in the SNO design phase [125].

time profile. In particular, this can be combined with coincidence timing to remove Bi-Po background events; the decay of ^{212}Bi (α/β emission, $t_{1/2} \sim 60$ mins) followed by ^{212}Po decay (α/β , $t_{1/2}^\beta \sim 3$ mins, $t_{1/2}^\alpha \sim 0.30\ \mu\text{s}$). An example of the scintillation time profiles for β - and α -particles is shown in Figure 3.14.

Past studies of the scintillator mixtures for SNO+ [126, 127] have found that the scintillation timing profile for β - and α -particles can be well characterised as a linear combination of three exponential decay profiles;

$$I = I_0 \sum_{i=1}^3 N_i \exp(-t/\tau_i), \quad \sum_{i=1}^3 N_i = 1, \quad (3.7)$$

where N_i are normalisation constants.

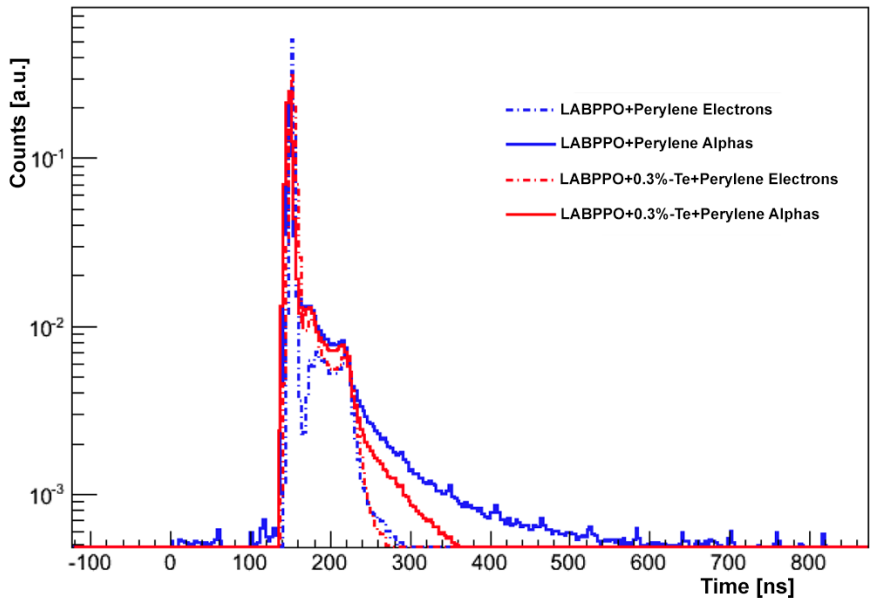


FIGURE 3.14: The scintillation time profiles for β - and α -particles in LABPPO+perylene (blue) and LAB+perylene+0.3% tellurium (red). In both mixtures, the α -particle profile has a longer and larger tail following the main peak due to increased delayed fluorescence. Measurements made at the University of Pennsylvania by S. Grullon [126].

3.5 Quenching

Following prolonged exposure to ionising radiation, the efficiency of a scintillator will deteriorate. Degradation is due to ionisation; the liberation of electrons from the bound states with their parent nuclei. Highly energetic particles such as cosmogenic muons and α -particles ionise atoms in the scintillator as they pass through it. The ionisation density associated with these particles is enough to temporarily or permanently damage the molecules. Recovery from temporary damage is via ion-recombination. Studies suggest that $\sim 75\%$ of ion-recombination is into triplet states, thus slowing the fluorescence process; the fast component of the scintillator. Permanent damage results in impurities in the scintillator, making the affected molecules unavailable for the production of luminescence [120]. Collectively these effects are known as *quenching*. For sufficiently energetic ionising radiation, quenching limits the increase in light yield of a scintillator.

Experimental evidence suggests that as the energy of the incident IR increases, the change in light yield of the scintillator becomes non-linear and approaches a constant, maximum value. The quenching curve for anthracene; a scintillating

aromatic compound is shown in Figure 3.15. In this example, protons, β - and α -particles reach an energy at which the increase in the light yield begins to plateau.

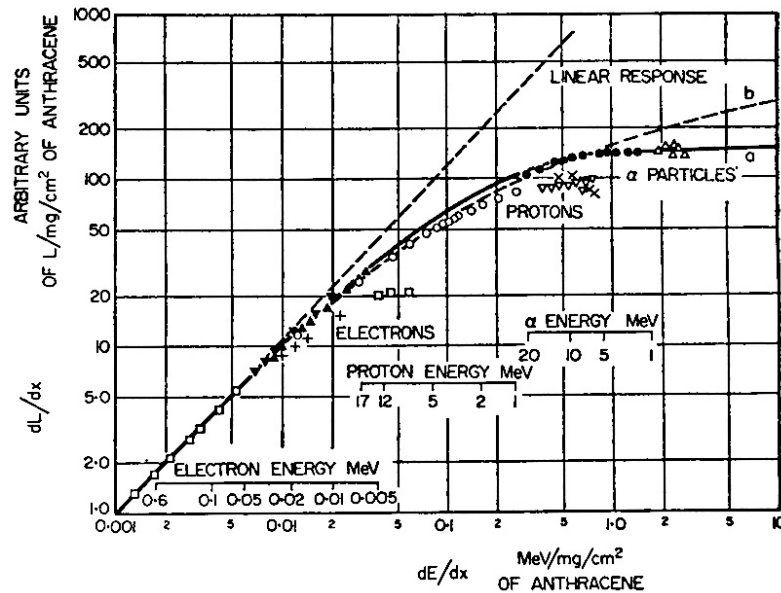


FIGURE 3.15: [120] The quenching of the scintillating compound, anthracene. As the incident energy of the IR increases ($\propto dE/dx$) the change in the light yield (dL/dx) becomes non-linear and plateaus due to quenching.

It is useful to define two quantities which relate the change in light yield, dL/dx of the scintillator to the change in energy of the ionising radiation along its path, dE/dx . At low energies the scintillator response is linear;

$$\frac{dL}{dx} = S \frac{dE}{dx}, \quad (3.8)$$

where S is the efficiency of the scintillator to convert energy into luminescence. A relation known as *Birk's law* characterises the non-linear response of the scintillator at higher energies [120];

$$\frac{dL}{dx} = \frac{S \frac{dE}{dx}}{1 + k_B \frac{dE}{dx}}, \quad (3.9)$$

where k_B is an IR and material specific quantity known as Birk's constant or quenching factor. This characterises the rate of plateau of the scintillator response at higher energies. At low energies ($dE/dx \ll 1$) Equation 3.9 returns to the expression in Equation 3.8. At high energies ($dE/dx \gg 1$) the change in light

yield approaches a constant value;

$$\frac{dL}{dx} \simeq \frac{S}{k_B} = \text{const.} \quad (3.10)$$

Members of the SNO+ collaboration recently published measurements of k_B for α -particles in LAB obtained using three independent methods [128];

$$[\text{LAB}, \alpha] : 0.0066 \pm 0.0016 < k_B < 0.0076 \pm 0.0003 \text{ cm MeV}^{-1}. \quad (3.11)$$

These results provided the first accurate account of quenching for α -particles in LAB. This is of use to not only SNO+, but also other LAB based experiments who hope to use the discriminating power of scintillator to identify particle types.

3.6 The SNO+ Scintillator Plant

The D₂O purification facility used in SNO has been removed and replaced with a scintillator plant for use in SNO+, located in an adjacent drift to the detector cavity as shown in Figure 3.16. This facility consists of 39 volumes varying between 0.5-4 m³ : 13 vessels, 17 kettles and 9 columns. These are all interconnected with approximately 2 km of pipeline. The main function of the plant is to purify and mix the various scintillator components; the solvent (LAB), the fluors/WLS (PPO and bis-MSB/perylene), the surfactant (PRS) and the tellurium.

After contractual work to assemble the scintillator plant itself was completed, the plant entered a phase of stringent assessments and post processing in order to comply with the strict background requirements of the experiment. This involved helium leak checking of all volumes and pipelines. This is discussed in Section 3.7.3.

Starting in January 2013, construction and assessment of the plant took approximately two and a half years to complete. Given the associated logistical and engineering constraints, the strict safety regulations imposed by VALE and the cleanliness standards of SNOLAB itself, the construction of an industrial sized scintillator plant 2 km underground is one of greatest achievements of the SNO+ commissioning phase.

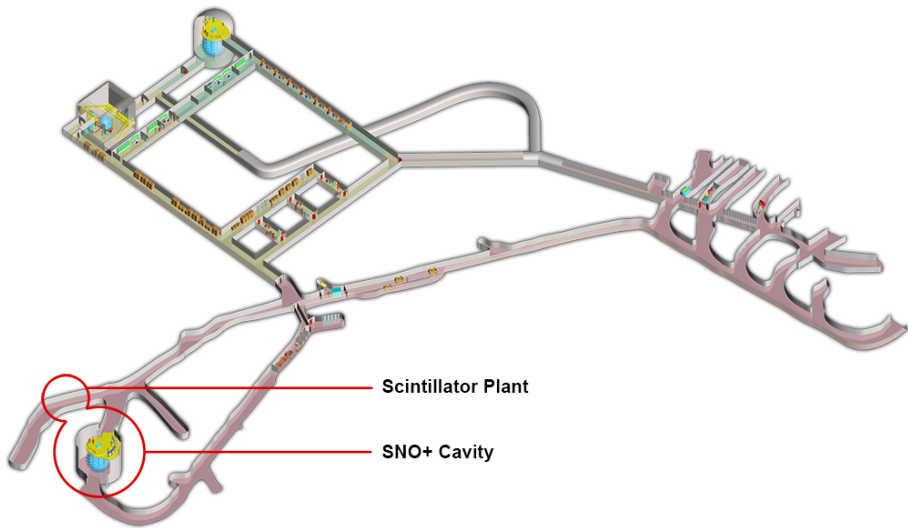


FIGURE 3.16: Three-dimensional plan layout of SNOLAB. Shown are the locations of the SNO+ detector cavity and the approximate location of the scintillator plant in the adjacent drift.

3.7 A Deep Rooted Plant

The scintillator plant is central to the overall strategy of processing LAB at SNOLAB; transporting it underground, purifying it, putting it into the AV and ultimately returning it to the surface once SNO+ completes collecting data. It is located as close to the detector as possible in order to minimise backgrounds induced by exposing the LAB to cosmogenic activity which would otherwise accumulate at a higher rate through surface storage. In addition, once the individual scintillator components arrive underground, the plant applies various purifying techniques to ensure the final mixture is compliant with the background requirements of the experiment itself.

A consequence of the plant location highlights several associated logistical and technical considerations; the safety regulations imposed by VALE on the transportation and storage of chemicals underground, and the highly constrained containment area available for construction of the plant inside SNOLAB itself.

3.7.1 Transportation & Storage of LAB

The main task when transporting and storing LAB is to minimise its exposure to cosmogenic activity on the surface. Consequently, the available infrastructure available to SNOLAB has been maximised in order to transport as much LAB as possible in a working day whilst maintaining cleanliness requirements.

LAB is sourced from CEPSA Química SA who deliver to SNOLAB three times a week using road tankers with a capacity of 22 tonnes each, $66 \text{ tonnes week}^{-1}$. Once delivered, the LAB is temporarily stored in the surface transfer facility, a 70 m^3 holding tank which acts as the loading terminal for six rail tanker trucks, each with a capacity of 3 m^3 , equivalent to 2.2 tonnes of LAB, see Figure 3.17. The rail tankers transport the LAB underground and return once a day. This equates to approximately $13 \text{ tonnes day}^{-1}$ of LAB. Assuming a 5-day weekly working schedule, the rail tankers are able to deliver $66 \text{ tonnes week}^{-1}$ underground. The 1000 kg hr^{-1} flow rate of the scintillator plant is therefore sufficient to process all the LAB arriving underground within the week of its arrival [97]. Ultimately, the rate of LAB transported underground is limited only by the capacity and number of rail tankers.



FIGURE 3.17: The surface rail tankers (left) used to transport the LAB from the SNOLAB surface transfer facility (right).

3.7.2 Construction of the Plant

The scintillator plant occupies the same area as the D₂O processing facility previously used in SNO, situated within a 15.3 m × 4.6 m containment area. The plant exists on two levels that are separated by a grated steel mezzanine floor [129]. The first and second levels have overhead clearances of 3 m and 2-3 m respectively (the ceiling height on the second level varies due to the cavernous nature of the rock in the drift ceiling). An additional 2 m pit was excavated from the drift floor on the first level to make room for the larger columns as shown in Figure 3.18.

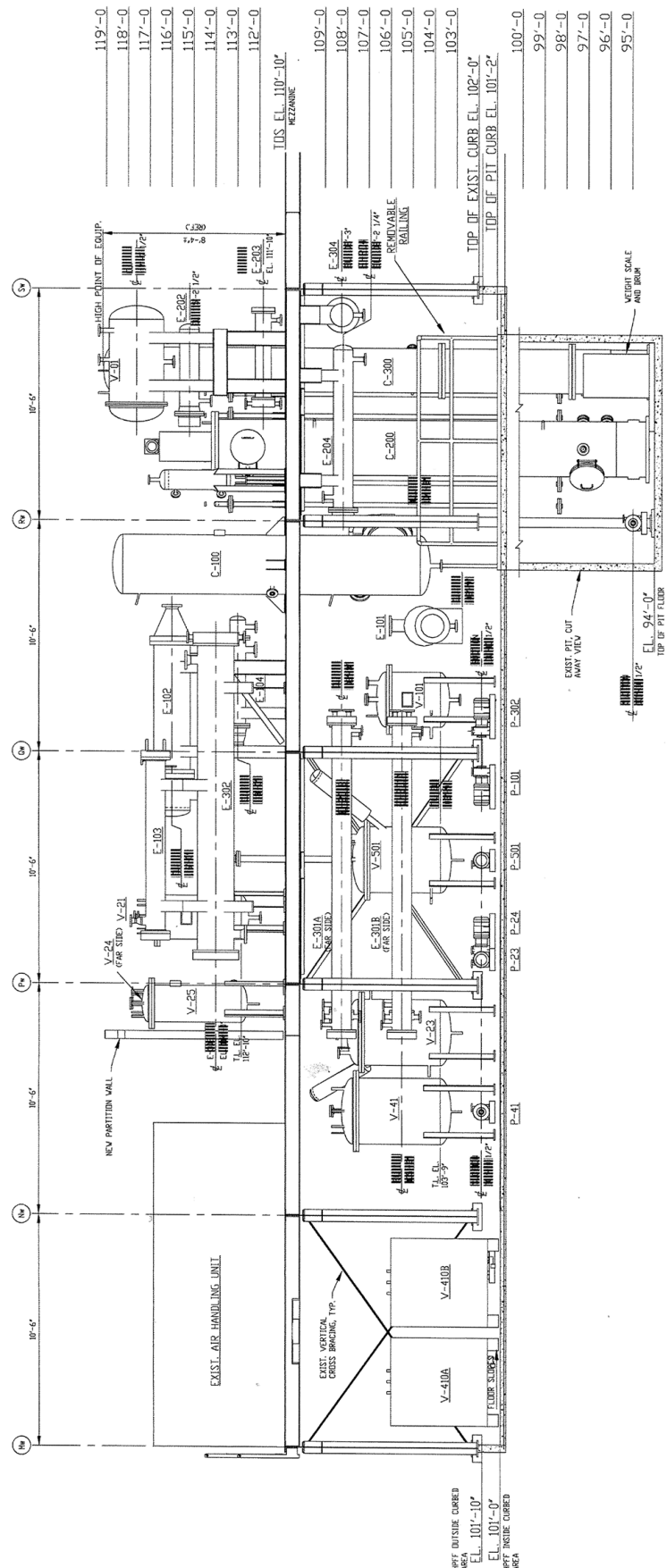


FIGURE 3.18: An example cross sectional technical drawing by Koch Modular Process Systems LLC of the SNO+ scintillator plant. Labelled are the vessels (V-XXX), kettles (E-XXX) and columns (C-XXX). The plant spans three levels with an upper and lower level and an additional, newly excavated pit area in order to fit large stripping and scavenger columns.



FIGURE 3.19: The lower (left) and upper (right) levels of the scintillator plant.

3.7.3 Helium Leak Checking

The scintillator plant must operate in compliance with the stringent radiopurity levels required by the experiment. The mine rock from which the lab is excavated regularly emanates radon, and hence the operating components of the plant must be sealed to prevent the accumulation of backgrounds in the scintillator prior to deployment into the AV. The seal integrity of all the vessels and pipelines were checked using a helium leak detector. For the target levels of $^{238}\text{U} = 1.6 \times 10^{-17} \text{ g/g}$ and $^{232}\text{Th} = 6.8 \times 10^{-18} \text{ g/g}$ in LABPPO, the equivalent leak rate (LR) for each connection between every component is required to be $\leq 1 \times 10^{-9} \text{ mBar L s}^{-1}$ [102, 129]. The author spent eight months helium leak checking between March - December 2014 with a team of other collaborators. An overview of the leak checking procedure is now given.

The scintillator plant is designed to act as a single operating entity, in which scintillator is continuously processed, flowing through the plant whilst being stripped of backgrounds and mixed with other components. Leak checking the entire plant in a single pass is infeasible, and therefore the plant was leak checked systematically by identifying subsets of components e.g. vessels and interconnected pipes, and isolating them from the rest of the plant to form a closed loop or spool.

Leak checking of a loop/spool is composed of four steps;

- **Loop isolation:** The isolation of a vessel or pipeline involves the installation of blind flanges or caps onto one or several of its ports. The interface of these blinds can vary from $1/4''$ - $1''$ VCR Swagelock gaskets to $1''$ - $12''$ diameter conflat flanges. Hand-valves located on the pipes can also be closed to provide a termination point. One port in the loop is then selected to attach a KF adapter to which a vacuum pump can be attached. Aluminium tape is applied around all joints, seals and welds that are to be tested.
- **Achieving vacuum in the vessel:** An Edwards nXDS6i or XDS-5 [130] scroll pump is attached to the KF adapter and used to evacuate the loop, reducing the internal pressure from an initial 1000 mBar to 0.1 mBar. In achieving this level of vacuum, any traces dust or water vapour are removed from inside the loop. Dust and water vapour is damaging to the pump and spectrometer contained in the helium leak detector. It is for this reason a scroll pump that is more robust to particulates is used first. Next, the loop is sealed off temporarily by use of a needle valve such that the scroll pump can be replaced with a helium leak detector (model: Leybold INFICON UL 200 [131]). The leak detector also features a vacuum pump which is used to further increase the vacuum inside the loop from 0.1 to 10^{-3} mBar [132].
- **Helium injection:** The helium leak detector is switched into *detect* mode. Inside the helium leak detector is a helium-calibrated mass spectrometer. In detect mode a small internal inlet valve is opened exposing the spectrometer to the vacuum of the loop. A small hole is then pierced through the aluminium tape on one of the testing locations on the loop, and using a helium cannister attached to a probe a short injection of helium is sprayed into the hole. A waiting period ensues in order to see if any helium is registered at the leak detector (i.e. to see if the testing location leaks). Based on the proximity of the injection point to the detector, the waiting period can vary between 1-60 mins.
- **Vessel reconnection:** If the LR at each of the testing locations meets or is below the required 10^{-9} mBar L s $^{-1}$ threshold then the loop is disassembled and final connections are made to reintegrate the loop into the rest of the plant. If any of the tests fail then the problem is diagnosed and fixed before testing again. A commonly encountered problem was misalignment of the gasket between two components. Before retesting a further waiting period is required to evacuate all the helium from the loop. For this reason, testing

locations closest to the pump were checked first such that in the case of a leak any residual helium could be quickly removed from the loop.

In practice, the procedure is complicated for a number of reasons. For example, some hand-valves use a Teflon diaphragm which is not sufficient to use as a termination point along a pipeline. In addition, some valves were actuated, and could only be opened with an air supply; a series of airlines needed to be installed in such cases. Also, many of the flow-valves, by design, restrict back pressure meaning they can only be evacuated from one direction. The most important consideration is the making of final connections, once a connection was tested as part of one loop, it could not be disassembled in preparation for another. This ultimately constrained the choice of loops, making some large. Large loops required both morning and night shifts to prepare and pump down in order to achieve a vacuum. An illustrative summary of the leak checking procedure is shown in Figure 3.20. Photos of the components which have been described are shown in Figure 3.21.

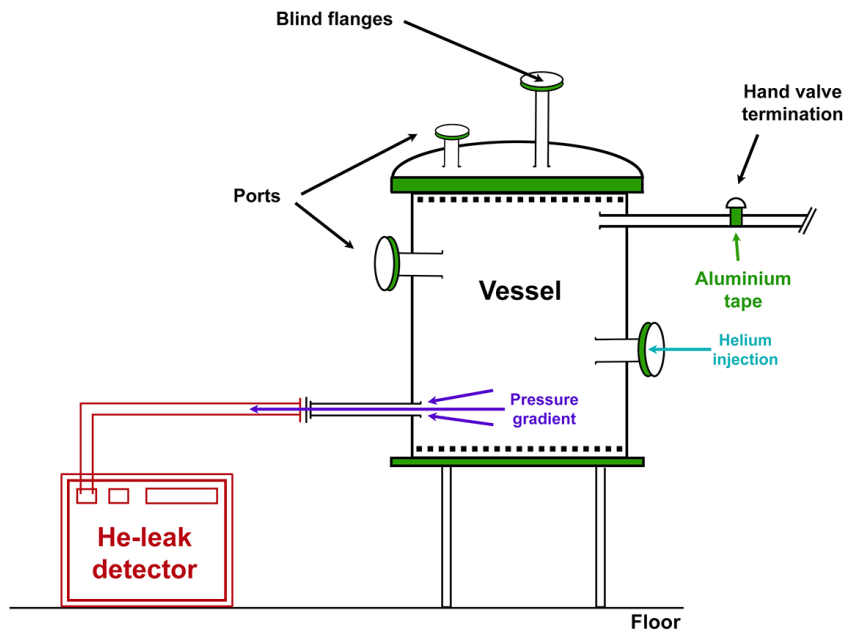


FIGURE 3.20: Illustrative diagram of helium leak checking. A vessel and its connecting pipelines and ports are blinded or terminated and sealed with aluminium tape. The helium leak detector ensures a vacuum of 10^{-3} mBar L s $^{-1}$. Helium is injected at one of the seals. If helium enters the vacuum it is eventually detected by the leak detector.



FIGURE 3.21: Top-left: helium leak detector and vacuum pump. Top-right: scroll vacuum pump. Middle-left: needle valve. Middle-right: pipelines and hand-valves. Bottom-left: author beside vessel. Bottom-right: join sealed with aluminium tape, a hole is pierced in order to inject helium.

Following completion of helium leak checking. The plant underwent cleaning and passivation in which water and acid was forced through the plant to clean the inner surfaces of the vessels and pipes. Cleaning and passivation was completed in 2015. As of 2016, the final work has begun on integrating the electronics and power systems to the instruments in the plant that will monitor the purification chain of the final scintillator mixture. As discussed, the final composition of this mixture has yet to be decided upon, and therefore some operational aspects of the plant may be subject to change once a final decision has been made. The scintillator plant will be operated for a first time during the initial scintillator phase some time in 2017.

4

Characterising Optical Response

*These things move within you as lights and shadows in pairs that cling.
And when the shadow fades and is no more, the light that lingers becomes
a shadow to another light.*

The Prophet, Kahlil Gibran

Thus far, chapters 2 and 3 provided individual descriptions of the SNO+ detector and the principle fiducial material; scintillator. However, in practice both need to be combined and understood as a coherent entity - how do the characteristics of one affect the other? Indeed, the PMT efficiency can be accurately measured in a lab; similarly, the emission profile of the scintillator can be well characterised under the same conditions. But what if there are ~ 9000 PMTs? What if there is ~ 780 tonnes of scintillator? Do all PMTs behave the same? Does a small sample of scintillator reflect the characteristics of a bulk quantity at the tonne scale? The answer is no, and although this may appear obvious, it motivates a further and ultimately more crucial consideration; how does the large scale nature of the SNO+ detector in its many components and bulk materials impinge upon the sensitivity to a physics event, and in the case of $0\nu\beta\beta$ -decay, an event whose ROI is narrow, 2.47-2.70 MeV [74]. And, given all this, does the detector correctly *interpret* the true energy of these physics events? These are the questions to be answered by a full detector calibration, a component of which is the optical calibration; a measurement of the detector response using controlled light sources deployed *in-situ*: inside the detector.

As described in Chapter 2, there are two optical calibration sources. The focus of the discussion presented here is under the context of one of these, the laserball. Henceforth, this chapter and those which follow seek to address and characterise the *optical response* of the SNO+ detector in both the water and scintillator phases of the experiment using laserball data.

4.1 Optical Response

In the planned water and scintillator (with or without tellurium) phases, the scintillator or water will be sensitive to ionising radiation within the detector. This radiation will arise from both physics events of interest and undesired background events. The scintillation or Cherenkov light produced from these events subsequently propagates through the detector and is the messenger of the physics event information. It is important to understand the behaviour of this light as it reaches the PMT. In characterising the optical response of the detector, an understanding of the following aspects is required;

- **Optical effects:** As photons propagate through the detector it will be subject to optical processes such as refraction, reflection, absorption and a variety of energy dependent scattering interactions; Rayleigh, Compton and Mie. The prominence of these effects is governed by the material properties of the detector; the water or scintillator in the inner AV region, the acrylic of the AV itself and the outer AV water region in the cavity. In particular, it is of interest to measure the combined effect of the absorption and scattering effects, collectively known as attenuation, as described in Section 3.3.
- **Detector components:** The measurement of a physics event rate involves summing reconstructed events in a variety of locations throughout the detector. The PMTs then need to be sensitive to light from these different positions. Therefore, it is important to determine the combined efficiency of the PMTs and their surrounding reflectors across the different wavelengths and incident angles that light is expected to reach them. In practice the AV is not only a spherical vessel surrounded by PMTs, but it is also surrounded by several structures that support the AV itself. For a given source of light inside the AV, these structures will obstruct light reaching certain

PMTs, effectively *shadowing* them from the light source. This also needs to be accounted for.

- **Intrinsic scintillator properties:** Based on the scintillator composition, certain wavelengths of light will be absorbed and reemitted by wavelength shifters. Probing this process and the time period over which it occurs is necessary as it will manifest changes in the timing distribution of light detected at PMTs.

The characterisation of these three items will be discussed here alongside their implementation into a parameterised model that can be used with laserball data. In addition, it is also important to consider the effect these aspects have on the overall physics objectives of SNO+ in searching for physics events at the 1-3 MeV scale.

4.1.1 Energy & Physics Sensitivity to Optical Effects

To understand physics in SNO+ is to understand the energy response of the detector; to understand this response is to understand the optical effects that underpin them. The expected energy resolution in scintillator is several hundreds of keV, which translates to a \sim 4-8% uncertainty in the $0\nu\beta\beta$ -decay ROI. Background events are the main challenge in achieving this target sensitivity to possible $0\nu\beta\beta$ -decay events. A variety of background sources cumulatively provide a near diffuse source of β -, α - and γ -particles in the detector across a range of energies, 0.1-10.0 MeV. These backgrounds need to be well understood, and through appropriate techniques rejected to a high degree of efficiency e.g. $> 99.99\%$ for Bi-Po [74]. The success of these rejection techniques relies on the accuracy of the PMT hit distributions to reflect not only the true temporal and spacial nature of an event, but also the energy scale at which it occurred. The success of background rejection is therefore directly related to the response of the detector to light; later interpreted as the energy of an event.

The energy reconstruction of an event is strongly related to the detector response which is itself dependent on attenuation and the PMT response. To illustrate this, shown in Figure 4.1 are two MC examples of the reconstructed energies of 2.0 MeV electrons distributed uniformly throughout the inner AV region filled with

LABPPO scintillator. The top figure shows the reconstructed energy for different scalings of the scintilllator attenuation length; scaling both the absorption and Rayleigh scattering lengths by a given percentage. Similarly, the bottom plot highlights the change in the reconstructed energy for different values of the PMT reflector reflectivity. As one would expect, both shorter attenuation lengths and smaller reflectivity decrease the reconstructed energy; the light information has been lost.

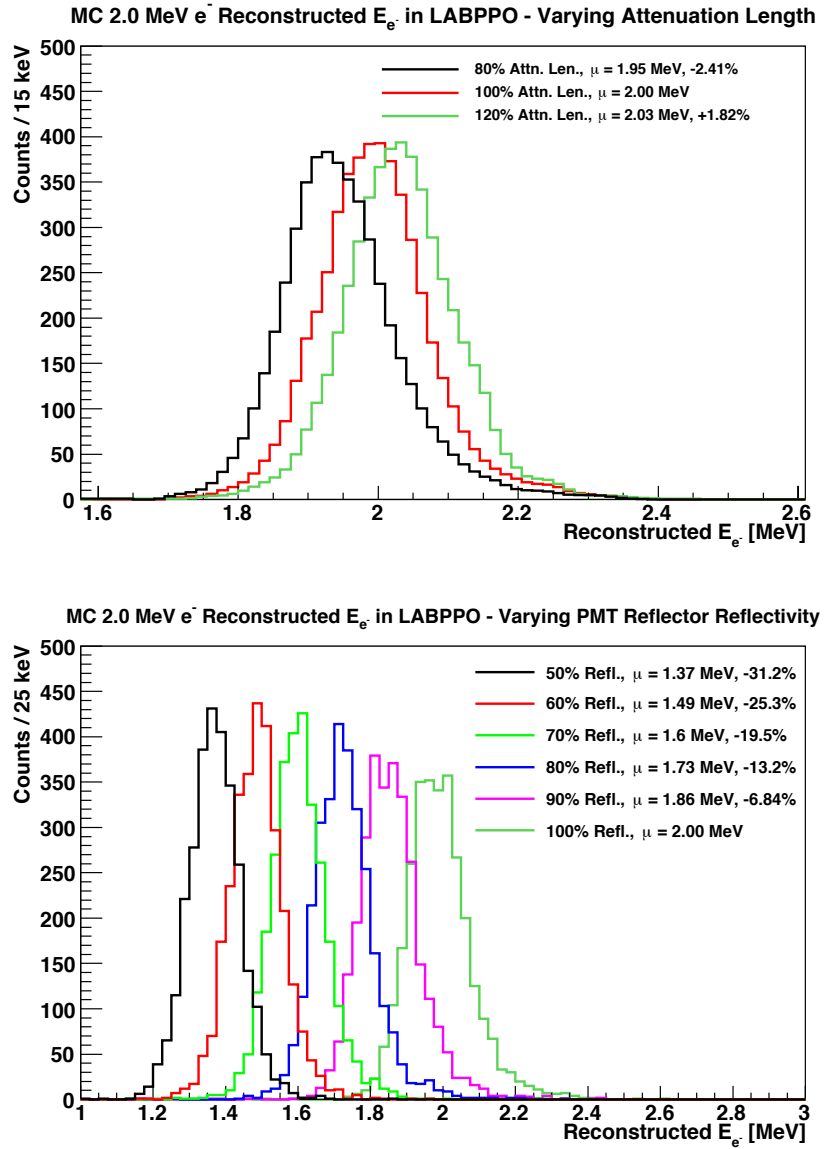


FIGURE 4.1: Reconstructed energies of MC 2.0 MeV electrons distributed uniformly throughout the inner AV region in LABPPO scintillator with different scalings of the attenuation length (top) and PMT reflector reflectivity (bottom). The smaller the scaling-%, the larger the rate of attenuation or loss of light respectively. Deviations from the expected mean of each distribution, μ are shown in the legend.

It is reasonable to expect changes in attenuation and the reflector reflectivity; over time contaminants may leech from the detector components or cavity walls causing an increase in attenuation; the PMT reflectors may degrade and lose reflectivity. A characterisation of the optical response allows these properties to not only be measured, but also monitored over time such that any drift in the optical response can be quantified. The following description of the optical model is based on the same model as studied in successive optical calibrations in all three phases of the original SNO experiment [133, 134].

4.2 Optical Response Model

Optical calibration with the laserball is sought by collecting individual PMT information over the course of a laserball *run*. A run consists of the laserball being moved to a specific position inside the inner AV region and triggered, pulsing near-isotropic light at a fixed wavelength. For a laser pulse rate of 28-40 Hz, the run will last \sim 20-30 minutes. Many laserball runs are performed at the same wavelength in different positions, some in *central* positions (where the laserball is positioned at the centre of the AV) and some *off-axis* (not at the centre). Collectively, this forms a complete set of runs known as a laserball *scan*. A complete laserball data set consists of several scans at different wavelengths.

For a given laserball run i , the number of photons expected at PMT j , N_{ij} can be modelled (N_{ij}^{model}) as the product of the following terms;

$$N_{ij}^{\text{model}} = N_i \epsilon_j \Omega_{ij} T_{ij} R_{ij} L_{ij} \exp \left(- \sum_k d_{ij,k} \alpha_k \right), \quad (4.1)$$

where the sum over the index k denotes the different regions of the detector, $k =$ inner AV, AV and outer AV regions. Each term in this expression is as follows:

- **Laserball intensity normalisation, N_i :** The number of photons emitted by the laserball and detected at all PMTs within a prompt time window (described in Section 4.2.3) throughout the run.

- **PMT efficiency, ϵ_j :** The intrinsic efficiency of PMT j and its associated electronics. This is the combined efficiency of the PMT to convert incident light to a photoelectron, and for the subsequent accumulation of charge at the PMT anode to pass the discriminator threshold, registering a hit.
- **PMT solid angle, Ω_{ij} :** The solid angle subtended by PMT j from the laserball position in run i .
- **Fresnel transmission coefficient, T_{ij} :** For a laserball deployed in the inner AV region, this is the combined transmission probability necessary for light crossing two detector media boundaries in order to reach the PMT; the inner AV/AV and AV/outer AV interface boundaries.
- **PMT angular response, R_{ij} :** The efficiency of the PMT reflectors to redirect light entering the PMT bucket onto the PMT face, specifically light entering the PMT bucket beyond the solid angle area subtended by the PMT face. This is a function of the incident angle at which light enters the bucket, θ_γ i.e. $R_{ij}(\theta_{\gamma,ij})$.
- **Laserball light distribution, L_{ij} :** This is the relative intensity of the laserball based on the predicted direction at which light leaves the laserball surface to reach a PMT. This is typically parameterised using the local angular coordinate frame of the laserball i.e. $L_{ij}(\cos\theta_{LB}^{ij}, \phi_{LB}^{ij})$.
- **Distance through detector region, $d_{ij,k}$:** This is the calculated distance that light travels through each of the inner AV, acrylic and outer AV regions to reach the PMT.
- **Detector region attenuation coefficient, α_k :** The attenuation coefficient (the reciprocal of the attenuation length, $\alpha_k = L_{k,\text{attn}}^{-1}$) of each of the inner AV, acrylic and outer AV regions.

The product of these terms describe an effective probability for light emitted by the laserball to be converted into PMT hits. Based simply on the relative position between a PMT and the laserball, some of these terms can be directly calculated analytically; $\Omega_{ij}, T_{ij}, d_{ij,k}$. And, as will be discussed, other terms such as

N_i , R_{ij} , L_{ij} and α_k are calculated using a statistical fit of the model over laserball data. However, in both instances these parameters require the information contained in a vector description of the light path between the laserball and the PMT in order to provide $\theta_{\gamma,ij}$, $d_{ij,k}$, $\cos\theta_{LB}^{ij}$ and ϕ_{LB}^{ij} . It is therefore important to calculate this description of the light path as it travels through the detector.

4.2.1 Calculation of a Light Path

A light path can be characterised by a starting and finishing location within the detector. In the context of a physics event, these two locations would be a reconstructed event vertex and a PMT position. For laserball studies, the laserball position replaces the event vertex. In general, a solution for a light path between these two points is non-unique. There can exist several physically plausible paths between these two points, each with different path lengths. Therefore, a third constraint, the initial direction vector from the laserball, is required to ensure that the shortest of these possible paths is calculated. In terms of a likelihood, the shortest path is the most probable, and best represents the average distance travelled by photons contributing to the prompt signal recorded by the PMT.

What follows is a calculation of the light path that approximates the path through the detector between any two given points. These points are defined in the global detector coordinates, with the origin located at the centre of the AV, as shown in Figure 4.2. This calculation was implemented into RAT's *light path calculator* utility [135].

4.2.1.1 Mathematical Description of a Path

As an example, let \vec{r}_i be the starting position of the light path somewhere inside the scintillator region and let \vec{r}_j be the position of some PMT, j in the PSUP. Let \vec{r}_1 and \vec{r}_2 be the locations, respectively on the inner and outer surface of the AV where the path transitions between the inner AV/AV and AV/outer AV regions;

$$\begin{aligned}\vec{r}_i &:= \text{Path start position,} \\ \vec{r}_j &:= \text{Path end position (PMT position).}\end{aligned}$$

The above definitions of \vec{r}_i and \vec{r}_j can be used to define a set of coordinates (x', y', z') that determine the geometric plane containing both \vec{r}_i and \vec{r}_j and the connecting path between them;

$$x' = \hat{\vec{r}}_i, \quad z' = x' \times \hat{\vec{r}}_j, \quad y' = z' \times x'. \quad (4.2)$$

- x' -direction : The direction defined by the radial vector pointing from the origin (centre of the AV) to the starting position i.e. $\hat{x}' = \hat{\vec{r}}_i$.
- z' -direction : The direction perpendicular to both the radial vector from the origin to the starting position and the radial vector from the origin to the PMT position. Mathematically, the z' -direction unit vector defines the plane in which the path is calculated.
- y' -direction : The direction defined by the cross product of the x' - and z' -directions: $y' = z' \times x'$. The y' -direction is therefore perpendicular to both the x' - and z' -directions, but lies in the same plane as the x' -direction.

As shown in Figure 4.2, in the plane as defined above, the angles between subsequent vector pairs;

$$\{\vec{r}_i, \vec{r}_1\} : \theta_{i1}, \quad \{\vec{r}_1, \vec{r}_2\} : \theta_{12}, \quad \{\vec{r}_2, \vec{r}_j\} : \theta_{2j}, \quad (4.3)$$

collectively define the required angular displacement between the start and PMT position i.e.

$$\theta_{i1} + \theta_{12} + \theta_{2j} = \theta_{ij} = \cos^{-1} \left(\hat{\vec{r}}_i \cdot \hat{\vec{r}}_j \right). \quad (4.4)$$

Using Snell's law of refraction for light passing through material A (refractive index n_A) to material B (refractive index n_B);

$$n_A \sin \theta_A = n_B \sin \theta_B, \quad (4.5)$$

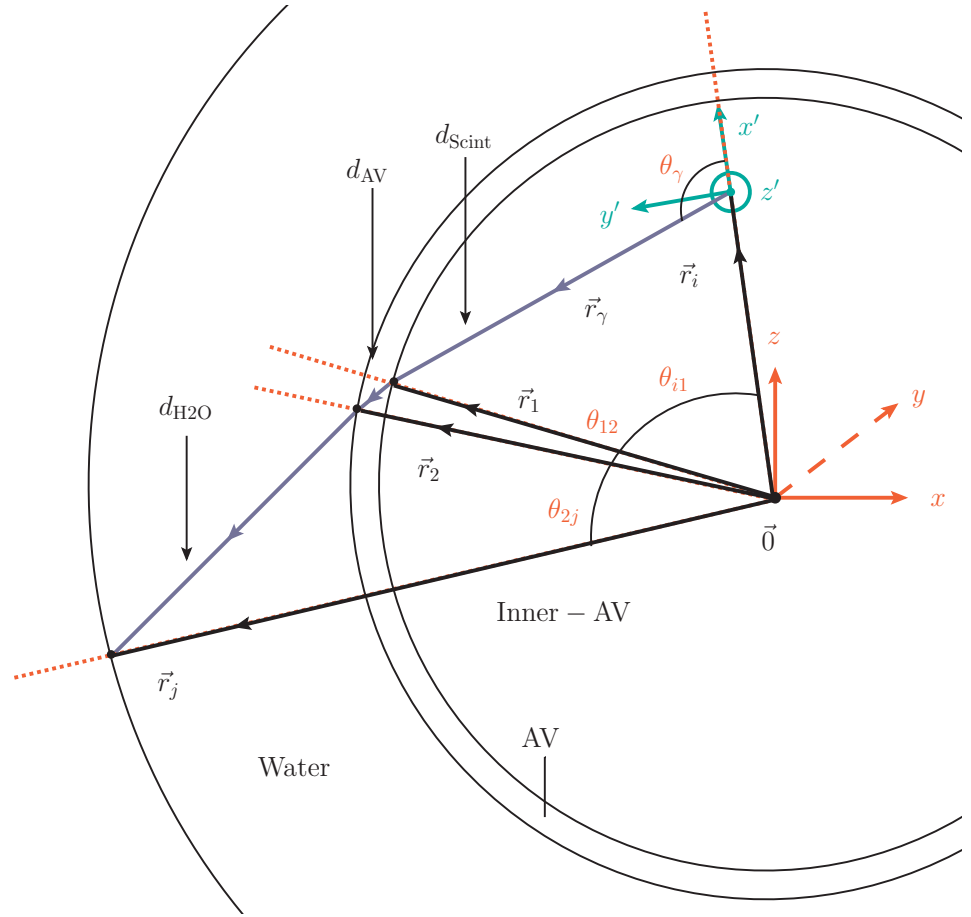


FIGURE 4.2: Shown is an example illustration of a refracted light path between the start position, \vec{r}_i and the PMT position, \vec{r}_j in the plane as defined by z' (out of the page). The vectors \vec{r}_1 and \vec{r}_2 are the respective vectors to the intersection points of the path with the inner AV/AV and AV/outer AV interfaces. The angles θ_{i1}, θ_{12} and θ_{2j} are the respective angles between \vec{r}_i and \vec{r}_1 , \vec{r}_1 and \vec{r}_2 and \vec{r}_2 and \vec{r}_j . The global coordinate frame is denoted by the red axes, the path coordinate frame is in turquoise.

and a combination of sine and cosine rules (see Appendix A.1 for a full derivation), these three angles can be analytically described as a function of the angle between the radial starting position vector, \vec{r}_i and the initial photon direction, \vec{r}_γ :

$$\theta_\gamma = \cos^{-1} \left(\hat{\vec{r}}_i \cdot \hat{\vec{r}}_\gamma \right), \quad (4.6)$$

$$\cos \theta_{i1} (\theta_\gamma) = \frac{|\vec{r}_i|}{|\vec{r}_1|} \sin^2 \theta_\gamma + \cos \theta_\gamma \sqrt{\left(1 - \left(\frac{|\vec{r}_i|}{|\vec{r}_1|} \sin \theta_\gamma \right)^2 \right)}, \quad (4.7)$$

$$\begin{aligned} \cos \theta_{12} (\theta_\gamma) &= \frac{1}{|\vec{r}_1| |\vec{r}_2|} \left(\frac{n_{\text{Scint}}}{n_{\text{AV}}} r_i \sin \theta_\gamma \right)^2 \\ &\quad + \left[\sqrt{1 - \left(\frac{|\vec{r}_i|}{|\vec{r}_1|} \frac{n_{\text{Scint}}}{n_{\text{AV}}} \sin \theta_\gamma \right)^2} \right. \\ &\quad \left. \times \sqrt{1 - \left(\frac{|\vec{r}_i|}{|\vec{r}_2|} \frac{n_{\text{Scint}}}{n_{\text{AV}}} \sin \theta_\gamma \right)^2} \right], \end{aligned} \quad (4.8)$$

$$\begin{aligned} \cos \theta_{2j} (\theta_\gamma) &= \frac{1}{|\vec{r}_2| |\vec{r}_j|} \left(\frac{n_{\text{Scint}}}{n_{\text{H}_2\text{O}}} |\vec{r}_i| \sin \theta_\gamma \right)^2 \\ &\quad + \left[\sqrt{1 - \left(\frac{|\vec{r}_i|}{|\vec{r}_2|} \frac{n_{\text{Scint}}}{n_{\text{H}_2\text{O}}} \sin \theta_\gamma \right)^2} \right. \\ &\quad \left. \times \sqrt{1 - \left(\frac{|\vec{r}_i|}{|\vec{r}_j|} \frac{n_{\text{Scint}}}{n_{\text{H}_2\text{O}}} \sin \theta_\gamma \right)^2} \right]. \end{aligned} \quad (4.9)$$

Using equations 4.7 - 4.9 an expression for $\theta_{ij} (\theta_\gamma)$ is thus obtained;

$$\theta_{ij} (\theta_\gamma) = \cos^{-1} (\cos \theta_{i1} (\theta_\gamma)) + \cos^{-1} (\cos \theta_{12} (\theta_\gamma)) + \cos^{-1} (\cos \theta_{2j} (\theta_\gamma)). \quad (4.10)$$

Based on the initial event position, \vec{r}_i and the position of the hit PMT, \vec{r}_j , the calculation of a path between these two points, d_{Path} should provide the individual distances - assumed straight lines themselves - through the scintillator, d_{Scint} , acrylic, d_{AV} and water, $d_{\text{H}_2\text{O}}$ such that;

$$d_{\text{path}} = d_{\text{Scint}} + d_{\text{AV}} + d_{\text{H}_2\text{O}} \geq |\vec{r}_j - \vec{r}_i|, \quad (4.11)$$

where equality holds only for cases of normal incidence i.e. $|\hat{\vec{r}}_i \cdot \hat{\vec{r}}_j| = 1$.

4.2.2 Time Residuals & Group Velocity

The distance information provided by a path can be combined with additional information, such as the photon group velocity in each material to calculate what is known as the *time residual*, t_{res} ;

$$t_{\text{res}} + t_0 = t_{\text{PMT}} - t_{\text{ToF}} = t_{\text{PMT}} - \sum_k \frac{d_k}{v_{g,k}} - t_{\text{bucket}}(\theta_\gamma), \quad (4.12)$$

where values of d_k and $v_{g,k}$ denote the distances and group velocities of the photon in the respective detector regions as before. The value $t_{\text{bucket}}(\theta_\gamma)$ is a small correction $\sim 0.45\text{-}0.7$ ns to account for the fact that the path is calculated to the entrance of the PMT bucket, not the face of the PMT itself. $t_{\text{bucket}}(\theta_\gamma)$ therefore accounts for the time spent inside the bucket region of the PMT prior to hitting the PMT face; it is related to the incident angle and discussed here [136] and in Appendix A.2. The time residual, t_{res} can be thought of as the corrected, instantaneous event time which accounts for the light propagation time to the PMT, t_{ToF} relative to the time of an event epoch, t_0 and a PMT hit time, t_{PMT} . Calculation of the time residuals from the PMT hit times are used for reconstruction e.g. event identification. The distributions are themselves interesting, as they reveal both detector reflections and PMT characteristics, an example is shown in Figure 4.4.

Both the distances and group velocities are wavelength dependent. The distances are governed by the level of refraction between each material interface and thus the refractive index, $n(\lambda)$. The group velocity is related to the refractive index (and hence the wavelength) through the following relation;

$$v_g(\lambda) = \frac{c}{n(\lambda) - \lambda \frac{\partial n(\lambda)}{\partial \lambda}}, \quad (4.13)$$

where $c = 3 \times 10^8$ m s $^{-1}$. The refractive indices and group velocities for LABPPO scintillator, acrylic and water are shown in Figure 4.3.

With a treatment of the light path now presented, it may be used to provide the necessary values of the distances d_{Scint} , d_{AV} and $d_{\text{H}_2\text{O}}$ and the angular information; $(\cos \theta_{\text{LB}}, \phi_{\text{LB}})$, obtained from \vec{r}_γ and the incident angle at the PMT using \vec{r}_2 and \vec{r}_j .

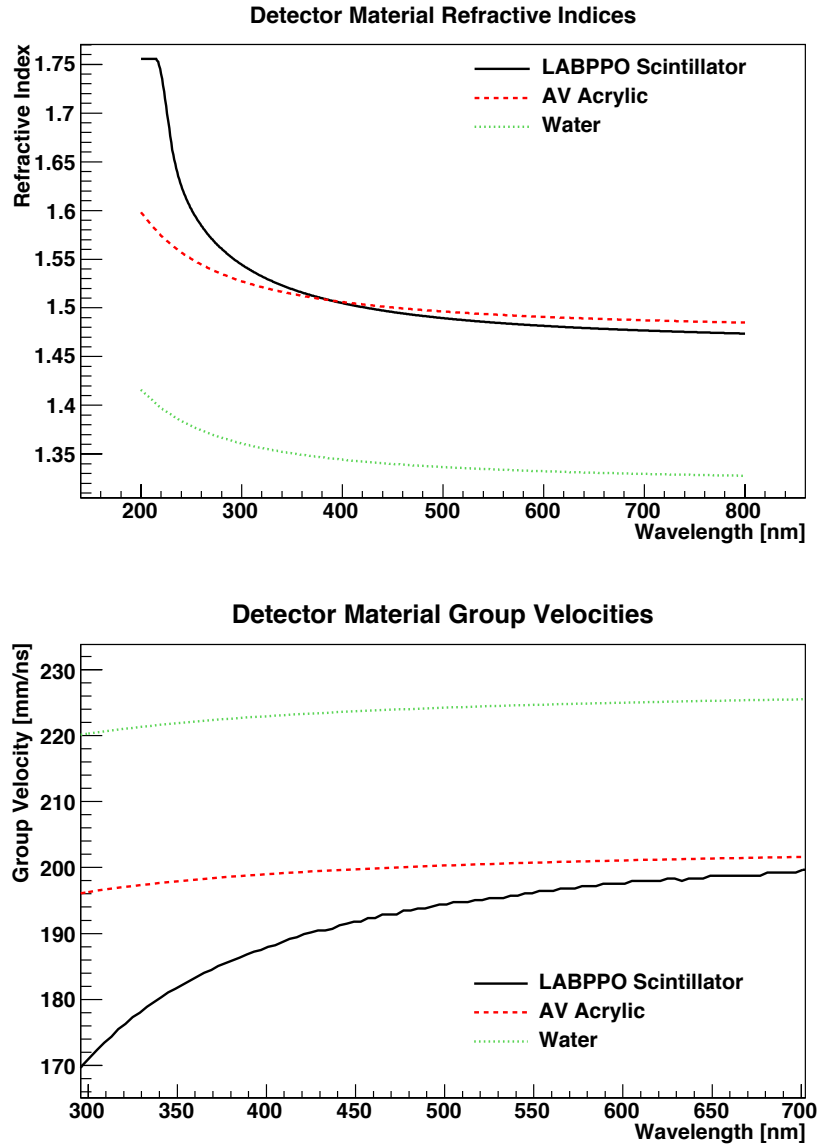


FIGURE 4.3: The dependency of the refractive indices (top) and group velocities (bottom) with wavelength. Shown are the refractive indices and group velocities for LABPPO scintillator (black), the acrylic of the AV (red) and the outer AV water (green).

4.2.3 Prompt Peak Count Calculation

In the model description, the calculation of the light path assumes no reflections or perturbations to the path distance or direction due to reflections or scattering; it therefore only describes the path of the prompt light, identified as the global peak of the time residual distribution. Similarly then, the observed number of prompt counts, N_{ij}^{data} is calculated by integrating the number of counts within a

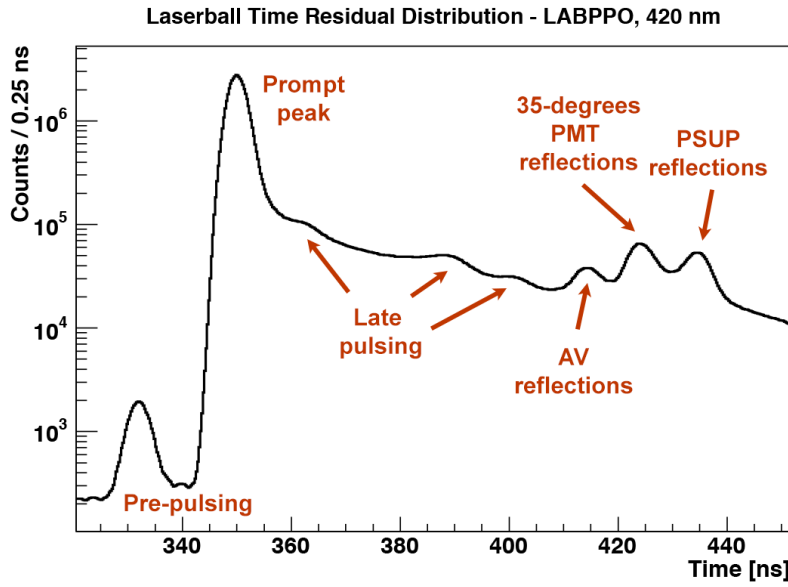


FIGURE 4.4: Shown is the laserball time residual distribution across all PMTs in LABPPO at 420 nm simulated in RAT with the laserball positioned at the centre of the AV. The distribution reveals populations of reflected light from various detector components (the 35° PMT reflection is described in Section 4.2.4). Revealed also are the intrinsic properties of the PMTs themselves, with both pre- and late-pulsing populations either side of the prompt peak.

time window about the prompt peak. First, the global time residual distribution across all PMTs is calculated as in Equation 4.12. A peak finding routine is used to identify the central time value of the global peak, which is known as the *global time offset* (GTO); it is the approximate time that the laserball was triggered, t_0 within a nominal time window. An example of the time residual distribution and global time offset are shown in Figure 4.5 for an MC simulation of a central laserball run in LABPPO at 505 nm.

The global time offset is subtracted from the time residual distribution of each PMT such that its prompt peak is centred about $t = 0$. The value of N_{ij}^{data} is then the total number of counts ± 4 ns either side of the central peak value. The value of 4 ns is chosen to maximise the prompt light without including tails from the pre- or late-pulsing of the PMTs. This value was used previously in SNO [133, 134, 137]. The integration of the prompt peak at an example PMT is shown in Figure 4.6.

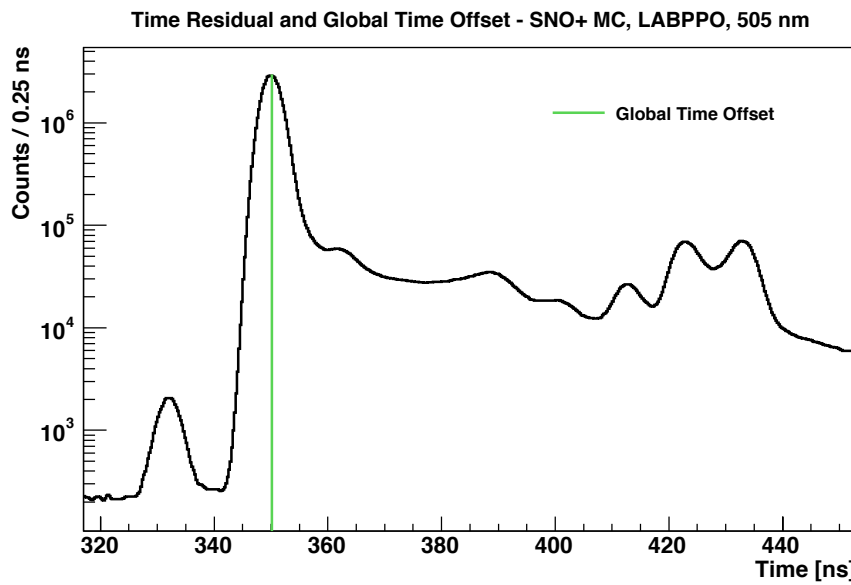


FIGURE 4.5: Shown is the time residual distribution for a SNO+ MC central laserball run in LABPPO at 505 nm. The central value of the global peak is identified as the global time offset for the event window.

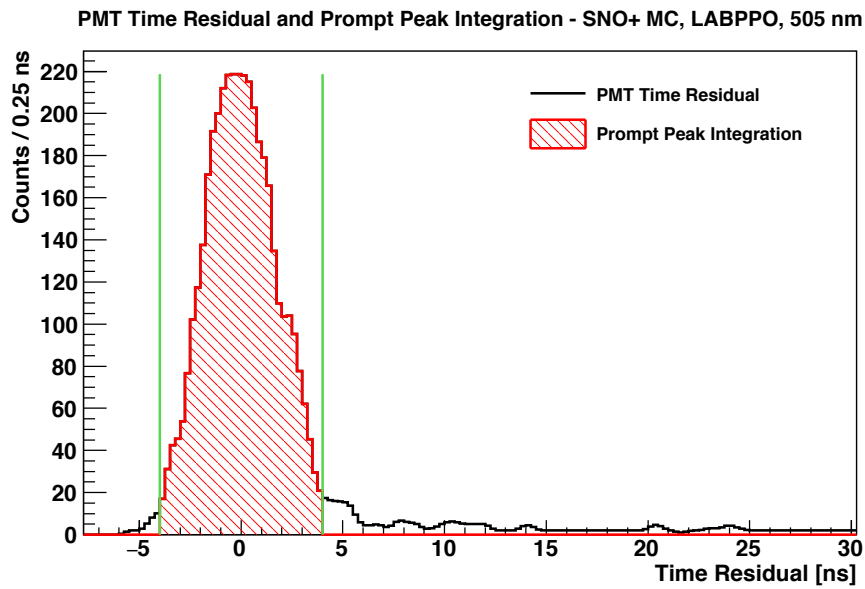


FIGURE 4.6: Shown is the individual time residual distribution for a PMT in a SNO+ MC central laserball run in LABPPO at 505 nm. The time residual is centred about zero following subtraction of the global time offset. The prompt peak count of the PMT, N_{ij}^{data} is the integrated number of counts in a window ± 4 ns either side of the peak centre.

The central time value of the peak, t_{peak} is used to calculate what is known as the PMT time *centroid*, the average PMT time;

$$t^{\text{centroid}} = t_{\text{peak}} + t_{\text{ToF}}(\vec{r}_{\text{manip.}}) + t_{\text{GTO}}, \quad (4.14)$$

where t_{peak} is the central time value of the peak, t_{ToF} is the time of flight as in Equation 4.12 and t_{GTO} is the global time offset. One technicality is that the time of flight is calculated from the manipulator position, $\vec{r}_{\text{manip.}}$ not the laserball position, \vec{r}_{LB} . However, the time centroid can be used to fit for the laserball position as will be discussed in Section 5.2.2. The error on the centroid is taken as the RMS of the peak, $\delta t^{\text{centroid}} = \sigma_{\text{RMS}}^{\text{centroid}}$.

4.2.4 PMT Angular Response

Each of the inward facing PMTs in the detector are surrounded by a circular series of concave petal-like reflectors shaped into a Winston cone [125]. A Winston cone acts to concentrate light from a large opening aperture e.g. the PMT bucket entrance, and focus it onto a smaller area such as the PMT face. The reflectors effectively increase the PMT sensitivity to light by a factor of 1.74 [133]. The PMT angular response is the efficiency of these reflectors and is related to the incident angle that light enters the PMT bucket, θ_γ which is defined as the angle to the normal of the entrance plane as shown in Figure 4.7. The Winston cone design of the PMT bucket and reflector assembly was subject to a detailed study in the pre-production phase of SNO [125]. For light at normal incidence, the position of the PMT face with respect to the reflectors means that light can be *back-reflected* out of the PMT bucket at a characteristic angle of 35° , see Figure 4.7. Light is also reflected out of the bucket at large incident angles as well. Back-reflected light is eventually received at other PMTs on the far side of the PSUP, leading to a peak that can be identified in time residual distributions such as that which was shown in Figure 4.4.

A photo of a PMT and its reflectors is shown in Figure 4.8. As suggested by the photo, the complete removal of a reflector reduces its efficiency to collect light. SNO+ uses the same reflectors as those in SNO which are now ~ 20 years old. Over this time the reflectors have been exposed to a variation in the cavity environment between experiments. As a consequence the reflectors have begun to degrade.

Two examples of degraded reflectors are shown in Figure 4.9. The rate and type of reflector degradation does not follow a standardised pattern between PMTs. Regardless, in all cases the efficiency of the reflectors, the angular response, is reduced.

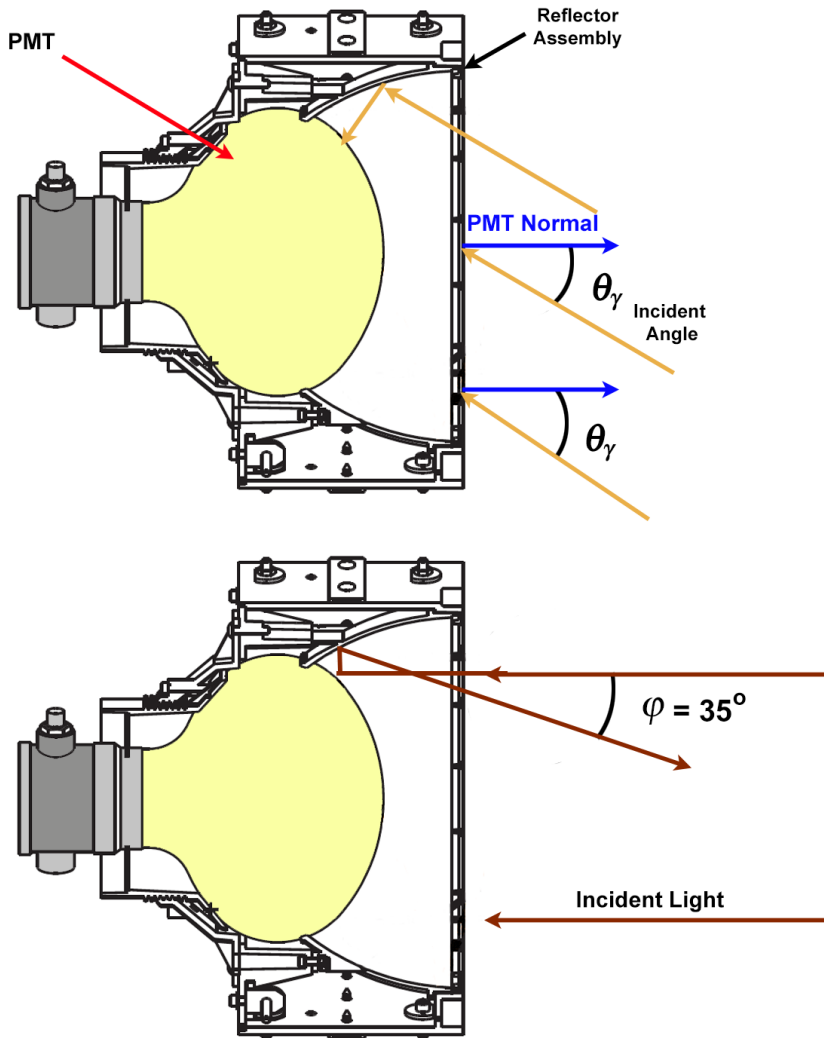


FIGURE 4.7: Shown are two side-on technical diagrams of the PMT and the reflector assembly. Top: The definition of the incident angle, θ_γ is given as the incident angle into the plane of the bucket entrance, defined by a normal vector (blue). Bottom: In certain instances, light is back-reflected out of the PMT at a characteristic 35° angle.

For a given laserball position inside the detector, the range of incident angles which can be probed is fixed. This range increases as the laserball moves closer to the PMTs as illustrated in Figure 4.10. For laserball deployment in the inner AV region $|\vec{r}_{LB}| \in (0.0, 5500)$ mm, the range of sampled incident angles is approximately

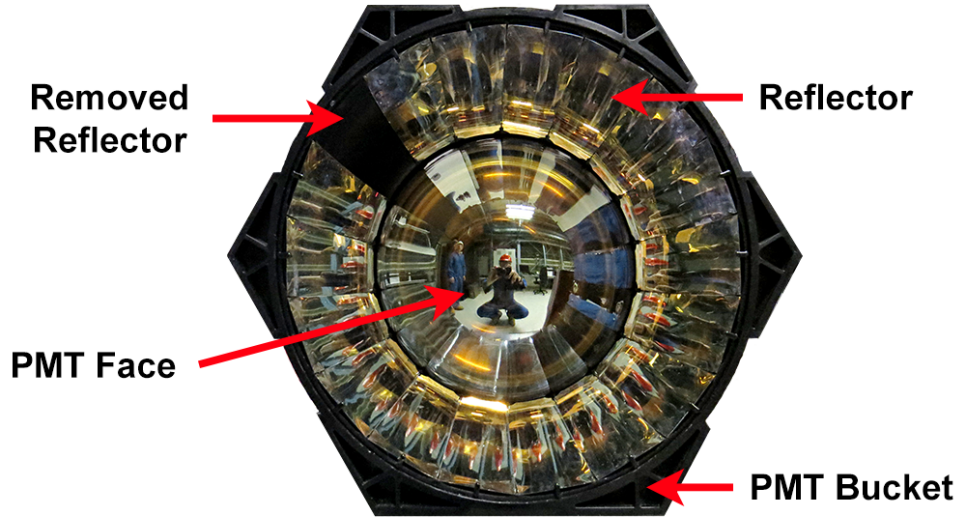


FIGURE 4.8: Photo of a PMT, its surrounding reflectors and the bucket in which they are contained.

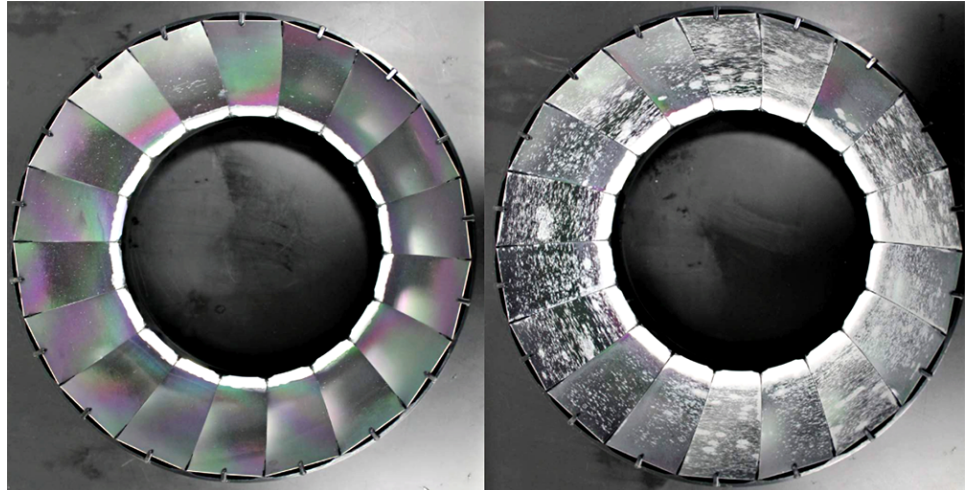


FIGURE 4.9: [138] Shown are two sets of reflectors previously used in the SNO detector. Either set show signs of degradation. The left set appears to show signs of reduced reflectivity which resemble that found on the surface of a thin film. The right set show specular flaking of the mirrored surface revealing white, non-reflective plastic underneath.

$\theta_\gamma \in (0^\circ, 50^\circ)$. As indicated by the z -axis of Figure 4.10 the sampling of incident angles is non-uniform. This motivates the deployment of the laserball at a range of different position radii, $|\vec{r}_{LB}|$ for a given scan.

For the purposes of the optical model, it is useful to define the *relative* PMT angular response; the response of the PMT to light at a given value of θ_γ relative

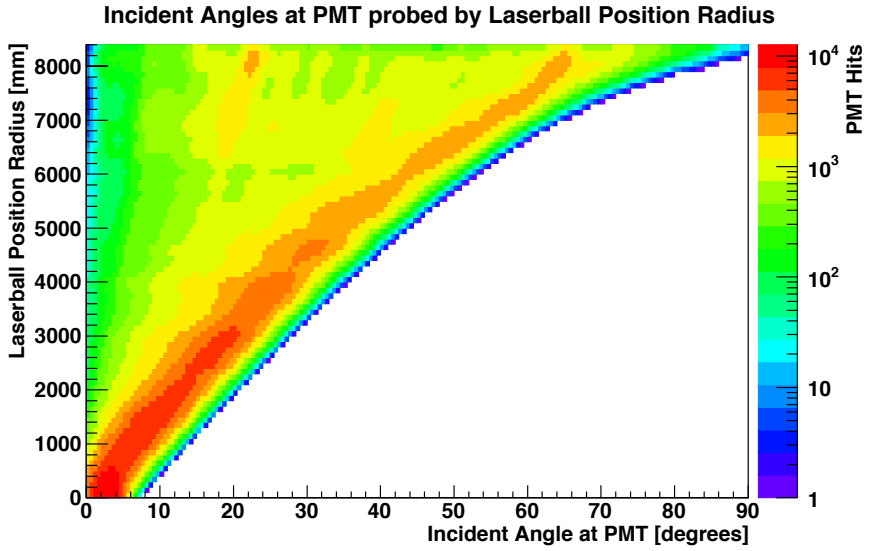


FIGURE 4.10: The variation in the range of incident angles which can be probed at different laserball position radii. As the laserball moves closer to the PMTs the range of sampled angles broadens.

to the response at normal incidence, $\theta_\gamma = 0^\circ$. The reason for this is that a central laserball run will typically only probe a small range of angles close to normal incidence; these central runs are important and will feature as part of the statistical fit which is discussed in Section 4.3.

The relative PMT response varies with the incident angle and wavelength (as does the standard response in general), this variation is shown in Figure 4.11 for an example MC data set. The angular response is binned per degree of incident angle. In the range $\theta_\gamma \in (0^\circ, 30^\circ)$ the response is quasi-linear and thereafter decreases based on the wavelength. At higher incident angles, $\theta_\gamma \gtrsim 45^\circ$ the relative response becomes less than 1, as light is reflected back out of the PMT bucket.

4.2.5 Laserball Light Distribution

For a given light path to a PMT, the initial photon direction provides the local angular $(\cos \theta_{LB}, \phi_{LB})$ coordinates on the laserball where the light was emitted. The laserball is designed to provide an isotropic distribution of light. In practice, it is only near-isotropic, and some anisotropies are present. For example, the mounting hardware that supports the laserball flask from above introduces shadowing; the

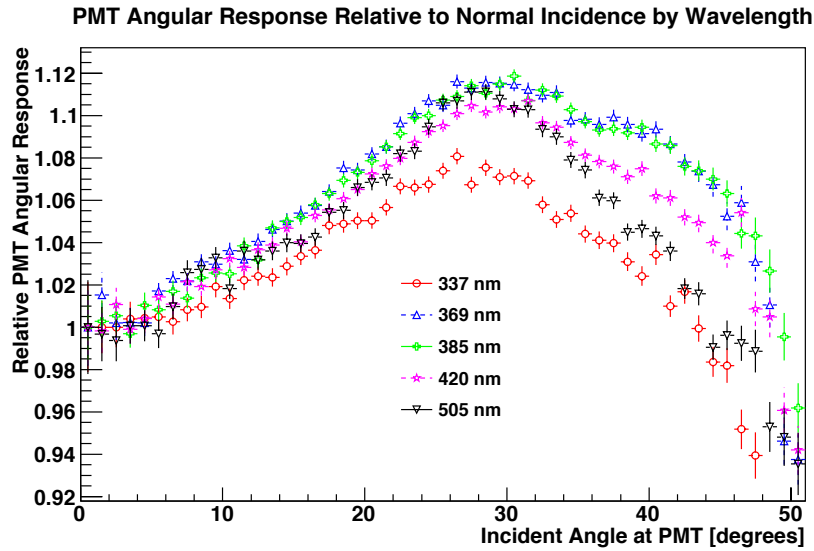


FIGURE 4.11: Shown is the angular response relative to normal incidence ($\theta_\gamma = 0^\circ$) across different wavelengths. The relative response drops below 1 at large incident angles, where light is reflected back out of the PMT bucket.

intensity of light emitted upwards, $\cos \theta_{LB} \simeq 1$ is generally smaller than that emitted downwards, $\cos \theta_{LB} \simeq -1$. This characteristic is visible when comparing the relative number of PMT hits by PMT position in $\cos \theta_{PMT}$ for a central laserball run as shown in Figure 4.12. A laserball *mask function*, $P_4(\cos \theta_{LB})$ is used to describe this variation;

$$P_4(\cos \theta_{LB}) = 1 + \sum_{k=1}^4 a_k (1 + \cos \theta_{LB})^k, \quad (4.15)$$

where the coefficients in the sum, a_k are determined by a statistical fit and the variation is described about a fixed normalised value, $a_0 = 1$. Prior studies in SNO identified that a polynomial mask function of order four (1 + 4 parameters) was the minimum order degree polynomial required to accurately describe the relative intensity variation in $\cos \theta_{LB}$ of the laserball [139].

Given the spherical symmetry shared by both the PSUP and the laserball, the PMT and laserball coordinate systems share a 1:1 mapping; they are coincident. Therefore observations in the PMT hits by PMT position provide information on the relative intensity of the laserball in $(\cos \theta_{LB}, \phi_{LB}) (\equiv (\cos \theta_{PMT}, \phi_{PMT}))$.

In addition, small irregularities in the distribution of the glass beads inside the

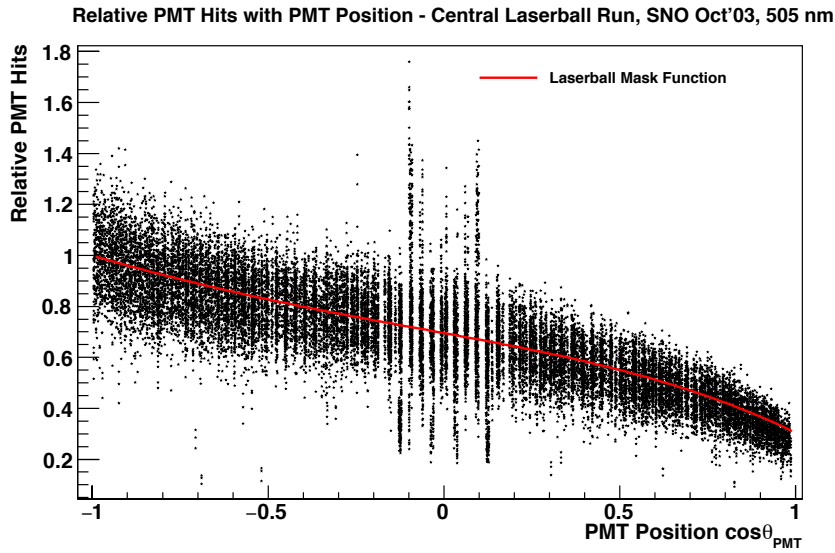


FIGURE 4.12: Shown is the relative change in the number of PMT hits with the PMT position $\cos \theta_{\text{PMT}}$ coordinate from a central laserball run at 505 nm. The decrease in PMT hits with increasing $\cos \theta_{\text{PMT}}$ is indicative of the intensity variation of the laserball in $\cos \theta_{\text{LB}}$. The mask function, P_4 that describes this variation is shown in red. Data is from the original SNO experiment in October 2003.

laserball flask lead to both $\cos \theta_{\text{LB}}$ and ϕ_{LB} angular anisotropies in the light intensity. This is observed by comparing the ratio of PMT hits by PMT position in ϕ_{PMT} for two central laserball runs at different orientations. An example is shown for the laserball used in an optical calibration of SNO in August 2006 in Figure 4.13. This angular distribution can be characterised in one of two ways:

- **Binned angular distribution** $H_{\text{bin}}(\cos \theta_{\text{LB}}, \phi_{\text{LB}})$: The angular distribution in $(\cos \theta_{\text{LB}}, \phi_{\text{LB}})$ is divided into $(12, 36)$ corresponding bins, each of which becomes an independent parameter in the optical model. This approximation is good if there is no prior assumption on the nature of the angular anisotropy. However, one disadvantage of this method is that it introduces many parameters ($12 \times 36 = 432$) into the model.
- **Sinusoidal angular distribution**, $H_{\text{sin}}(\cos \theta_{\text{LB}}, \phi_{\text{LB}})$: Prior observations of the laserball in SNO describe a sinusoidal variation in ϕ_{LB} of the angular anisotropy [134, 137, 139]. This is evident in the SNO August 2006 measurement of the laserball angular isotropy in Figure 4.13. The sinusoidal model splits the angular distribution into several $\cos \theta_{\text{LB}}$ slices, typically 24. For

each $\cos \theta_{\text{LB}}$ slice the relative intensity of the laserball is described as follows:

$$H_{\sin}^k(\phi_{\text{LB}}) = 1 + A_k \sin(\phi_{\text{LB}} + \delta_k), \quad k = [1, 24], \quad (4.16)$$

where A_k controls the amplitude of the anisotropy and δ_k provides an overall phase shift in ϕ_{LB} for the k -th $\cos \theta_{\text{LB}}$ slice. This model introduces $24 \times 2 = 48$ parameters in total.

The total laserball light distribution $L(\cos \theta_{\text{LB}}, \phi_{\text{LB}})$ is therefore a composite value consisting of the two-dimensional angular distribution, $H(\cos \theta_{\text{LB}}, \phi_{\text{LB}})$ multiplied by the mask function, $P_4(\cos \theta_{\text{LB}})$;

$$L(\cos \theta_{\text{LB}}, \phi_{\text{LB}}) = P_4(\cos \theta_{\text{LB}}) \times H(\cos \theta_{\text{LB}}, \phi_{\text{LB}}). \quad (4.17)$$

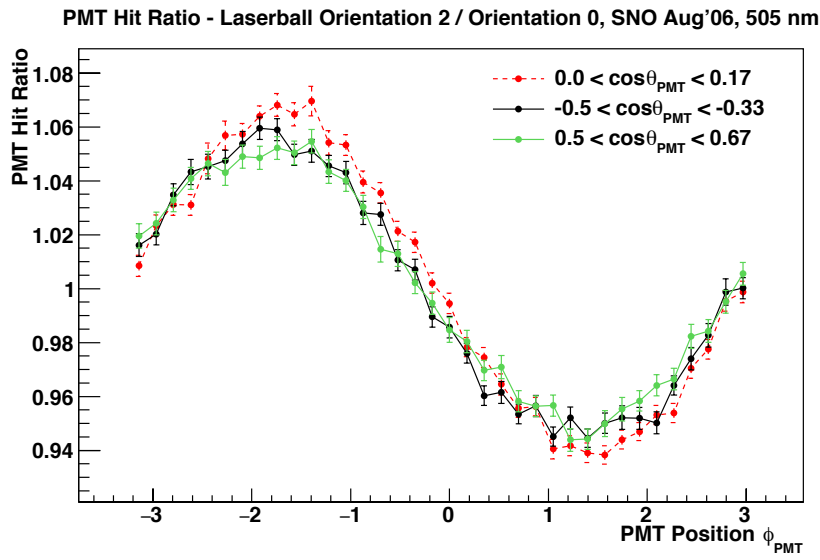


FIGURE 4.13: Shown is the ratio of PMT hits between two central laserball runs at different orientations: $0 \equiv \phi_{\text{LB}} = 0$ and $2 \equiv \phi_{\text{LB}} = \pi$. The ratio is plotted against the PMT ϕ_{PMT} coordinate which shares a 1:1 mapping with ϕ_{LB} . The PMT ratios relate to an intensity anisotropy of $\pm 6\%$ in ϕ_{LB} . The angular anisotropy is not necessarily constant in $\cos \theta_{\text{LB}}$ ($\equiv \cos \theta_{\text{PMT}}$) and therefore the PMTs are grouped into $\cos \theta_{\text{PMT}}$ slices. Three examples are shown. The plots shown are from SNO+ MC data generated using the SNO August 2006 laserball anisotropies.

4.2.6 Solid Angle

The solid angle is the area subtended by the face of the PMT from the laserball position. Specifically it is the subtended area of the PMT face projected onto the inner AV surface as illustrated in Figure 4.14. The calculation procedure is to define four points (P_1, P_2, P_3 and P_4 in Figure 4.14) along the perimeter of the PMT face, and calculate the light path to each of these points, using the four intersection points on the inner AV surface to define an ellipse. The four points form pairs that define the major and minor axes of the ellipse. The angles α and β between the points of each pair are used to calculate the solid angle, Ω on the unit sphere, centred about the laserball;

$$\Omega \simeq \pi \times \frac{\alpha\beta}{4}, \quad (4.18)$$

where the equality is sufficient for small angles α and β .

The nominal solid angle of a PMT from the centre of the AV is 8.8×10^{-3} and overall follows an inverse square relation between the laserball position and the PMT. The relative change in the solid angle with respect to the centre of the AV is therefore non-negligible as shown in Figure 4.15.

4.2.7 Fresnel Transmission Coefficient

The Fresnel transmission coefficient is a second-order effect on the optical model and denotes the probability of light traversing across a material interface. This probability is calculated for each interface the light path encounters. For a laserball position in the inner AV region these interfaces are between the inner AV/AV and AV/outer AV regions. The transmission coefficient relies on the calculated light path information for the incident and refracted angles at each interface as well as the refractive indices of both media. The explicit formulae used can be found in Appendix A.3. Given the wavelength dependence of the refractive indices, the Fresnel transmission coefficient also varies slightly with wavelength as shown in Figure 4.16.

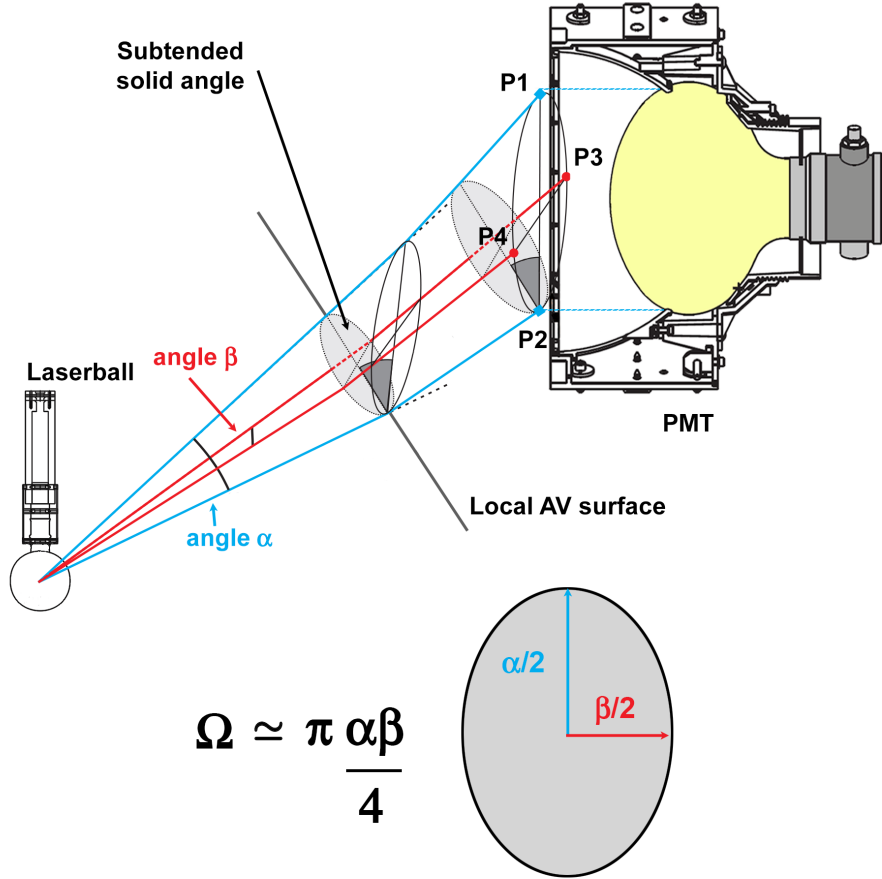


FIGURE 4.14: Illustrative diagram of the solid angle area subtended by the PMT face relative to the laserball position. The solid angle is the projection of the subtended area onto the inner surface of the AV. Figure is a modified version from that originally appearing in [133].

4.3 Implementation of the Optical Model

In order to constrain the parameter space the model prediction for the number of photons at a PMT, N_{ij}^{model} for a given run is divided by the expected value from a run with the laserball located at the centre of the detector, N_{0j}^{model} :

$$\frac{N_{ij}^{\text{model}}}{N_{0j}^{\text{model}}} = \frac{N_i \Omega_{ij} T_{ij} R_{ij} L_{ij}}{N_0 \Omega_{0j} T_{0j} R_{0j} L_{0j}} \exp \left(- \sum_k (d_{ij,k} - d_{0j,k}) \alpha_k \right). \quad (4.19)$$

By taking the ratio between an *off-axis* (i.e. not in the centre of the AV) and a central laserball run, the dependency on the PMT efficiency, ϵ_j is removed,

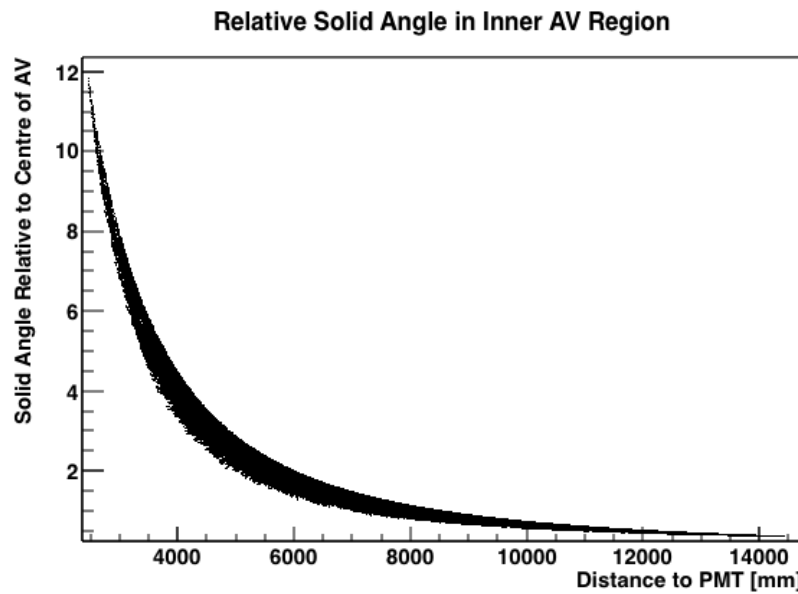


FIGURE 4.15: Shown is the variation in the relative solid angle with the distance from the laserball to the PMT. Here, *relative* denotes the comparison with the calculated solid angle to that at the centre of the AV, corresponding to a distance of ~ 8500 mm.

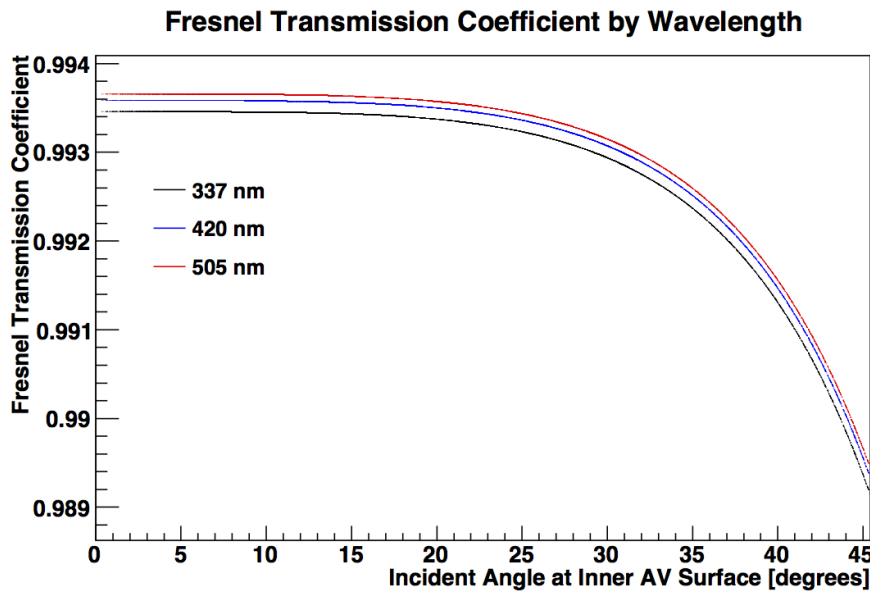


FIGURE 4.16: Shown is the Fresnel transmission coefficient for light paths in LABPPO in the inner AV region. The coefficient varies based on the incident angle at the first material interface; the inner AV/AV interface. The value of the coefficient varies slightly with wavelength due to a dependency on the refractive indices, $n(\lambda)$ at each boundary.

eliminating about 9000 parameters from the model. With respect to the equivalent observed ratio in data i.e. $N_{ij}^{\text{data}}/N_{0j}^{\text{data}}$, it is useful to first define what is known as the *occupancy*, which is related to N_{ij}^{data} as follows;

$$O_{ij}^{\text{data}} = \frac{N_{ij}^{\text{data}}}{N_i^{\text{pulses}}}, \quad (4.20)$$

where N_i^{pulses} is the number of laserball pulses triggered in run i . In general, the collection of hits at a PMT follow Poisson counting statistics. Multiple photoelectrons (MPEs) produced in the same time window at a PMT will only be registered as a single hit. This effectively underestimates the intensity of the laserball. Assuming the mean of the Poisson distribution, ξ_{ij} reflects the true occupancy of the PMT, this can be used to determine the multiple photoelectron corrected occupancy, O_{ij}^{MPE} ;

$$\begin{aligned} \text{Prob.} (\geq 1 \text{ Hit} | O_{ij}^{\text{data}}) &= 1 - \text{Prob.} (0 \text{ Hits} | O_{ij}^{\text{data}}), \quad O_{ij}^{\text{data}} \sim \text{Poisson}(\xi_{ij}), \\ \Rightarrow O_{ij}^{\text{data}} &= 1 - \frac{(\xi_{ij})^0 e^{-\xi_{ij}}}{0!} = 1 - e^{-\xi_{ij}}, \\ \Rightarrow \xi_{ij} &= -\ln(1 - O_{ij}^{\text{data}}) = O_{ij}^{\text{MPE}}. \end{aligned} \quad (4.21)$$

Note that the model does not account for MPE effects, and therefore this is a correction that is only applied to the data. For sake of notation, henceforth references to O_{ij}^{data} imply O_{ij}^{MPE} .

The number of pulses N_i^{pulses} is known exactly as it is purposefully triggered, the error in O_{ij}^{data} is therefore only attributed to the uncertainty in N_{ij}^{data} :

$$\delta N_{ij}^{\text{data}} = \sqrt{N_{ij}^{\text{data}}}. \quad (4.22)$$

Using equations 4.20, 4.21 and 4.22 the uncertainty on O_{ij}^{data} is thus obtained;

$$\delta O_{ij}^{\text{data}} = \frac{\partial(O_{ij}^{\text{data}})}{\partial N_{ij}^{\text{data}}} \delta N_{ij}^{\text{data}} = \frac{\sqrt{N_{ij}^{\text{data}}}}{N_i^{\text{pulses}} - N_{ij}^{\text{data}}}. \quad (4.23)$$

Following the definition of the occupancy, the occupancy ratio, OR_{ij}^{data} is therefore the ratio of the PMT occupancy from the off-axis run relative to the central run;

$$OR_{ij}^{\text{data}} = \frac{O_{ij}^{\text{data}}}{O_{0j}^{\text{data}}}. \quad (4.24)$$

Given that the solid angles, Ω_{ij}, Ω_{0j} and Fresnel transmission coefficients T_{ij}, T_{0j} can be directly calculated, and are implicit to the data values, they can be used to correct the ratio;

$$OR_{ij}^{\text{data}} = \frac{O_{ij}^{\text{data}}}{O_{0j}^{\text{data}}} \rightarrow \frac{O_{ij}^{\text{data}}}{O_{0j}^{\text{data}}} \times \left(\frac{\Omega_{0j} T_{0j}}{\Omega_{ij} T_{ij}} \right). \quad (4.25)$$

The uncertainty on OR_{ij}^{data} follows;

$$\delta OR_{ij}^{\text{data}} = OR_{ij}^{\text{data}} \sqrt{\left(\frac{\delta O_{ij}^{\text{data}}}{O_{ij}^{\text{data}}} \right)^2 + \left(\frac{\delta O_{0j}^{\text{data}}}{O_{0j}^{\text{data}}} \right)^2}. \quad (4.26)$$

Applying the same correction to the model (multiplying by $\Omega_{0j} T_{0j}/\Omega_{ij} T_{ij}$) the model prediction can similarly be written in terms of an occupancy ratio, OR_{ij}^{model} :

$$OR_{ij}^{\text{model}} = \frac{O_{ij}^{\text{model}}}{O_{0j}^{\text{model}}} = \frac{O_i R_{ij} L_{ij}}{O_0 R_{0j} L_{0j}} \exp \left(- \sum_k (d_{ij,k} - d_{0j,k}) \alpha_k \right), \quad (4.27)$$

where the intensity normalisations $N_i, N_0 \rightarrow O_i, O_0$ become occupancy normalisations and denote the total occupancy of all PMTs within a prompt timing window. Apart from the distances, $d_{ij,k}$ the model occupancy ratio is now an expression that is entirely characterised by parameters that can be determined by a statistical fit. This is now discussed.

4.3.1 Occupancy Ratio Method

The quantities OR_{ij}^{model} and OR_{ij}^{data} are used as the respective predictions and observations for a goodness of fit test using a chi-square (χ^2) test statistic;

$$\chi^2 = \sum_i^{N_{\text{runs}}} \sum_j^{N_{\text{PMTs}}} \frac{(OR_{ij}^{\text{data}} - OR_{ij}^{\text{model}})^2}{\sigma_{\text{stat.,}ij}^2 + \sigma_{\text{PMT}}^2(\theta_{\gamma,ij})}, \quad (4.28)$$

where $\sigma_{\text{stat.,}ij} = \delta OR_{ij}^{\text{data}}$ as given in Equation 4.26. The term $\sigma_{\text{PMT},ij}(\theta_{\gamma,ij})$ is an additional correction that accounts for a residual uncertainty in the PMT efficiency based on the incident angle light enters the PMT bucket, θ_γ . The calculation of this uncertainty is discussed in Section 4.3.2.

The minimisation of χ^2 in Equation 4.28 is a non-linear least squares problem. The non-linear component is the OR_{ij}^{model} parameter space and for this reason the Levenberg-Marquardt (LM) [140] algorithm is used to perform the minimisation. The LM algorithm is an adaptive technique which behaves as two methods based on the proximity of its current guess for the solution to the minimum. At large distances from the minimum it employs a gradient descent method that generally performs well in a many parameter problem such as this. Closer to the minimum the algorithm uses the Gauss-Newton method of minimisation which converges quicker than the gradient descent method. The LM algorithm is implemented into the SNO+ optical fit software, OCA which is discussed in Section 5.2.3.

4.3.2 PMT Variability

The physical interpretation of the PMT variability is likely due to a combination of performance and irregularities between PMTs. For example, the photocathode thickness about the PMT face may not be entirely uniform [133]. Similarly, the degradation, if at all, of the PMT reflectors such as those in Figure 4.9 are unique to each set of reflectors. Both of these features act to affect the PMT efficiency at different incident angles. To quantify this effect, the PMT variability can be understood by considering the estimator of the PMT efficiency, ϵ_{ij} that appears in Equation 4.1. This is initially removed as part of the occupancy ratio method but can be retrieved once the optical fit has been minimised as in Section 4.3.1 with $\sigma_{\text{PMT}}(\theta_{\gamma,ij}) = 0$. ϵ_{ij} represents the PMT efficiency of the model predicted

occupancy in relation to that observed in data;

$$\begin{aligned} \epsilon_{ij} \times O_{ij}^{\text{model}}|_{\chi^2_{\min}} &= O_{ij}^{\text{data}} \\ \Rightarrow \epsilon_{ij} &= \frac{O_{ij}^{\text{data}}}{O_{ij}^{\text{model}}} \Big|_{\chi^2_{\min}}. \end{aligned} \quad (4.29)$$

The individual PMT efficiencies can be compared between runs through normalisation;

$$\epsilon_{ij} \rightarrow \hat{\epsilon}_{ij} = \frac{\epsilon_{ij}/\bar{\epsilon}_j}{\bar{\epsilon}}, \quad (4.30)$$

where $\bar{\epsilon}_j$ is the average efficiency of PMT j across all runs and $\bar{\epsilon}$ is the average efficiency of all PMTs across all runs;

$$\bar{\epsilon}_j = \frac{1}{N_{\text{runs}}} \sum_i^{N_{\text{runs}}} \epsilon_{ij}, \quad \bar{\epsilon} = \frac{1}{N_{\text{PMTs}}} \sum_j^{N_{\text{PMTs}}} \bar{\epsilon}_j. \quad (4.31)$$

Past studies from SNO note an overall variation in the spread of the normalised efficiencies with incident angle, θ_γ [137]. This can be observed by computing the normalised efficiency for each PMT j , $\hat{\epsilon}_{ij}$ and binning it by its associated incident angle, $\theta_{\gamma,ij}$ into a histogram, one-degree per bin. The coefficient of variation, c_v for the resulting distribution formed in each bin, $\theta_\gamma = t$ is calculated as follows;

$$c_v(\theta_\gamma = t) = \frac{\sigma_t^{\text{RMS}}}{\mu_t}, \quad (4.32)$$

where σ_t^{RMS} and μ_t are the respective RMS and mean of the distribution in the t -th bin. The coefficient value varies across different incident angles. An example is shown in Figure 4.17 for the 505 nm wavelength scan from SNO in October 2003. As shown in the figure, the coefficient values are in excess of the statistical uncertainty on the occupancy, $\delta O_{ij}^{\text{data}}$. It is this excess variation in incident angle that is known as the PMT *variability*, $\delta v_{ij}(\theta_{\gamma,ij})$. The variability is a systematic that contributes an excess uncertainty beyond that associated with the statistical uncertainty. The variability is therefore defined as the residual of the coefficient of variation once this statistical uncertainty has been subtracted;

$$\delta v_{ij}(\theta_{\gamma,ij}) = \sqrt{c_v^2(\theta_{\gamma,ij}) - (\delta O_{ij}^{\text{data}})^2}. \quad (4.33)$$

As also shown in Figure 4.17, a fitted linear or polynomial function can be used to parameterise an estimator function for the coefficient of variation. Using Equation 4.33 this can subsequently be used to estimate the PMT variability. This is discussed in the results of the optical fit on original SNO data in Section 6.2.3.

The final variability error term, $\sigma_{\text{PMT}}(\theta_{\gamma,ij})$ featured in Equation 4.28 is related to $\delta v_{ij}(\theta_{\gamma,ij})$ by a multiplicative factor of the occupancy ratio;

$$\sigma_{\text{PMT}}(\theta_{\gamma,ij}) = OR_{ij}^{\text{data}} \times \delta v_{ij}(\theta_{\gamma,ij}). \quad (4.34)$$

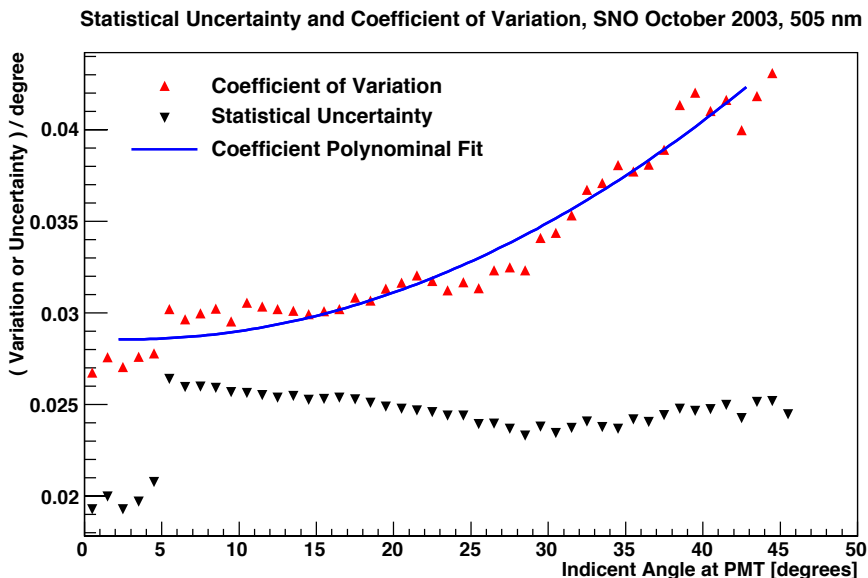


FIGURE 4.17: The coefficient of variation (red) and mean statistical uncertainty (black) on the occupancy binned by incident angle, θ_γ for the SNO October 2003 laserball scan at 505 nm. A fitted polynomial function (blue) is used to provide an estimator of the coefficient of variation. The PMT variability is the excess contribution to the coefficient of variation above the statistical uncertainty.

4.4 Data Selection

Prior to the minimisation of χ^2 , three selection criteria are applied to each of the PMTs in every run. Only PMTs that pass all three of these selection criteria are chosen. The three criteria are as follows:

- **PMT type and hardware status:** The channel hardware status of the PMT is checked to ensure it was operating during the time of the laserball run. Only the *normal* inward facing PMTs are selected for the data sample. Special PMT types e.g. PMTs in the neck of the AV and the OWL PMTs on the outer PSUP are not included.
- **Prompt peak counts:** For a given PMT, j a minimum number of prompt counts from the off-axis run, i and central run, $i = 0$ is imposed;

$$\begin{aligned} N_{ij}^{\text{data}} \geq 1000 &\Rightarrow \delta O_{ij}^{\text{data}} \leq 3\%, \\ N_{0j}^{\text{data}} \geq 4000 &\Rightarrow \delta O_{0j}^{\text{data}} \leq 1\%. \end{aligned} \quad (4.35)$$

A typical laserball scan at a given wavelength consists of 39 runs, of which only four are central runs. However, the occupancy of each PMT is paired with the value from a central run as required by the occupancy ratio method described in Section 4.3. Therefore, the error on each data point can be reduced by imposing a more stringent error requirement of $\leq 1\%$ on the occupancy values of PMTs from central runs. It is for this reason that the central laserball runs contain approximately quadruple the statistics (see Table 5.3). In practice, the additional running time of a central laserball run in order to achieve such an increase in statistics is reasonable 1-1.5 hours.

- **PMT shadowing:** Detector components located between the AV and the PSUP intercept light from the laserball reaching certain PMTs. Over the duration of a run this reduces the PMT occupancy. For each PMT in a run, the calculated light path from the laserball to the PMT is checked to see if it intersects, to within a given tolerance, with the known location of a piece of detector geometry. If so, the PMT is removed from the data sample.

4.4.1 PMT Shadowing

The predominant source of low occupancy PMTs is from the shadowing of PMTs by various detector components that are located between the AV and the PSUP. Such components include; support ropes, AV hold-down ropes, belly plates, NCD anchors, the AV neck boss and AV pipes. For a given laserball position, the

exposure of some PMTs to the laserball light is obscured by such components. Over the duration of the laserball run this effectively shadows the PMTs resulting in a reduced occupancy. Given the location of the laserball for a particular run and the known locations of the detector geometry, the light path to each PMT is tested for shadowing. A PMT is removed from the fit if the closest point of approach of the light path is within 150.0 mm of an obscuring piece of the detector geometry. The associated light path for each PMT in both its off-axis and central run representations are tested for shadowing. An example of the PMT shadowing in SNO and SNO+ for a central and off-axis run is shown in figures 4.18 and 4.19. Due to the addition of the AV hold-down ropes, more PMTs will be shadowed in SNO+ than in SNO.

Across different laserball positions, the AV hold-down ropes have the potential to shadow most of the PMTs as the ropes cover almost the entire range of $\cos \theta_{\text{PMT}}$ positions. Shown in Figure 4.20 is the relative number of PMT hits for a central laserball run with PMT position in $\cos \theta_{\text{PMT}}$. Below the main distribution are a series of scattered points. In the approximate range $\cos \theta_{\text{PMT}} \in (-0.8, 1.0)$ a fraction of these points denote PMTs shadowed by the AV hold-down ropes (in comparison to the less scattered distribution in SNO, see Figure 4.12). Shown also are those shadowed by the NCD anchors, $\cos \theta_{\text{PMT}} \in (-1, -0.8)$ and the AV neck boss, $\cos \theta_{\text{PMT}} \in (0.9, 1)$. In the case of the belly plates, $\cos \theta_{\text{PMT}} \in (-0.1, 0.1)$, the curved and bevelled nature of the plates act as an acrylic lens, focussing the light and increasing the occupancy of some PMTs above average.

Table 4.1 provides a breakdown of the percentage of PMTs shadowed by each detector component for two example laserball positions at 420 nm. The percentage value given for each component is independent to that of another. In general, two components may shadow the same PMT meaning the total percentage of shadowed PMTs is less than the sum of the individual percentages. The shadowing cuts are therefore applied sequentially, one detector component at a time to ensure the true total is calculated e.g if a PMT is shadowed by both a belly plate and support rope and the belly plate cut is applied first, it won't be considered by the support rope cut. The values given in figures 4.19 and 4.18 reflect the true total percentage of shadowed PMTs.

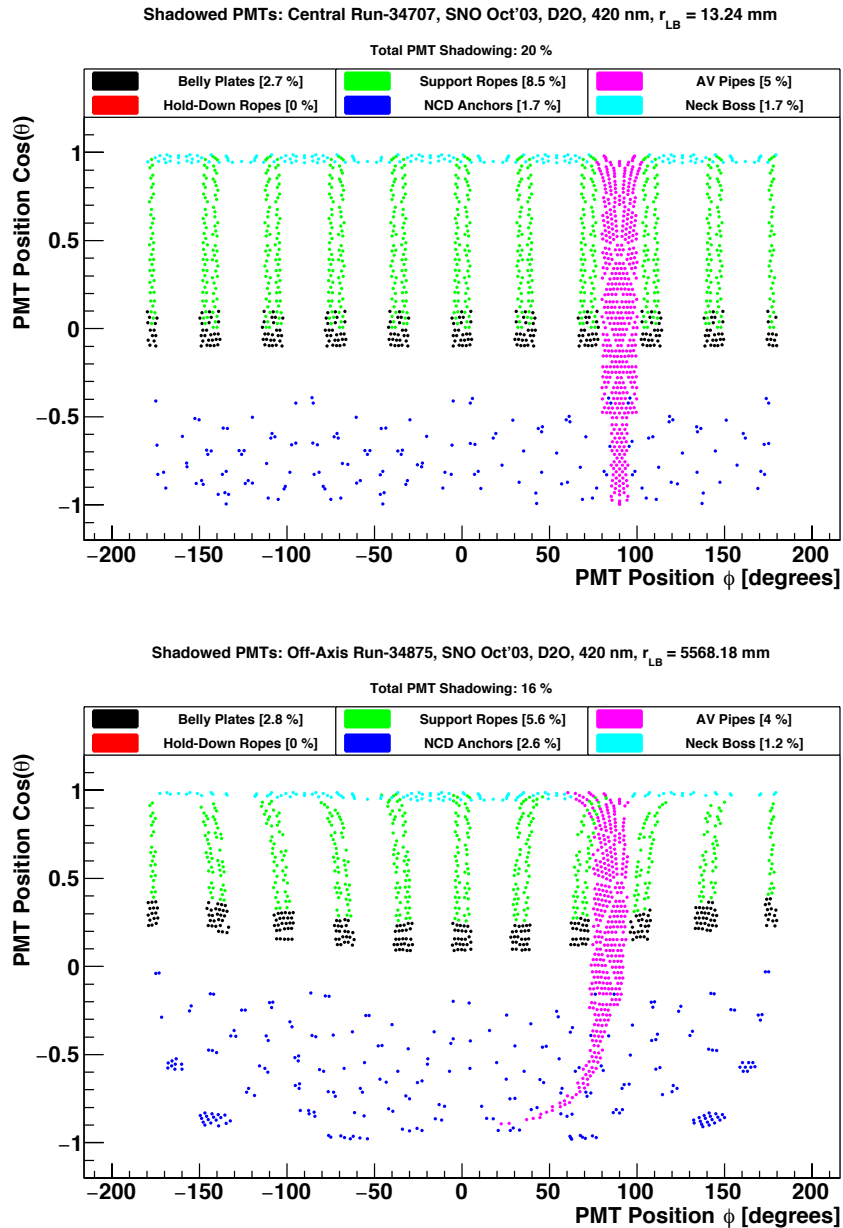


FIGURE 4.18: PMT shadowing for a central and off-axis laserball run at 420 nm from SNO, October 2003. Each point on the graph represents a PMT and its position, $(\phi_{PMT}, \cos \theta_{PMT})$ in the detector coordinate system. PMTs are colour coded based on the geometry which shadows its associated light path from the laserball.

4.4.2 Chi-Square Selection Cuts

A selection of χ^2 cuts are applied to remove data points from the sample. In general, it is perhaps bad practice to use such a cut, eliminating data from the sample which doesn't agree with the hypothesised model. However, given the number of

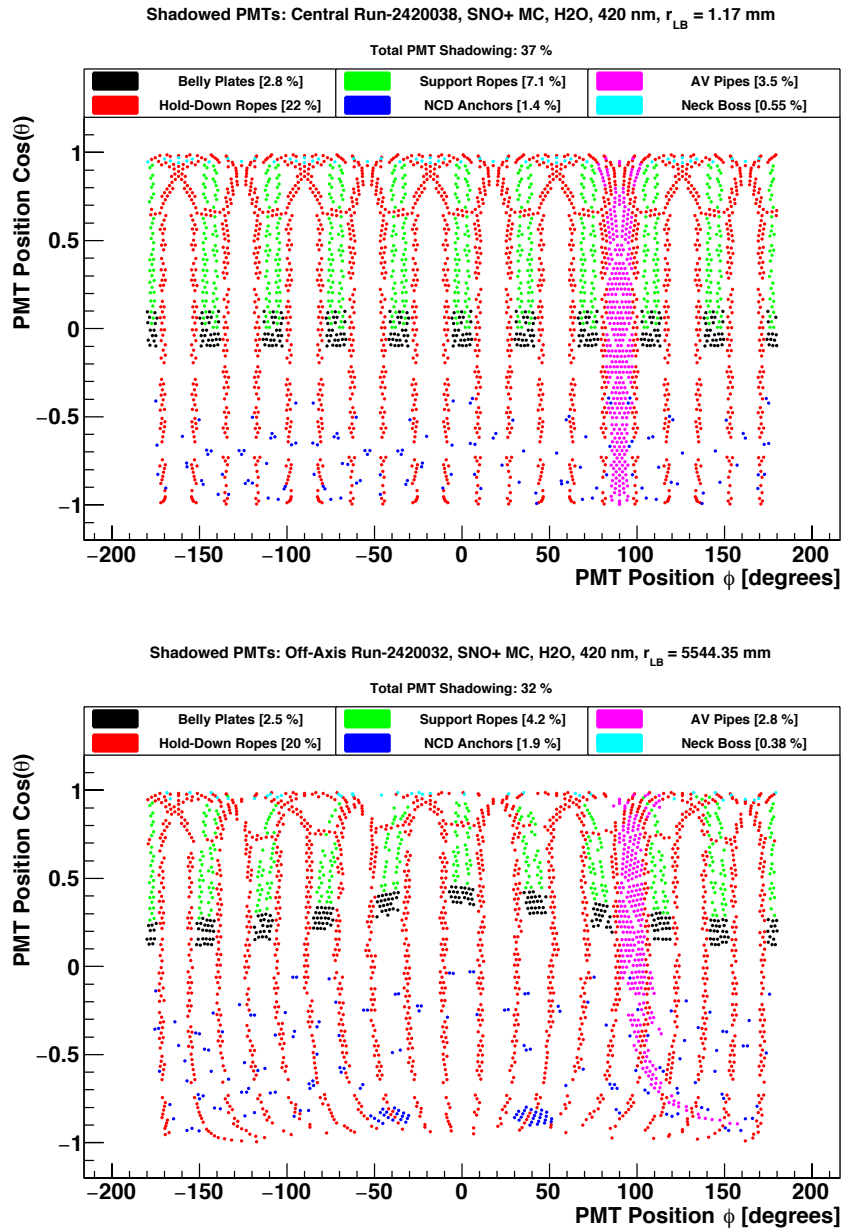


FIGURE 4.19: PMT shadowing for an MC central and off-axis laserball run at 420 nm in the SNO+ detector. Each point on the graph represents a PMT and its position, $(\phi_{PMT}, \cos \theta_{PMT})$ in the detector coordinate system. PMTs are colour coded based on the geometry which shadows its associated light path from the laserball.

data points and many configurations of the laserball run position contained within the sample, it is not unreasonable to expect some PMTs to undergo irregular exposure to the light which is unaccounted for by the model. The model essentially assumes near-uniform efficient PMTs surrounding a perfectly smooth and transparent vessel. However, the AV is not perfectly smooth, it contains tile bonds

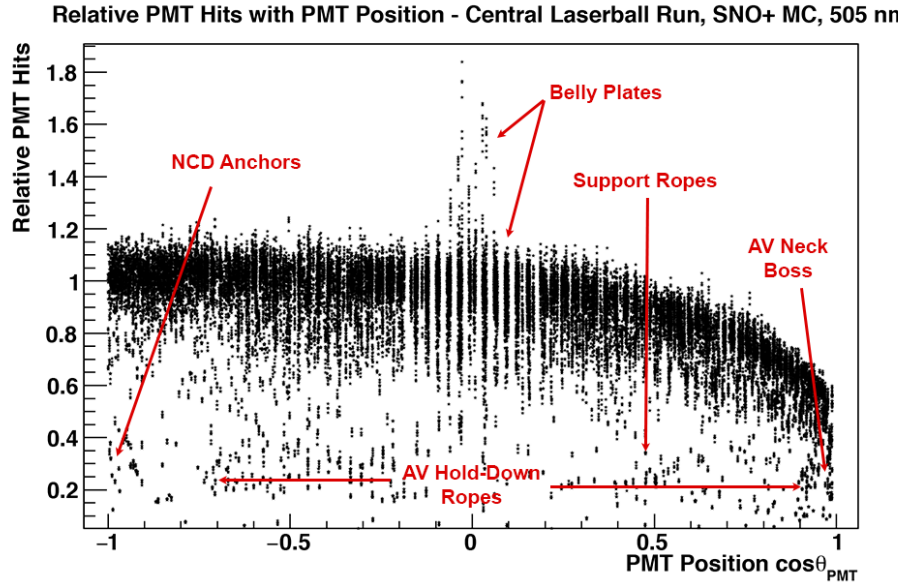


FIGURE 4.20: Shown is the relative change in the number of PMT hits with the PMT position $\cos \theta_{\text{PMT}}$ coordinate from a central laserball run at 505 nm. Data is from SNO+ MC. In different ranges of $\cos \theta_{\text{PMT}}$ some PMTs have a reduced relative number of hits due to shadowing by different detector components.

PMT Shadowing by Individual Components, 420 nm

Detector Component	PMTs Shadowed % $ \vec{r}_{\text{LB}} = 0.0 \text{ mm}$	PMTs Shadowed % $ \vec{r}_{\text{LB}} = 5500.0 \text{ mm}$
Belly Plates	2.98%	6.56%
AV Hold-Down Ropes	21.53%	20.10%
Support Ropes	10.75%	8.32%
NCD Anchors	6.93%	5.76%
AV Pipes	5.10%	3.71%
Neck Boss	2.32%	1.92%

TABLE 4.1: Shown are the percentages of PMTs shadowed by each type of detector component. The amount of shadowing varies according to the laserball position in the AV. Two examples are shown for a central laserball position, $|\vec{r}_{\text{LB}}| = 0.0 \text{ mm}$ and an off-axis position, $|\vec{r}_{\text{LB}}| = 5500.0 \text{ mm}$. The total shadowing is less than the sum of the individual contributions as some components may shadow the same PMT e.g. a belly plate and a support rope.

whose surface, in practice, is blemished. In addition, some detector components may deflect light to certain PMTs which aren't considered shadowed. The use of a prompt time window intends to suppress this. Ultimately, PMTs subject to irregular reflections or scattering of the light will contribute to populations of the

sample that do not reflect the underlying physics of the model, and as such they are removed for this reason.

Following the initial selection cuts, the optical fit proceeds by minimising the optical model over the data throughout several iterations. For each iteration PMTs whose χ^2 value exceeds a given upper limit are removed. An initial upper limit of $\chi_{\text{lim}}^2 = 1000$ is chosen as it is sufficiently large to include almost all the PMTs which pass the aforementioned selection criteria. Minimisation is then repeated using the following upper χ^2 limits for each iteration:

$$\chi_{\text{lim}}^2 = \{100, 50, 25, 16, \chi_{\text{lim,f}}^2, \chi_{\text{lim,f}}^2\}, \quad (4.36)$$

where $\chi_{\text{lim,f}}^2$ is the final upper χ^2 limit which is nominally repeated to ensure stability of the fit. The progressive sequence of decreasing upper limits is used to avoid the introduction of any initial bias into the data sample and the minimisation about local minima in the parameter space. To avoid a sequential minimisation over the same subset of the sample, all PMTs, even those previously removed, are reconsidered in each iteration. The purpose of this is to re-include previously cut PMTs whose χ^2 may have peripherally exceeded a prior limit, but for which a more recent parameter state produces a χ^2 value within the current limit.

The value of $\chi_{\text{lim,f}}^2$ is informed by studying the distribution of the *data point pull*;

$$\text{Data Point Pull} = \frac{OR_{ij}^{\text{model}} - OR_{ij}^{\text{data}}}{\sigma_{\text{stat},ij}}, \quad (4.37)$$

which is a measure of the deviation between the model predicted and measured value of the occupancy ratio; it is the square-root of the argument that is summed over to calculate χ^2 as in Equation 4.28. By sampling data points one effectively samples a *parent* distribution that has a mean and variance but whose form cannot be assumed. However, provided the model prediction of the occupancy ratio is a good approximation of the data, the pulls should follow a known distribution type, which in this case is expected to be Gaussian. Figure 4.21 shows the data point pull distribution for an example SNO+ MC laserball scan in water at 420 nm. The final upper χ^2 limits were determined by first fitting a Gaussian function to the pull distribution in a narrow range between $(-1, 1)$, after which this range was gradually extended. It was found that for both the data and MC data sets,

the pull distribution became non-Gaussian at a distance of $\sim 2\sigma$ from the mean, μ ($\simeq 0$); beyond this distance the goodness of fit deteriorated. It is in this non-Gaussian region that the model prediction no longer provides a good description of the data. Therefore, the distance of 2σ can be used to define an upper limit. To be consistent across all wavelengths, the average width across all wavelength scans in a particular data set is used to define the final upper χ^2 limit as follows:

$$\chi_{\text{lim,f}}^2 = (2\langle\sigma_\lambda\rangle)^2, \quad \langle\sigma_\lambda\rangle = \frac{1}{n_\lambda} \sum_i \sigma_i, \quad n_\lambda = \text{No. wavelength scans.} \quad (4.38)$$

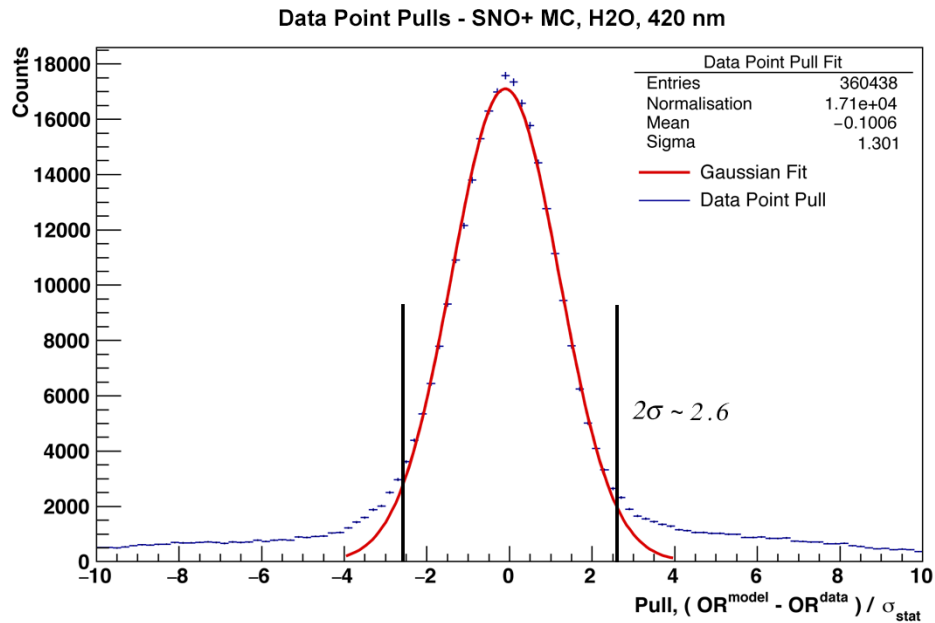


FIGURE 4.21: The data point pull distributions for a SNO+ MC laserball scan in water at 420 nm. The pull values are normally distributed about zero in the range $(-2.6, 2.6)$ for the SNO+ MC scan. This range is equivalent to a distance of $\sim 2\sigma$ either side of the origin based on the sigma value of the associated Gaussian fit (red) in the respective range. Beyond these ranges the distribution becomes non-Gaussian as shown.

As will be discussed in Section 6.1.1, given the small variation in the Gaussian widths between different wavelength scans of the same data set, the value of the final upper χ^2 value is conservatively rounded to the nearest whole integer, i.e.

$$\chi_{\text{lim,f}}^2 \rightarrow \lceil \chi_{\text{lim,f}}^2 \rceil = \lceil (2\langle\sigma_\lambda\rangle)^2 \rceil. \quad (4.39)$$

4.5 Scintillator Response

One of the new phenomena introduced into SNO+ by the use of scintillator is that of absorption and reemission. As discussed in Chapter 3, based on the scintillator mixture, certain wavelengths of light will be prone to being absorbed and reemitted at a wavelength according to the respective WLS. The optical model as expressed in Equation 4.1 does not directly account for absorption and reemission¹. In the context of laserball studies, these effects do not impact the intensity of the prompt light significantly; it merely scales it by the reemission probability, ϵ_p of the scintillator. Ultimately, this is a scaling factor which becomes part of the normalisation terms, O_i and O_0 in Equation 4.27. Rather, the impact of absorption and reemission is characterised by the time profile of the scintillator, which is driven by the exponential nature of fluorescence as in Equation 3.5. Here, the optical model is instead used to seed a new type of model that aims to characterise absorption and reemission through the extraction of an in-situ time profile from the time residual distribution.

4.5.1 In-situ Scintillator Time Profile

To demonstrate the impact of absorption and reemission it is useful to compare the time residual distributions from a central laserball run between two wavelengths; one at a short wavelength for which the light is entirely absorbed and remitted, and another at a wavelength that matches the peak of the reemission profile. For example, in LABPPO at 337 nm the absorption length is small, ~ 100 mm (see Figure 3.11). For a central laserball run, the minimum distance through the inner AV region is 6000 mm (the radius of the AV) which guarantees that the majority of the 337 nm light will be absorbed. As will be discussed in Section 5.1.1, at 337 nm in LABPPO, the average wavelength of the reemitted light is ~ 400 nm. Therefore, a comparison of the time residual distributions in LABPPO at 337 nm and 400 nm illustrate the impact of absorption and reemission. An example using this comparison is shown in Figure 4.22. Two distinct features are present:

- **Scintillation emission time:** Between 337 nm and 400 nm there is an overall shift in the time residual distribution by +1.35 ns, identified as the

¹It will be discussed in Chapter 7 that although the model does not parameterise absorption or reemission, the other optical parameters are directly affected by these effects.

difference between the central values of the respective prompt peaks. This overall shift is driven by the delay associated with the fluorescence of the wavelength shifter (PPO), characterised by an exponential decay with time constant, τ_s .

- **Photon walk:** In addition to the convolved emission delay, the smearing of the time residuals and the reduced prominence of the smaller peaks; the pre- and late-pulsing either side of the prompt peak and the populations of reflected light in the range 415–435 ns is due to *photon walk*. Photon walk is the random displacement between the initial position of the laser light and the final position of the remitted light that leaves the AV. Depending on the scintillator mixture, the light may be absorbed and reemitted multiple times as part of general radiative transfer between the solvent and wavelength shifters. The random element of this *walk* arises from the nature of scintillation light, whose emitted direction is random. The effective emission point of the resulting scintillation light is therefore displaced from the initial position in the centre of the detector, broadening the range of possible reflections.

4.5.2 Scintillator Time Profile Model

Taking into account the scintillator emission time and the photon walk, the arrival time at the PMT can be expressed as follows;

$$t_{\text{PMT}} = \sum_{n=1}^{N_{\text{abs}}} \left[\frac{d_{n,\text{walk}}(\alpha_w(\lambda_{n-1}), \vec{r}_{n-1}, \vec{r}_n)}{v_{g,\text{Scint}}(\lambda_{n-1})} + t_{\text{emit}}(\tau_s) \right] \Big|_{|\vec{r}_n| < R_{\text{AV}}} \\ + \sum_k \frac{d_k(\vec{r}_n)}{v_{g,k}(\lambda_{\text{emit}})} \Big|_{n=N_{\text{abs}}} + t_{\text{bucket}}(\theta_\gamma | \vec{r}_n), \quad (4.40)$$

where

$$\lambda_n = \begin{cases} \lambda_{\text{LB}} & \text{if } n = 0 \\ \lambda_{\text{emit}} & \text{if } n \geq 1 \end{cases}, \quad \text{and} \quad \vec{r}_0 \equiv \vec{r}_{\text{LB}}. \quad (4.41)$$

Here, the sum over the index n denotes the number of absorptions and reemissions, N_{abs} . λ_{LB} and λ_{emit} are the respective wavelengths of the laserball and the reemitted light. The value t_{emit} is the emission time of the scintillator parameterised by

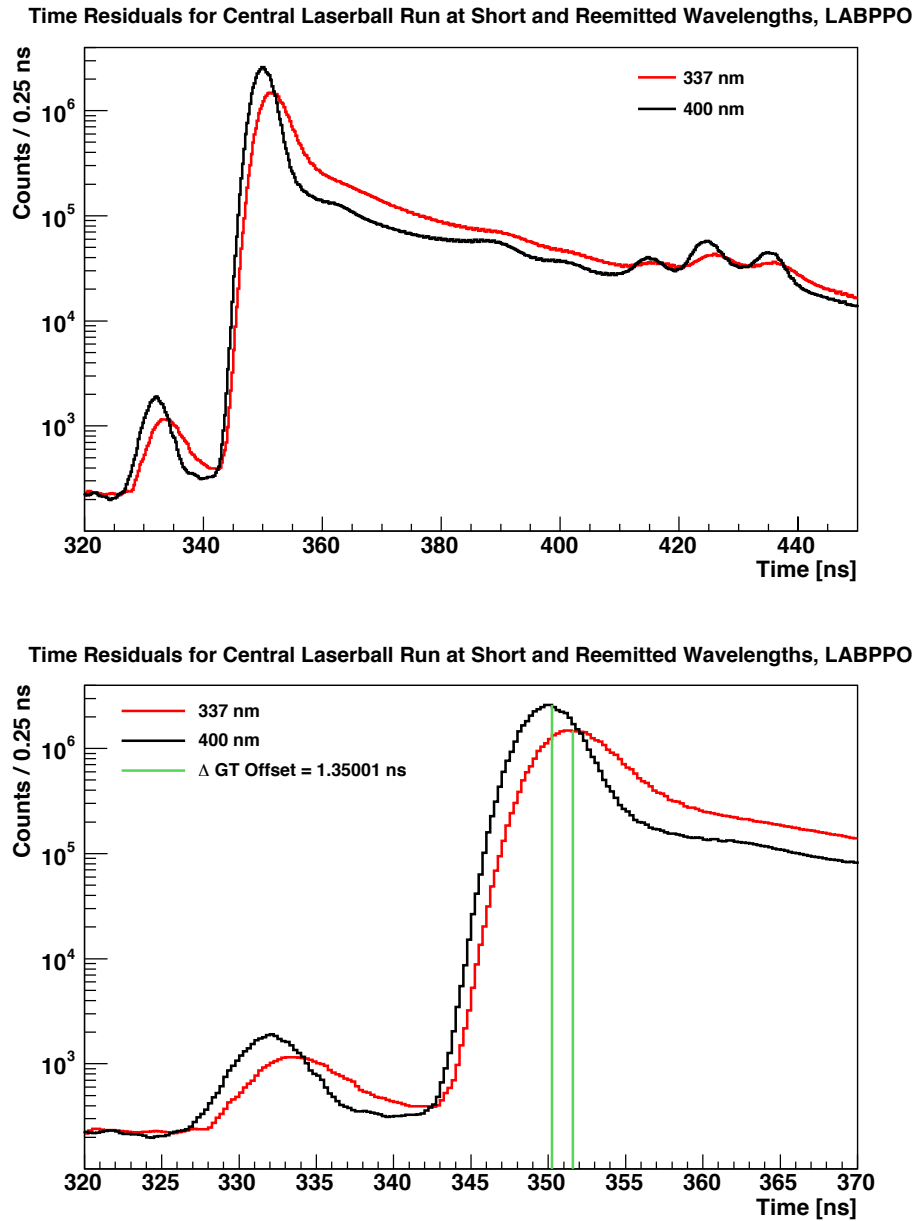


FIGURE 4.22: The time residual distributions for SNO+ MC central laserball runs in LABPPO at 337 (red) and 400 nm (black). Shown are the global distributions (top) and the distributions about the prompt peak (bottom). In LABPPO, at 337 nm the light is absorbed and reemitted at an average wavelength of 400 nm. At 400 nm the light is not absorbed to the same extent, in comparison the result is a +1.35 ns change in the global time offset (ΔGT) at 337 nm due to absorption and reemission.

the exponential time constant, τ_s . The value $d_{n,\text{walk}}$ is the distance between the

current absorption position, \vec{r}_n and the prior emission point \vec{r}_{n-1} , i.e.

$$d_{n,\text{walk}} = |\vec{r}_n - \vec{r}_{n-1}|, \quad (4.42)$$

where the magnitude of $d_{n,\text{walk}}$ is dependent on the mean photon walk length for the previously emitted wavelength, $\alpha_w(\lambda_{n-1})$.

Absorption and reemission only occurs in the scintillator region, and thus $|\vec{r}_n| < R_{\text{AV}}$. As in Equation 4.12, the index k is summed over the three detector regions; inner AV, AV and outer AV, where the distances d_k are calculated from the final emission position before light escapes the scintillator region, \vec{r}_n for $n = N_{\text{abs}}$.

Figure 4.23 illustrates the process behind the model expression in Equation 4.40. At each absorption point (denoted by encircled nodes) the new direction of the reemitted photon is determined at random over a uniform distribution.

From this the time residual is the PMT hit time, t_{PMT} corrected for the (assumed) time of flight from the initial laserball position to the PMT as follows;

$$t_0 + t_{\text{res}} = t_{\text{PMT}} - \sum_k \frac{d_k(\vec{r}_{\text{LB}})}{v_{g,k}(\lambda_{\text{emit}})} - t_{\text{bucket}}(\theta_\gamma), \quad (4.43)$$

where it is important to emphasise the difference between the time of flight over the distances $d_k(\vec{r}_{\text{LB}})$ that are calculated from the initial laserball position unlike those in Equation 4.40. Indeed setting $n = 0$ in Equation 4.40 returns the standard time residual relation.

The values of $d_{n,\text{walk}}$ and t_{emit} cannot be analytically resolved for a specific PMT. However, their values are related to the respective absorption/scattering lengths and time decay constants of the scintillator which are naturally described by exponential relations as in equations 3.3 and 3.5. Therefore, for many photons arriving at a PMT, the values of $d_{n,\text{walk}}$ and t_{emit} are also distributed exponentially;

$$d_{n,\text{walk}} \sim \text{Exp}(1/\alpha_w(\lambda_{n-1})), \quad t_{\text{emit}} \sim \text{Exp}(1/\tau_s). \quad (4.44)$$

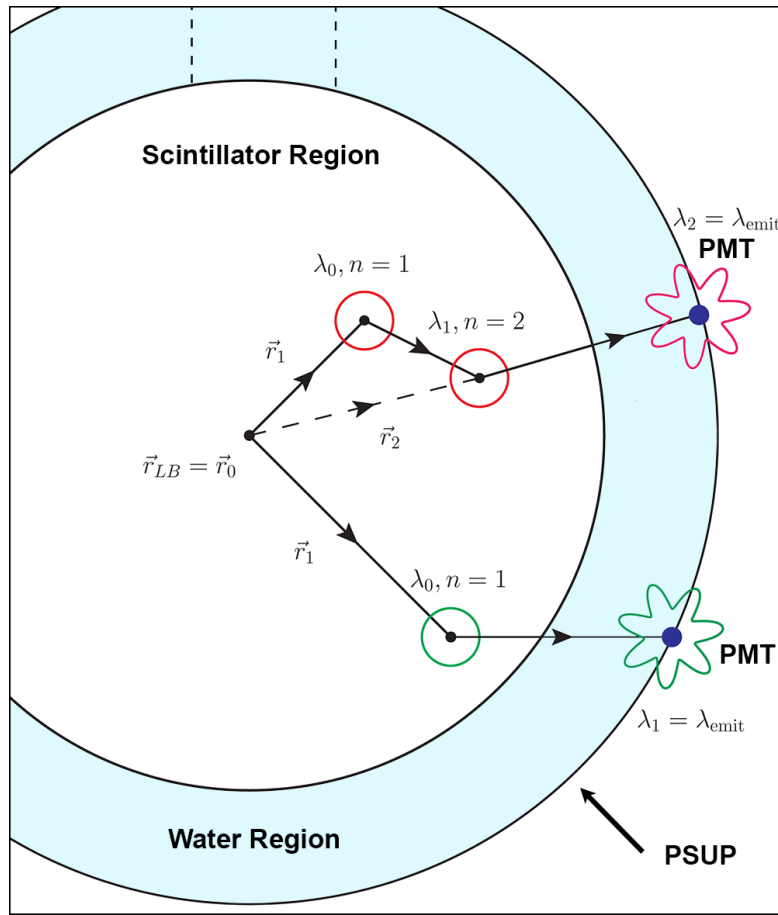


FIGURE 4.23: Illustrative diagram of the path taken by light initially emitted at the centre of the detector which undergoes absorption and reemission. Two examples are shown, one where the light is absorbed twice (red) and another once (green). At each absorption point (circles) the direction of the reemitted photon can be in any direction, and is chosen at random. This is the random walk of the photon.

One point to note is that the reemission times are sampled over the following reemission window;

$$\text{Reemission Time Window : } (\tau_s, 3\tau_s), \quad (4.45)$$

This is the window used by **GLGScint** in MC simulations (RAT) to model the emission of light by the scintillator. There is also a subtlety associated with α_w . From one PMT time calculation to the next, the number of absorptions may be different, and in practice, the absorptions may be between different components of the scintillator itself e.g. radiative transfers: LAB \rightarrow PPO, LAB \rightarrow bis-MSB, PPO \rightarrow perylene etc. Each of these components will have its own emission profile

for which the photon walk length prior to the next absorption (if at all) will be different. α_w is therefore an effective attenuation length that encapsulates a variety of micro-physical processes occurring within the scintillator prior to the emission of light. Therefore, to avoid over parameterisation of the model, the implementation presented here will assume the following;

$$d_{n,\text{walk}} \sim \begin{cases} \text{Exp}(1/\alpha_w(\lambda_{\text{LB}})) & \text{if } n = 0 \\ \text{Exp}(1/\alpha(\bar{\lambda}_{\text{emit}})) & \text{if } n \geq 1 \end{cases}, \quad (4.46)$$

where $\alpha(\bar{\lambda}_{\text{emit}})$ is the attenuation length of the scintillator at the mean emitted wavelength, $\bar{\lambda}_{\text{emit}}$. It will be shown in Chapter 7 that $\alpha(\bar{\lambda}_{\text{emit}})$ can be determined using the optical response model described in Section 4.2 and therefore be used as an input.

Following a description of the scintillator time profile model, the objective is to parameterise the observed time residuals in scintillator according to $\alpha_w(\lambda_{\text{LB}})$ and τ_s .

4.5.3 Scintillator Time Profile Model Log-Likelihood

A log-likelihood method is used to fit for the optimum values of $\alpha_w(\lambda_{\text{LB}})$ and τ_s . In practice, the form of a time residual distribution in scintillator is the result of several physical and instrumental effects which are convolved together; the PMT response, the time profile of the laser emittance, the absorption of photons and the isotropic emission of scintillation photons. Subsequently, an analytical probability distribution function (PDF) involves multiple integrals over all physically possible paths and detector responses such that it coincides with an observed PMT hit time. Such calculations are computationally exhaustive. Instead, the *forward problem* is considered whereby the parameter space is mapped to the *data-space* using an MC technique to produce a time residual distribution that is used to produce a PDF.

Using equations 4.40 and 4.43, the time residual distribution for given values of $\alpha_w(\lambda_{\text{LB}})$ and τ_s is generated by calculating the PMT hit time t_{PMT} for all PMTs in the detector from the centre of the AV many times $\sim 5 \times 10^6$. For simplicity, the centre is chosen to be the starting position in order to preserve the symmetry about the detector.

For each calculation, the values of $d_{n,\text{walk}}$ and t_{emit} are randomly sampled according to their respective exponential distributions. Values are sampled until the path leaves the AV region. The initial and remitted direction of the light is chosen randomly each time. The final direction of the light is that of the last reemission whose following sample length took the path outside of the inner AV region. To emulate the laser emission and detector response, randomly sampled times from the laser emission profile, $t_{\sigma,\text{LB}}$ and the PMT response, $t_{\sigma,\text{PMT}}$ are included (see Appendix A.4);

$$\begin{aligned} t_{\text{PMT}} &\rightarrow t_{\text{PMT}} + t_{\sigma,\text{LB}} + t_{\sigma,\text{PMT}}, \\ t_{\sigma,\text{LB}} &\sim \text{Gaus}(\mu = 0.0, \sigma = 0.7) \text{ ns}, \\ t_{\sigma,\text{PMT}} &\sim \text{Gaus}(\mu = 0.0, \sigma = 1.7) \text{ ns}. \end{aligned} \quad (4.47)$$

The MC time residuals are stored in histograms using a 0.25 ns binning, and then interpolated between to produce a PDF, $P(t_{\text{res}}|\alpha_w(\lambda_{\text{LB}}), \tau_s)$. These PDFs are used in the log-likelihood fit over the observed time residuals, minimising over the function, \mathcal{L} ;

$$\mathcal{L} = - \sum_{q=0}^{N_{\text{data}}} \ln(P(t_{q,\text{res}}|\alpha_w(\lambda_{\text{LB}}), \tau_s)), \quad (4.48)$$

where N_{data} is the total number of PMT hit times in the data sample.

Examples of MC generated distributions for different values of $\alpha_w(\lambda_{\text{LB}})$ and τ_s are shown in Figure 4.24 for a laser wavelength $\lambda_{\text{LB}} = 337$ nm in LABPPO with an average reemitted wavelength $\bar{\lambda}_{\text{emit}} = 400$ nm. Variations in both $\alpha_w(\lambda_{\text{LB}})$ and τ_s characterise the shape of the time residual distribution. In particular, changes in $\alpha_w(\lambda_{\text{LB}})$ introduce minor shifts in the prompt peak location whereas τ_s characterises the tail of the distribution.

4.6 Conclusion on Optical Response

A model that characterises the optical response of the detector has been presented within the context of the laserball calibration hardware. The laserball is to be deployed in both the water, scintillator and tellurium phases of SNO+. Using

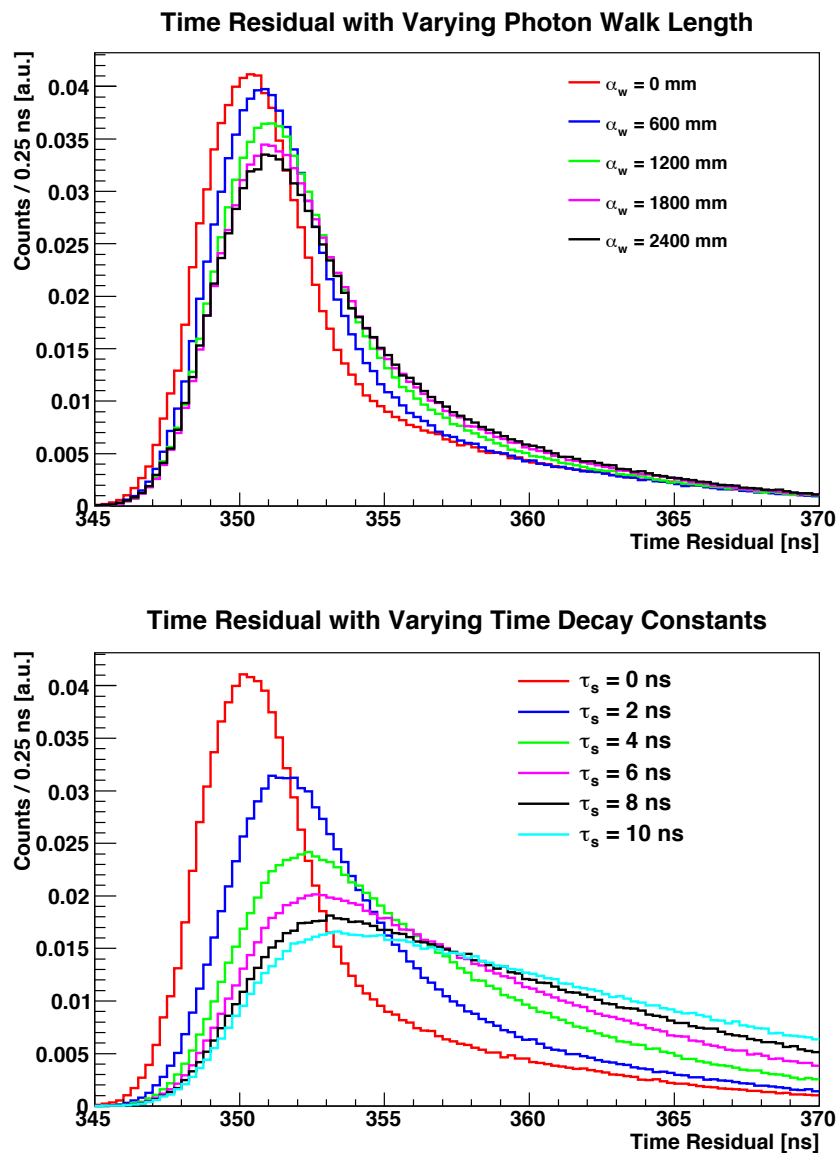


FIGURE 4.24: Generated time residual distributions for variations in α_w (λ_{LB}) (top) and in τ_s in LABPPO for a laser wavelength of $\lambda_{LB} = 337 \text{ nm}$ ($\bar{\lambda}_{\text{emit}} = 400 \text{ nm}$). For the variations in α_w (λ_{LB}) a small value of $\tau_s = 0.01 \text{ ns}$ was used with a nominal attenuation length value of $\alpha_w(\bar{\lambda}_{\text{emit}}) = 10^6 \text{ mm}$ for the reemitted light. Similarly, for the plots describing the variations in τ_s values of $\alpha_w(\lambda_{LB}) = 0.1 \text{ mm}$ and $\alpha_w(\bar{\lambda}_{\text{emit}}) = 10^6 \text{ mm}$ was used. For the plotted distributions at $\alpha_w(\lambda_{LB}) = 0$ and $\tau_s = 0$, no random sampling was performed.

laserball data the attenuation and PMT response can be characterised. This can be combined with the output of other calibration systems as part of the full detector calibration. The optical model does not explicitly account for the absorption and reemission expected in scintillator. Therefore, a second model that aims to characterise the time profile of the scintillation light has also been presented.

Collectively, both the optical and time profile model can be used to characterise the behaviour of the scintillator in SNO+, and its impact on the optical response.

As discussed in Chapter 3, SNO+ is currently considering two candidate fluors to be used as a secondary WLS in the tellurium phase; bis-MSB and perylene. The results of the optical fit and time profile model over laserball scans in scintillator are discussed in Chapter 7, and consider the base LABPPO mixture and those containing bis-MSB (LABPPO+0.3%Te+bis-MSB) and perylene (LABPPO+0.3%Te+perylene). The data used for this analysis are produced using simulations of the laserball in **RAT**. **RAT** is also used to produce laserball scan simulations of the water phase. The results of which are discussed in Chapter 6. The production of this SNO+ MC laserball data is now discussed.

5

Production and Processing of Data

Holmes: Ah, I have no data. I cannot tell.

Watson: Well, there seems to me to be only one possible solution... .

The Adventure of the Copper Beeches, Arthur Conan Doyle

5.1 Monte-Carlo Production

Prior to collecting laserball data, preliminary studies make use of simulated data generated by RAT; the SNO+ MC software. RAT features a laserball *generator* that emulates the in-situ action of the laserball in an MC representation of the detector. The laserball generator is characterised by sampling a combination of lab-based measurements and parameters obtained from laserball scans during the SNO experiment. This includes:

- The wavelength distributions, see Figure 5.1, of the N₂ laser and the laser-dyes:
 - N₂ laser, $\lambda_{LB} = 337$ nm
 - PBD dye, $\lambda_{LB} = 369$ nm
 - BBQ dye, $\lambda_{LB} = 385$ nm

- Bis-MSB dye, $\lambda_{LB} = 420$ nm
- COUMARIN-500 dye, $\lambda_{LB} = 505$ nm
- KITON-RED dye, $\lambda_{LB} = 620$ nm
- The laserball angular distribution, $H(\cos \theta_{LB}, \phi_{LB})$ and mask function, $P_4(\cos \theta_{LB})$ obtained from the laserball scan of each previous calibration period in SNO between September 2000 and August 2006. An example of the COUMARIN-500 sinusoidal angular distribution is shown in Figure 5.2. Examples of the mask function are shown in Figure 5.3.
- The timing information of the laser pulse. This is modelled as a Gaussian function with $(\mu, \sigma) = (0.0, 0.7)$ ns that is truncated with minimum and maximum time values, $(t_{low}, t_{high}) = (-1.5, 10.0)$ ns (see Appendix A.4). The 0.7 ns width is attributed to the dispersion of the laser pulse in the 40 m long optical fibres between the laser source and the laserball.

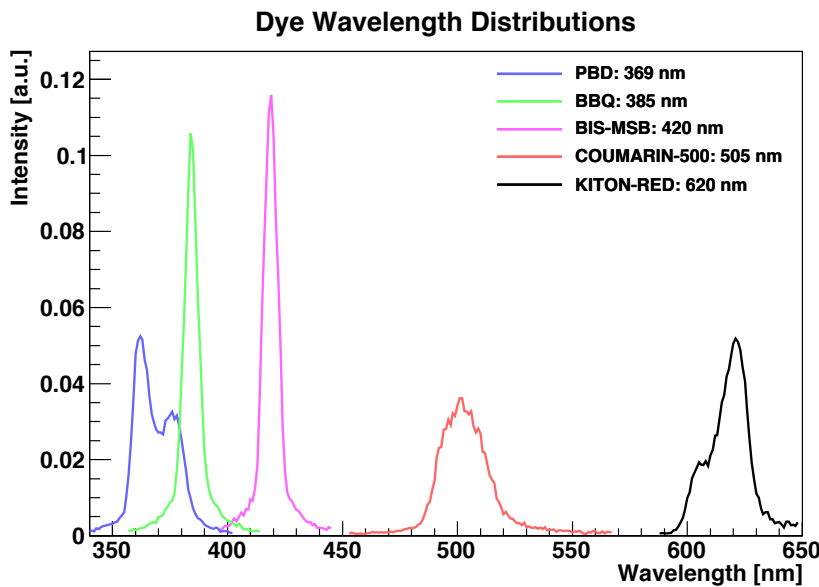


FIGURE 5.1: The wavelength distributions of the five different laser-dyes stimulated by an N₂ ($\lambda_{LB} = 337$ nm) laser. Values are obtained from ex-situ measurements made by J. Maneira at Queen's University [141].

In effect, the laserball as understood during SNO, in-situ, is being convolved with the RAT Monte-Carlo in order to understand how the physical and material properties of the detector affect the optical response. Of particular interest in SNO+ is how the inclusion of the new AV hold-down rope net and the use of scintillator reduce or enhance this response.

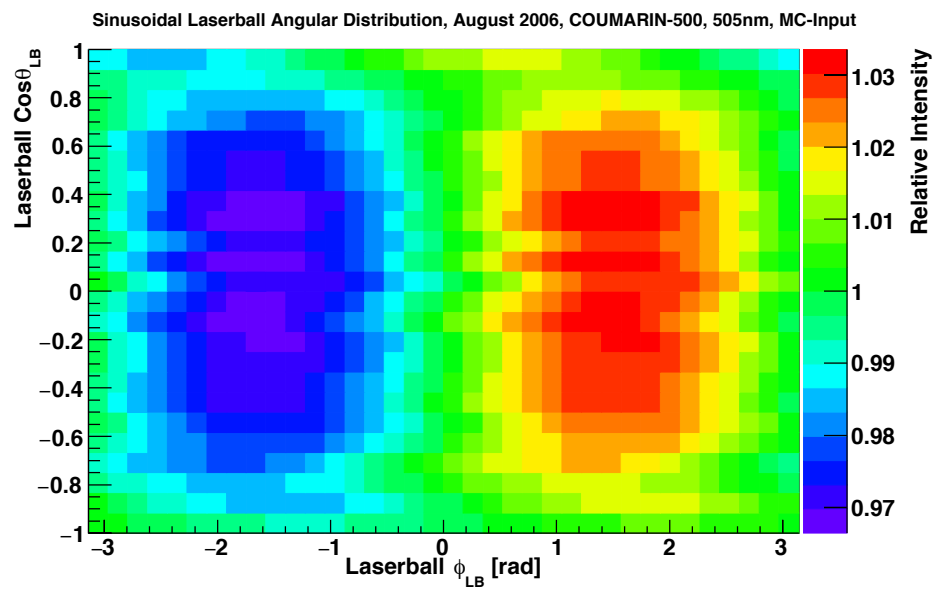


FIGURE 5.2: The relative sinusoidal laserball angular distribution as measured in SNO for the COUMARIN-500 dye during the August 2006 calibration period. This is used as an input to the laserball angular distribution in RAT at this wavelength.

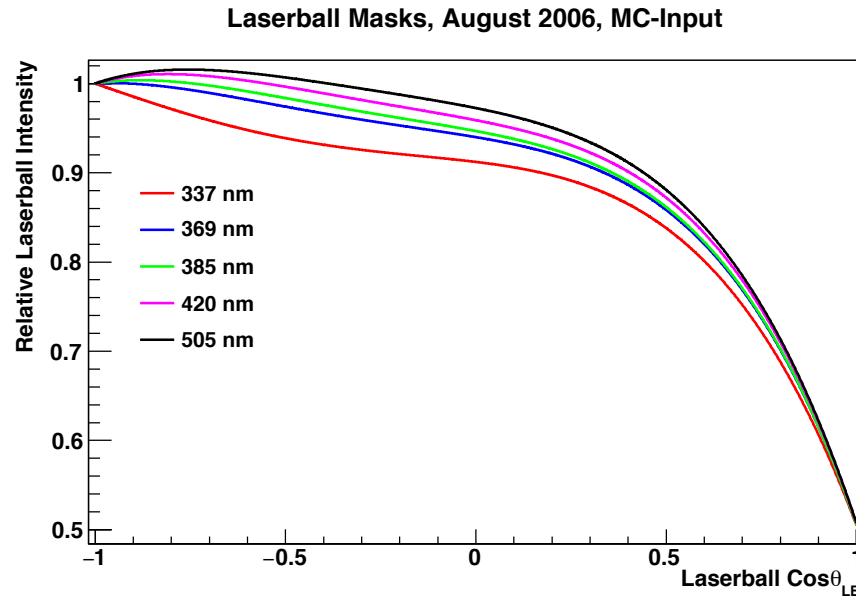


FIGURE 5.3: The laserball mask functions as fitted in SNO during the August 2006 calibration period. These are used as inputs for the relative laserball intensity distributions in RAT at the respective wavelengths shown.

5.1.1 Selection of Laser Intensity & Wavelength

Laserball data was simulated using the SNO August 2006 laserball light distribution (angular distribution and mask function) in **RAT** v.5.2.2 for all four target materials; water, LABPPO,

LABPPO+0.3%Te+bis-MSB and LABPPO+0.3%Te+perylene. Data was generated such that the average occupancy per pulse was 3%. As shown in figures 5.4 and 5.5, the required intensity to achieve this target occupancy is different across different wavelengths and materials. This is due to varying PMT efficiencies (both in angular response and quantum efficiency) and attenuation across different wavelengths. The target level of 3% occupancy is chosen such that the PMTs are in a single photoelectron regime. As described in Section 4.3, multiple photoelectrons produced in the same time window at the same PMT will only be registered under a single PMT hit. The probability of multiple photoelectrons increases as the laserball intensity increases, but in only registering single hits the effect underestimates the intensity of the laserball. Therefore, the target occupancy of the laserball runs needs to be great enough such that as many PMTs as possible register hits, but do so with only single photoelectrons. Any possible corrections are made through Equation 4.21. In practice, the ND filters are used to limit the intensity of the laser light for each wavelength scan. In **RAT**, the number of photons emitted per pulse of the laserball is adjusted. The intensity chosen for each MC wavelength scan in the target materials is shown in Table 5.1¹.

Laserball Photons Per Pulse for 3% Detector Occupancy

Wavelength [nm]	Water	LABPPO	LABPPO+0.3%Te +Bis-MSB	LABPPO+0.3%Te +Perylene
N2 : 337	8,200 γ	8,400 γ	18,050 γ	12,400 γ
PBD: 369	6,300 γ	7,400 γ	13,750 γ	10,000 γ
BBQ: 385	6,950 γ	6,400 γ	14,150 γ	9,400 γ
Bis-MSB: 420	5,750 γ	5,500 γ	20,700 γ	9,250 γ
COUMARIN: 505	9,950 γ	7,300 γ	7,600 γ	7,700 γ

TABLE 5.1: The required intensities, γ pulse $^{-1}$ in **RAT** for the simulation of a 3% occupancy run in each of the four target materials.

¹The omission of the KITON-RED dye, $\lambda_{LB} = 620$ nm was due to simulation reasons. At 620 nm the efficiencies of the PMTs are very small, and hence few hits are registered. To compensate, this would require many more photons per pulse to be computed by **RAT**, $> 10^6\gamma$ pulse $^{-1}$ which is computer exhaustive, see appendix B.1. Further, for the scintillation profiles of interest here, none emit at 620 nm.

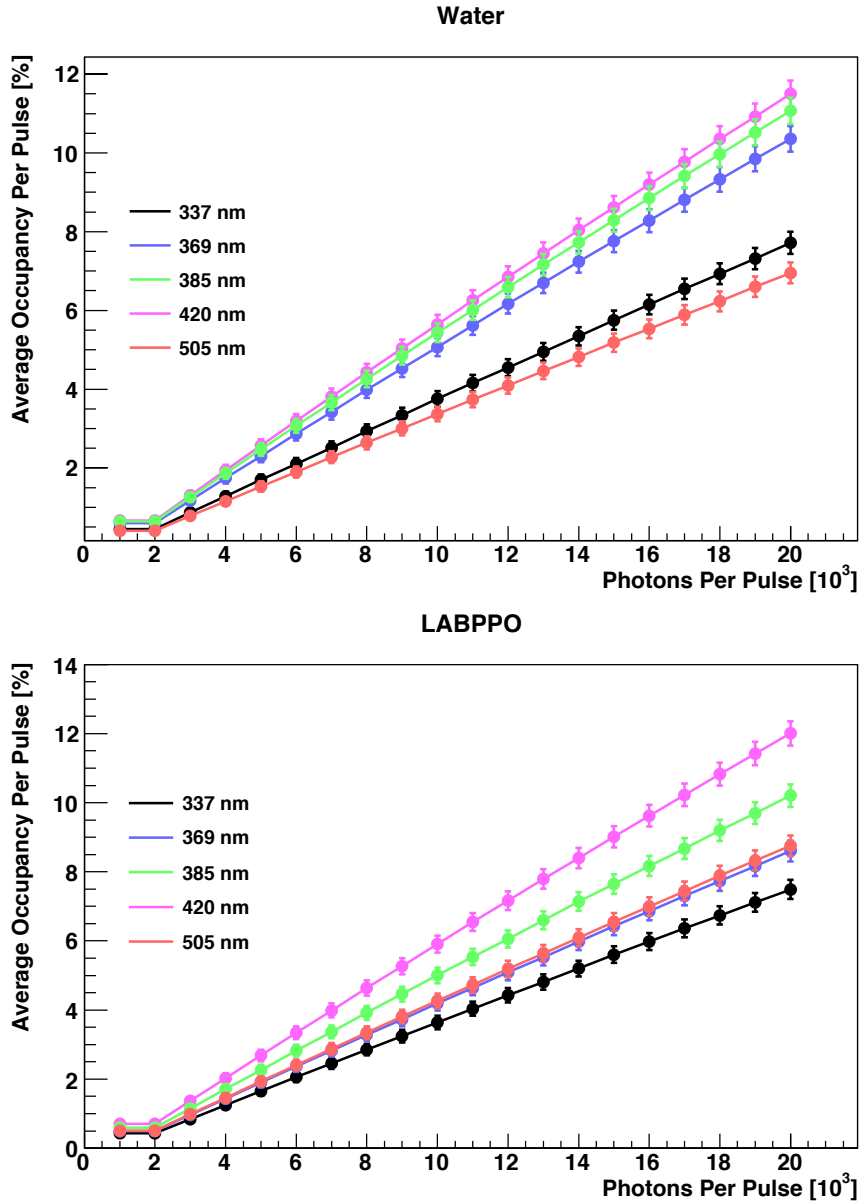


FIGURE 5.4: Values for the average occupancy (%) per pulse for the laserball at wavelengths 337, 369, 385, 420 and 505 nm in water (top) and LABPPO (bottom). Here, the average occupancy is the ratio of the mean number of hits, \bar{N}_{Hits} to the total number of PMTs, $n_{\text{PMT}} = 9728$. Errors are statistical, $\pm \sqrt{\bar{N}_{\text{Hits}}}$. Photon units are in photons $\times 10^3$ as simulated in RAT.

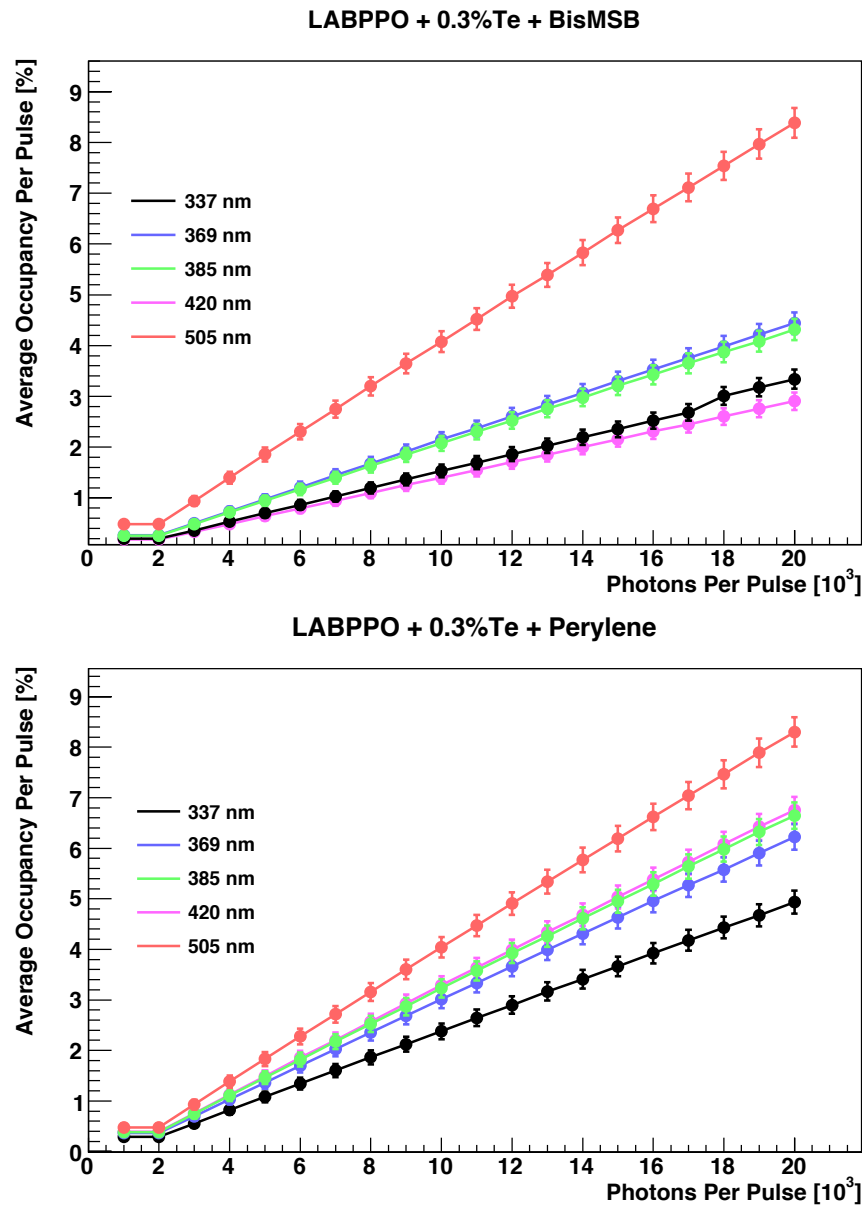


FIGURE 5.5: Values for the average occupancy per pulse for the laserball at wavelengths 337, 369, 385, 420 and 505 nm in LABPPO+0.3%Te+bis-MSB (top)/perylene (bottom). Here, the average occupancy is the ratio of the mean number of hits, \bar{N}_{Hits} to the total number of PMTs, $n_{\text{PMT}} = 9728$. Errors are statistical, $\pm \sqrt{\bar{N}_{\text{Hits}}}$. Photon units are in photons $\times 10^3$ as simulated in RAT.

5.1.1.1 Average Reemitted Wavelengths

As described in Section 3.4.4, the action of absorption and reemission by the scintillator changes the detected spectrum of wavelengths at the PMT; this spectrum being characteristic of the active wavelength shifting components in the scintillator. For example, as shown in Figure 5.6 at 337 nm, the detected wavelengths in LABPPO, LABPPO+0.3%Te+bis-MSB/perylene all vary based on the active wavelength shifting component; PPO, bis-MSB and perylene. The mean wavelength, μ_λ and width, σ_λ of the wavelengths detected at the PMTs in each of the four materials considered here is shown in Table 5.2. The values obtained in water reflect the convolution of the PMT efficiencies with the intrinsic widths of the laser-dyes. In the three scintillator mixtures they reflect the convolution of the PMT efficiencies with the respective emission spectra of the wavelength shifters².

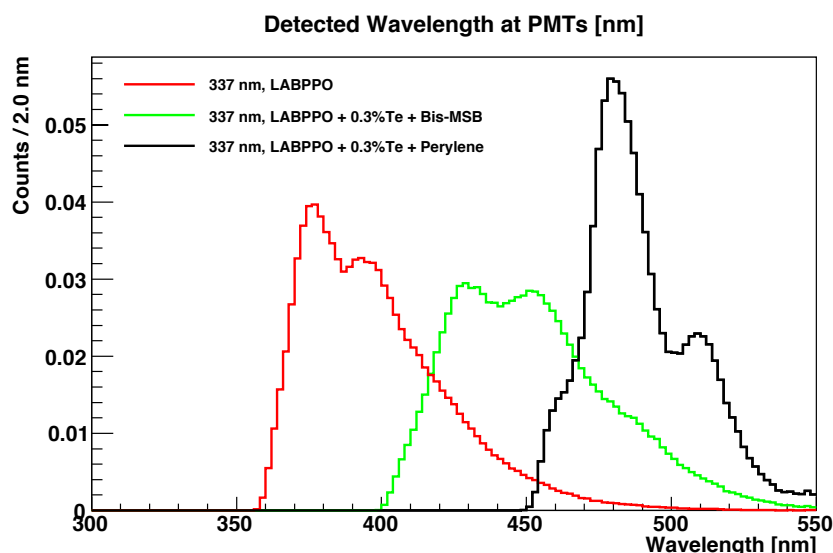


FIGURE 5.6: The reemission profile detected at PMTs for light generated at 337 nm inside one of three scintillator mixtures; LABPPO (red), LABPPO+0.3%Te+bis-MSB (green) and LABPPO+0.3%Te+perylene (black). None of the initial 337 nm light is detected because it is absorbed and reemited by the scintillator. The detected profiles therefore reflect the active wavelength shifters in each of the scintillator mixtures. The distributions do not reflect the true reemission profile of the wavelength shifters entirely as the distribution becomes convolved with the wavelength dependence of the PMT detection efficiency.

²In addition, for all materials considered some attenuative effects will also be present based on the distribution width.

Detected Wavelength Distributions at PMTs
Mean & RMS ($\mu_\lambda, \sigma_{\lambda, \text{RMS}}$) nm

Wavelength [nm]	Water	LABPPO
N2 : 337	(337.10, 0.02)	(398.75, 25.51)
PBD: 369	(369.30, 9.55)	(388.64, 22.92)
BBQ: 385	(384.60, 6.97)	(391.87, 16.98)
Bis-MSB: 420	(418.99, 6.02)	(420.75, 9.76)
COUMARIN-500: 505	(500.76, 11.80)	(501.87, 12.25)
Wavelength [nm]	LABPPO+0.3%Te +Bis-MSB	LABPPO+0.3%Te +Perylene
N2 : 337	(452.55, 27.45)	(489.67, 18.73)
PBD: 369	(453.95, 27.40)	(489.79, 18.70)
BBQ: 385	(453.70, 27.53)	(489.81, 18.71)
Bis-MSB: 420	(424.78, 14.42)	(489.76, 18.69)
COUMARIN-500: 505	(502.42, 11.90)	(503.01, 11.52)

TABLE 5.2: The respective mean and RMS values for the wavelength distribution detected across all PMTs from a central laserball run using different laser-dyes. Values are obtained from MC information in RAT and are representative of photons that led to the creation of a photoelectron at the PMT photocathode.

The selection of the five laser-dyes considered thus far was based on the intention of probing the Cherenkov light distribution in SNO. In SNO+, the scintillator reemission spectrum is instead of interest. For this reason, an additional wavelength scan in each of the scintillator mixtures is used. The wavelength chosen for each mixture is intended to coincide with the mean wavelength of the scintillation spectrum detected by the PMTs. Three commercial laser-dyes are available whose emission peak coincide in the region of these mean values [142];

- LABPPO:
 - α -NPO, $\lambda \in (391\text{-}425)$ nm, $\lambda_{\text{peak}} = 400$ nm
- LABPPO+0.3%Te+Bis-MSB:
 - COUMARIN-440, $\lambda \in (420\text{-}475)$ nm, $\lambda_{\text{peak}} = 446$ nm
- LABPPO+0.3%Te+Perylene:
 - COUMARIN-481, $\lambda \in (461\text{-}549)$ nm, $\lambda_{\text{peak}} = 490$ nm

Hence, for each scintillator mixture, an additional scan was simulated at the peak wavelength of these three dyes; 400 nm, 446 nm and 490 nm. Similarly to scans at

other wavelengths, these runs target a 3% detector occupancy with the following intensities; 5750 (400 nm), 9750 (446 nm) and 7050 (490 nm) γ pulse $^{-1}$.

5.1.2 Laserball Scan Positions

Monte-Carlo data is simulated using detector settings that are as close to those which will be enforced during the actual calibration phase. Most notably, this means generating laserball data in a series of positions that are realistically obtainable by the detector rope manipulator system, see Figure 5.7. At each wavelength in each of the four materials 39 laserball runs, each with a different position or orientation of the laserball was performed, see Table 5.3. As described in Section 4.4, given the nature of the occupancy ratio method, central runs contain quadruple the statistics of off-axis runs.

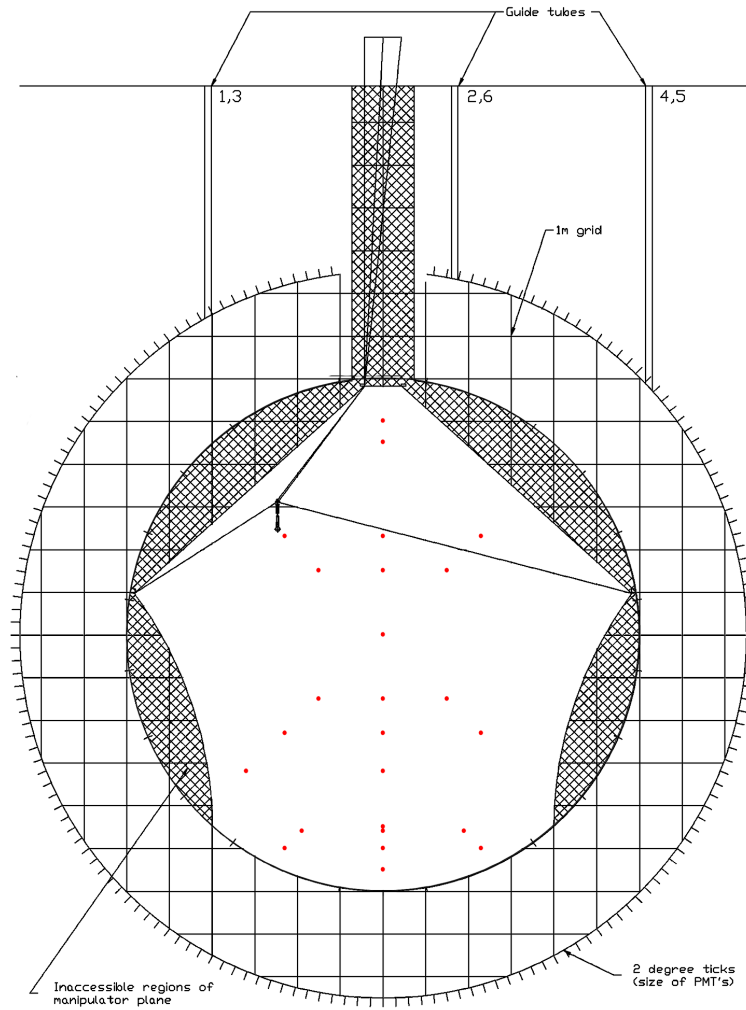


FIGURE 5.7: Laserball deployment in the inner AV region. Shown are the laserball positions in the xz -plane (the positions are the same in the yz -plane, $x \rightarrow y$). Each run position is shown as a red dot. The shaded inner AV regions denote where the rope guide system is unable to reach.

Laserball Scan Positions

Orientation (θ_{LB}, ϕ_{LB}) [rad.]	x [cm]	y [cm]	z [cm]	$ \vec{r}_{LB} $ [cm]	No. Pulses [10^3]
(0, π)	-150.0	0.0	-150.0	212.13	50
(0, π)	-150.0	0.0	150.0	212.13	50
(0, π)	-190.0	0.0	-460.0	497.70	50
(0, π)	-230.0	0.0	-230.0	325.27	50
(0, π)	-230.0	0.0	-500.0	550.36	50
(0, π)	-230.0	0.0	230.0	325.27	50
(0, π)	-320.0	0.0	-320.0	452.54	50
(0, $\pi/2$)	0.0	-150.0	-150.0	212.13	50
(0, $\pi/2$)	0.0	-150.0	150.0	212.13	50
(0, $\pi/2$)	0.0	-190.0	-460.0	497.70	50
(0, $\pi/2$)	0.0	-230.0	-230.0	325.27	50
(0, $\pi/2$)	0.0	-230.0	-500.0	550.36	50
(0, $\pi/2$)	0.0	-230.0	230.0	325.27	50
(0, $\pi/2$)	0.0	-320.0	-320.0	452.54	50
(0, π)	0.0	0.0	-230.0	230.0	50
(0, π)	0.0	0.0	-450.0	450.0	50
(0, π)	0.0	0.0	-500.0	500.0	50
(0, π)	0.0	0.0	-550.0	550.0	50
(0, 0)	0.0	0.0	0.0	0.0	200
(0, $\pi/2$)	0.0	0.0	0.0	0.0	200
(0, π)	0.0	0.0	0.0	0.0	200
(0, $-\pi/2$)	0.0	0.0	0.0	0.0	200
(0, π)	0.0	0.0	230.0	230.0	50
(0, π)	0.0	0.0	450.0	450.0	50
(0, $\pi/2$)	0.0	0.0	500.0	500.0	50
(0, $\pi/2$)	0.0	150.0	-150.0	212.13	50
(0, $\pi/2$)	0.0	150.0	150.0	212.13	50
(0, $\pi/2$)	0.0	190.0	-460.0	497.70	50
(0, $\pi/2$)	0.0	230.0	-230.0	325.27	50
(0, $\pi/2$)	0.0	230.0	-500.0	550.36	50
(0, $\pi/2$)	0.0	230.0	230.0	325.27	50
(0, $\pi/2$)	0.0	320.0	-320.0	452.54	50
(0, π)	150.0	0.0	-150.0	212.13	50
(0, π)	150.0	0.0	150.0	212.13	50
(0, π)	190.0	0.0	-460.0	497.70	50
(0, π)	230.0	0.0	-230.0	325.27	50
(0, π)	230.0	0.0	-500.0	550.36	50
(0, π)	230.0	0.0	230.0	325.27	50
(0, π)	320.0	0.0	-320.0	452.54	50

TABLE 5.3: Positions of the laserball for each wavelength scan. The orientation is defined as the azimuthal angle of the laserball, ϕ_{LB} about its local z -axis which points vertically upwards through the laserball manipulator with $\phi_{LB} = 0 \equiv$ PSUP-East and $\phi_{LB} \in (-\pi, \pi)$.

5.2 Processing

The processing chain for laserball data is handled by RAT and OCA. OCA is a suite of optical calibration (OCA) software utilities that performs a statistical fit of the optical model presented in Section 4.2 over laserball data. The OCA fit routine is comprised of two programs; `soc2oca` and `oca2fit`. The procedure begins by converting laserball run data, initially handled by RAT in the form of SNO+ Optical Calibration (SOC) files into a format used by OCA. OCA converts the SOC-run files into OCA-run files (`soc2oca`) and uses these to perform a fit (`oca2fit`) that returns the parameters of the optical model. These parameters can then be used to monitor the detector response and be reimplemented into RAT for future simulations. An additional OCA program, `rdt2soc` allows for the conversion of original SNO RDT-run laserball files into SOC-run files. This enables OCA to fit optical parameters across both SNO and SNO+ scans. The RAT and OCA processing chain is outlined in Figure 5.8.

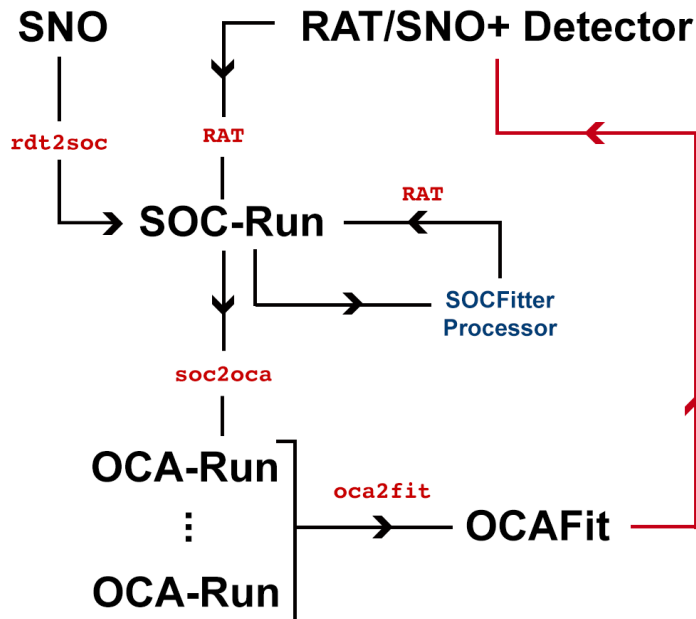


FIGURE 5.8: Flow diagram illustrating the chain of processes involved in converting SNO and SNO+ data into the required OCA-run format prior to an optical fit. Entities in black denote a data structure of stored information. Labelled in red are the names of the programs used to convert and or extract one data structure into another. The SOCFitter processor (blue) is the RAT processor used to calculate additional information required for the fit, see Section 5.2.2.

5.2.1 The SOC-run File

The SOC-run file is a ROOT structured file produced by RAT (either through MC or from the detector) that stores information about a single laserball run. The information is stored at the run level such that all the hit times for a single PMT in the run are stored as a single array and not divided event-by-event i.e. pulse-by-pulse. Each SOC-run file is structured in the form of a `RAT::DS::SOC` C++ object that contains the following daughter objects and information;

- **RAT::DS::Calib:** The configuration settings of the laser for the run:
 - The source identifier (source ID) which is either the laserball or one of the other deployed sources.
 - The laserball intensity and wavelength (dye name). For MC the intensity is the simulated number of photons per pulse. For data it is defined by the neutral density (ND) filter used to limit the intensity of the laser.
 - The position and orientation/direction of the manipulator as measured by the rope guide system. The orientation of the manipulator (and hence laserball) is given as the slot number, 0, 1, 2 or 3, that the laserball was connected to the manipulator side ropes (0: $\phi_{LB} = 0$, 1: $\phi_{LB} = \pi/2$, 2: $\phi_{LB} = \pi$, 3: $\phi_{LB} = -\pi/2$).
 - The trigger time, as determined by the detector clock (50 Mhz) of each laser pulse in a nominal 500 ns time window.
- **RAT::DS::FitResult:** The fitted vertex (position and trigger time) of the laserball.
- **RAT::DS::SOCPMT:** A collection of `SOCPMT` objects, one per PMT as featured in the run. Each `SOCPMT` object contains the following run-level information:
 - The ID of the PMT. This can be used to query the database for the PMT bucket position and orientation.
 - The time for each registered hit at the PMT within the run.
 - The value of the associated short- and long-time integration charge values for each hit; QHS and QHL.

In addition, both the **SOC** and **SOCPMT** objects each contain fields that store values calculated using a **RAT processor** (see Figure 5.9). A processor is a **RAT** function that acts on the raw run-level information (e.g. hit times) to calculate fitted information such as the laserball position on the **FitResult** object. The position is required for the light path calculation in order to produce the time residual distribution from which the prompt peak integration is performed. For laserball runs, **RAT**'s **SOCFitter** processor is used to calculate values for the following fields on the **SOC** and **SOCPMT** objects:

- **SOC**
 - Global Time Offset: The central time value of the prompt peak in the global time residual distribution across all PMTs (see Figure 4.5).
- **SOCPMT**
 - Time of Flight: The estimated time of flight for light to reach the PMT from the laserball position.
 - Prompt Peak Time: The central time value of the prompt peak in the time residual distribution of the PMT (see Section 4.2.3).
 - Prompt Peak Counts: The integrated number of counts ± 4 ns either side of the prompt peak time (see Figure 4.6).

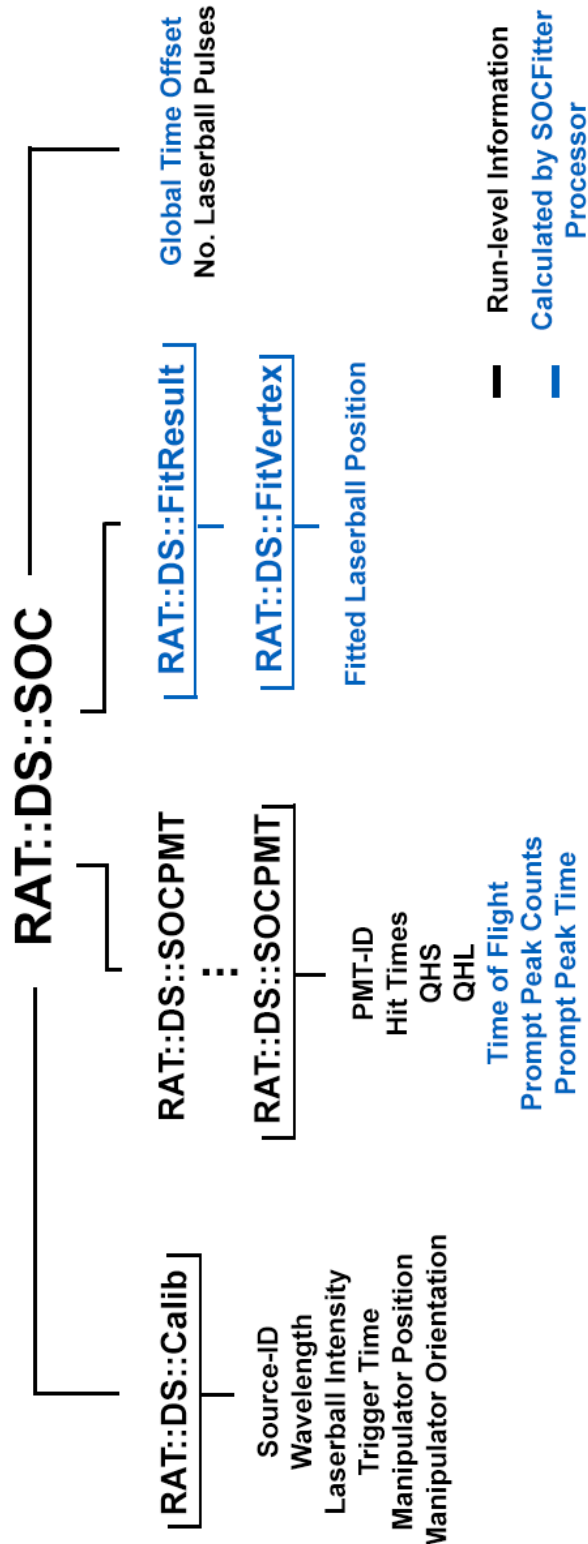


FIGURE 5.9: The `RAT::DS::SOC` object data structure. Each SOC-run file contains a `RAT::DS::SOC` object that contains a `SOCPMT` representation for every PMT featured in the run. It also contains the laser calibration settings (`Calib`), the fitted laserball position (`FitResult`) and the global time offset. These latter two are calculated using the `SOCFitter` processor in `RAT`, as are the time of flight and prompt peak counts and time for each `SOCPMT`.

5.2.2 RAT's SOCFitter Processor

The purpose of the **SOCFitter** processor is to fit for the laserball position, \vec{r}_{LB} and trigger time, t_0 using the PMT information. In practice only the coordinates of the manipulator are known, not the laserball flask itself which is held tens of centimetres below the manipulator. Similarly, the 50 MHz clock used by the detector provides insufficient time resolution to determine when in the event window the laser was triggered. The 1.7 ns resolution of the PMTs therefore provide the most precise source of available information in the detector and are used to determine the laserball position and trigger time. The **SOCFitter** performs a minimisation of the χ^2 statistic;

$$\chi_{\text{LB}}^2 = \sum_j^{N_{\text{PMTs}}} \frac{(t_j^{\text{centroid}} - t_{\text{ToF},j}(\vec{r}_{\text{LB}}) - t_0)^2}{(\sigma_{\text{RMS}}^{\text{centroid}})^2}, \quad (5.1)$$

where t_j^{centroid} is the PMT centroid time as in Equation 4.14. Here, the time of flight, $t_{\text{ToF},j}$ generates the dependency of χ^2 on the current guess of the laserball position.

In calculating the time centroid, the **SOCFitter** processor performs the prerequisite calculations of the global time offset and the individual PMT prompt peak integrations as described in Section 4.2.3. The difference between the true and fitted laserball position coordinates in all x -, y - and z -directions from MC data sets in water and the three scintillator mixtures at 505 nm are shown in figures 5.10 and 5.11. Overall, the average uncertainty in the x - and y - directions of the laserball is ~ 10 mm, but can be larger, 20-30 mm in the z -direction. In particular, the uncertainty in the laserball z -direction increases slightly as the laserball position radius approaches the AV radius at 6 m. The uncertainties in the laserball position introduce systematics into the optical model that are discussed as part of the results in Section 6.2.6 for water and Section 7.1.5 for scintillator. In addition, it is important to note that the trigger time, t_0 is essentially the global time offset calculated using the fitted laserball position. It will be shown in Section 7.2 that in scintillator this value contains information about absorption and reemission, and therefore doesn't reflect the *true* trigger time.

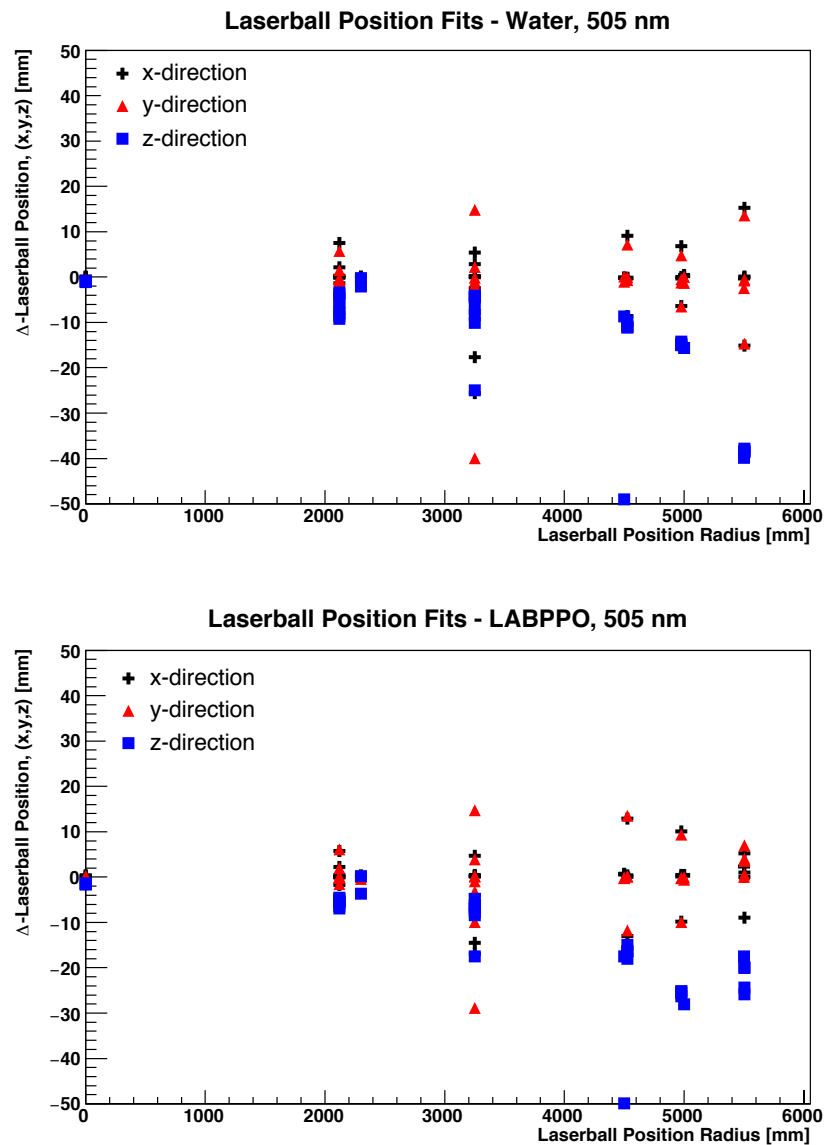


FIGURE 5.10: Shown are the uncertainties in each of the x -, y - and z -directions of the fitted laserball position with respect to the true known position in MC in water (top) and LABPPO (bottom) at 505 nm.

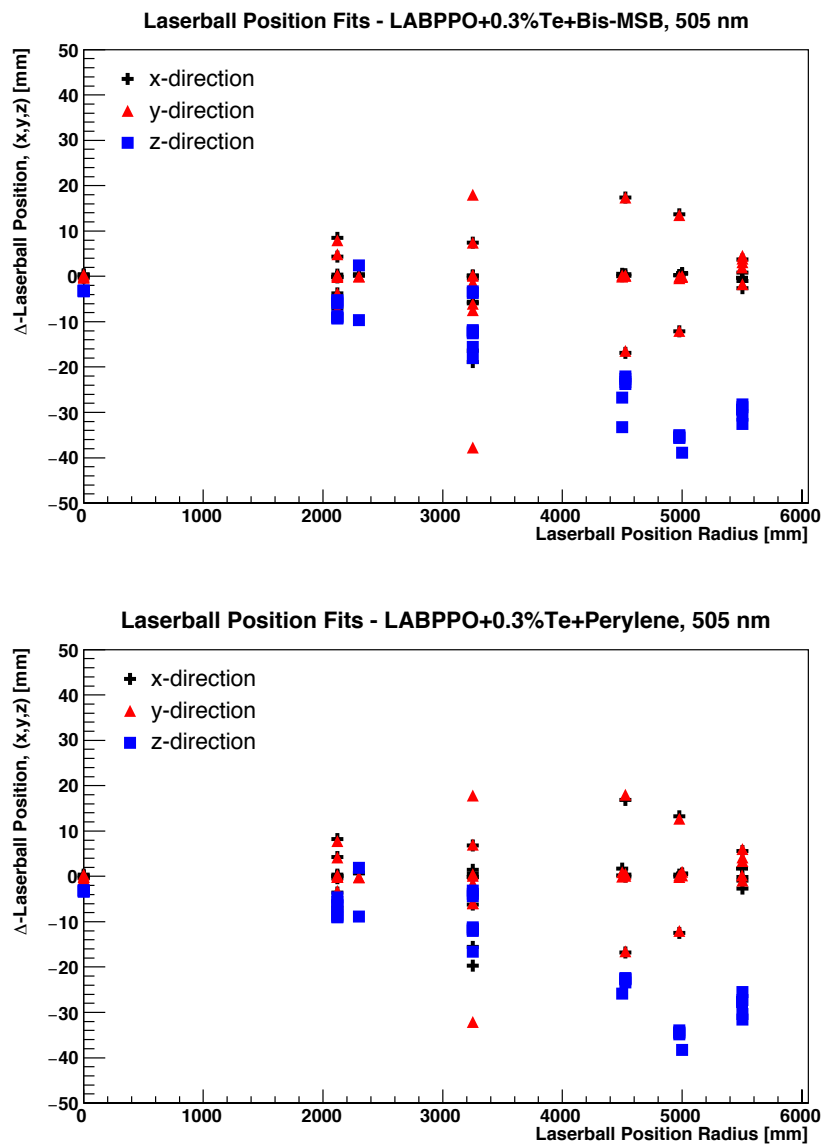


FIGURE 5.11: Shown are the uncertainties in each of the x -, y - and z -directions of the fitted laserball position with respect to the true known position in MC in LABPPO+0.3%Te+bis-MSB (top) and LABPPO+0.3%Te+perylene (bottom) at 505 nm.

5.2.3 OCA Processors

The SOC-run file is the standardised file format for an optical calibration run in SNO+, be it with the laserball or any other deployed source. The OCA-run file is a bespoke structure for the optical model as presented in Chapter 4 using laserball data. It therefore requires further information such as the light path information

and the values of the solid angle and Fresnel transmission coefficients. In addition, given that the model uses the occupancy ratio, information from both the off-axis and central runs need to be brought together such that they can be stored in a single file. The conversion of off-axis and central SOC-run files into an OCA-run file is performed by the `soc2oca` program. Once all the necessary OCA-run files have been created for a particular laserball scan, the optical fit is performed by `oca2fit`.

5.2.3.1 `soc2oca`

An OCA-run file representation of a laserball run at a wavelength λ_{LB} is stored in an `OCA::OCARun` object created by the `soc2oca` utility as follows;

$$\left. \begin{array}{l} \text{SOC [off-axis, } \lambda_{LB}] \\ \text{SOC [central, } \lambda_{LB}] \\ \text{SOC [off-axis, } \lambda_{LB} = 505 \text{ nm]} \end{array} \right\} \xrightarrow{\text{soc2oca}} \text{OCA [off-axis, } \lambda_{LB}]. \quad (5.2)$$

The off-axis and central run files at λ_{LB} are used to calculate the occupancy ratio and the necessary model parameters which at this stage can be done analytically. Similarly to the SOC-run files, the relevant off-axis and central information for each PMT on an OCA-run file is held within an `OCA::OCAPMT` object stored in the `OCARun` object. An `OCAPMT` object stores the observed occupancy ratio and the following model parameters from both off-axis and central runs; solid angle, Fresnel transmission coefficient, distances through the detector, incident angle at the PMT bucket and the initial path direction. The data structure of the `OCARun` and `OCAPMT` objects is shown in Figure 5.12. In the case where the required OCA-run file is that of a central run, a central run using a different laserball orientation (ϕ_{LB}) is used e.g.

$$\left. \begin{array}{l} \text{SOC [central, } \phi_{LB} = 0, \lambda_{LB}] \\ \text{SOC [central, } \phi_{LB} = \pi/2, \lambda_{LB}] \\ \text{SOC [central, } \phi_{LB} = 0, \lambda_{LB} = 505 \text{ nm}] \end{array} \right\} \xrightarrow{\text{soc2oca}} \text{OCA [central, } \phi_{LB} = 0, \lambda_{LB}], \quad (5.3)$$

these types of OCA-run files are important for determining the angular anisotropy of the laserball as discussed in Section 4.2.5.

Of note in this process is the inclusion of the third file featured as an input; the equivalent run at $\lambda_{LB} = 505$ nm. As will be presented in Chapter 6, at 505 nm the acrylic of the AV is optically transparent and the light is subject to less attenuation. In practice, laserball runs are performed across all wavelengths at a given position before moving the laserball to the next. Given this, the fitted position of the laserball at $\lambda_{LB} = 505$ nm is used as the best estimate of the location from which light path calculations are made in order to calculate the necessary values to be stored on the OCA-run file.

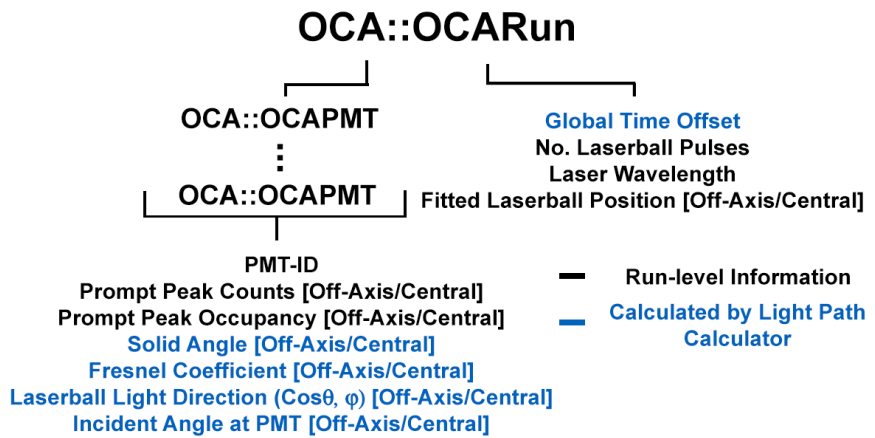


FIGURE 5.12: The `OCA::OCARun` object data structure. Each OCA-run file contains an `OCA::OCARun` object which contains an `OCAPMT` representation for each PMT featuring in the run. Each `OCAPMT` contains an occupancy value from both the off-axis and central runs. Contained also are the model values from both runs used to calculate the predicted occupancy ratio. These model values are calculated by the light path calculator in `RAT` which calculates light paths from the laserball to all PMT positions as discussed in Section 4.2.1.1.

5.2.3.2 oca2fit

Once all the necessary OCA-run files for a laserball scan have been created, they are used as inputs to the `oca2fit` routine;

$$\left. \begin{array}{l} \text{OCA [off-axis, } \lambda_{\text{LB}}] \\ \vdots \\ \text{OCA [central, } \lambda_{\text{LB}}] \\ \vdots \end{array} \right\}_{N_{\text{runs}}} \xrightarrow{\text{oca2fit}} \alpha_k, R(\theta_\gamma), L(\cos \theta_{\text{LB}}, \phi_{\text{LB}}), \quad (5.4)$$

where the output is the set of optical model parameters determined by a statistical fit over χ^2 as in Equation 4.28. Namely, these parameters are the attenuation coefficients, α_k , the PMT angular response, $R(\theta_\gamma)$ and the laserball light distribution, $L(\cos \theta_{LB}, \phi_{LB})$.

The optical fit performed by `oca2fit` is a reimplementation of the `Fitmrq` numerical routine originally featuring in [143], and as previously implemented in `LOCAS`; the software used in SNO to perform a fit of the optical model to laserball data. The routine makes use of the LM algorithm in order to minimise the non-linear least squares problem posed by the optical model.

5.2.3.3 `rdt2soc`

An additional routine, `rdt2soc` provides backwards compatibility with SNO laserball data. The original processing chain of laserball data in SNO involved several file formats (see [133]), one of which was a *root delta time* (RDT) file, one RDT file per laserball run. One disadvantage is that the RDT files are summary files; the full PMT hit information is no longer present. However, it was verified that the prompt hit and time information pre-existing on the files was calculated using the same methods as discussed in this work. Given this, `rdt2soc` converts the RDT file to a SOC-run file, but does not subject it to the calculations performed by the `SOCFitter` processor.

Using original SNO data also requires the PMT channel hardware status flags for each of the laserball runs. These were made available in the form of DQXX files which are the SNO equivalent to the channel hardware status (CHS) files used in SNO+.

5.3 Summary of Data Production

The SNO+ MC software, `RAT` provides the opportunity to produce an MC laserball data set that aims to resemble - as best possible - the expected data collected during laserball deployment in the SNO+ water, scintillator and tellurium phases. Combined with `OCA`, the model of the detector optical response can be fitted to either this MC data or original SNO data in order to quantify the optical properties of the detector. Fitting to MC data allows for tuning of the software and the

optical model. Comparisons with original SNO data provides insight into optical effects which are not accounted for by RAT, but that can be expected in future calibrations with the laserball in SNO+. A discussion of the results obtained from a fit of the optical model to both SNO+ MC and original SNO data using OCA is now presented over the next two chapters; first in water using a combination of SNO+ MC and SNO data and then in scintillator using SNO+ MC data only.

6

Optical Fit in Water

*Water, water, every where,
And all the boards did shrink;
Water, water, every where,
Nor any drop to drink.*

The Rime of the Ancient Mariner, Samuel Taylor Coleridge

The first phase of SNO+ will be a water phase, where water (H_2O) will occupy both the inner and outer AV regions of the detector. Prior to this it is useful to compare MC predictions of the expected detector optical response with an example of the true response. As SNO+ has yet to collect data, this is done by comparing SNO+ MC data with SNO data. Presented here are the results from two sets of laserball scans; one produced in RAT using the SNO+ MC geometry for the water phase, and another from SNO in October 2003 where heavy water (D_2O) occupied the inner AV region:

- **SNO laserball scans, data in D_2O , October 2003**
 - Laser wavelengths [nm]: 337, 369, 385, 420, 505, 620.
- **SNO+ laserball scans, MC Data in H_2O**
 - Laser wavelengths [nm]: 337, 369, 385, 420, 505.

A comparison between MC and real data are of interest for two reasons:

- **Verification of new OCA software:** Values of the heavy water and water attenuation coefficients in RAT were obtained from SNO data using the original optical fit software, LOCAS. These values therefore characterise any subsequent MC data RAT produces. By using OCA to re-perform the optical fit of the attenuation coefficients from original SNO data, the values obtained through OCA can be verified against the MC-inputs in RAT.
- **Comparison between data and MC-data of the PMT response:** Previous studies of the PMT angular response from SNO suggest several discrepancies in the PMT efficiencies that are unaccounted for in RAT. These irregularities primarily concern the progressive degradation of the PMT reflectors as well as the non-uniformity of the PMT efficiencies. This will be discussed in Section 6.2.2.

6.1 Data Selection

For a single wavelength, a typical laserball scan consists of 39 runs each with around 9000 calibrated normal-type PMTs. Each PMT from each run is a candidate data point for the optical fit. This means approximately 351,000 data points enter the fit at the *top-level*, the stage prior to minimisation of the model over the data. The three selection criteria as discussed in Section 4.4 are applied sequentially to the data set to remove PMTs from runs which may be uncalibrated, subject to a low number of prompt counts or shadowed by detector geometry.

For a nominal laserball run, the total PMT shadowing in the SNO+ detector fluctuates between 30-40% with the main contribution being from the AV hold-down rope net which shadows 18-22% of the PMTs. The AV hold-down net was not present in SNO and therefore the total PMT shadowing is less for the heavy water data set, 15-20%. A combination of the prompt count cut and the PMT shadowing removes at least 35-40% of the calibrated PMTs from each run. The total number of PMTs removed is largest for laserball runs in the near AV region, $r_{LB} \simeq 5500.0$ mm where as many as $\sim 67\%$ of the PMTs are removed. The percentage per run is large, and therefore motivates the need for laserball runs in as many different locations inside the detector as possible. The main constraint in this selection process is the removal of PMTs based on their central run status. PMTs removed based on insufficient statistics from the central run, or shadowing

from the central position will effectively remove their PMT off-axis counterparts from being included in the fit. A breakdown of the number of PMTs removed per cut is shown in Table 6.1 for two example runs from each of the data and MC data sets.

Sequential Data Selection Cuts

Central Run-34707, SNO Oct'03, D₂O, 420 nm, $r_{LB} = 13.24$ mm

Selection Cut	No. PMTs Pass : Fail	PMTs Removed (%)
1) $N_{\text{prompt}}^{\text{off-axis}} > 1000$	8013 : 764	8.70%
2) $N_{\text{prompt}}^{\text{central}} > 4000$	6461 : 1552	17.68%
3) Central PMT Shadowing	5470 : 991	11.29%
4) Off-Axis PMT Shadowing	5451 : 19	0.22%
Total PMTs: 8777	5451 : 3326	37.89%

Off-Axis Run-34875, SNO Oct'03, D₂O, 420 nm, $r_{LB} = 5568.18$ mm

Selection Cut	No. PMTs Pass : Fail	PMTs Removed (%)
1) $N_{\text{prompt}}^{\text{off-axis}} > 1000$	3402 : 5375	61.24%
2) $N_{\text{prompt}}^{\text{central}} > 4000$	3361 : 41	0.47%
3) Central PMT Shadowing	3008 : 338	3.85%
4) Off-Axis PMT Shadowing	2790 : 218	2.48%
Total PMTs: 8777	2790 : 5972	68.04%

Central Run-2420038, SNO+ MC, H₂O, 420 nm, $r_{LB} = 1.17$ mm

Selection Cut	No. PMTs Pass : Fail	PMTs Removed (%)
1) $N_{\text{prompt}}^{\text{off-axis}} > 1000$	8976 : 266	2.88%
2) $N_{\text{prompt}}^{\text{central}} > 4000$	8458 : 518	5.60%
3) Central PMT Shadowing	5434 : 3024	32.72%
4) Off-Axis PMT Shadowing	5433 : 1	0.01%
Total PMTs: 9242	5433 : 3809	41.13%

Off-Axis Run-2420032, SNO+ MC, H₂O, 420 nm, $r_{LB} = 5544.35$ mm

Selection Cut	No. PMTs Pass : Fail	PMTs Removed (%)
1) $N_{\text{prompt}}^{\text{off-axis}} > 1000$	5661 : 3581	38.75%
2) $N_{\text{prompt}}^{\text{central}} > 4000$	5620 : 41	0.44%
3) Central PMT Shadowing	3915 : 1705	18.45%
4) Off-Axis PMT Shadowing	3117 : 798	8.63%
Total PMTs: 9242	3117 : 6125	66.27%

TABLE 6.1: Example of the sequential data selection cuts made across all normal type PMTs for two given laserball runs in the central and near AV regions in D₂O (SNO) and H₂O (SNO+ MC). Cuts are applied at the top-level and sequentially (1)-(4) prior to the minimisation of the optical model over the data. Here *sequentially* denotes that the sum of the pass-to-fail ratio for cuts (2)-(4) is equal to the number of PMTs which passed the preceding cut. The number of PMTs removed for a given cut is shown as a percentage.

6.1.1 Chi-Square Cuts

Using the definition of the data point pull as in Equation 4.37, the individual pull distributions for each wavelength scan was studied. Figure 6.2 shows two examples of these pull distributions for the 505 nm scan from the SNO and SNO+ MC data sets. The widths, σ_λ for all wavelengths in each of the data sets are shown in Figure 6.1. From this, the method described in Section 4.4.2 was applied, using the rounded average value, $\lceil(2 \times \langle \sigma_\lambda \rangle)^2\rceil$ as an estimator of the final upper χ^2 limit for each data set:

$$\langle \sigma_\lambda^{\text{MC}} \rangle = 1.32 \Rightarrow \chi_{\text{lim,f}}^{2,\text{MC}} = \lceil(2 \times 1.32)^2\rceil = 7, \quad (6.1)$$

$$\langle \sigma_\lambda^{\text{Data}} \rangle = 1.53 \Rightarrow \chi_{\text{lim,f}}^{2,\text{Data}} = \lceil(2 \times 1.53)^2\rceil = 9. \quad (6.2)$$

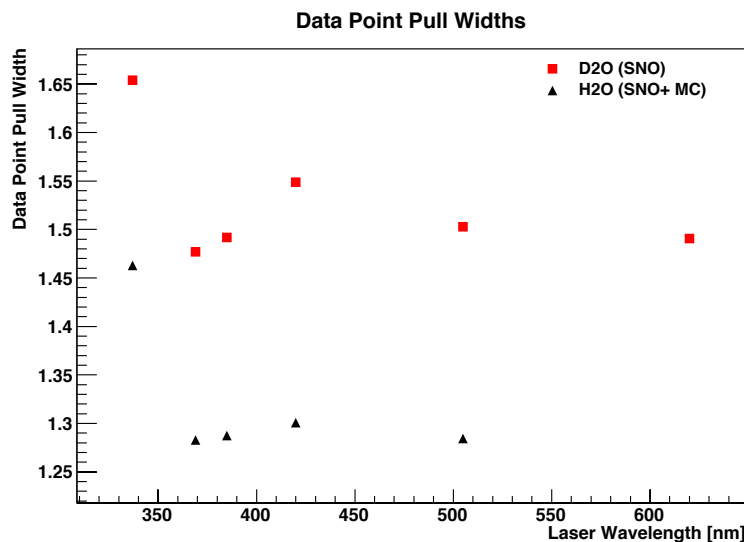


FIGURE 6.1: The fitted values of the Gaussian width, σ_λ for each of the data point pull distributions from each laserball scan in the SNO (red) and SNO+ MC (black) data sets.

Although the two are not directly comparable, the pull widths of the SNO scans are larger in comparison to the SNO+ MC data set. This is likely to be reflective of a discrepancy between the modelling of the PMT efficiencies in RAT and the actual PMTs themselves; the PMT variability. This is discussed in Section 6.2.2.

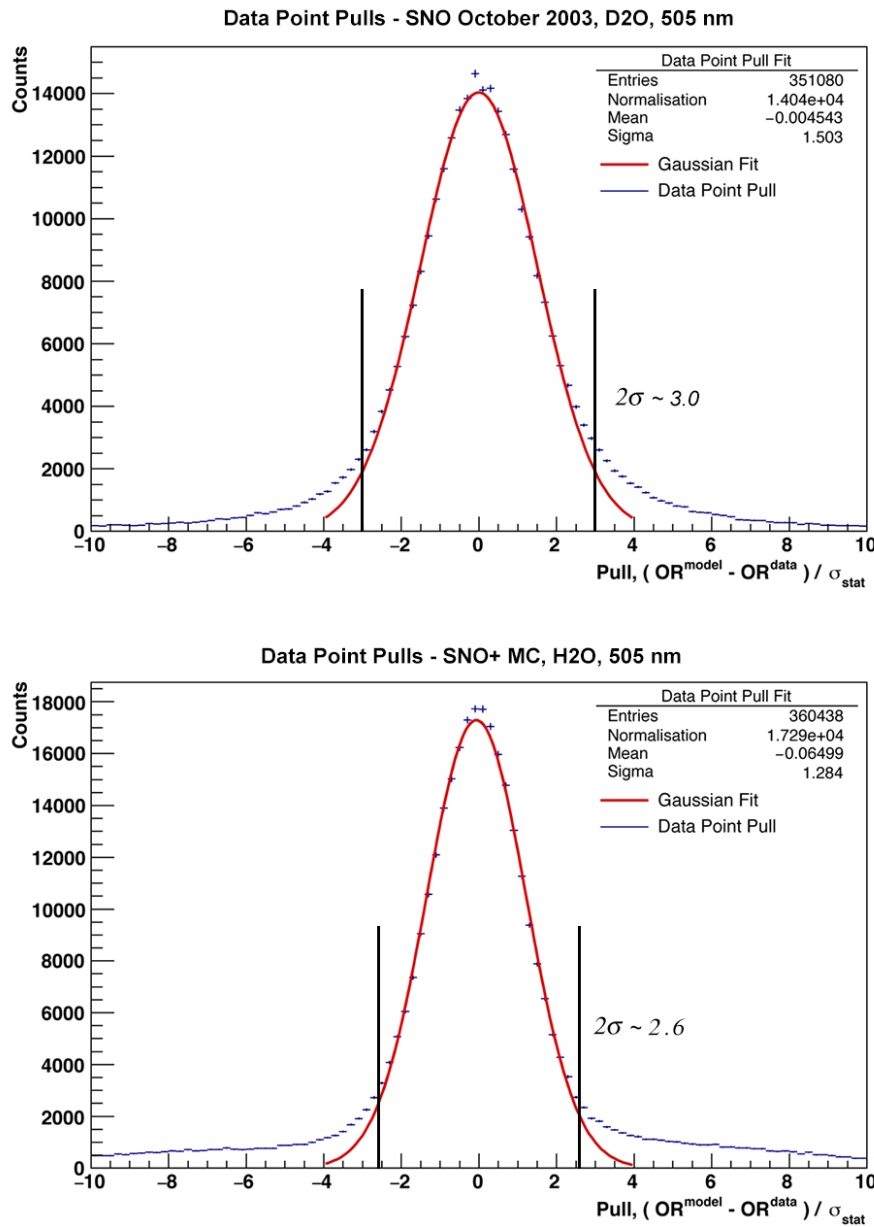


FIGURE 6.2: The data point pull distributions for a SNO (top) and SNO+ MC (bottom) laserball scan at 505 nm. In both cases the pull values are normally distributed about zero in the ranges $(-3.0, 3.0)$ for the SNO scan and $(-2.6, 2.6)$ for the SNO+ MC scan. These ranges are equivalent to a distance of $\sim 2\sigma$ either side of the origin based on the sigma value of the associated Gaussian fit (red) in the respective range. Beyond these ranges the distribution becomes non-Gaussian as shown.

It is clear that the size of the data sample, and hence the final result of the fit is informed by the choice of the final upper χ^2 limit. Although the choice of this final limit has been reasoned in the above, it is important to test the sensitivity of the final fit result to different final limits. This can therefore be considered a systematic for which a treatment is presented in Section 6.2.6.

6.2 Optical Fit Results: Data & Monte-Carlo

The water phase of SNO+ provides a unique opportunity to improve the measurements of two of the optical parameters:

- **Improved sensitivity to the water attenuation coefficient, $\alpha_{\text{H}_2\text{O}}$:**

Due to the nature of the detector geometry, the distance travelled by light in the outer water region between the AV and the PMTs is restricted to an approximate range of (2.2, 4.0) m. This range is small in comparison to the range of distances that light can travel inside the AV (0.5, 11.5) m; the only limitation being the placement of the laserball in the near AV region, $r_{\text{LB}} \geq 5.5$ m. Consequently, values of the inner AV attenuation coefficient are known to a better degree of statistical certainty, and are more robust against systematic variations given that path lengths in this region are sampled over a broader range. For a water filled detector, both the inner and outer AV regions may be treated as the same material. By considering the maximum and minimum path lengths, the sampled range is broadened to (2.7, 12.0) m, over which to fit for a combined water attenuation coefficient, $\alpha_{\text{H}_2\text{O}}^{\text{comb}}$, with improved sensitivity. The original SNO experiment did not have a water phase; the SNO+ water phase will be the first opportunity to fit for such a combined attenuation coefficient over the inner and outer AV regions.

- **In-situ measurement of the acrylic attenuation coefficient, α_{AV} :**

Light emitted inside the AV will only travel a small distance, between a range of (55.0, 98.0) mm through the 55.0 mm thick acrylic vessel. For a nominal light path from the centre of the detector, this distance accounts for <1% of the total path length. Furthermore, the distance of light through the acrylic and outer AV water regions are strongly correlated as shown in Figure 6.3. This correlation is present in all scenarios where the inner

and outer AV materials are different e.g. D₂O (SNO), LABPPO (SNO+), LABPPO+0.3%Te+bis-MSB/perylene (SNO+). This makes an in-situ measurement of the acrylic attenuation coefficient, α_{AV} difficult. As a result, previous studies during SNO would typically fix this parameter in the fit to an ex-situ lab measurement. As shown in Figure 6.3, for a water phase scenario, by combining the path lengths in the inner and outer AV water regions as described above, the direct correlation between the distances in acrylic and water may be broken. In doing this, the acrylic attenuation coefficient becomes parametrically unconstrained, making an in-situ measurement more feasible.

To summarise, the SNO heavy water data was used to fit for the D₂O and H₂O attenuation coefficients, α_{D_2O} and α_{H_2O} with the acrylic attenuation coefficient fixed to ex-situ measurements. The SNO+ MC water data was used to fit for a combined H₂O attenuation coefficient, $\alpha_{H_2O}^{comb.}$ and the acrylic attenuation coefficient, α_{AV} . In both instances all other parameters in the model were allowed to vary; the laserball light distribution, the PMT angular response and the laserball intensity normalisation (in the form of the occupancy normalisation as in Equation 4.27).

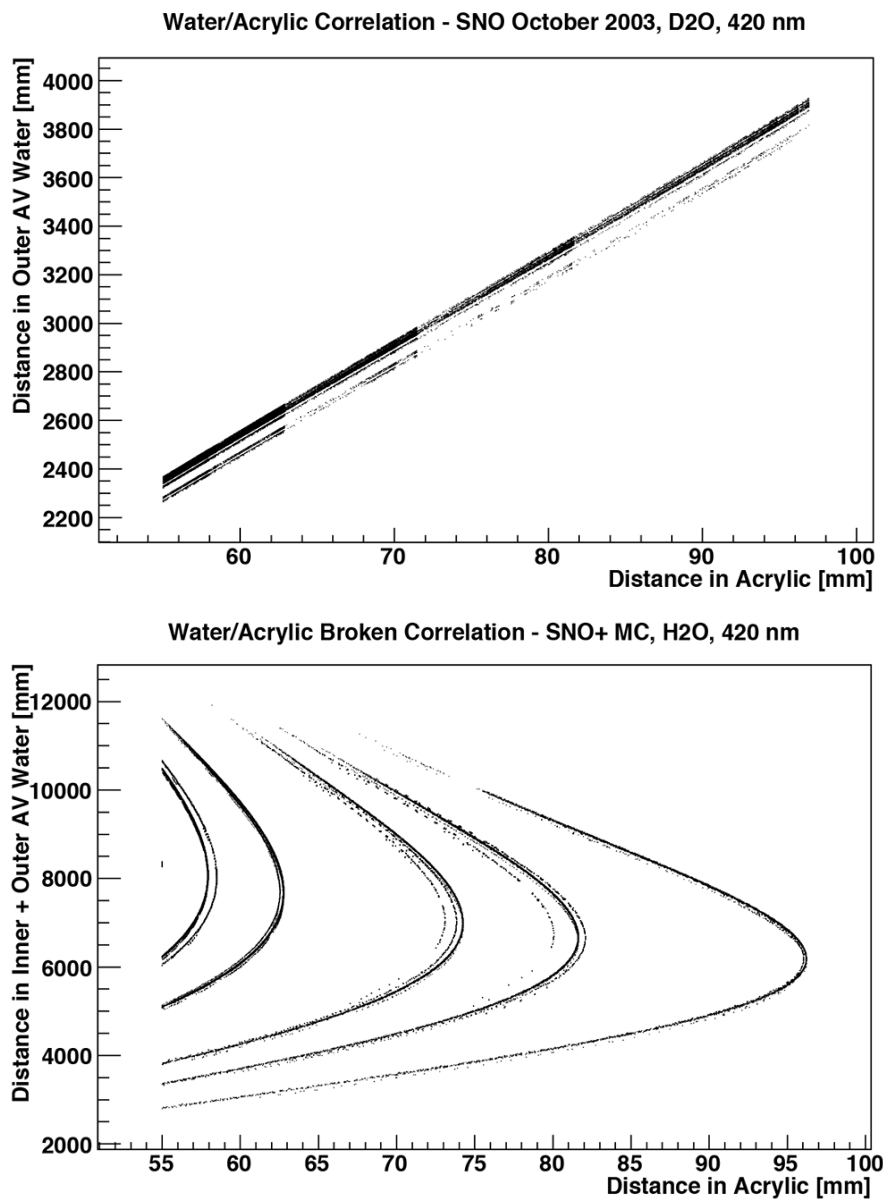


FIGURE 6.3: Top: The correlation between the distance through the acrylic and outer AV water regions in SNO at 420 nm. The banding of the distribution is due to PMTs housed in the PSUP at different radii from the centre of the detector. Bottom: The relation between the distance through the acrylic and the combined distance through the inner and outer AV water regions for the SNO+ water phase. The direct correlation is broken. The individual curves remain locally banded as above; the global separation in the curves is due to different laserball positions at different radii, $r_{LB} \in (0, 5500.0)$ mm.

6.2.1 Attenuation Coefficients

Fitted values of the attenuation coefficients for the SNO and SNO+ MC data sets alongside their associated reduced χ^2 value are shown in Table 6.2. Both the statistical and systematic errors are shown. The statistical error is extracted from the parameter covariance matrix, and the systematic error represents the combined uncertainty due to a variety of systematic contributions that are discussed in Section 6.2.6. These systematic uncertainties contribute most to the uncertainty on each attenuation coefficient, in particular for the outer water, $\alpha_{\text{H}_2\text{O}}$ and acrylic, α_{AV} regions. Given the sufficient size of the data samples in each scan, $\gtrsim 100,000$ data points, the statistical uncertainty is generally small in the inner AV region 0.23-2.7%. The statistical uncertainty associated with the acrylic and outer water regions can be larger, ranging from 0.6-10.7% and 0.73-14% respectively based on the wavelength. As discussed previously, this is reflective of the narrow range of paths lengths over which these materials are sampled.

SNO October 2003, $\alpha \pm \text{stat.} \pm \text{sys.}$

λ [nm]	$\alpha_{\text{D}_2\text{O}}$ [10^{-5} mm $^{-1}$]	$\alpha_{\text{H}_2\text{O}}$ [10^{-5} mm $^{-1}$]	$\chi^2/\text{d.o.f.}$ [2 d.p.]
337	$1.44 \pm 0.01 \pm 0.01$	$3.89 \pm 0.26 \pm 2.60$	$157259 / 129600 = 1.21$
369	$0.93 \pm 0.01 \pm 0.12$	$2.78 \pm 0.25 \pm 1.49$	$116568 / 117717 = 0.99$
385	$0.80 \pm 0.01 \pm 0.12$	$3.90 \pm 0.23 \pm 1.88$	$115150 / 117197 = 0.98$
420	$0.59 \pm 0.01 \pm 0.14$	$1.77 \pm 0.22 \pm 2.15$	$101370 / 98689 = 1.03$
505	$0.31 \pm 0.01 \pm 0.09$	$4.87 \pm 0.17 \pm 1.92$	$170710 / 165044 = 1.03$
620	$0.37 \pm 0.01 \pm 0.06$	$32.68 \pm 0.24 \pm 1.57$	$147591 / 148257 = 0.99$

SNO+ MC, $\alpha \pm \text{stat.} \pm \text{sys.}$

λ [nm]	$\alpha_{\text{H}_2\text{O}}^{\text{comb.}}$ [10^{-5} mm $^{-1}$]	α_{AV} [10^{-3} mm $^{-1}$]	$\chi^2/\text{d.o.f}$ [2 d.p.]
337	$2.70 \pm 0.01 \pm 0.21$	$4.81 \pm 0.03 \pm 0.49$	$128303 / 128040 = 1.00$
369	$2.05 \pm 0.01 \pm 0.21$	$1.39 \pm 0.04 \pm 0.41$	$118928 / 118929 = 1.00$
385	$1.88 \pm 0.01 \pm 0.21$	$0.64 \pm 0.03 \pm 0.41$	$126743 / 126378 = 1.00$
420	$2.05 \pm 0.01 \pm 0.22$	$0.29 \pm 0.04 \pm 0.41$	$122996 / 121078 = 1.02$
505	$4.30 \pm 0.01 \pm 0.22$	$0.28 \pm 0.03 \pm 0.39$	$129906 / 128132 = 1.01$

TABLE 6.2: Top: Attenuation coefficients of the inner AV D₂O and outer AV H₂O regions from the SNO data set. Bottom: The combined inner and outer AV water regions and the acrylic of the AV from the SNO+ MC water phase data set.

SNO October 2003 - D₂O & H₂O

Values of α_{D_2O} and α_{H_2O} are shown in Figure 6.4. The fitted D₂O attenuation coefficients are consistent with those obtained in SNO, and which are present in RAT. Also shown are the ex-situ attenuation coefficients measured by Boivin et al. using a long-path-length transmittance method [144]. These measurements were made in 1986 following the initial proposal of the SNO experiment. The fitted D₂O attenuation coefficients from the October 2003 laserball scans are found to be smaller than those obtained by Boivin et al.; this has similarly been observed in previous studies of SNO laserball data [133]. This discrepancy is likely due to a limitation of the Boivin et al. technique which used a relatively short 50.3 cm water-cell, and improvements in the purification techniques of heavy water between 1986 and the start date of SNO in 2000. Variations in the D₂O attenuation coefficient across all three phases of the SNO experiment have also been previously noted, observing a drift in α_{D_2O} between optical calibration runs that took place between September 2000 and August 2006 [134].

Values of α_{H_2O} obtained for the outer water region are also consistent with original measurements made in SNO (and included in RAT). Again, measurements of the attenuation coefficients by Boivin et al. are shown for consistency. Included also are measurements by Pope et al. [145] of the water absorption coefficient between 348-700 nm. The values of α_{H_2O} are consistent and within systematic uncertainty of those reported by Boivin et al. in the 310-440 nm region. Beyond this, in the $\lambda \geq 500$ nm region, the fitted values agree very well with the previous SNO result, whereas the lab measurements by Boivin et al. coincide with the absorption spectrum in the 540-580 nm region. This particular measurement illustrates the importance of an in-situ characterisation of the attenuation coefficients. Despite a relative consistency within the two types of in-situ and ex-situ data, the types themselves exhibit non-negligible variations in different regions of the wavelength spectrum.

The obtained values of α_{D_2O} and α_{H_2O} occupy a minimum in a smooth parameter space. A scan of the reduced χ^2 for the surrounding parameter space in the physical regions of this minimum are shown for the 385 and 505 nm scan in Figure 6.5 and suggests that the minimum identified by the OCA fit is both global and unique.

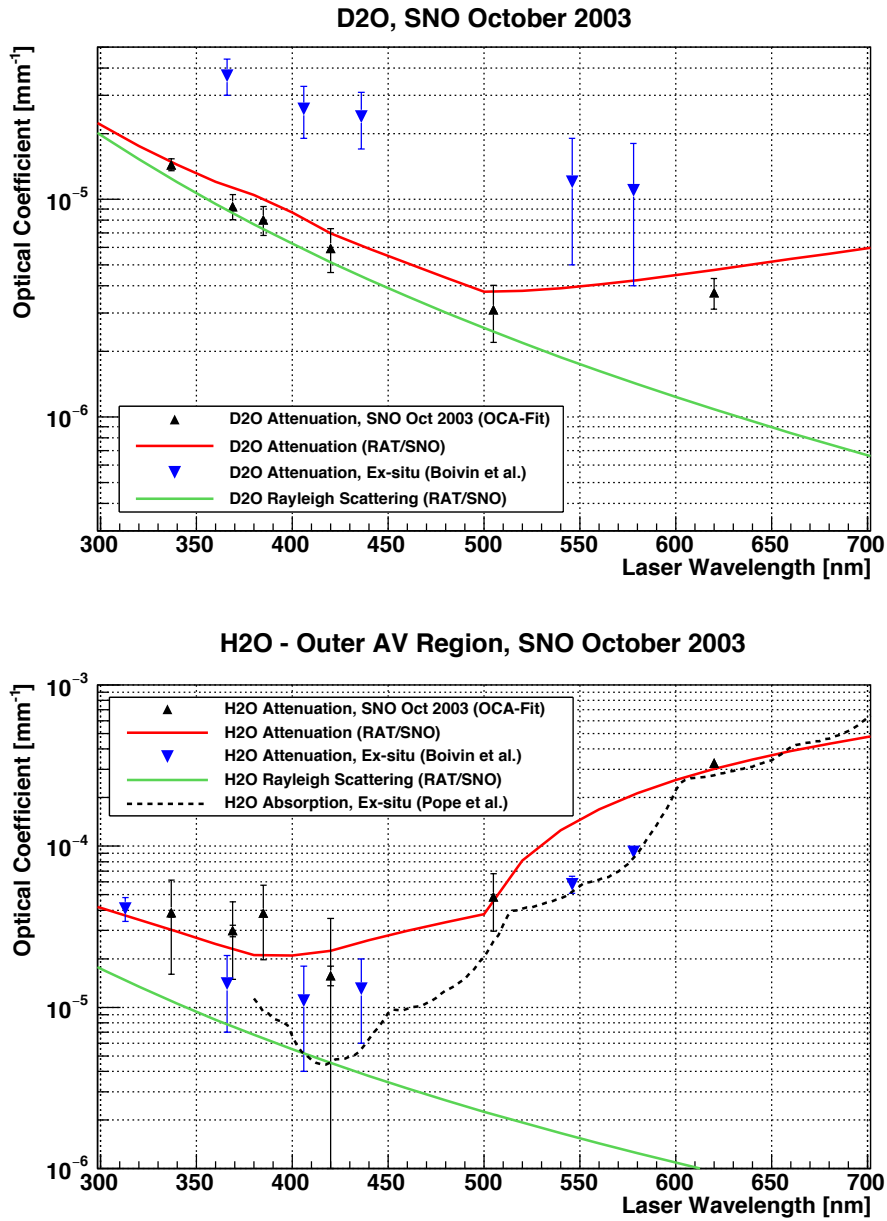


FIGURE 6.4: The fitted attenuation coefficients for D₂O (top) and H₂O in the outer AV region (bottom) obtained from the SNO October 2003 data set. Errors shown are both statistical and systematic. Shown in each respective plot are the attenuation coefficients obtained by Boivin et al. [144] (blue) and the current RAT Rayleigh scattering (green) and attenuation coefficients (red) which are based on measurements from SNO. Shown also on the bottom plot is the water absorption spectrum (dashed line) as measured by Pope et al. [145].

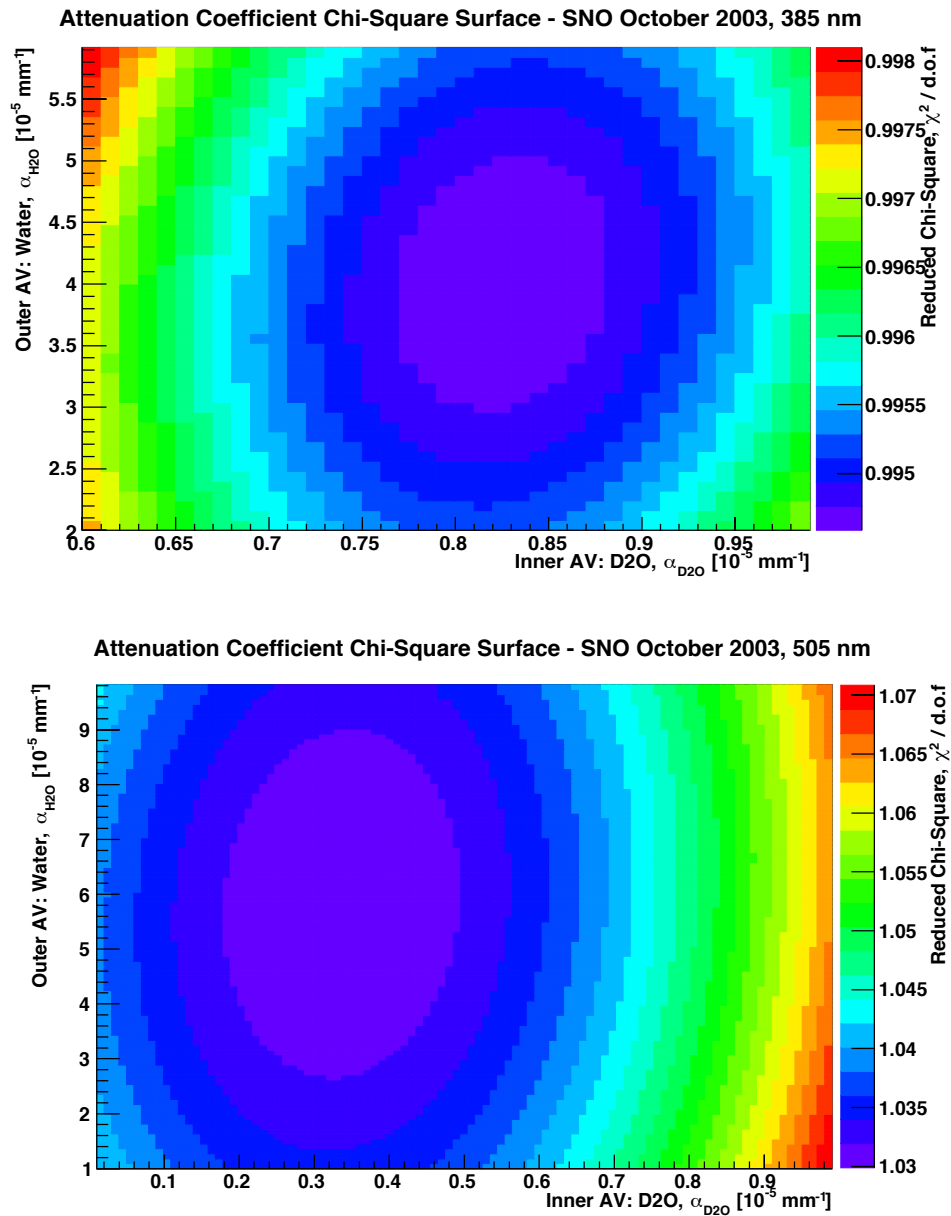


FIGURE 6.5: The reduced χ^2 surface between the inner and outer AV water attenuation coefficients for the 385 and 505 nm laserball scan in D₂O from SNO October 2003. The contours are smooth, with a colour scale that represents the minimised reduced χ^2 value at each combination of α_{D_2O} and α_{H_2O} .

SNO+ MC - H₂O & Acrylic

The attenuation coefficient of water for the combined inner and outer AV regions, $\alpha_{\text{H}_2\text{O}}^{\text{comb}}$, from the SNO+ MC data set are shown in Figure 6.6. In comparison with the values of $\alpha_{\text{H}_2\text{O}}$ obtained from the SNO data set, the values here are identified with improved statistical uncertainty, <1%. In addition, by combining the inner and outer regions into a single effective material, the values are more robust against systematic changes that introduce uncertainties in the range 5-12% based on wavelength.

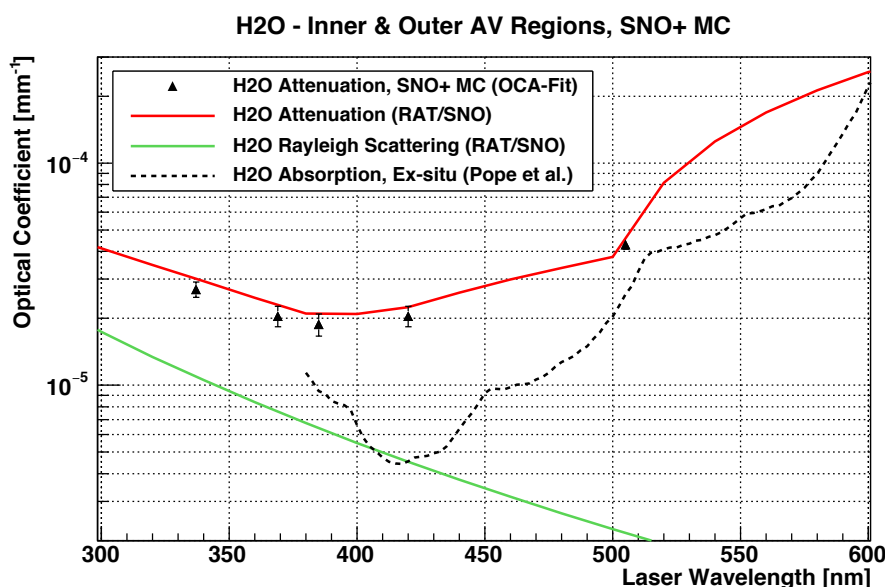


FIGURE 6.6: Shown in black are the fitted attenuation coefficients of the combined inner and outer AV water regions, $\alpha_{\text{H}_2\text{O}}^{\text{comb}}$, obtained from the SNO+ MC data set. Errors shown are both statistical and systematic. Shown also are the current RAT Rayleigh scattering (green) and attenuation coefficients (red). Points along the black dashed line represent absorption measurements made by Pope et al. [145].

It is also of interest to consider the inner and outer AV water regions as different materials and test for equivalence of the attenuation coefficients either side of the acrylic boundary imposed by the AV. For MC data, it is expected that the attenuation coefficients are equivalent. However, in practice the inner and outer AV water regions are exposed to different environments, particularly in the outer region where slight impurities may leech into the water from detector components and the cavity liner. Subsequently, any contamination of the water - for which there is precedent [134, 146] - may alter the attenuating properties of the water.

For this reason a control fit was performed on the data wherein the inner and outer AV water regions were treated as different materials to test the ability of the fit to identify equivalence between the two. The values of α_{H_2O} in the outer AV region from the control fit are shown in Figure 6.7. As expected, the values are equivalent to those obtained in the inner AV region, but are subject to the larger systematic uncertainties associated with the outer AV region. The ratio of the attenuation coefficients, α_{H_2O} obtained for the separate treatment of the inner and outer AV regions as part of the control fit are shown in Figure 6.8 and are consistent with unity.

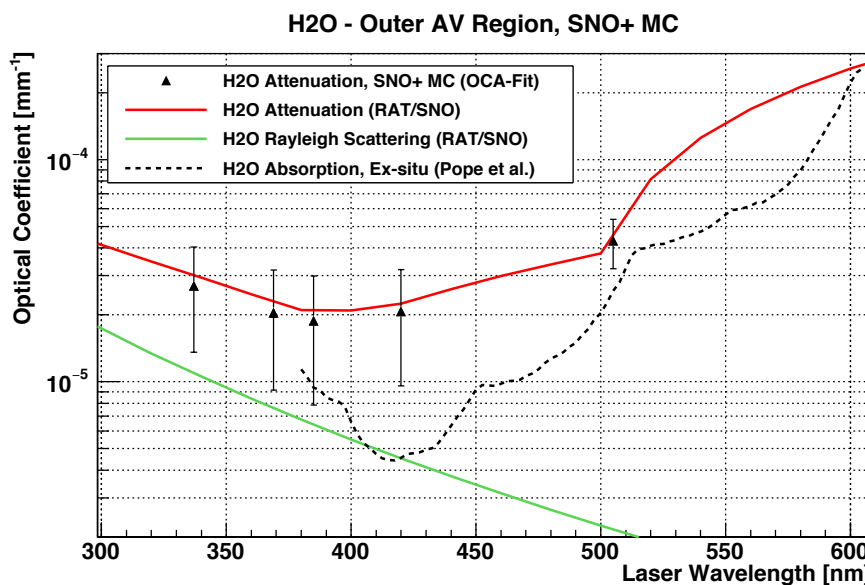


FIGURE 6.7: Shown in black are the fitted attenuation coefficients of the outer AV water region, α_{H_2O} obtained from the SNO+ MC data set. Errors shown are both statistical and systematic. Shown also are the current RAT Rayleigh scattering (green) and attenuation coefficients (red). Points along the black dashed line represent absorption measurements made by Pope et al. [145]. The values obtained in the outer water region are consistent with those obtained in the inner AV region, but are subject to a larger degree of systematic uncertainty.

The obtained values of the acrylic attenuation coefficient, α_{AV} are shown in Figure 6.9. The values of the acrylic in RAT come from ex-situ measurements made prior to SNO [147]. Despite probing only a very narrow range of path lengths through the acrylic region, the fit performs well, matching the expected shape of the attenuation curve between 337-505 nm. However, the values themselves are slightly underestimated and are generally smaller than the ex-situ measurements.

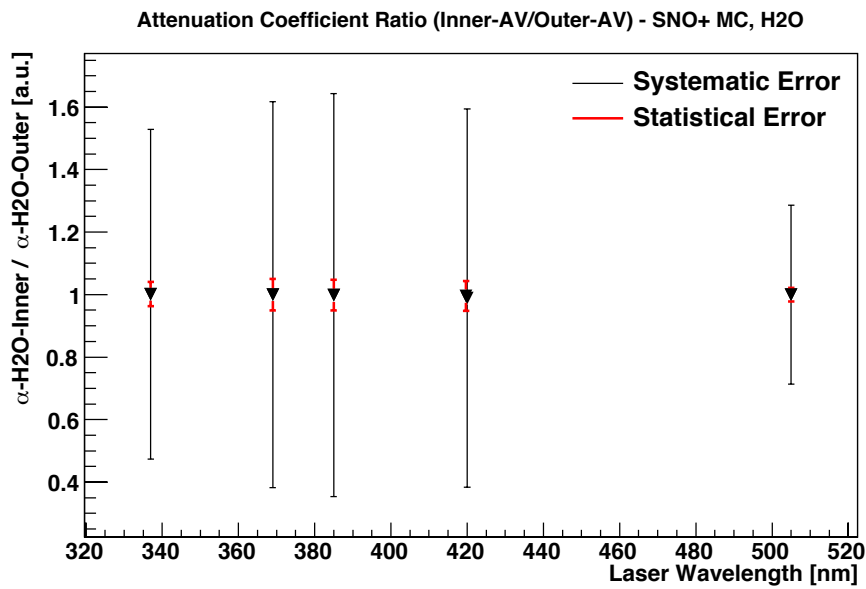


FIGURE 6.8: The ratio of the water attenuation coefficients, $\alpha_{\text{H}_2\text{O}}$ for the inner and outer AV water regions from the SNO+ MC data set. The ratio is consistent with unity, illustrating the ability of the fit to find equivalence between two detector regions that are made of the same material. Larger systematic contributions (black) come from the outer region values. Shown also in red is the statistical uncertainty.

In-situ measurements of the acrylic may be improved by performing laserball scans outside of the AV. This would further separate the correlation between the water and acrylic path lengths by sampling two new light path types; paths wherein the light only travels through the nearside water region directly to the PSUP and paths that intersect the AV twice. At time of writing, the possibility of such laserball deployment is currently being explored by members of the SNO+ optics group.

As before, the attenuation coefficients $\alpha_{\text{H}_2\text{O}}^{\text{comb.}}$ and α_{AV} are parameters in a very smooth parameter space. Example projections of the reduced χ^2 surface for the 337 and 369 nm scans are shown in Figure 6.10. The smooth parabolic nature of these surfaces is contoured by the parameter covariances, which is ultimately reflective of the statistical uncertainties in the single parameter values. However, these type of plots do not illustrate the relationship between the parameter space and the various systematic effects that drive the dominant uncertainties (see Section 6.2.6) in the parameter values.

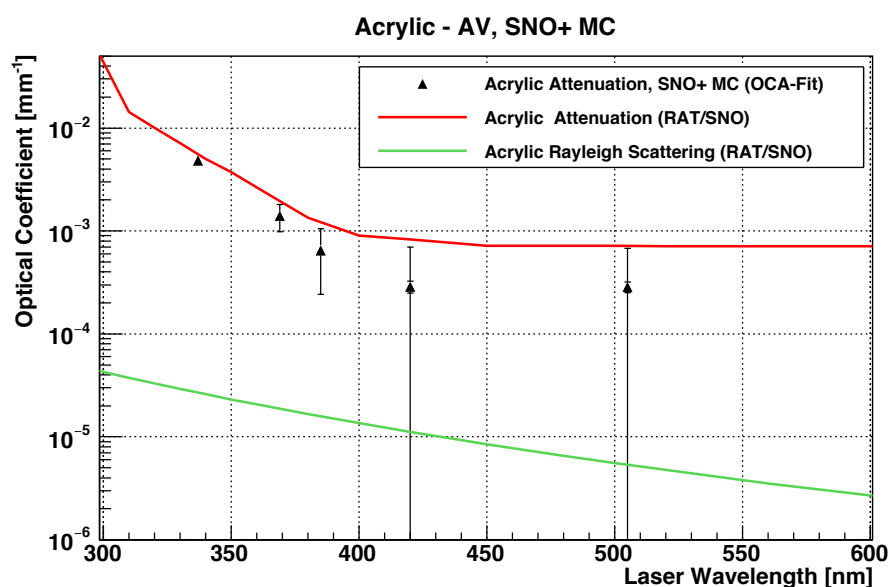


FIGURE 6.9: Shown in black are the fitted attenuation coefficients of the AV acrylic obtained from the SNO MC+ data set. Errors shown are both statistical and systematic. Show also are the current RAT Rayleigh scattering (green) and attenuation coefficients (red) for acrylic which are based on ex-situ measurements from SNO.

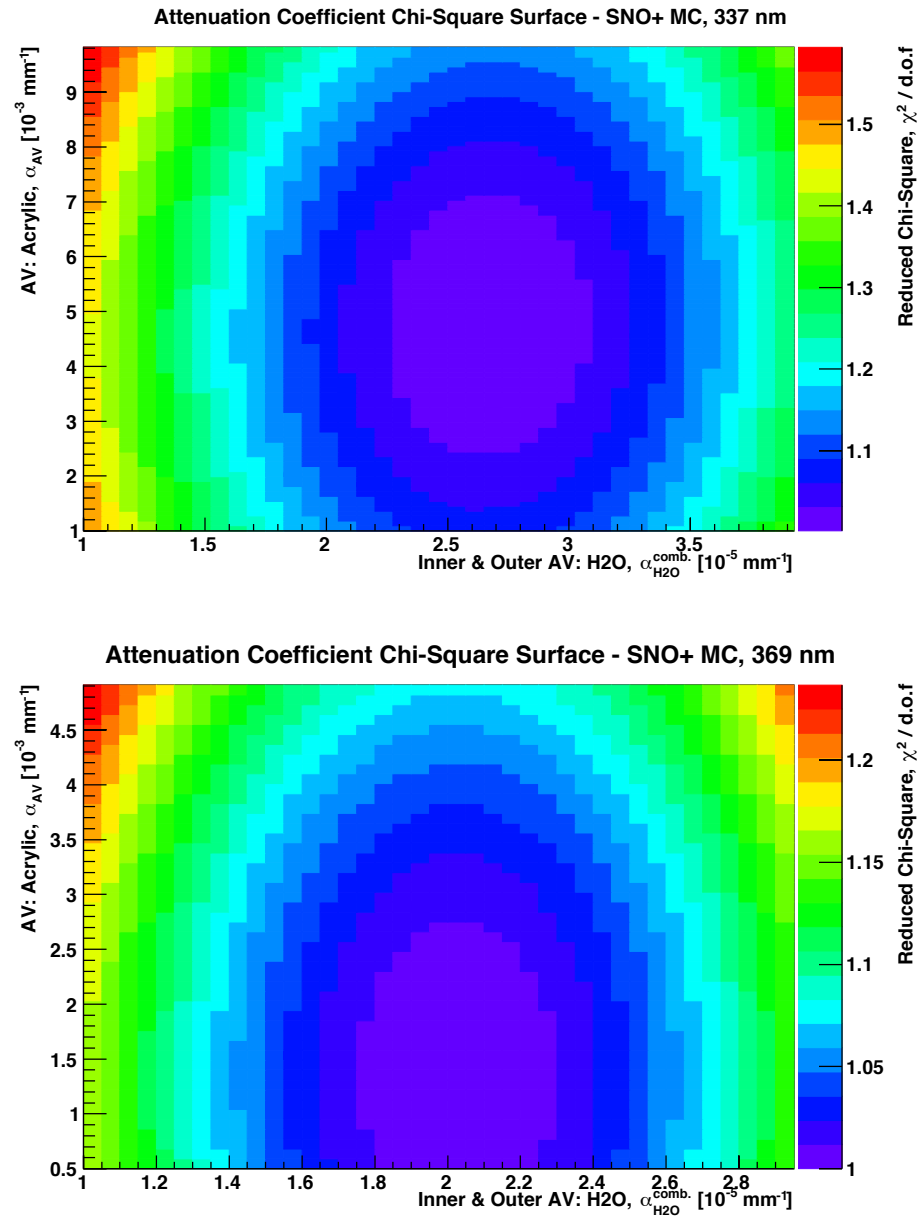


FIGURE 6.10: The reduced χ^2 surface between the combined inner and outer AV water and AV acrylic attenuation coefficients for the 337 and 369 nm laserball scans produced by RAT. The contours are smooth, with a colour scale that represents the minimised reduced χ^2 value at each combination of $\alpha_{\text{H}_2\text{O}}^{\text{comb.}}$ and α_{AV} .

6.2.2 PMT Angular Response

The fitted relative PMT angular response obtained from the SNO heavy water and SNO+ MC water phase data sets are shown for all associated wavelengths in figures 6.11 and 6.13 respectively. In general, this angular response distribution varies across different wavelengths and incident angles. This is indicative of the effective response of the PMT reflector assembly and the intrinsic efficiency of the PMT itself to light at different wavelengths and incident angles.

In comparing different wavelength scans from the SNO data in Figure 6.11, the $\theta_{\text{PMT}} \in (0^\circ, 30^\circ)$ range of the distributions are generally consistent and near-linear, increasing with slight variations in the gradient as the incident angle becomes larger. Thereafter, at incident angles $\theta_{\text{PMT}} \in (30^\circ, 42^\circ)$ the distributions deviate and increase or decrease based on the wavelength. For all wavelengths the response decreases at $\theta_{\text{PMT}} \geq 42^\circ$. The results obtained for this data set using the OCA fit procedure are consistent with those obtained through the original SNO software equivalent, LOCAS. An example comparison between the fitted angular response from OCA and LOCAS is shown for the 420 nm scan in Figure 6.12.

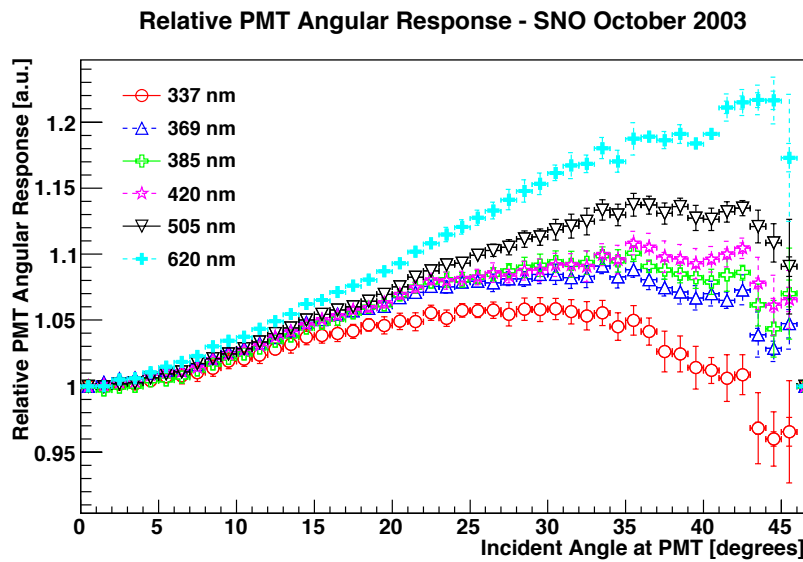


FIGURE 6.11: The fitted relative PMT angular response for the SNO October 2003 heavy water data set. Errors are both statistical and systematic.

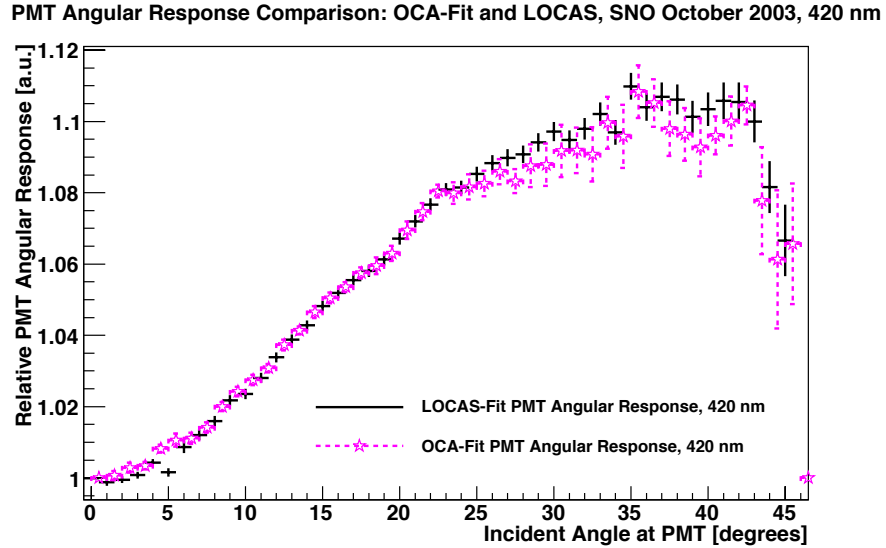


FIGURE 6.12: A comparison of the fitted relative PMT angular response at 420 nm for the SNO October 2003 heavy water data set as calculated by OCA and the original LOCAS fit procedure. Errors are both statistical and systematic.

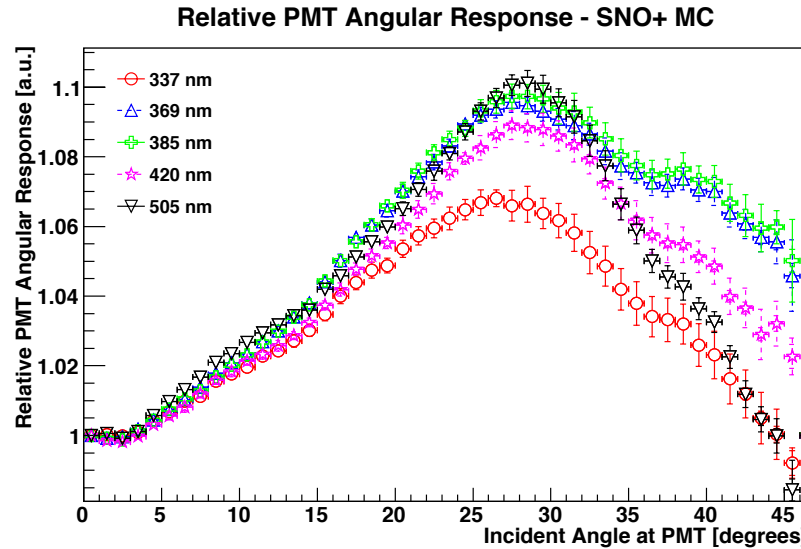


FIGURE 6.13: The fitted relative PMT angular response for the SNO+ MC water phase data set. Errors are both statistical and systematic.

The angular response distributions obtained from the SNO+ MC data set share similar features to the SNO response in the region $\theta_{\text{PMT}} \in (0^\circ, 27^\circ)$, exhibiting a consistent near-linear increase across all wavelengths. However, the peak of the response across all wavelengths resides in the range $\theta_{\text{PMT}} \in (27^\circ, 30^\circ)$ and thereafter decreases for incident angles $\theta_{\text{PMT}} \geq 30^\circ$. In the case of the 337 and 505 nm scans, the decrease of the relative response at these larger angles becomes less than 1. This is an effect that is induced by the geometry of the PMT reflector, which is, in part, determined by both its length and radius of curvature. Based on the entry of light into the plane of the PMT bucket, there will be a limiting angle above which light that enters is reflected back out and away from the face of the PMT, subsequently reducing the PMT response. This effect was observed in pre-production studies of the PMT geometry for SNO [125]. As shown in Figure 6.14, the fitted angular response spectrum obtained from this MC data set is consistent with the expected angular response shape present in RAT. Variations in the size of the spectra are maximal about the peak, 2-3% and overall are attributed to correlations between the response and the laserball intensity which is discussed in Section 6.2.5.

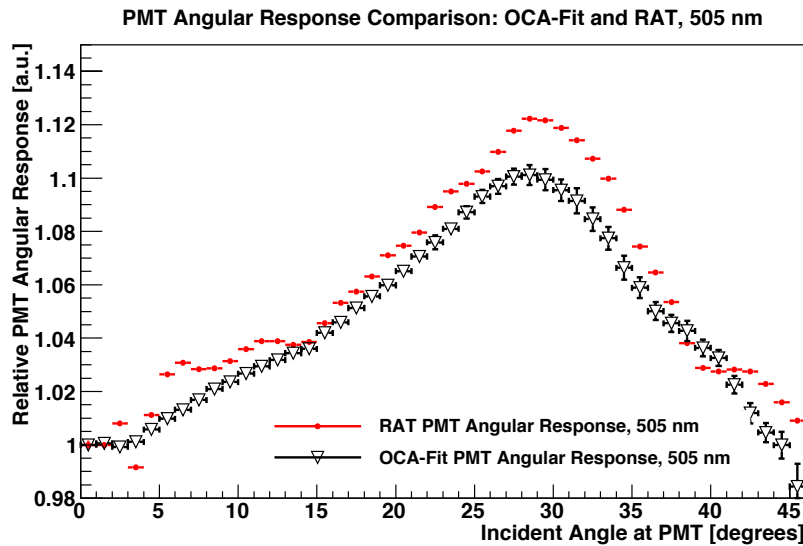


FIGURE 6.14: A comparison of the fitted relative PMT angular response at 505 nm for the SNO+ MC data set as calculated by the OCA fit procedure and from MC studies in RAT. Errors are both statistical and systematic for the OCA fit distribution and only statistical for the RAT distribution.

The PMT angular response is robust to systematic uncertainties associated with the laserball position. The fitted angular response and that obtained from a systematic fit in which the laserball position radius is increased by 1% is shown

Figure 6.15 for both SNO and SNO+ MC data sets at 420 nm. The fractional change in the response is small, and in most cases $< 0.1\%$, only increasing above $\sim 1\%$ for $\theta_{\text{PMT}} \geq 40^\circ$ where the sampling of the response is statistically limited.

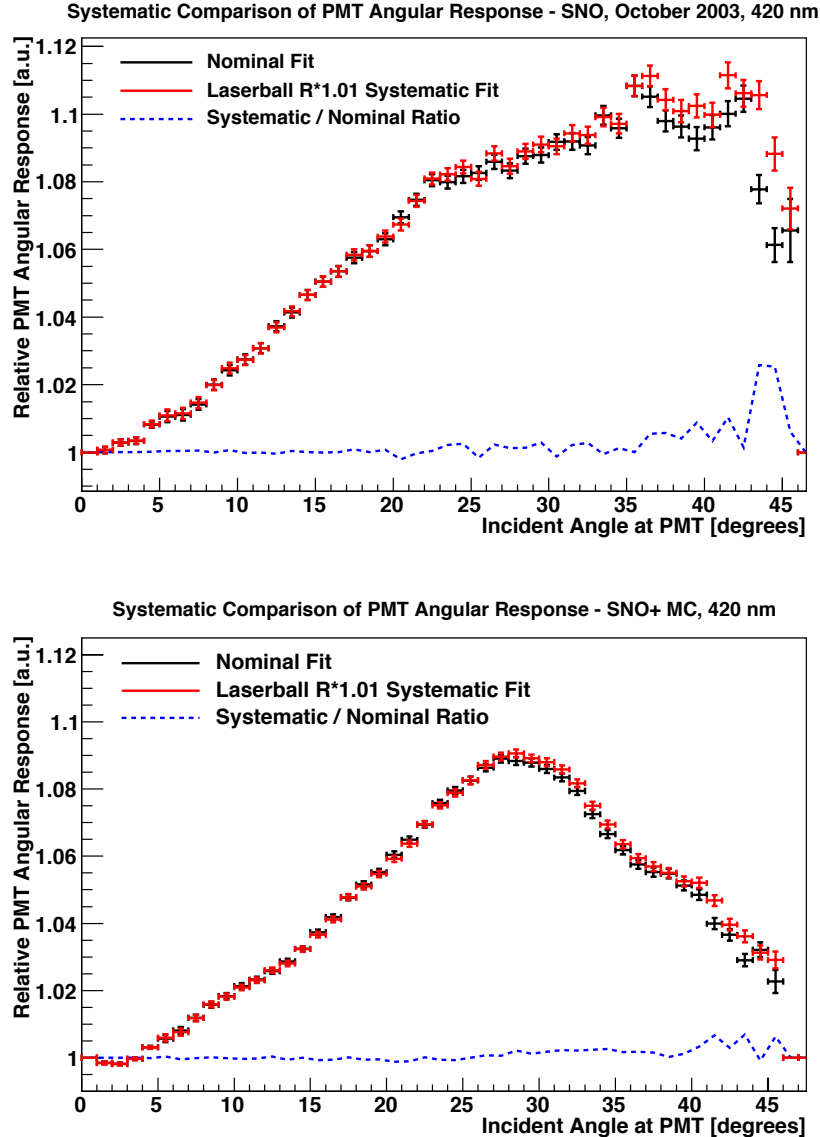


FIGURE 6.15: Comparison of the fitted relative PMT angular response at 420 nm (black) from the SNO (top) and SNO+ MC (bottom) data sets with those obtained from a systematic fit (red) wherein the laserball position radius is increased by 1%. Only statistical errors are shown. The blue dashed-line represents the systematic-to-nominal ratio of the two distributions.

6.2.2.1 Discrepancies between Data & Monte-Carlo

It is clear by direct comparison of the angular response from both data sets that there are discrepancies between the real and MC performance of the PMTs and their reflectors. This is particularly evident at larger incident angles, and is illustrated by the data-to-MC ratio of the response as shown in Figure 6.16. Across all wavelengths the fractional changes between data and MC can vary at the very most between $(-4\%, +12\%)$ in the region $\theta_{\text{PMT}} \geq 30^\circ$.

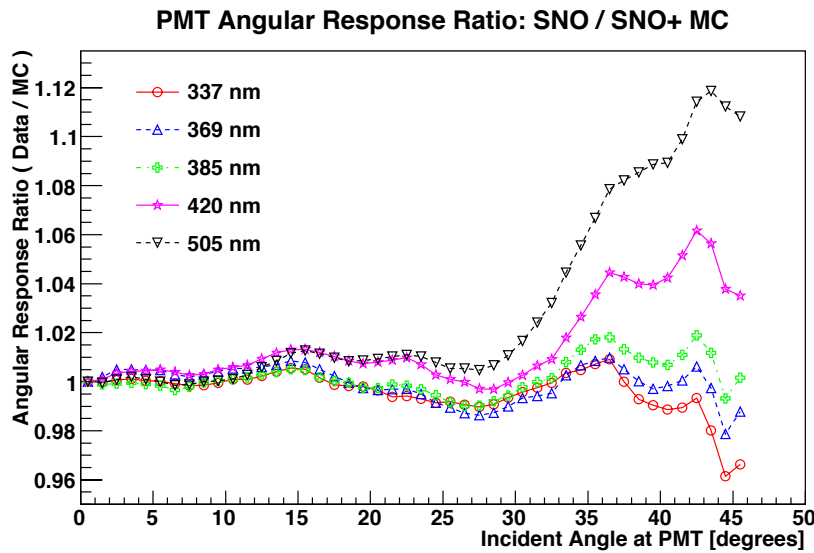


FIGURE 6.16: The data-to-MC ratio of the relative PMT angular response parameters obtained from the SNO and SNO+ MC data sets.

The relative PMT angular response is an effective treatment designed to characterise the response of all normal-type PMTs and their reflectors. For MC studies, this is reasonable as RAT assumes that all PMTs have the same efficiency and are surrounded with *as-new* reflectors. However, in practice each individual PMT will have its own intrinsic efficiency, and each set of reflectors will have its own collection efficiency; a measure of the effectiveness of the reflectors to redirect light onto the PMT face. These efficiencies are in part eliminated from the optical fit by using the occupancy ratio method. Despite this there are two main in-situ phenomena which affect the PMT response that are not yet accounted for by RAT. As discussed in Section 4.2.4, one of these is the degradation of the reflectors over time. At time of writing, a full ageing model of the PMT concentrators is not currently implemented in RAT, but is the subject of an ongoing investigation at UC Berkeley [104, 148].

6.2.3 PMT Variability

In addition to the ageing of the reflectors, the other effect unaccounted for by RAT is the PMT variability, $\delta v(\theta_\gamma)$. As discussed in Section 4.3.2, the PMT variability characterises the observed correlation of increasing width in the effective PMT efficiencies at larger incident angles; this increase being beyond that of the counting statistics associated with the occupancies of the PMTs. The measure of this width is given by the coefficient of variation, of which the variability is the residual uncertainty once the statistical uncertainty has been subtracted (see Equation 4.33). Shown in Figure 6.17 is an example comparison of the coefficient of variation between the SNO and SNO+ MC data sets for a scan at 420 nm. For the SNO+ MC data set, the variation is relatively constant with values in the range 0.023-0.027, which are consistent with the uncertainty on the occupancy, $\lesssim 3\%$. There are therefore no contributions from the variability based on the incident angle in MC data produced by RAT. The variation in the SNO data is larger, and increases at larger incident angles i.e. $\delta v(\theta_\gamma) \neq 0$. In both data sets, the coefficient of variation is suppressed at small incident angles, $\theta_{\text{PMT}} \in (0^\circ, 5^\circ)$ due to the improved statistics of the central runs ($\times 4$ those of off-axis runs) for which all incident angles are small. It is the overall smaller variation in the SNO+ MC data which results in the narrower data point pull distributions (and hence smaller final χ^2 limits) which were discussed in Section 6.1.1.

As shown in Figure 6.18 the trend of increasing variation with incident angle is similar across all wavelengths in the SNO scans. To account for this at each PMT in the sample of the fit, linear and second-order degree polynomial functions are fitted to the coefficient of variation distribution, two examples are shown in Figure 6.19 for scans at 337 and 420 nm. This can then be used to estimate the individual PMT variability in a given run, $\delta v_{ij}(\theta_{\gamma,ij})$ using Equation 4.33. The fitted functions are only intended to be an approximation to the coefficient of variation, which can be parameterised by only two or three parameters based on the order of the polynomial¹.

The optics fit for the SNO data set is corrected for by introducing the PMT variability term. A full fit without consideration for this effect yields reduced χ^2

¹In practice, there is nothing to stop one from using the individual variability values at each incident angle. However, this introduces around 45 new parameters into the fit. It was verified that this approach did not change the overall fit result compared to using two or three parameter to define a function.

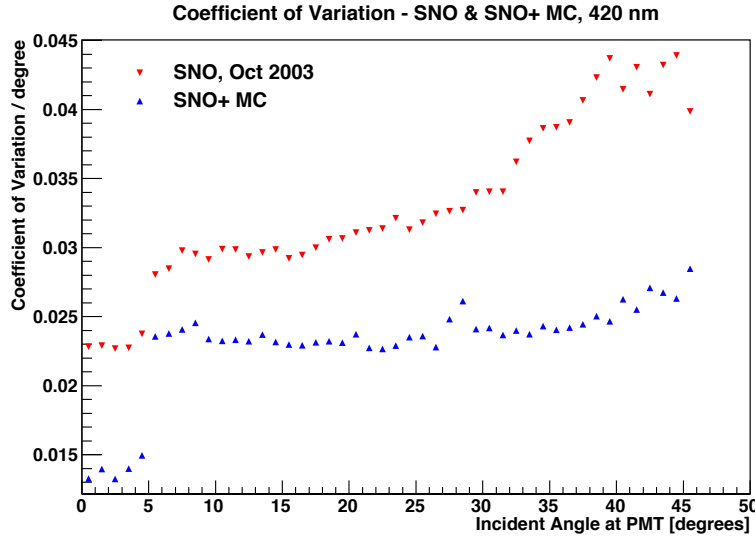


FIGURE 6.17: Comparison between the calculated coefficient of variation for SNO (red) and SNO+ MC (blue) data at 420 nm. The variation of the SNO data increases with incident angle ($\delta v(\theta_\gamma) \neq 0$) whereas little variability is exhibited by the MC data.

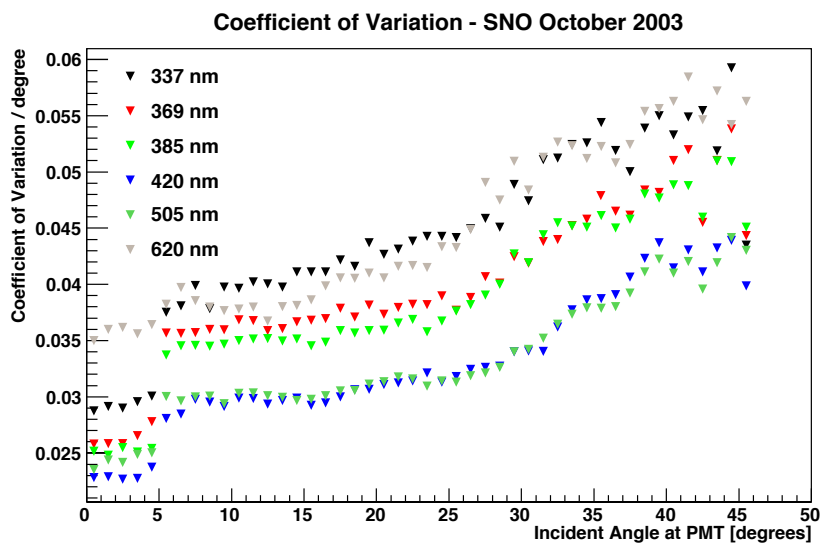


FIGURE 6.18: The coefficient of variation across all wavelengths of the SNO October 2003 data set.

values $\sim 1.6\text{--}1.8$, this is unreasonable given a fit consists of $\gtrsim 100,000$ data points. Including the variability term restores the values of the reduced χ^2 to ~ 1 .

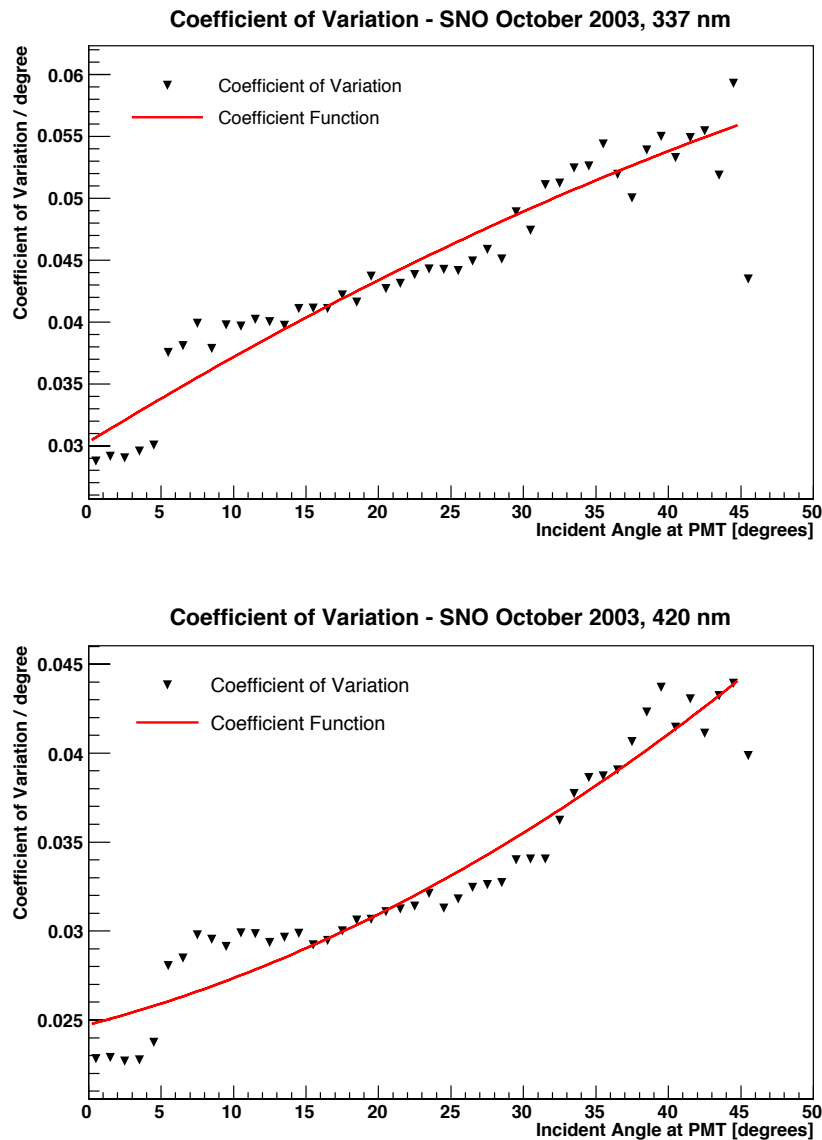


FIGURE 6.19: The coefficient of variation for the SNO October 2003 data set at 337 nm (top) and 420 nm (bottom). Shown is the calculated coefficient of variation for each 1° of the incident angle (black). The fitted polynomials (red) are used to estimate the coefficient of variation from which the PMT variability can be calculated.

6.2.4 Laserball Light Distribution

The total light distribution of the laserball, $L(\cos \theta_{LB}, \phi_{LB})$ is a composite value consisting of a two-dimensional angular distribution, $H(\cos \theta_{LB}, \phi_{LB})$ multiplied

by a degree-four polynomial mask function, $P_4(\cos \theta_{LB})$;

$$L(\cos \theta_{LB}, \phi_{LB}) = P_4(\cos \theta_{LB}) \times H(\cos \theta_{LB}, \phi_{LB}). \quad (6.3)$$

Here, $H(\cos \theta_{LB}, \phi_{LB})$ characterises the relative angular anisotropy in the local $(\cos \theta_{LB}, \phi_{LB})$ coordinate frame of the laserball. $P_4(\cos \theta)$ characterises the overall intensity of the laserball, which is generally smaller near the mounting hardware at the top of the flask ($\cos \theta_{LB} \simeq 1$), and maximal near the bottom ($\cos \theta_{LB} \simeq -1$). As discussed in Section 4.2.5, the angular distribution can either be defined as a two-dimensional histogram with (12, 36) binning in $(\cos \theta_{LB}, \phi_{LB})$; a total of $12 \times 36 = 432$ parameters, or alternatively as a sinusoidal distribution binned in 24 $\cos \theta_{LB}$ slices, each with its own relative amplitude, A_k and sinusoidal phase, δ_k ; a total of $24 \times 2 = 48$ parameters. Given the fewer parameters required by the sinusoidal model this was chosen to be the distribution used in the fit. However, as will be discussed, the binned distribution is useful to verify the sinusoidal input used by **RAT** as the input for the SNO+ MC data set.

6.2.4.1 Laserball Mask Function

The laserball mask function, $P_4(\cos \theta_{LB})$ for each wavelength scan obtained from both SNO and SNO+ MC data sets are shown in Figure 6.20. The function is normalised to unity at the expected maximum, $\cos \theta \simeq -1$. In the high $\cos \theta_{LB}$ region the intensity decreases as a result of intrinsic shadowing introduced by the mounting hardware which holds the laserball flask from directly above, $\cos_{LB} \theta \simeq 1$.

In the case of the SNO+ MC data set, this data was produced by **RAT** which uses a known form of the laserball mask obtained from measurements in SNO during the August 2006 calibration period (see Section 5.1, Figure 5.3). Therefore, the mask function obtained through the OCA fit procedure can be directly compared to the MC-input used in simulations of the laserball. This provides a good test of the OCA fit convergence to the true MC-inputs. The ratio of the fitted and MC-input of the laserball mask function, $P_4(\cos \theta_{LB})$ for each comparable wavelength is shown in Figure 6.21. In general, the fitted mask function is in good agreement with the **RAT** input, with a fractional difference of at most 4.7% which occurs for the 420 nm wavelength scan. For all wavelengths the fractional difference is greatest near the very top of the laserball, $\cos \theta_{LB} \simeq 1$. This discrepancy is

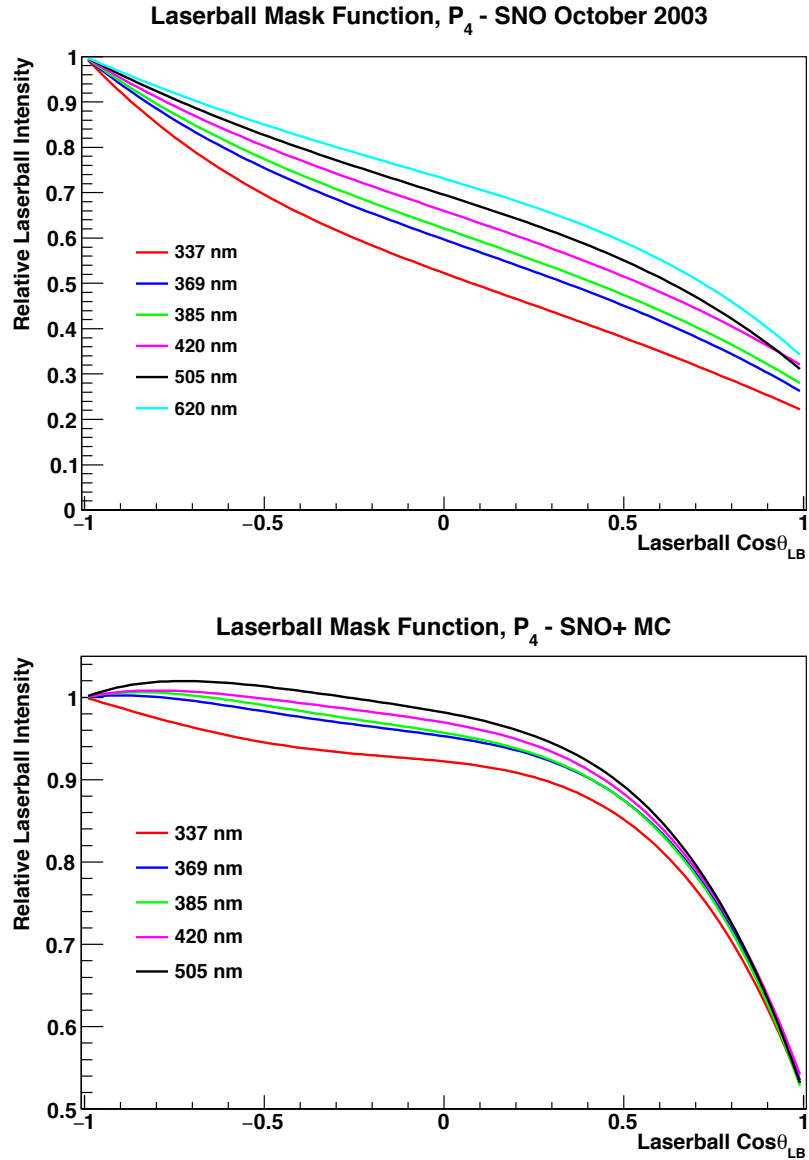


FIGURE 6.20: Shown are the fitted laserball distribution mask functions obtained from the SNO (top) and SNO+ MC (bottom) data sets. The mask function is normalised near the expected maximum intensity region, $\cos\theta_{LB} \simeq -1, \theta_{LB} \simeq \pi$.

reasonable to expect as it is an unphysical region in which to expect light output due to the shadowing caused by the mounting hardware.

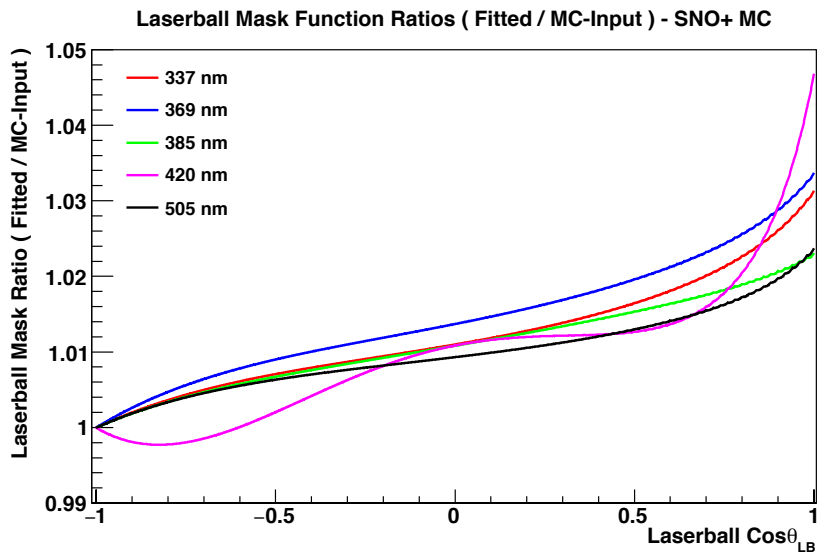


FIGURE 6.21: The fitted-to-MC-input ratio of the fitted laserball mask obtained through OCA to that which is used by RAT to simulate the laserball. The fractional differences are shown for all wavelengths of the SNO+ MC data set.

6.2.4.2 Laserball Angular Distribution

The fitted sinusoidal forms of the laserball angular distributions from the SNO and SNO+ MC data sets are shown in figures 6.22 and 6.23 respectively. In both cases the sinusoidal variation of 3-4% in the relative intensity about ϕ_{LB} is evident. The clarity of this sinusoidal form is particularly clear in the SNO+ MC data set, as this data was simulated using a sinusoidal characterisation of the laserball obtained from SNO (see Section 5.1).

One feature to note about the angular distributions from the SNO data set is that there are artefacts of the fitting procedure in the 337, 369, 385 and 420 nm data sets at $\cos \theta_{LB} \simeq 1$. In this region, the anisotropy is discontinuous. Similarly to the laserball mask functions in this region of $\cos \theta_{LB}$, the parameters are sampled less by the data as they define the very top of the laserball flask which is shadowed by the mounting hardware. There is no laserball geometry included in RAT and therefore this feature does not appear in the distributions obtained from the SNO+ MC data set.

Ultimately, the strength of the OCA fit to identify any intrinsic angular anisotropy of the laserball distribution is governed by the inclusion of runs wherein the laserball is positioned at one of the four different orientations inside the detector. In doing this, any correlations between the angular distribution and mask function is broken; this is illustrated in Section 6.2.5 by studying the covariance matrix returned by the fitting procedure.

One final verification of the OCA fit procedure on the angular distribution is to assume the SNO+ MC data was not produced with a sinusoidal model (even though it was) and to fit for the angular distribution using the aforementioned binned distribution, $H(\cos\theta_{LB}, \phi_{LB}) \equiv 12 \times 36$ bins. The advantage of a binned distribution is that each of the 432 parameters are independent of one another, and not characterised by any functional form as in the sinusoidal model. In doing this, no prior bias is assumed on the form of the angular distribution. An example of a fit using a binned distribution is shown for the 505 nm scan in Figure 6.24. Comparing with the true input (see Section 5.1, Figure 5.2) the OCA procedure is able to successfully identify the true sinusoidal nature of the RAT input to within 1%.

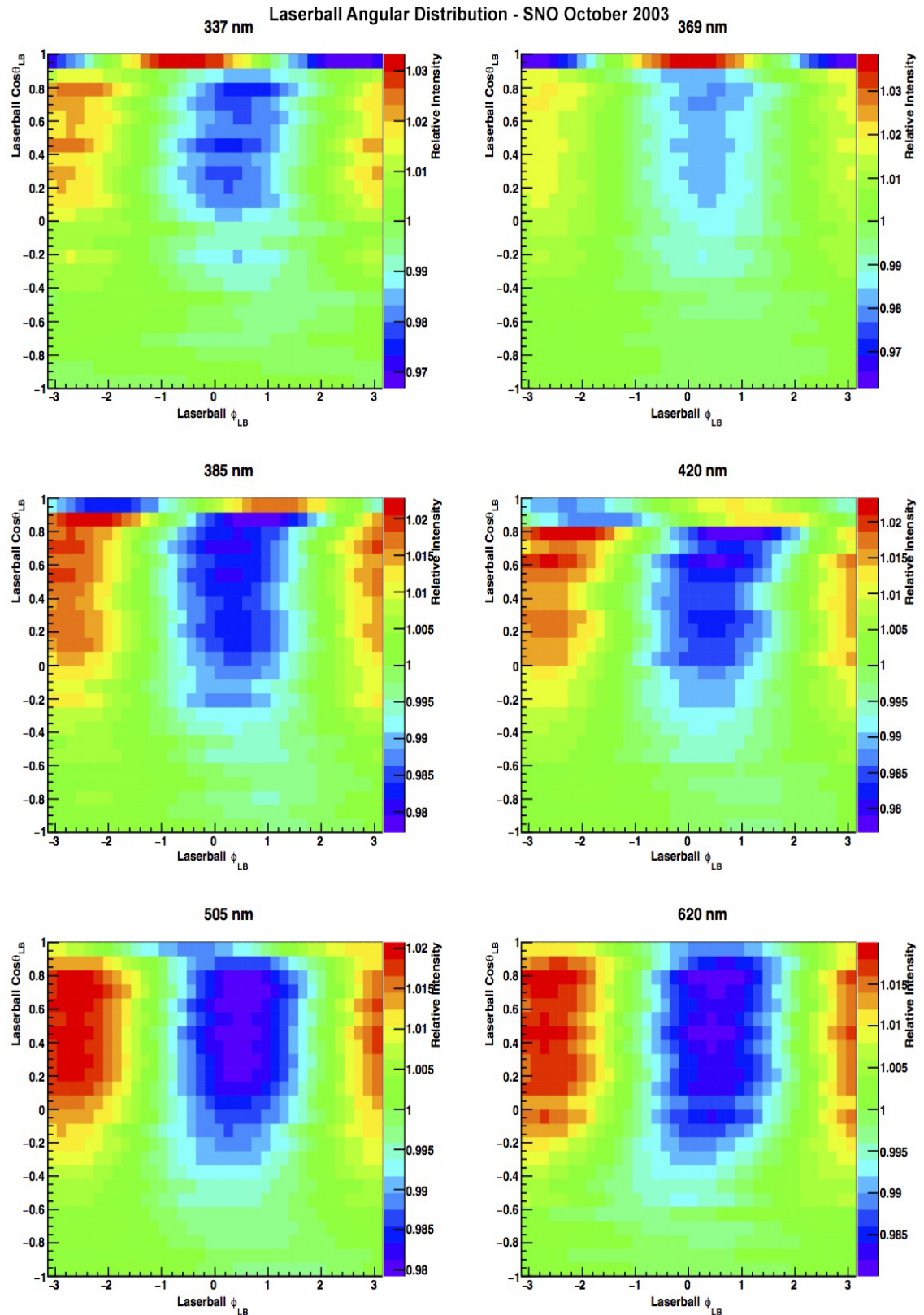


FIGURE 6.22: The fitted laserball angular distributions from the SNO October 2003 data set. Distributions were fitted using a sinusoidal model composed of 24 $\cos \theta_{LB}$ slices.

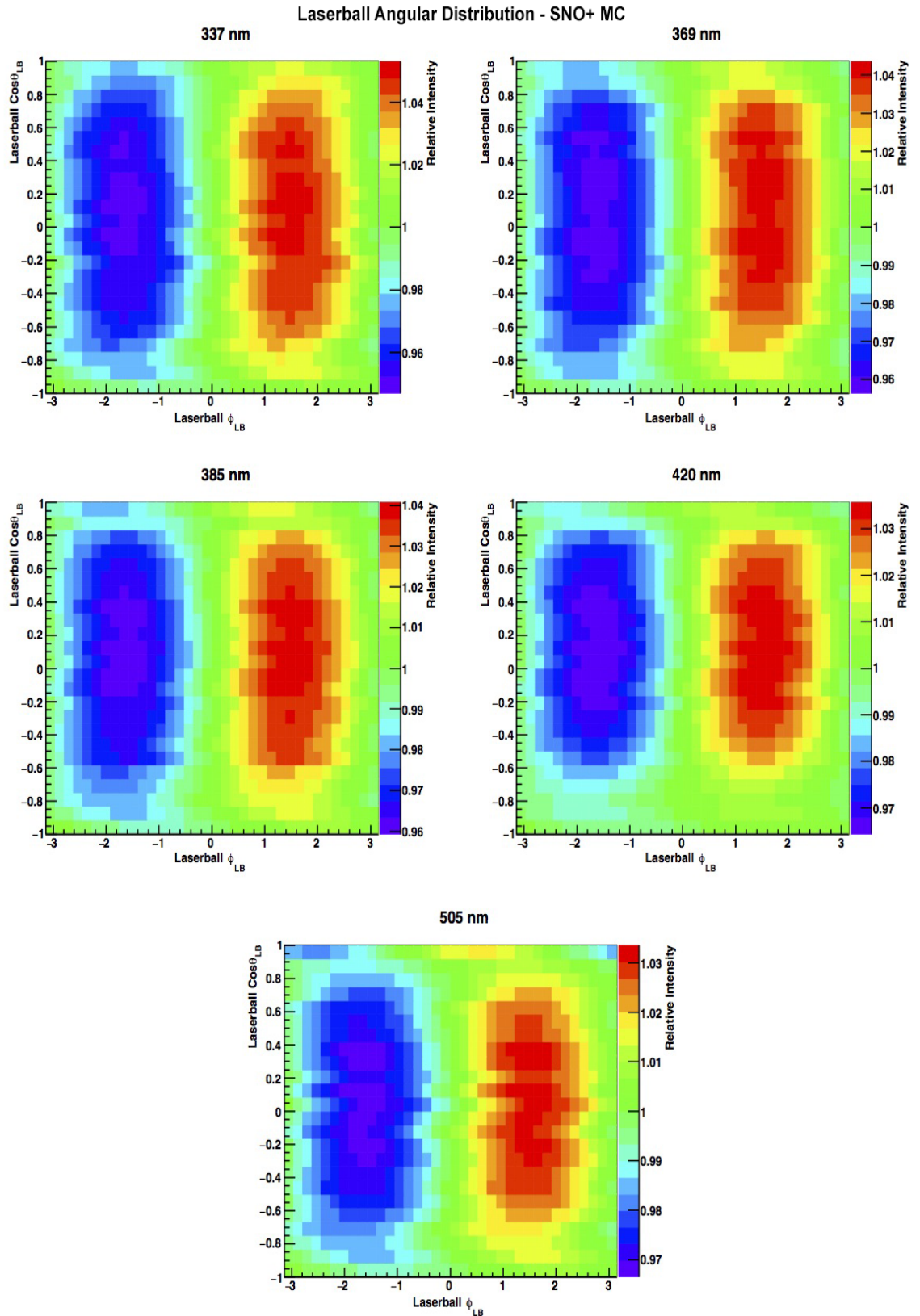


FIGURE 6.23: The fitted laserball angular distributions from the SNO+ MC data set. Distributions were fitted using a sinusoidal model composed of 24 $\cos \theta_{LB}$ slices.

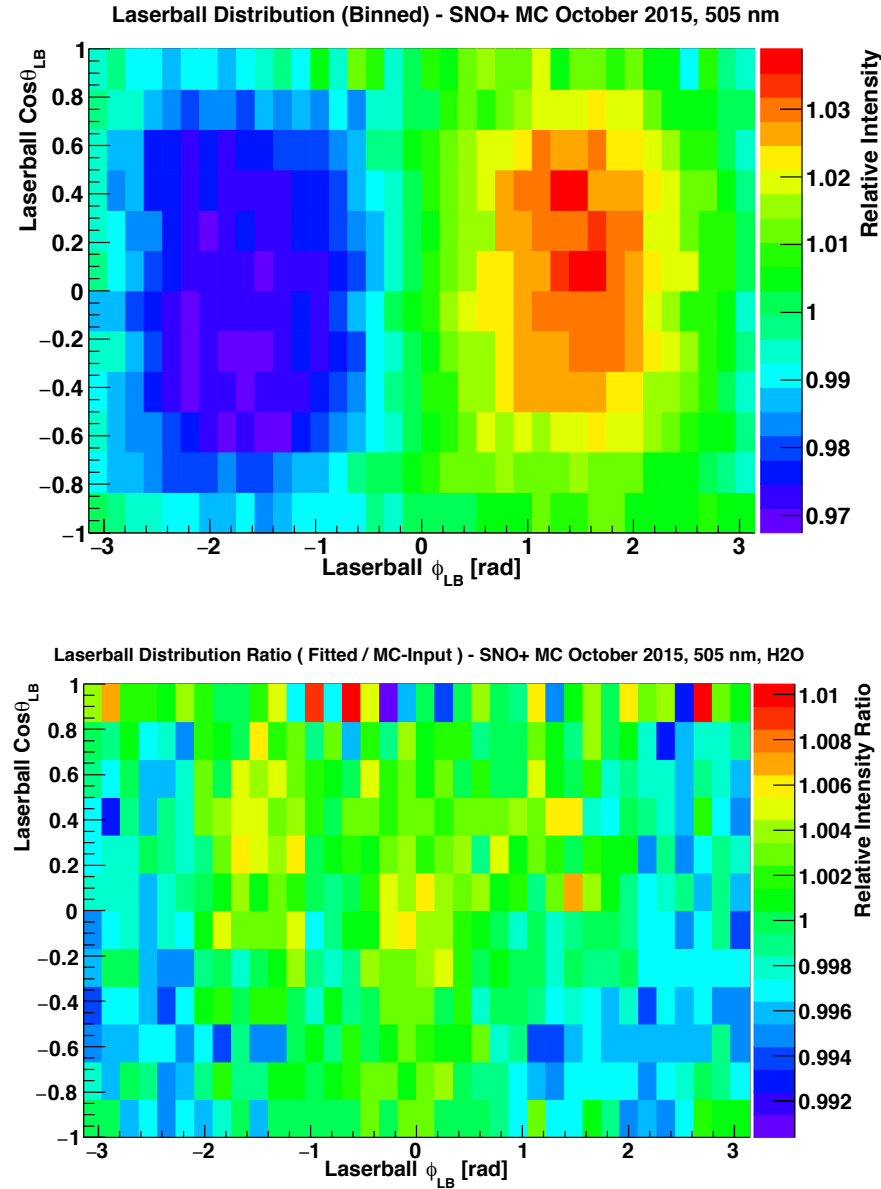


FIGURE 6.24: Shown is the fitted laserball angular distribution from the 505 nm scan of the SNO+ MC data set (top). This distribution was obtained using a binned approximation to the angular anisotropy. Shown also (bottom) is the ratio of this distribution to the true MC-input distribution used by RAT. The OCA fitting procedure obtains a fitted distribution to within 1% of the true MC-input distribution.

6.2.5 Covariance Matrix & Parameter Correlations

The covariance matrix is returned at the end of each fit. It is an $N_{\text{par}} \times N_{\text{par}}$ -dimensional matrix, where N_{par} is the number of the parameters in the fit. The specific ordering of the parameters is as follows;

- **Index [1]** - Inner AV region attenuation coefficient.
- **Index [2]** - AV acrylic attenuation coefficient.
- **Index [3]** - Outer AV region H₂O attenuation coefficient.
- **Indices [4 : 8]** - Laserball mask function, $P_4(\cos \theta_{\text{LB}})$. Polynomial of order four → 4 + 1 parameters.
- **Indices [9 : 89]** - Relative PMT angular response, $R(\theta_{\text{PMT}})$. Incident angles between 0 - 90 degrees, with one parameter per degree.
- **Indices [90 : 137]** - Laserball light distribution, $L(\cos \theta_{\text{LB}}, \phi_{\text{LB}})$. Sinusoidal model with 24 cos θ_{LB} slices, with two parameters per slice → 48 parameters.
- **Indices: [138 : (137 + N_{runs})]** - N_{runs} occupancy normalisations, one per run.

A typical fit therefore returns a covariance matrix for 176 parameters (a typical SNO+ MC wavelength scan contains $N_{\text{runs}} = 39$ runs). However, not all the parameters vary in the fit, and in most cases some are fixed for which there is no meaningful covariance information. The following subsets of parameters are fixed:

- **Fixing of attenuation coefficients:** For the SNO October 2003 data set, the acrylic attenuation coefficient, α_{AV} is fixed to ex-situ measurements. For the SNO+ MC data set, the inner and outer AV regions are combined, $\alpha_{\text{H}_2\text{O}}^{\text{comb.}}$ as explained in Section 6.2, requiring one less parameter.
- **Fixing of relative PMT angular response:** For most laserball scans, the range of incident angles probed at the PMTs is in the range $\theta_{\text{PMT}} \in [0^\circ, 50^\circ]$. Therefore, approximately 40 parameters corresponding to the $\theta_{\text{PMT}} \in (50^\circ, 90^\circ]$ range are not sampled and subsequently fixed.

As a result of this parameter fixing, the subset of parameters which are of interest (those which are not fixed) form a covariance matrix featuring 130-140 parameters. In the following discussion, the covariance matrices, from which correlation matrices are obtained, represent these subsets of varying parameters.

6.2.5.1 Correlation Matrices

The covariance matrix, C_V consists of covariance values between parameters which all vary based on the overall magnitude of the parameter value itself; this can be between 10^{-6} - 10^2 depending on the particular parameter. It is therefore useful to define a correlation matrix, C_R which normalises the relationship between the parameters to the range $[-1, 1]$; where values close to -1 or +1 denote a respective tendency towards negative or positive correlation;

$$C_R = D_V^{-1} C_V D_V^{-1}, \quad \text{where } D_V = \sqrt{\text{Diag.}(C_V)}. \quad (6.4)$$

In general, all equivalent parameters share the same correlations across both SNO and SNO+ MC data sets and the different wavelength scans therein. An example of the global parameter correlation space is shown in Figure 6.25 for the SNO+ MC data set at 420 nm. In particular it is interesting to note the correlations, if any, between the three main composite subsets of parameters in the optical model; the relative PMT angular response, the laserball angular distribution and the intensity normalisations. The most prominent feature here is the slight negative correlation between the PMT angular response and the laserball intensity. This is reasonable to expect as there is a slight positive correlation between both the laserball intensity and the PMT angular response with the laserball position radius; specifically in the $|z|$ -coordinate direction. An example of this relationship is shown in Figure 6.26 for a scan at 505 nm. The negative correlation between the angular response and the laserball intensity can then be reasoned by considering that for a given number of hits, N_{hit} at a single PMT, this value will be directly proportional to both the efficiency of the PMT (itself related to the angular response i.e. $\epsilon(R(\theta_{\text{PMT}}))$) and the amount of light emitted by the laserball, N_γ ;

$$N_{\text{hit}} \propto \epsilon(R(\theta_{\text{PMT}})) \times N_\gamma. \quad (6.5)$$

Therefore, increases in one of either the angular response or the intensity are compensated for by decreases in the other, thus resulting in a negative correlation.

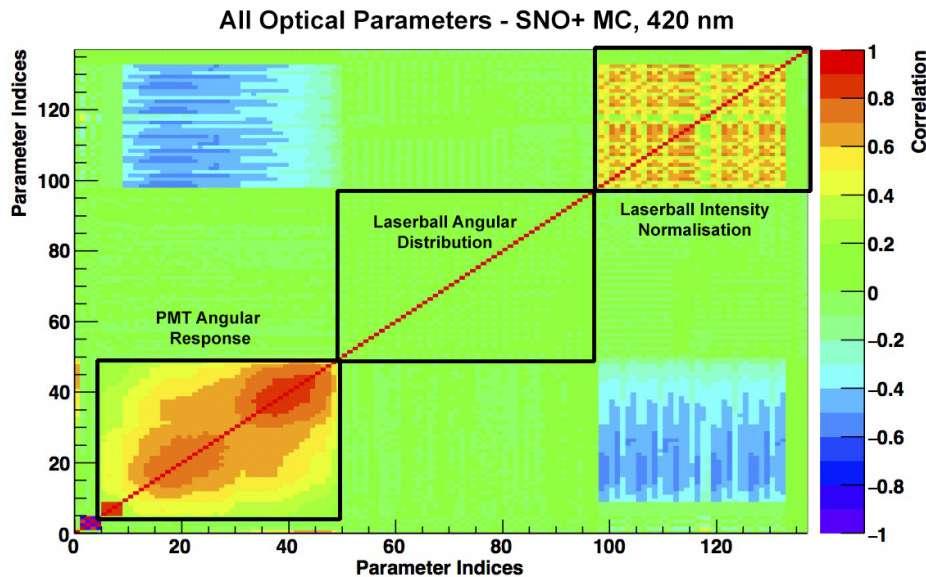


FIGURE 6.25: The global correlation space for the varying parameters from the SNO+ MC data set at 420 nm. Shown are the three main composite parameter subsets; the relative PMT angular response, the laserball angular distribution and the intensity normalisations. In the case of the PMT angular response, only the correlations for the parameters in the range $\theta_{\text{PMT}} \in (0^\circ, 50^\circ)$ are shown.

As expected, the intrinsic laserball anisotropy characterised by the angular response is not correlated to either the intensity of the laserball or the response of the PMTs. More importantly however, and as shown in Figure 6.27, is that the angular distribution does not share any correlations with the parameters that define the mask function which characterises the $\cos \theta_{\text{LB}}$ dependence of the laserball intensity. This supports the use of multiple laserball runs in the same position, but at different angular orientations as it ensures that the fit can dissociate separate ϕ_{LB} and $\cos \theta_{\text{LB}}$ dependencies in the overall laserball light distribution.

The attenuation coefficients of the optical model only share correlations with the PMT angular response. Specifically, it is only the attenuation coefficient of the outer most region which shares a strong correlation; $\alpha_{\text{H}_2\text{O}}$ in the case of the SNO data set and α_{AV} in the case of the SNO+ MC data set (the outer water region is combined with the inner region as part of $\alpha_{\text{H}_2\text{O}}^{\text{comb}}$). As shown in Figure 6.28, the correlation is greatest in the high incident angle region, $\theta_{\text{PMT}} \in (30^\circ, 45^\circ)$. The increase in the correlation is reflective of the quadratic relationship between

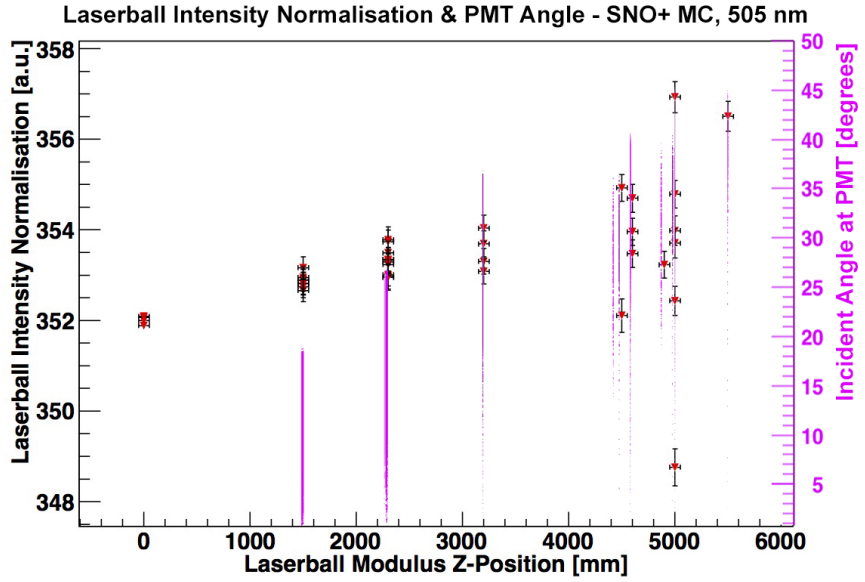


FIGURE 6.26: Shown is the correlation in the fitted intensity normalisations (black, left-axis) and the incident PMT angles (magenta, right-axis) at different laserball positions in the $|z|$ -direction. Data is taken from the SNO+ MC data set at 505 nm.

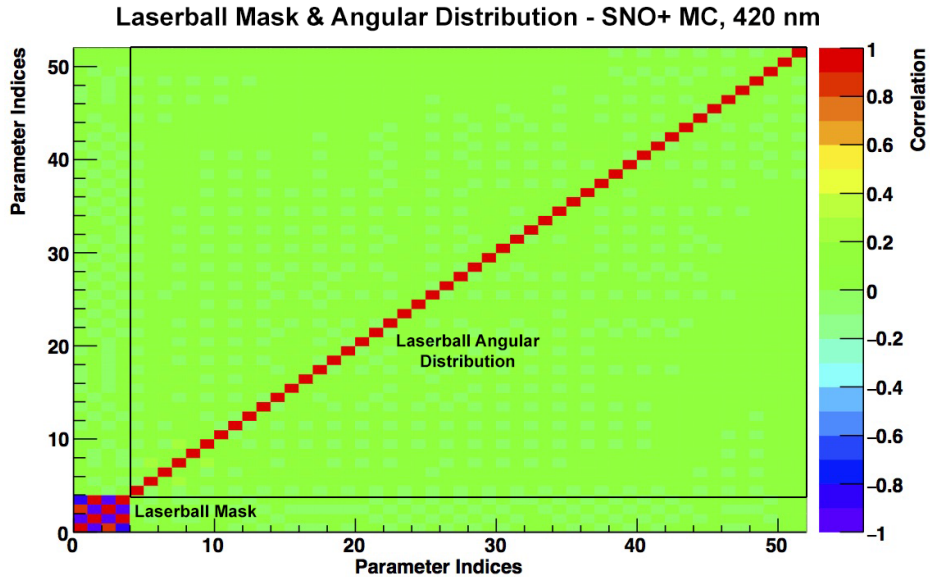


FIGURE 6.27: The correlation matrix for the laserball intensity mask and angular distribution parameters. No correlation is exhibited between these two sets of parameters.

the path lengths in the outer most region, from which the attenuation coefficient

is sampled, and the incident angle of the light at the PMT. An example of this quadratic form is shown in Figure 6.29.

Parameters within the angular response distribution are themselves correlated with other parameters within the distribution. This arises as a consequence of the interpolation between neighbouring parameters performed for the evaluation of each θ_{PMT} value in the fit. For example, in Figure 6.28 there is a particularly strong correlation shared between the parameters with indices 3-6 $\equiv \theta_{\text{PMT}} \in (0^\circ, 3^\circ)$. This occurs as a result of the fixing of the zeroth-degree parameter to 1 and the aforementioned effects introduced by interpolation which propagate to the neighbouring parameters $\theta_{\text{PMT}} \in (0^\circ, 3^\circ)$ thereafter.

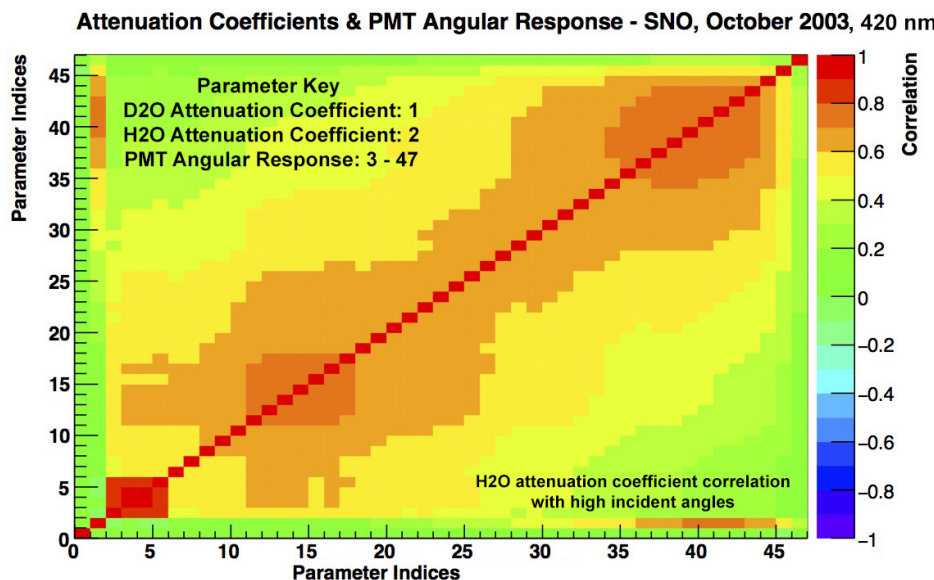


FIGURE 6.28: The correlation matrix for the fitted attenuation coefficients, $\alpha_{\text{D}_2\text{O}}$ and $\alpha_{\text{H}_2\text{O}}$ with the relative PMT angular response for the SNO October 2003 data set at 420 nm. The angular response is shown for values $\theta_{\text{PMT}} \in (0^\circ, 45^\circ)$. A strong correlation arises between $\alpha_{\text{H}_2\text{O}}$ and the angular response in the $\theta_{\text{PMT}} \in (30^\circ, 45^\circ)$ region.

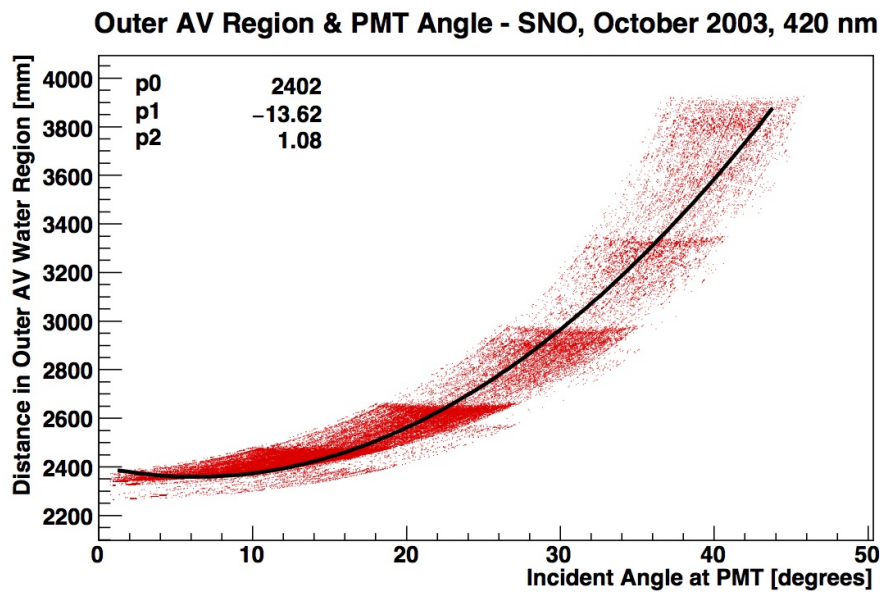


FIGURE 6.29: Shown is the incident angle and the corresponding distance travelled in the outer AV water region (red) for each PMT featured in the SNO October 2003 fit at 420 nm. Overlaid is a fit of a quadratic function (black) with corresponding coefficients p_0 , p_1 and p_2 . Overall, the distance through the water region increases quadratically with increasing incident angle.

6.2.6 Systematic Errors

Systematic errors are introduced through uncertainties in the calibration variables, in particular those related to the laserball e.g. position, light distribution and wavelength. In addition, and as discussed in Section 6.2.3, the PMT variability which features in the SNO data set is also a systematic that needs to be accounted for. The overall objective is to understand how robust the optical parameters are - in particular the attenuation coefficients - to these systematic changes. The following systematics were investigated:

- (1) **Laserball radial 1% shift, $|r_{LB}| \times 1.01$:** The radius of the laserball position in each run is moved outward by 1%. This effectively reduces the average time of flight for light to reach the PMTs from the laserball. This therefore accounts for uncertainties related to the group velocity of the detector materials and the timing of individual PMTs.
- (2) **Laserball (x, y, z) -coordinate discrete shift, $r_{x,y,z} \pm 50.0$ mm:** Based on the uncertainties of the fitted laserball position in the x -, y - and

z -coordinates from Figure 5.10 the position of the laserball is shifted by an exaggerated value of 50.0 mm in either the positive or negative x -, y - or z -directions.

- (3) **Laserball wavelength shift, $\lambda \pm \lambda_{\text{RMS}}$** : From MC studies of the detected wavelength distributions at PMTs for each of the laser dyes as reported in Table 5.2, the wavelength is both increased and decreased by the associated RMS value of its respective distribution. This small change in wavelength is designed to test the change in the refractive indices and consequently the related incident angles at the PMTs, θ_γ .
- (4) **Squared laserball angular anisotropy, $H^2(\cos_{\text{LB}}, \phi_{\text{LB}})$** : The laserball angular anisotropy is squared in order to probe the effect of the angular distribution on the optical parameters. This increases the maximal nominal laserball anisotropy in ϕ_{LB} from 4% to 8%.
- (5) **Flat laserball angular anisotropy, $H(\cos_{\text{LB}}, \phi_{\text{LB}}) = 1.0$** : Similar to the above, the assumption of a perfectly flat i.e. isotropic laserball angular distribution is enforced in order to gauge its effect on the optical parameters.
- (6) **Final upper χ^2 limit, $\chi^2_{\text{lim,f}} = 16, 9$** : As discussed in Section 6.1.1, the choice of the final upper χ^2 limit determines the size of the data sample over which the fit is performed. The upper limit is relaxed to $\chi^2_{\text{lim,f}} = 16$ in the case of the SNO and SNO+ MC data sets. An additional final limit of $\chi^2_{\text{lim,f}} = 9$ is also imposed on the SNO+ MC data for which the nominal limit is smaller ($\chi^2_{\text{lim,f}} = 7$).
- (7) **Zero PMT variability, $\sigma_{\text{PMT}} = 0$** : The PMT variability term, σ_{PMT} which was observed for the SNO data set is removed from the calculation of the χ^2 . This systematic is not applied for the SNO+ MC data set as no variation was implemented into RAT.
- (8) **Laserball flask radius, $d_{\text{innerAV}}^{-50.0\text{mm}}$** : The distance in the inner AV, d_{innerAV} region is reduced by 50.0 mm (the approximate radius of the laserball flask) to account for the fact that light will be emitted at the flask surface, not the centre. This systematic is only applied to the SNO data set (the SNO+ MC data set was not produced using a laserball geometry).

For each systematic featured above, the systematic change was applied to the associated variable and the entire optical fit was repeated. The subsequent output parameters were then used to calculate the systematic change in the nominal attenuation coefficient values. This systematic change was calculated by multiplying the fractional difference in the two parameter values by a scaling factor, s_i . In some cases, the systematic is applied to an exaggerated degree to ensure that the change probes any sensitivity of the optical parameters to a significant extent. In these cases the change is thereafter scaled down i.e. $s_i < 1$. The scaling factor used for each systematic is shown in Table 6.3.

Systematic Scaling Factors

No.	Systematic	Scaling Factor, s_i
1	$ r_{LB} \times 1.01$	0.2
2	$r_{x,y,z} \pm 50.0 \text{ mm}$	$r_{x,y} = 0.2, r_z = 0.5$
3	$\lambda \pm \lambda_{\text{RMS}} \text{ nm}$	1.0
4	$H^2(\cos \theta_{LB}, \phi_{LB})$	0.05
5	$H(\cos \theta_{LB}, \phi_{LB}) = 1.0$	0.05
6	$\chi_{\text{lim,f}}^2 = 16, 9$	1.0
7	$\sigma_{\text{PMT}} = 0$	1.0
8	$d_{\text{innerAV}}^{-50.0\text{mm}}$	1.0

TABLE 6.3: Systematic scaling factors.

The scaling factors, s_i are determined by the uncertainty on the aspect of the optical response they affect. For example, the scaling of the laserball radius by 1% is multiplied by a factor of $s_1 = 0.2$ to 0.2% in order to coincide with the approximate uncertainty associated with the material group velocities and PMT timings. Shifts in the laserball position by $\pm 50.0 \text{ mm}$ in the x - and y - directions are scaled by a factor of $s_2 = 0.2$ to approximate the 10.0 mm uncertainty associated with the laserball position in these directions. As shown in Figure 5.10, the z -coordinate is known to a lesser degree of accuracy, for which a larger scaling factor of $s_2 = 0.5$ is enforced. Variations in the laser wavelengths $\lambda \pm \lambda_{\text{RMS}}$, used to calculate the light paths and subsequent incident angles at the PMTs are expected to be small, for this reason the systematic changes remain unscaled ($s_3 = 1.0$). Modifications to the laserball angular distribution (systematics 4 and 5) are scaled by a value of $s_{4,5} = 0.05$ to reflect what is, at most, a $\sim 5\%$ uncertainty associated with variations in the angular distribution. Changes in the final upper χ^2 limit, $\chi_{\text{lim,f}}^2$ remain unscaled ($s_6 = 1.0$) as a change in this limit does not reflect any physical uncertainties associated with the detector. Systematic 7 is also unscaled

($s_7 = 1.0$) as a conservative measure to test the full effect of the PMT variability being included as a systematic correction to the overall calculation of the χ^2 . Finally, systematic 8 is unscaled ($s_8 = 1.0$) as the shift enforced is equal to a well known measurement of the laserball flask radius.

6.2.6.1 Systematic Variations

The range of uncertainties in the fitted attenuation coefficients for both the SNO and SNO+ MC data sets across all wavelengths for each systematic are shown in Table 6.4. The corresponding range of reduced χ^2 values for each of the fits wherein the systematic was applied for each data set is shown in Table 6.5². Examples of the individual systematic contributions to the total uncertainty in α_{D_2O} and α_{H_2O} for the SNO data set is shown in tables 6.6 and 6.7 for two wavelength scans at 369 and 505 nm. Similarly, tables 6.8 and 6.9 provide the same information on the systematics for $\alpha_{H_2O}^{comb.}$ and α_{AV} obtained from the SNO+ MC data set in water at 369 and 505 nm. Information for all wavelengths scans in both data sets can be found in Appendix C.1.

Attenuation Coefficient Uncertainties by Systematic

Systematic	SNO, Oct'03, D ₂ O		SNO+ MC, H ₂ O	
	α_{D_2O}	α_{H_2O}	$\alpha_{H_2O}^{comb.}$	α_{AV}
$ r_{LB} \times 1.01$	3.58-16.85%	2.51-32.41%	1.39-2.90%	4.85-68.04%
$r_{x,y,z} \pm 50.0$ mm	0.04-7.69%	0.06-30.57%	0-1.09%	0.02-69.88%
$\lambda \pm \lambda_{RMS}$ nm	0.02-1.11%	0.04-4.23%	0-0.01%	0.01-1.49%
$H^2(\cos \theta_{LB}, \phi_{LB})$	0-0.03%	0-0.16%	0-0.01%	0.01-0.07%
$H(\cos \theta_{LB}, \phi_{LB}) = 1.0$	0.04-0.68%	0.09-0.89%	4.71-10.82%	0.36-7.47%
$\chi^2_{lim,f} = 16$	0.02-11.50%	1.24-74.52%	0.29-0.96%	4.66-66.74%
$\chi^2_{lim,f} = 9$	N/A	N/A	0.03-0.29%	1.14-12.98%
$\sigma_{PMT} = 0$	2.79-18.86%	1.29-78.34%	N/A	N/A
$d_{innerAV}^{-50.0mm}$	0-0.19%	0.01-1.50%	N/A	N/A
Total	6.21-29.24%	4.8-121.21%	5.01-11.42%	10.30-141.84%

TABLE 6.4: Shown is the range of systematic uncertainties across all wavelength scans in the SNO and SNO+ MC data sets for their respective fitted attenuation coefficients; α_{D_2O} , α_{H_2O} (SNO) and $\alpha_{H_2O}^{comb.}$, α_{AV} (SNO+ MC).

²It was observed that the reduced χ^2 of the SNO 337 nm scan was large for both nominal and systematic fits, $\chi^2/\text{No.Dof} \geq 1.2$, these values are not included in Table 6.5. This has previously been observed and is possibly related to fluorescence in the optic fibre at this short wavelength [133].

Reduced χ^2 by Systematic		
Systematic	Reduced χ^2 , $\chi^2/\text{No.Dof}$	
	SNO, Oct'03, D ₂ O	SNO+ MC, H ₂ O
$ r_{LB} \times 1.01$	0.97-1.02	1-1.02
$r_{x,y,z} \pm 50.0 \text{ mm}$	0.97-1.03	1.02-1.04
$\lambda \pm \lambda_{\text{RMS}} \text{ nm}$	0.98-1.02	1-1.02
$H^2(\cos \theta_{LB}, \phi_{LB})$	0.98-1.03	1-1.02
$H(\cos \theta_{LB}, \phi_{LB}) = 1.0$	1.02-1.08	1.44-1.46
$\chi^2_{\text{lim,f}} = 16$	1.15-1.24	1.19-1.24
$\chi^2_{\text{lim,f}} = 9$	N/A	1.07-1.09
$\sigma_{\text{PMT}} = 0$	1.63-1.67	N/A
$d_{\text{innerAV}}^{-50.0\text{mm}}$	0.98-1.02	N/A

TABLE 6.5: Shown is the range of reduced χ^2 values across all wavelength scans in the SNO and SNO+ MC data sets.

From the SNO data set, the combined systematic uncertainty of α_{D_2O} is $\sim 6\text{-}30\%$ in the 337-620 nm region. The largest contributions to this uncertainty come from the radial laserball position shift, $|r_{LB}| \times 1.01$ and the removal of the PMT variability, $\sigma_{\text{PMT}} = 0$. Respectively, both these systematics contribute between $\sim 4\text{-}17\%$ and $\sim 3\text{-}19\%$ based on the wavelength. Similarly, the radial shift in the laserball position impacts the values of α_{H_2O} by up to $\sim 33\%$. However the largest contributions to the uncertainty on α_{H_2O} comes from relaxing the final upper χ^2 limit of the optical fit, $\chi^2_{\text{lim,f}} = 16$ leading to an uncertainty of up to $\sim 75\%$ and the removal of the PMT variability, $\sim 79\%$. Overall then, the value of α_{H_2O} varies between $\sim 5\text{-}122\%$. It is clear that the systematic uncertainties in the attenuation coefficients are non-negligible, especially in the case of α_{H_2O} where the uncertainty can exceed 100%. However, it is important to remember that these systematics are conservatively applied. Indeed, as shown in Table 6.5 the reduced χ^2 values of these larger contributions to the uncertainty are large $\chi^2/\text{No.Dof} \geq 1.15$, and it is arguable that these should be removed. In such cases the systematic uncertainty is reduced.

The SNO+ MC data set theoretically provides a better measurement of α_{H_2O} than the SNO data set as it combines the inner and outer AV regions. Values of $\alpha_{H_2O}^{\text{comb.}}$ are obtained with a systematic uncertainty in the range $\sim 5\text{-}12\%$. However, it is likely that in practice this uncertainty will be larger, as it would receive contributions from the PMT variability which is not currently modelled in RAT. For this MC data set, the largest contribution is from assuming a flat laserball angular

anisotropy; $L(\cos \theta_{LB}, \phi_{LB}) = 1.0$ which contributes $\sim 5\text{-}11\%$ uncertainty. Given that this data set was simulated with a known, non-flat distribution, removing this systematic from consideration reduces the overall uncertainty on $\alpha_{H_2O}^{\text{comb.}}$ to the order of 1-3%. A measurement of the acrylic attenuation length is very difficult overall. Values of α_{AV} are heavily affected by systematic changes in the laserball position, both by radial and linear shifts in the z -direction where the uncertainty can reach $\sim 70\%$. Overall the acrylic uncertainties range between 10-142%.

Attenuation Systematics - SNO October 2003, D₂O, 369 nm

Systematic	α_{D_2O} 10^{-5} mm^{-1}	$s_i \times \Delta\alpha/\alpha$	α_{H_2O} 10^{-5} mm^{-1}	$s_i \times \Delta\alpha/\alpha$	$\chi^2/\text{No.Dof}$
Nominal	0.93	0.00%	2.78	0.00%	0.98
$ r_{LB} \times 1.01$	0.67	-5.58%	-0.30	-22.16%	0.98
$r_x - 50.0 \text{ mm}$	0.93	0.14%	2.73	-0.40%	0.99
$r_x + 50.0 \text{ mm}$	0.91	-0.32%	2.71	-0.53%	0.99
$r_y - 50.0 \text{ mm}$	0.91	-0.40%	2.58	-1.49%	0.98
$r_y + 50.0 \text{ mm}$	0.94	0.30%	2.64	-1.00%	0.99
$r_z - 50.0 \text{ mm}$	0.98	2.89%	1.59	-21.44%	0.98
$r_z + 50.0 \text{ mm}$	0.87	-3.13%	3.79	17.97%	0.98
$\lambda - \lambda_{RMS} \text{ nm}$	0.92	-0.34%	2.74	-1.62%	0.98
$\lambda + \lambda_{RMS} \text{ nm}$	0.93	0.33%	2.83	1.71%	0.98
H^2	0.93	0.01%	2.78	-0.01%	0.98
$H = 1.0$	0.99	0.34%	3.16	0.68%	1.02
$\chi^2_{\text{lim,f}} = 16$	0.90	-2.62%	3.64	30.79%	1.16
$\sigma_{\text{PMT}} = 0$	1.03	10.76%	2.09	-24.93%	1.63
$d_{\text{innerAV}}^{50.0\text{mm}}$	0.93	0.04%	2.80	0.40%	0.98
Total		13.14%		53.41%	

TABLE 6.6: Systematic contributions to α_{D_2O} and α_{H_2O} from the SNO October 2003 data set with heavywater at 369 nm.**Attenuation Systematics - SNO October 2003, D₂O, 505 nm**

Systematic	α_{D_2O} 10^{-5} mm^{-1}	$s_i \times \Delta\alpha/\alpha$	α_{H_2O} 10^{-5} mm^{-1}	$s_i \times \Delta\alpha/\alpha$	$\chi^2/\text{No.Dof}$
Nominal	0.31	0.00%	4.87	0.00%	1.02
$ r_{LB} \times 1.01$	0.05	-16.85%	1.86	-12.36%	1.02
$r_x - 50.0 \text{ mm}$	0.31	-0.22%	4.71	-0.65%	1.03
$r_x + 50.0 \text{ mm}$	0.31	-0.13%	5.01	0.56%	1.03
$r_y - 50.0 \text{ mm}$	0.28	-2.03%	4.67	-0.81%	1.02
$r_y + 50.0 \text{ mm}$	0.34	1.97%	4.73	-0.58%	1.03
$r_z - 50.0 \text{ mm}$	0.35	6.67%	3.64	-12.61%	1.02
$r_z + 50.0 \text{ mm}$	0.26	-7.69%	6.14	13.03%	1.02
$\lambda - \lambda_{RMS} \text{ nm}$	0.31	-1.11%	4.80	-1.57%	1.02
$\lambda + \lambda_{RMS} \text{ nm}$	0.31	0.71%	5.08	4.23%	1.02
H^2	0.31	-0.01%	4.89	0.02%	1.03
$H = 1.0$	0.35	0.68%	4.96	0.09%	1.08
$\chi^2_{\text{lim,f}} = 16$	0.28	-10.07%	5.78	18.72%	1.24
$\sigma_{\text{PMT}} = 0$	0.37	18.86%	3.59	-26.41%	1.65
$d_{\text{innerAV}}^{50.0\text{mm}}$	0.31	-0.01%	4.87	0.02%	1.02
Total		29.24%		39.39%	

TABLE 6.7: Systematic contributions to α_{D_2O} and α_{H_2O} from the SNO October 2003 data set with heavywater at 505 nm.

Attenuation Systematics - SNO+ MC, H₂O, 369 nm

Systematic	$\alpha_{\text{H}_2\text{O}}$ 10^{-5} mm^{-1}	$s_i \times \Delta\alpha/\alpha$	α_{AV} 10^{-3} mm^{-1}	$s_i \times \Delta\alpha/\alpha$	$\chi^2/\text{No.Dof}$
Nominal	2.05	0.00%	1.39	0.00%	1.00
$ r_{\text{LB}} \times 1.01$	1.78	-2.61%	0.35	-14.96%	1.00
$r_x - 50.0 \text{ mm}$	2.05	-0.05%	1.39	-0.09%	1.02
$r_x + 50.0 \text{ mm}$	2.05	-0.03%	1.43	0.53%	1.02
$r_y - 50.0 \text{ mm}$	2.01	-0.43%	1.23	-2.30%	1.02
$r_y + 50.0 \text{ mm}$	2.09	0.36%	1.55	2.31%	1.02
$r_z - 50.0 \text{ mm}$	2.09	0.91%	0.90	-17.65%	1.00
$r_z + 50.0 \text{ mm}$	2.01	-1.09%	1.82	15.36%	1.00
$\lambda - \lambda_{\text{RMS}} \text{ nm}$	2.05	-0.01%	1.39	-0.01%	1.00
$\lambda + \lambda_{\text{RMS}} \text{ nm}$	2.05	-0.01%	1.40	0.31%	1.00
H^2	2.05	0.01%	1.39	-0.03%	1.00
$H = 1.0$	-2.11	-10.13%	1.66	0.97%	1.44
$\chi^2_{\text{lim,f}} = 16$	2.05	-0.29%	1.52	9.28%	1.19
$\chi^2_{\text{lim,f}} = 9$	2.05	0.06%	1.43	2.40%	1.07
Total		10.58%		29.58%	

TABLE 6.8: Systematic contributions to $\alpha_{\text{H}_2\text{O}}$ and α_{AV} from the SNO+ MC data set with water at 369 nm.**Attenuation Systematics - SNO+ MC, H₂O, 505 nm**

Systematic	$\alpha_{\text{H}_2\text{O}}$ 10^{-5} mm^{-1}	$s_i \times \Delta\alpha/\alpha$	α_{AV} 10^{-3} mm^{-1}	$s_i \times \Delta\alpha/\alpha$	$\chi^2/\text{No.Dof}$
Nominal	4.31	0.00%	0.29	0.00%	1.01
$ r_{\text{LB}} \times 1.01$	4.01	-1.39%	-0.69	-68.03%	1.02
$r_x - 50.0 \text{ mm}$	4.31	0.01%	0.33	3.41%	1.04
$r_x + 50.0 \text{ mm}$	4.31	0.00%	0.35	4.37%	1.03
$r_y - 50.0 \text{ mm}$	4.27	-0.19%	0.14	-10.42%	1.03
$r_y + 50.0 \text{ mm}$	4.35	0.18%	0.45	11.47%	1.03
$r_z - 50.0 \text{ mm}$	4.34	0.34%	-0.13	-72.97%	1.02
$r_z + 50.0 \text{ mm}$	4.27	-0.41%	0.67	68.11%	1.01
$\lambda - \lambda_{\text{RMS}} \text{ nm}$	4.31	0.00%	0.28	-1.49%	1.01
$\lambda + \lambda_{\text{RMS}} \text{ nm}$	4.31	0.00%	0.29	1.03%	1.01
H^2	4.31	0.00%	0.28	-0.07%	1.01
$H = 1.0$	0.25	-4.71%	0.57	4.99%	1.46
$\chi^2_{\text{lim,f}} = 16$	4.27	-0.79%	0.47	64.05%	1.24
$\chi^2_{\text{lim,f}} = 9$	4.30	-0.20%	0.32	12.98%	1.09
Total		5.01%		138.43%	

TABLE 6.9: Systematic contributions to $\alpha_{\text{H}_2\text{O}}$ and α_{AV} from the SNO+ MC data set with water at 505 nm.

6.3 Laserball Water Phase Prospects

The water phase of SNO+ will allow for the first full calibration of the detector since the end of SNO in 2006. This will provide clarification on any discrepancies in the modelling of the optical response between RAT and the true detector response. Most notably, the largest of these discrepancies is expected to be revealed by the true state of the PMT reflectors and their efficiencies. In the context of the optical model presented here, this will manifest in the PMT angular response. Indeed, a discrepancy in the angular response between RAT and original SNO data is already evident, with variations of up to 12% at large incident angles ($\theta_\gamma \geq 30^\circ$) between the MC and true response. This is largely due to the absence of an accurate PMT ageing model in RAT. Work on such a model is ongoing.

The advantage of a water phase is that, of all three phases, it allows for the most precise in-situ measurement of the water attenuation coefficient and the AV acrylic attenuation coefficient. Using the configuration of runs considered here, a combined treatment of the inner and outer AV water region has demonstrated that the maximum uncertainty on the attenuation coefficient is reduced from $\sim 120\%$ to $\sim 12\%$. In addition, this treatment of combining the inner and outer AV regions breaks the correlation between the acrylic and outer AV water regions. Despite being a very thin region of the detector volume, it has been demonstrated that such a treatment allows for the attenuation coefficient of the AV acrylic to be obtained. However, its value is subject to large systematic errors between 10-142% based on wavelength. In principle a scan consisting of laserball positions both inside and outside the AV should constrain and therefore reduce these uncertainties. The full, quantifiable extent of using laserball runs outside the AV is left for a future study.

Most importantly, and as will be discussed next, it should be emphasised that a determination of the water attenuation coefficient in the outer AV region during a scintillator-based phase is difficult with laserball data alone (similarly, measuring the AV acrylic attenuation is near impossible with scintillator in the detector). This is largely because the scintillator is more attenuating than water, and in cases of absorption and reemission the scintillation light is emitted isotropically. In addition, the isotropic and longer wavelength nature of this emitted light masks the PMT response at lower wavelengths. The water phase is therefore a critical prerequisite to the phases which will follow; it is the *only* opportunity to accurately

understand the optical properties which determine a significant component of the detector energy response; the attenuation coefficient of water and the PMT angular response (as illustrated by Figure 4.1). Such measurements are also important as they will be implemented into RAT for better tuning of MC data to that collected during the scintillator-based phases.

The significance of the proposed measurements described above should also be independently verified using data collected from the deployment of radioactive sources during the energy calibration. This will help to discriminate correlations associated with the model-dependent expectation of parameters presented here from the intrinsic values of the parameters themselves. Specifically, in this analysis neighbouring parameters in some regions of the PMT angular response are strongly correlated due to interpolation. This correlation is especially strong at low incident angles, $\theta_\gamma \in (0^\circ, 5^\circ)$. Furthermore, the angular response itself is negatively correlated to the intensity normalisations of individual laserball runs.

Finally, it is clear that further run positions may also be required in the inner AV to compensate for the increased shadowing of PMTs. For a nominal central run the shadowing is expected to increase from $\sim 11\%$ (SNO) to $\sim 33\%$ (SNO+) due to the AV hold-down ropes.

7

Optical Fit in Scintillator

Constant new discoveries in chemistry and optics are widening our field considerably and it is up to us to apply them to our technique; a technique that communicates what we see.

The Mind's Eye, Henri Cartier-Bresson

Presented in this chapter are the results from laserball scans in three different scintillator mixtures;

- SNO+ MC laserball scans in LABPPO
 - Laser wavelengths [nm]: 337, 369, 385, **400**, 420, 505.
- SNO+ MC laserball scans in LABPPO+0.3%Te+bis-MSB
 - Laser wavelengths [nm]: 337, 369, 385, 420, **446**, 505.
- SNO+ MC laserball scans in LABPPO+0.3%Te+perylene
 - Laser wavelengths [nm]: 337, 369, 385, 420, **490**, 505.

All three data sets were produced in RAT, each containing scans at five of the original laser wavelengths from SNO. The wavelength listed in bold is an additional wavelength designed to match the reemission peak of the wavelength shifting component of each mixture as described in Section 5.1.1.1. For brevity, henceforth and where not explicitly stated, the three data sets will be referred to by the wavelength

shifting component that characterises its scintillation profile, *PPO* (LABPPO), *bis-MSB* (LABPPO + 0.3%Te + bis-MSB) and *perylene* (LABPPO + 0.3%Te + perylene).

7.1 Optical Fit Results: LABPPO(+0.3%Te+Bis-MSB/Perylene)

The approach taken to perform the OCA-fit procedure on MC scintillator laserball data is no different to that used for the MC water laserball data as presented in Chapter 6. Subsequently, the same data selection criteria - cuts based on the prompt counts and PMT shadowing - as described in Section 4.4 are applied. The MC scintillator data also exhibits statistical characteristics similar to that of the MC water data; the data point pulls follow a Gaussian distribution with widths of a comparable size, see Figure 7.1. Therefore, the same final χ^2 upper limit ($\chi_{\text{lim},f}^2 = 7$) is used in the fitting procedure.

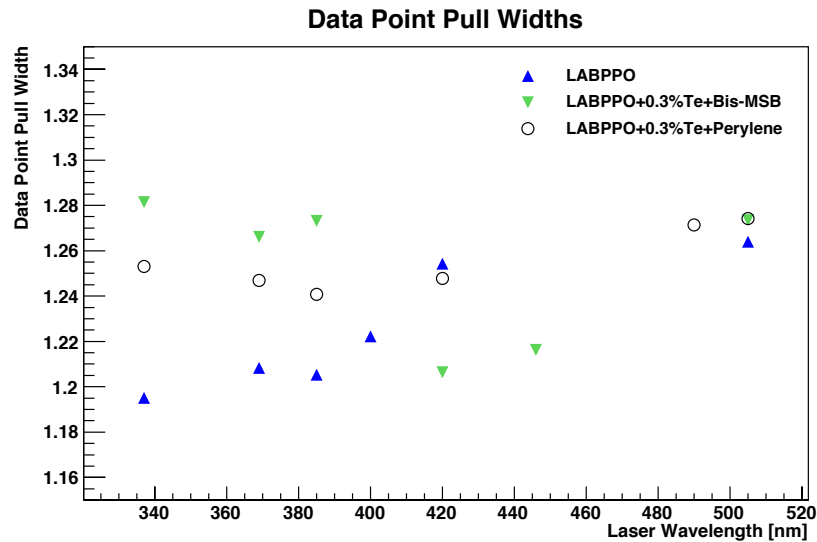


FIGURE 7.1: The fitted values of the Gaussian width, σ_λ for each of the data point pull distributions across all laserball scans in the three scintillator data sets.

7.1.1 Attenuation Coefficients

Values of the fitted attenuation coefficients, $\alpha_{\text{scint}}^{\text{ppo}}$, $\alpha_{\text{H}_2\text{O}}^{\text{bis.}}$ and $\alpha_{\text{H}_2\text{O}}^{\text{pery.}}$ alongside their respective statistical and systematic uncertainties are shown in Table 7.1. Also shown are the corresponding values of the water attenuation coefficients in the outer AV region, $\alpha_{\text{H}_2\text{O}}^{\text{ppo}}$, $\alpha_{\text{H}_2\text{O}}^{\text{bis.}}$ and $\alpha_{\text{H}_2\text{O}}^{\text{pery.}}$ as well as the reduced χ^2 values.

SNO+ MC - LABPPO, $\alpha \pm \text{stat.} \pm \text{sys.}$

λ [nm]	$\alpha_{\text{scint}}^{\text{ppo}}$ [10^{-5} mm $^{-1}$]	$\alpha_{\text{H}_2\text{O}}^{\text{ppo}}$ [10^{-5} mm $^{-1}$]	$\chi^2/\text{d.o.f.}$ [2 d.p.]
337	$10.66 \pm 0.01 \pm 0.22$	$9.21 \pm 0.10 \pm 2.02$	$137160 / 134109 = 1.02$
369	$15.04 \pm 0.01 \pm 0.25$	$9.81 \pm 0.10 \pm 1.98$	$121028 / 118564 = 1.02$
385	$10.22 \pm 0.01 \pm 0.22$	$5.06 \pm 0.08 \pm 1.82$	$131021 / 132776 = 0.99$
400	$6.88 \pm 0.01 \pm 0.26$	$4.96 \pm 0.08 \pm 1.48$	$115706 / 118545 = 0.98$
420	$5.06 \pm 0.01 \pm 0.24$	$4.86 \pm 0.08 \pm 1.56$	$117871 / 117670 = 1.00$
505	$2.37 \pm 0.01 \pm 0.24$	$6.65 \pm 0.09 \pm 1.55$	$114114 / 116871 = 0.98$

SNO+ MC - LABPPO+0.3%Te+Bis-MSB, $\alpha \pm \text{stat.} \pm \text{sys.}$

λ [nm]	$\alpha_{\text{scint}}^{\text{bis.}}$ [10^{-5} mm $^{-1}$]	$\alpha_{\text{H}_2\text{O}}^{\text{bis.}}$ [10^{-5} mm $^{-1}$]	$\chi^2/\text{d.o.f.}$ [2 d.p.]
337	$20.23 \pm 0.01 \pm 0.21$	$14.03 \pm 0.10 \pm 1.56$	$153472 / 132675 = 1.16$
369	$19.46 \pm 0.01 \pm 0.21$	$13.02 \pm 0.10 \pm 1.69$	$137958 / 122322 = 1.13$
385	$19.72 \pm 0.01 \pm 0.21$	$14.25 \pm 0.10 \pm 1.70$	$135668 / 119331 = 1.14$
420	$31.96 \pm 0.01 \pm 0.22$	$7.39 \pm 0.08 \pm 1.51$	$132680 / 127631 = 1.04$
446	$17.68 \pm 0.01 \pm 0.23$	$5.31 \pm 0.08 \pm 1.67$	$122536 / 123089 = 1.00$
505	$5.65 \pm 0.01 \pm 0.22$	$6.58 \pm 0.09 \pm 1.57$	$119010 / 120955 = 0.98$

SNO+ MC - LABPPO+0.3%Te+Perylene, $\alpha \pm \text{stat.} \pm \text{sys.}$

λ [nm]	$\alpha_{\text{scint}}^{\text{pery.}}$ [10^{-5} mm $^{-1}$]	$\alpha_{\text{H}_2\text{O}}^{\text{pery.}}$ [10^{-5} mm $^{-1}$]	$\chi^2/\text{d.o.f.}$ [2 d.p.]
337	$10.94 \pm 0.01 \pm 0.19$	$13.02 \pm 0.13 \pm 2.10$	$129457 / 121436 = 1.07$
369	$10.91 \pm 0.01 \pm 0.19$	$13.67 \pm 0.12 \pm 1.71$	$136878 / 127090 = 1.08$
385	$10.92 \pm 0.01 \pm 0.19$	$13.51 \pm 0.12 \pm 2.05$	$136771 / 128242 = 1.07$
420	$10.93 \pm 0.01 \pm 0.19$	$13.45 \pm 0.12 \pm 2.10$	$139176 / 128462 = 1.08$
490	$7.21 \pm 0.01 \pm 0.24$	$5.89 \pm 0.09 \pm 1.60$	$113591 / 115617 = 0.98$
505	$5.98 \pm 0.01 \pm 0.23$	$6.79 \pm 0.09 \pm 1.54$	$118106 / 119556 = 0.99$

TABLE 7.1: Attenuation coefficients of the inner AV scintillator and outer AV H_2O regions of the PPO (top), bis-MSB (middle) and perylene (bottom) data sets.

Across all data sets, each wavelength scan is fitted with a sample size consisting of $> 110,000$ data points. The statistical errors of the scintillator attenuation coefficients are therefore consistent with those obtained from studies of water data, $\leq 0.01 \times 10^{-5}$ mm $^{-1} \sim 0.03\text{-}0.17\%$. However, the systematic uncertainties are much smaller; the uncertainty on the scintillator attenuation coefficients is at

most $\sim 10\%$. As will be discussed, the absorption and reemission properties of the scintillator, and the overall higher attenuation in comparison to water reduces the impact of the systematic uncertainties. Using the reduced χ^2 as a measure of the fit, the optical model generally performs best in regions where the laser wavelength coincides, or is longer than the reemission peak of the wavelength shifting component. In these regions, the reduced χ^2 is close to 1, $\chi^2/\text{d.o.f.} \sim 1$. Therefore, absorption and reemission at shorter wavelengths reduces the accuracy to which the model can describe the data; the effectiveness of which varies based on the scintillator composition. This is related to the impact of absorption and reemission on the other parameters in the optical model; the PMT angular response and the laserball light distribution. A discussion of this impact is discussed in sections 7.1.2 and 7.1.3.

Shown for the PPO, bis-MSB and perylene data sets in figures 7.2 and 7.3 are the fitted attenuation coefficients (black) plotted against the expected total attenuation of the scintillator (red), and the absorption and reemission profiles of the relevant wavelength shifter (blue). Also shown for the bis-MSB and perylene data is the absorption spectrum for the tellurium surfactant, PRS.

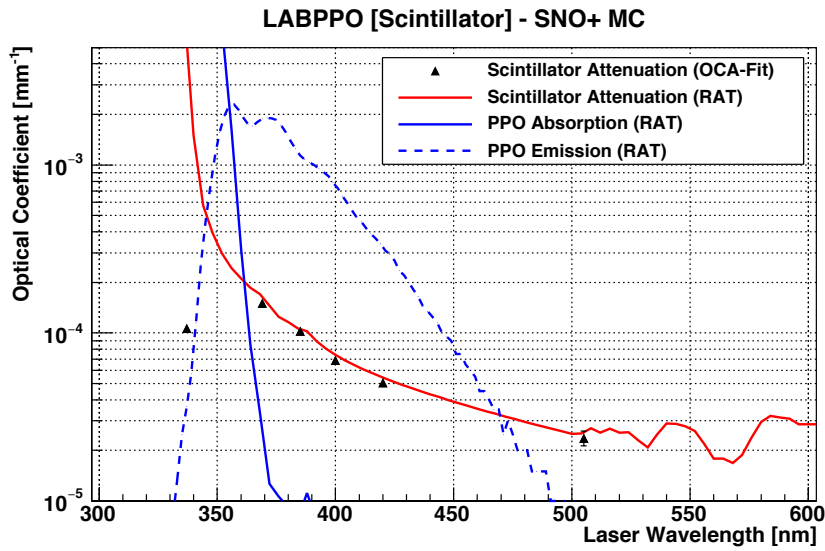


FIGURE 7.2: Shown are the fitted attenuation coefficient values for LABPPO (black). The expected attenuation of the scintillator as used by RAT is shown in red. In solid and dashed blue are the respective PPO absorption and reemission profiles. Both statistical and systematic errors are shown but are small.

Figures 7.2 and 7.3 illustrate three important and interesting characteristics that scintillator and the action of absorption and reemission has on the optical model.

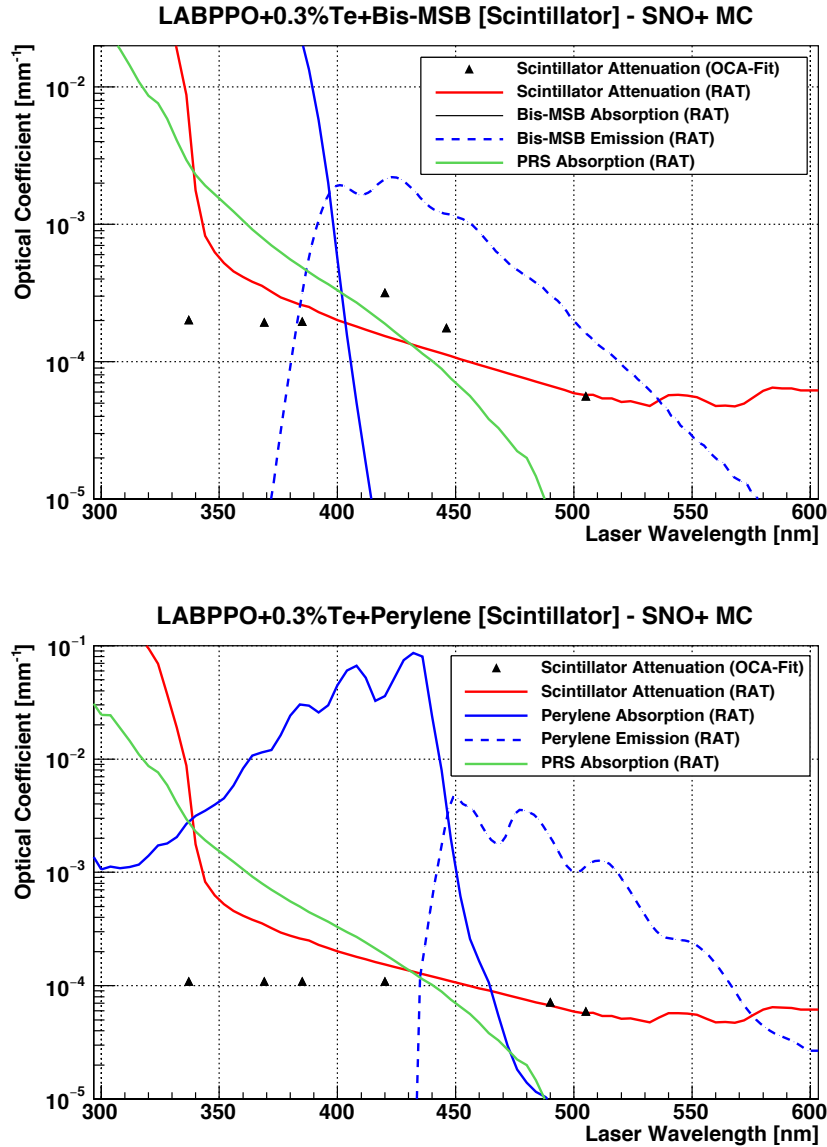


FIGURE 7.3: Shown are the fitted attenuation coefficient values for the bis-MSB (top) and perylene (bottom) data sets. The expected attenuation of the scintillator as used by RAT is shown in red. In solid and dashed blue are the respective bis-MSB/perylene absorption and reemission profiles. The absorption coefficient spectrum of PRS is shown in green. Both statistical and systematic errors are shown but are small.

The first feature of note is that for a given scintillator mixture, the effective attenuation coefficient at wavelengths for which light is absorbed and reemitted is the same, regardless of the initial laser wavelength - it is wavelength independent. This can be seen for the scans in bis-MSB at 368 and 385 nm, $\alpha_{\text{scint.}}^{\text{bis.}} \sim 20 \times 10^{-5} \text{ mm}^{-1}$,

and in perylene at 337, 369, 385 and 420 nm, $\alpha_{\text{scint}}^{\text{pery.}} \sim 10 \times 10^{-5} \text{ mm}^{-1}$.¹ Consequently, and as shown in Figure 7.3, the fitted attenuation coefficients appear to *flat-line* in these wavelength regions. This flat distribution coincides where the absorption length of the wavelength shifter is very small, $\sim 1\text{-}100$ mm. It is reasonable to expect; chemically, the wavelength shifter is *blind* to the specific energy of an absorbed photon provided it is sufficient to excite electrons through which a new reemission photon can be created.

The second important feature follows on from the first, and is related to the composite nature of the scintillator mixtures themselves. As described in Chapter 3, the emission of light by the scintillator is the result of an initial absorption by the solvent (LAB) followed by a series of radiative or non-radiative energy transfers that ultimately lead to the excitement of the wavelength shifter, emitting a characteristic scintillation profile. Therefore, to ensure a sufficient light yield, the wavelength shifter needs to be the most *active*, absorbing component during this energy transfer prior to emission. This is especially true for the bis-MSB and perylene mixtures which are required to shift the PPO emission spectrum to longer wavelengths. Subsequently, the effective attenuation of reemitted light should coincide with the attenuation of the most absorbing scintillator component in the reemission region. This is demonstrated well in the PPO data set for the 337 nm scan, for which the attenuation coefficient, $\alpha_{\text{scint}}^{\text{ppo}} \simeq 10 \times 10^{-5} \text{ mm}^{-1}$, coincides with the attenuation at ~ 385 nm, which resides within the main reemission region 340-400 nm.

This characteristic is made more complex in the bis-MSB and perylene data sets due to the presence of PRS. In the perylene data set, the perylene is far more absorbing than either the LAB or the PRS in the 340-465 nm region, and approximately equal to LAB at 337 nm. In the main reemission region 470-500 nm, the absorption lengths of LAB, perylene and PRS are sufficiently long (≥ 10 m) that the reemitted light can escape the AV without being reabsorbed. PRS becomes problematic within the main reemission region of the bis-MSB data set at around 420 nm where the absorption length is approximately 5 m; less than the radius of the AV. However, the fitted attenuations at 337, 369 and 385 nm for which light is absorbed and remitted is less than that at 420 nm. This suggests that the bis-MSB, on average, emits above 420 nm, which was indeed confirmed by MC

¹Light is only absorbed and reemitted for one wavelength in the PPO data set at 337 nm. However, more scans close to this wavelength would expect to reveal the same feature.

studies in Section 5.1.1.1, and which motivated the additional scan in bis-MSB at 446 nm. Ultimately, in bis-MSB shorter wavelength light circumvent the higher absorption regions of PRS, $\lambda \sim 390\text{-}430$ nm by being absorbed and reemitted at longer wavelengths, $\lambda \geq 430$ nm where the PRS is sufficiently transparent for it not to be reabsorbed.

The overall attenuation coefficient of the scintillator is determined by the individual properties of its constituent components. However, what is being measured here is an *effective* in-situ attenuation that is not only determined by the scintillator, but also the dimensions of the detector itself, specifically the radius of the AV. This is the third and final notable feature. As described in the previous paragraph, reemitted light is able leave the AV provided the absorption lengths of the individual scintillator components are sufficiently large. This explains why the fitted attenuation coefficient of reemitted light in the PPO and perylene data sets are roughly equivalent, $\alpha_{\text{scint}} \simeq 10 \times 10^{-5} \text{ mm}^{-1}$, corresponding to an attenuation length of ~ 10 m. Despite using different wavelength shifters the data sets are constrained by a fixed AV radius, whose dimensions ultimately impinge upon the final fitted value. The PPO and perylene are similar in that their respective wavelength shifters are the most absorbing components prior to reemission. This is not shared with the bis-MSB data, where instead the PRS is the most absorbing component in the reemission region. PRS does not reemit any light it absorbs, and as a result, the fitted attenuation coefficient of reemitted light in this data set is approximately twice as large, $\alpha_{\text{scint}}^{\text{bis.}} \simeq 20 \times 10^{-5} \text{ mm}^{-1}$ corresponding to an attenuation length of ~ 5 m.

Shown in Figure 7.4 is a comparison of the effective attenuation lengths of the three scintillator mixtures. Also shown, and in relation to these are the geometric aspects of the AV; its diameter, $d_{\text{AV}} = 12$ m and the range of mean light path lengths through the inner AV region, $\langle d_{\text{innerAV}} \rangle \in (5.2, 5.8)$ m. This illustrates the similarities between the attenuation lengths and the dimensions of the AV. In the 337-390 nm region, the attenuation lengths are less than the diameter of the AV, and as has been discussed, light is prone to being absorbed and reemitted (PPO, perylene) and/or lost (bis-MSB) in this region depending on the scintillator. All three scintillators are relatively transparent at long wavelengths, $\lambda \geq 480$ nm. This constraint of the detector geometry on the attenuation is perhaps the most important of the three discussed here. The perylene and bis-MSB are currently

candidate mixtures, and the loss of light through PRS absorption disfavours the bis-MSB mixture from being selected.

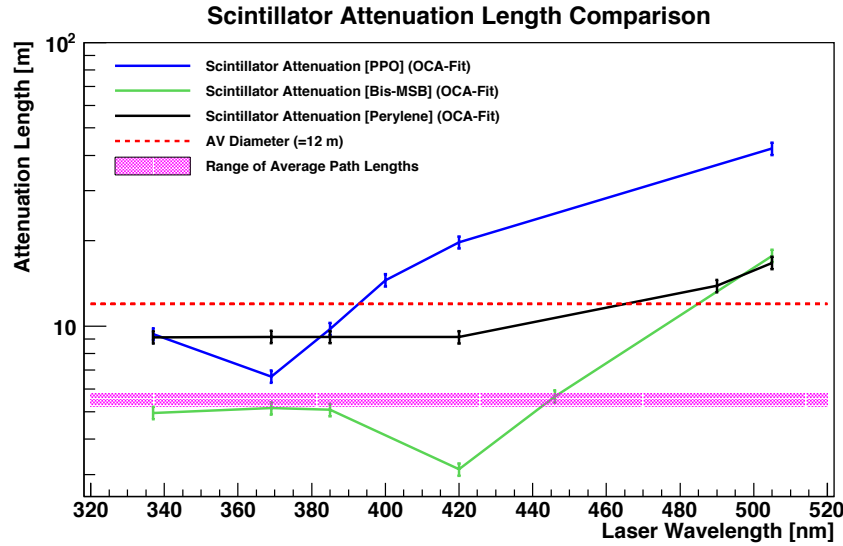


FIGURE 7.4: The effective attenuation lengths in the three different scintillator mixtures; PPO, bis-MSB and perylene. Values are based on the fitted attenuation coefficients obtained from the optical fit. The error on each point is both statistical and systematic. Shown also for comparison is the diameter of the AV ($d_{\text{AV}} = 12 \text{ m}$) and the range of average light path lengths through the inner AV (scintillator) region for a wavelength scan, $\langle d_{\text{innerAV}} \rangle \in (5.2, 5.8) \text{ m}$.

The fitted values of the water attenuations, $\alpha_{\text{H}_2\text{O}}^{\text{PPO}}$, $\alpha_{\text{H}_2\text{O}}^{\text{bis}}$ and $\alpha_{\text{H}_2\text{O}}^{\text{pery}}$ are inconsistent with the expected values used in RAT. As shown in Figure 7.5, the values are much larger, and at wavelengths that are absorbed and reemitted consistent with the attenuation of the scintillator itself, $\alpha_{\text{H}_2\text{O}} \simeq 10 \times 10^{-5} \text{ mm}^{-1}$. The only region for which the fit provides near-consistent results is in the optically transparent region at wavelengths 490 nm in perylene and at 505 nm in all three data sets. At 505 nm the values obtained are all consistent with one another, but still out of systematic uncertainty with the expected value.

A fit of the water region is therefore at a two-fold disadvantage in scintillator. First, the water region is only probed by light after it has passed through a more attenuating medium. Comparing the attenuation in scintillator with the water values obtained in Chapter 6, the attenuation in scintillator is up to 5 times stronger than in water. This is compounded further by the fact that, on average, $\sim 63\%$ of the path length is through this more attenuating medium. The strong attenuation

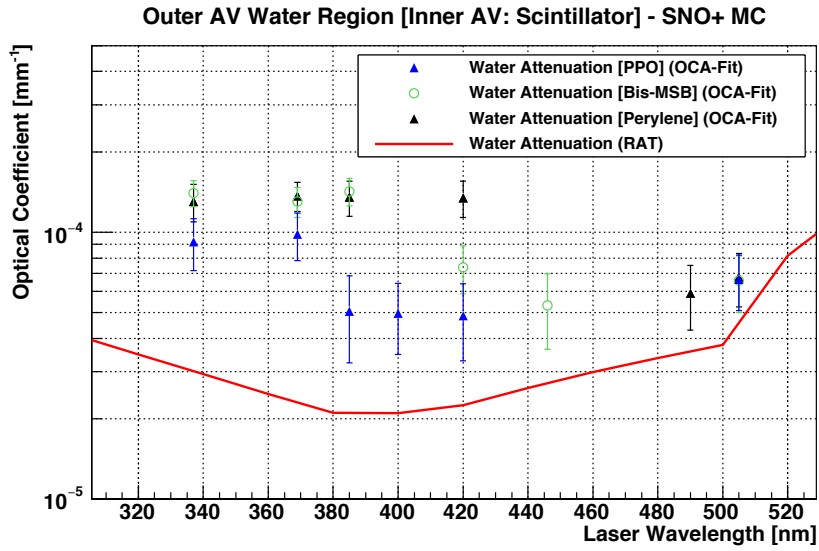


FIGURE 7.5: The fitted attenuations in the outer AV water region from the PPO (blue), bis-MSB (green) and perylene (black) scintillator data sets. Shown in red is the expected attenuation length used in RAT. Errors shown are both statistical and systematic. Overall, the values of the water attenuation are affected by absorption and reemission of light in the scintillator prior to leaving the inner AV region. The attenuation lengths therefore do not coincide with the expected value.

of the scintillator therefore biases the fitted values of the water attenuation coefficients. This can be illustrated by considering the attenuation weighted by path length;

$$\alpha_{\text{total}}^{\text{path}} = \sum_i^{\text{path}} f_i \alpha_i, \quad f_i = \langle d_i \rangle / \sum_i^{\text{path}} \langle d_i \rangle, \quad (7.1)$$

where i denotes the different components of the path length through the scintillator, acrylic and water, $\langle d_i \rangle$ denotes the average path length over all laserball positions in each of these regions and f_i denotes the weight of this distance as a fraction of the average total path length. A plot of this total attenuation is shown in Figure 7.6 for the PPO data set. At 337, 369, 385, 400 and 420 nm the water attenuations become biased by the strong attenuation of the scintillator. This effect is inverted at longer wavelengths such as 505 nm where the water is more attenuating.

The OCA-fit identifies the global χ^2 minimum of the scintillator and water attenuation coefficients. A χ^2 scan about the minimum is shown in Figure 7.7 for

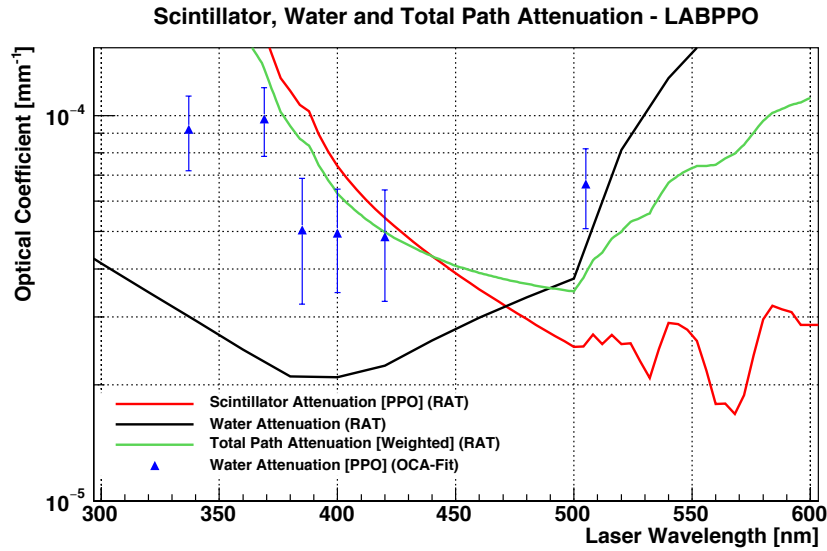


FIGURE 7.6: Shown in green is the weighted path attenuation in LABPPO as described by Equation 7.1. Shown in black and red are the attenuations of water and scintillator in RAT. The points plotted in blue are the fitted attenuations in the water regions obtained from an optical fit of laserball scans in LABPPO. Errors are both statistical and systematic.

the PPO and perylene data set at 385 nm. As shown, the parameter space is very steep in $\alpha_{\text{scint}}^{\text{ppo}}$ and $\alpha_{\text{scint}}^{\text{pery}}$ and broad in $\alpha_{\text{H}_2\text{O}}^{\text{ppo}}$ and $\alpha_{\text{H}_2\text{O}}^{\text{pery}}$. This is reflective of the aforementioned weakness of the fit to identify the expected attenuation in the water region due to the attenuating strength of the scintillator.

Aside from long wavelength regions where the scintillator is relatively transparent, both the attenuating strength of the scintillator and the action of absorption and reemission affect the OCA-fit description of the other optical parameters. Its impact on the water attenuation coefficient has been presented; what follows now is a summary of the impact it has on the other parameters; the relative PMT angular response and the laserball light distribution.

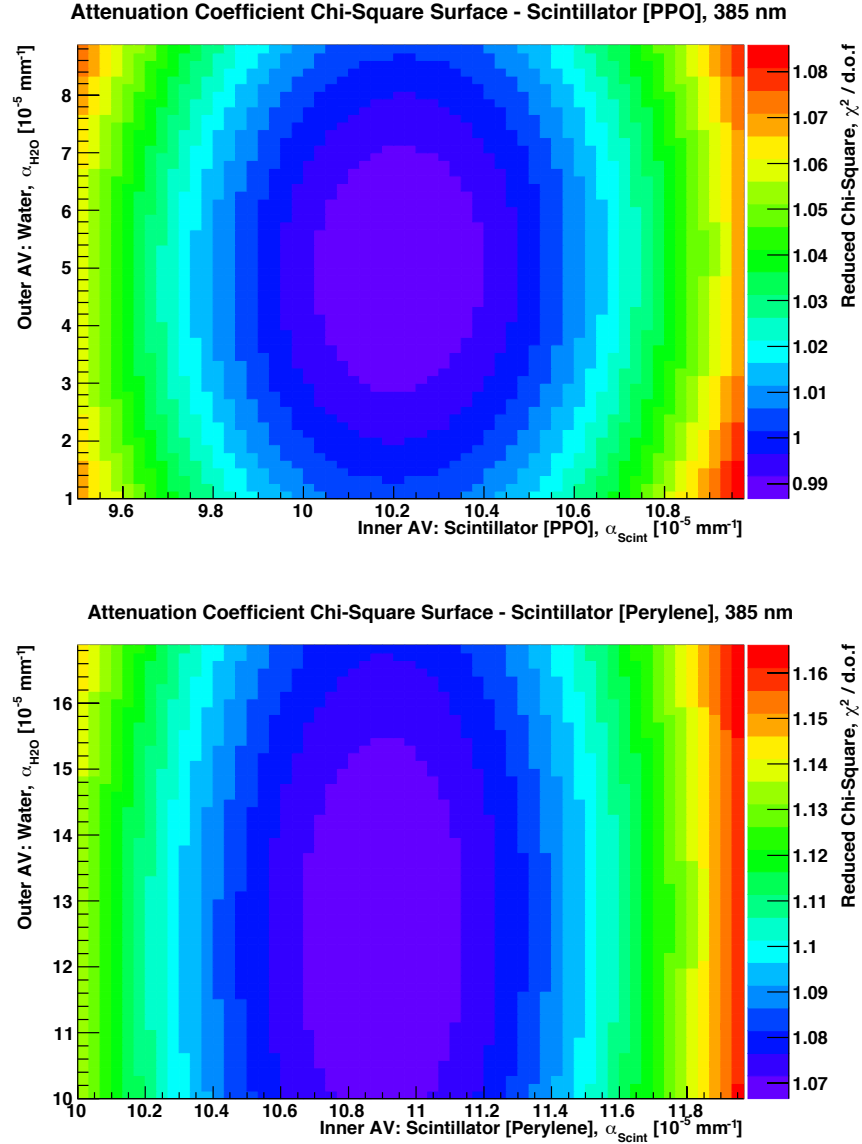


FIGURE 7.7: The reduced χ^2 surface between the inner scintillator and outer AV water attenuation coefficients for the 385 nm laserball scans in LABPPO (top) and LABPPO+0.3%Te+perylene (bottom). The surfaces are smooth with the fitted values identified by the OCA fit residing in a global minimum.

7.1.2 PMT Angular Response

The fitted relative PMT angular response distributions are shown in figures 7.8 and 7.9. These reflect the response at the wavelength at which light leaves the AV. Consequently, at wavelengths that are absorbed and reemitted, the distributions are equivalent, and reflect the response at the average reemission wavelength of the respective wavelength shifter. The equivalence of distributions at reemitted wavelengths is most prominent in the perylene data set, in which four of the six wavelengths are absorbed and reemitted; 337, 369, 385 and 420 nm. Similarly, the effect of absorption and reemission is exhibited in bis-MSB at 337, 369, and 385 nm and in PPO at 337 nm.

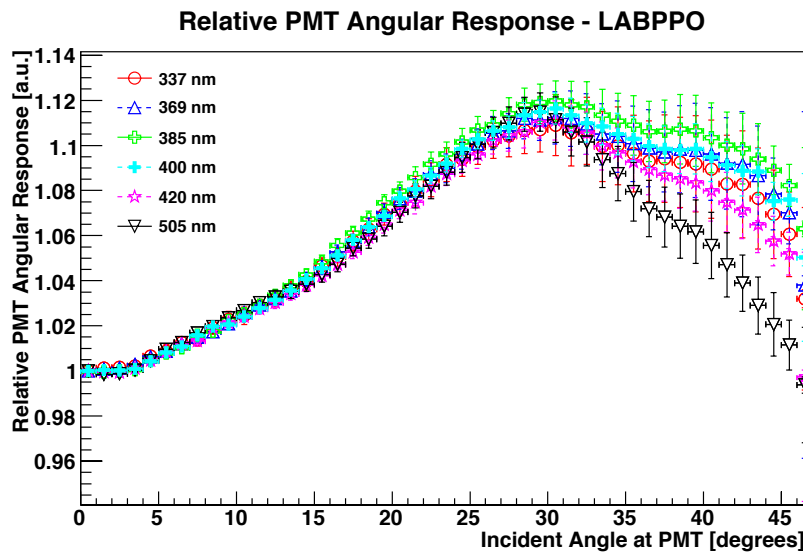


FIGURE 7.8: The fitted relative PMT angular response for the LABPPO data set. Errors are both statistical and systematic.

As expected, the PMT response is robust to systematic changes to the same extent as those obtained from MC water data discussed in Section 6.2.2. The combined statistical and systematic error on each parameter per degree of incident angle is small, $\sim 0.1\text{-}1\%$ in the range $\theta_{\text{PMT}} \in (0^\circ, 42^\circ)$ and at most $\sim 3\%$ at higher angles $\theta_{\text{PMT}} \geq 42^\circ$.

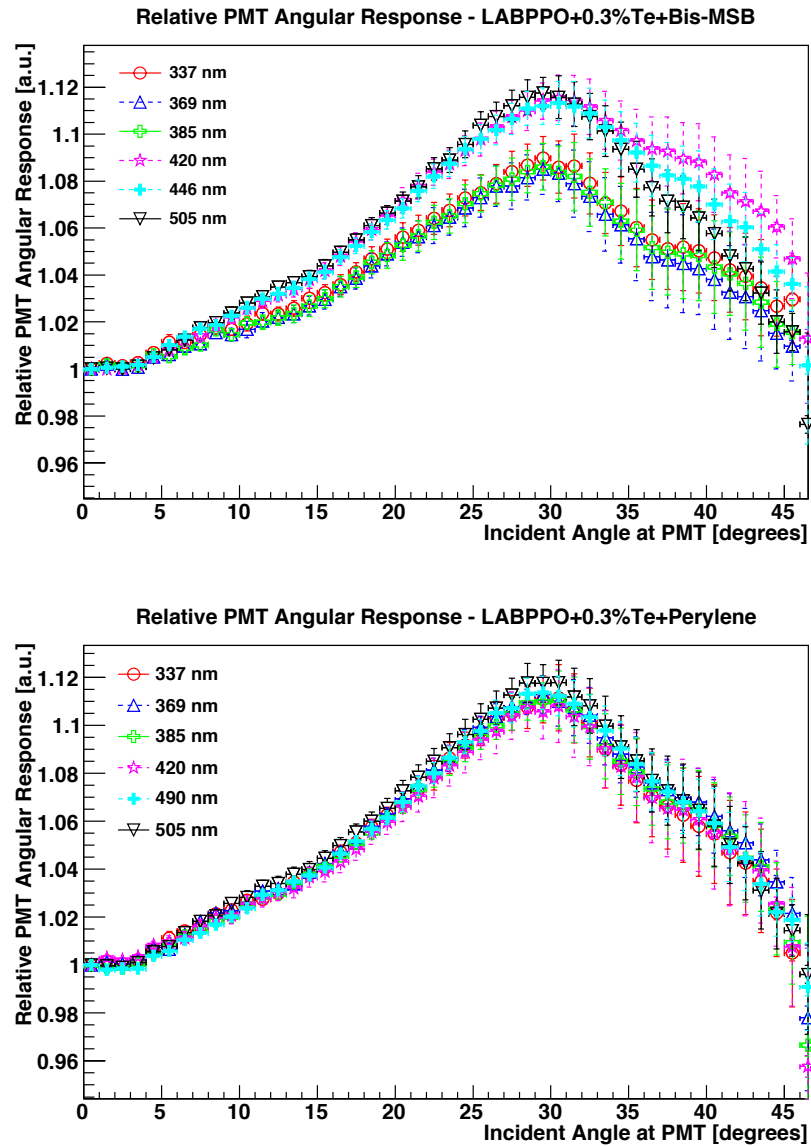


FIGURE 7.9: The fitted relative PMT angular response for the bis-MSB (top) and perylene (bottom) data sets. Errors are both statistical and systematic.

7.1.3 Laserball Light Distribution

At wavelengths that are absorbed, the isotropic nature of the subsequent scintillation light suppresses the directional information of the laserball anisotropy. Ultimately, this directional information is not preserved. This impacts the interpretation of the optical model to the laserball mask and angular distribution. The fitted laserball masks across all wavelengths of the PPO, bis-MSB and perylene data sets are shown in Figure 7.10. The angular distributions are shown in figures 7.11, 7.12 and 7.13. In the transparent wavelength regions the expected form of the mask is returned. At absorbed wavelengths the mask functions are relatively flat compared to the expected form. These flat distributions increase by at most $\sim 10\%$ above the normalisation value ($P_4 = 1, \cos \theta_{LB} = -1$) as $\cos \theta_{LB}$ increases. This behaviour is counter-intuitive; increasing in intensity towards the (known) shadowed regions of the laserball. This effect does not have a physical interpretation; rather it is likely to compensate for fluctuations in the effectively flat angular distributions at absorbed wavelengths.

Absorption and reemission mask the intrinsic $\pm 4\%$ angular anisotropy of the laserball distribution which is only preserved at wavelengths where the scintillator is optically transparent. This fact can be exploited to allow for a model-independent test of the optical transparency of the scintillator along the wavelength spectrum 337-505 nm. In general, the anisotropy of the laserball is revealed by calculating the ratio of PMT hits, N_{Hit} per PMT from two central laserball runs at different orientations (where the laserball is rotated about ϕ_{LB}). If the scintillator is strongly absorbing, this ratio is reduced to unity by the isotropic action of the reemission. This ratio can therefore be used as a measure of where along the wavelength spectrum a particular scintillator mixture transitions from being predominantly absorbing to relatively transparent. An example of these N_{Hit} ratios at five wavelengths are shown in Figure 7.14 for the PPO and bis-MSB data sets. Particularly in the case of the bis-MSB data set, this representation of the PMT N_{hit} ratios provides further evidence that the source of the high attenuation in the 390-430 nm region of this data set (see Section 7.1.1) is caused by the PRS (the laserball anisotropy is preserved at 420 nm) and not the reemission following absorption by the bis-MSB wavelength shifter.

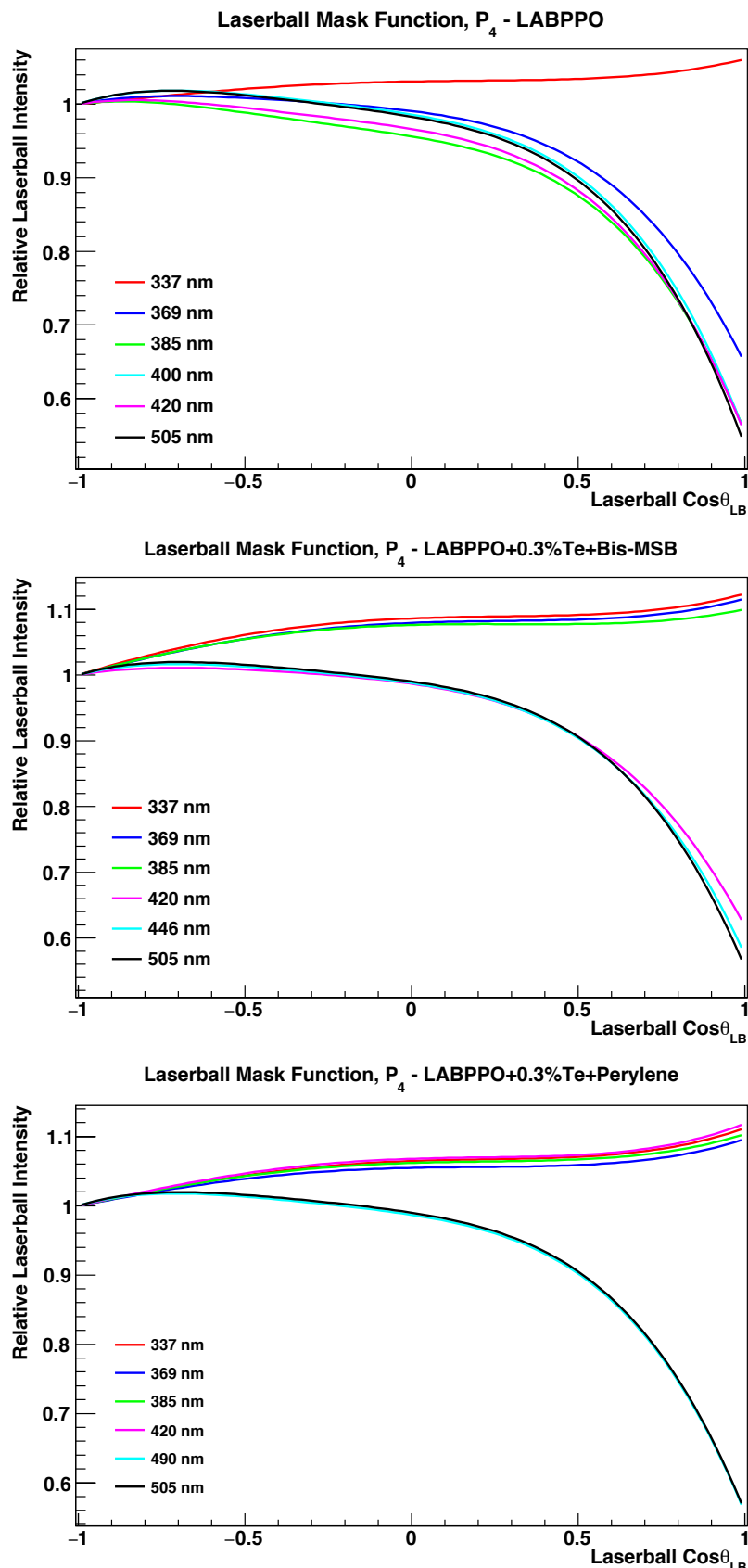


FIGURE 7.10: Shown are the fitted laserball masks at different wavelengths for each of the PPO (top), bis-MSB (middle) and perylene (bottom) data sets.

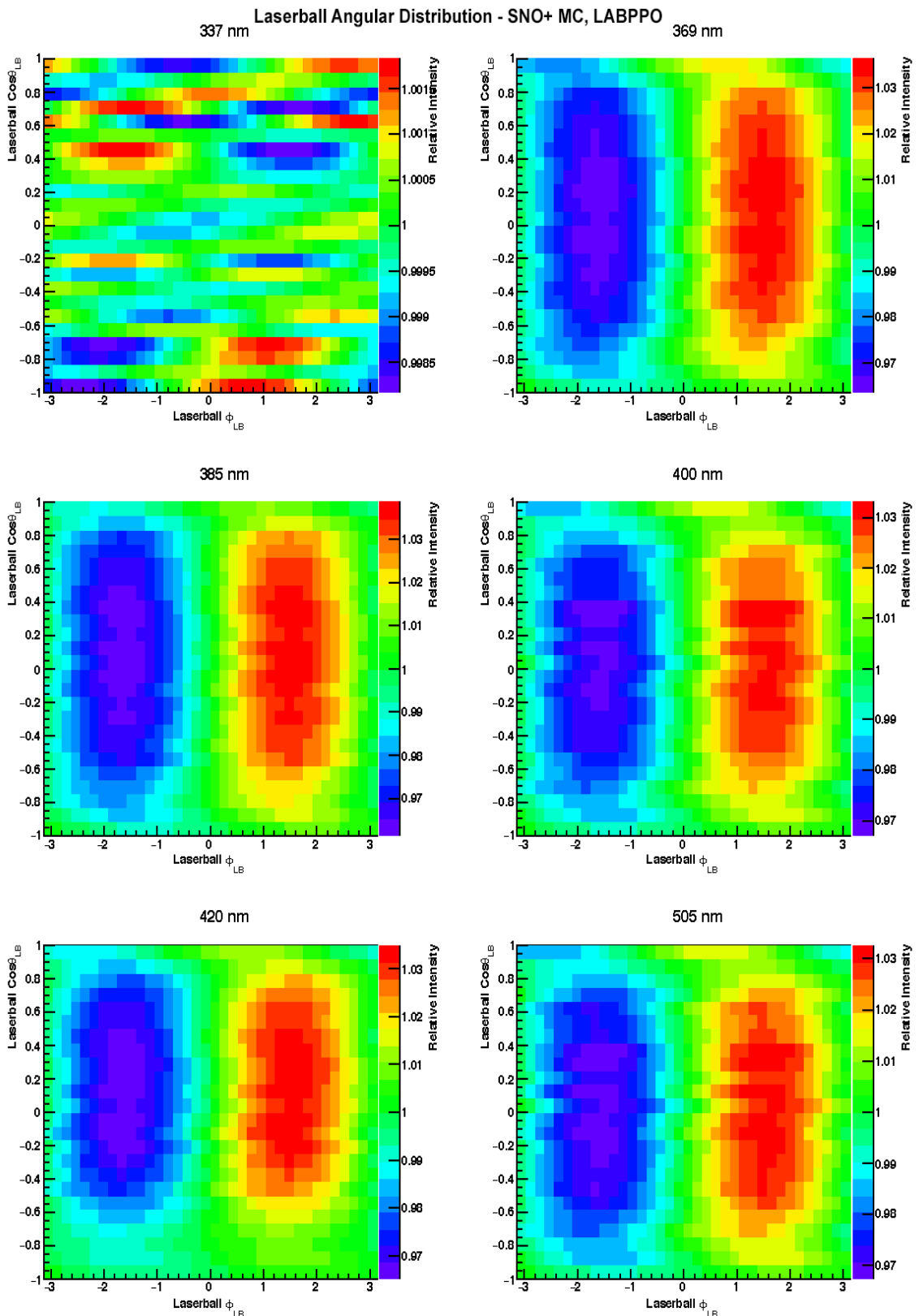


FIGURE 7.11: The fitted laserball angular distributions from the PPO data set. Distributions were fitted using a sinusoidal model composed of 24 $\cos \theta_{\text{LB}}$ slices. At 337 nm the angular distribution is reduced to being relatively flat as a result of absorption and reemission.

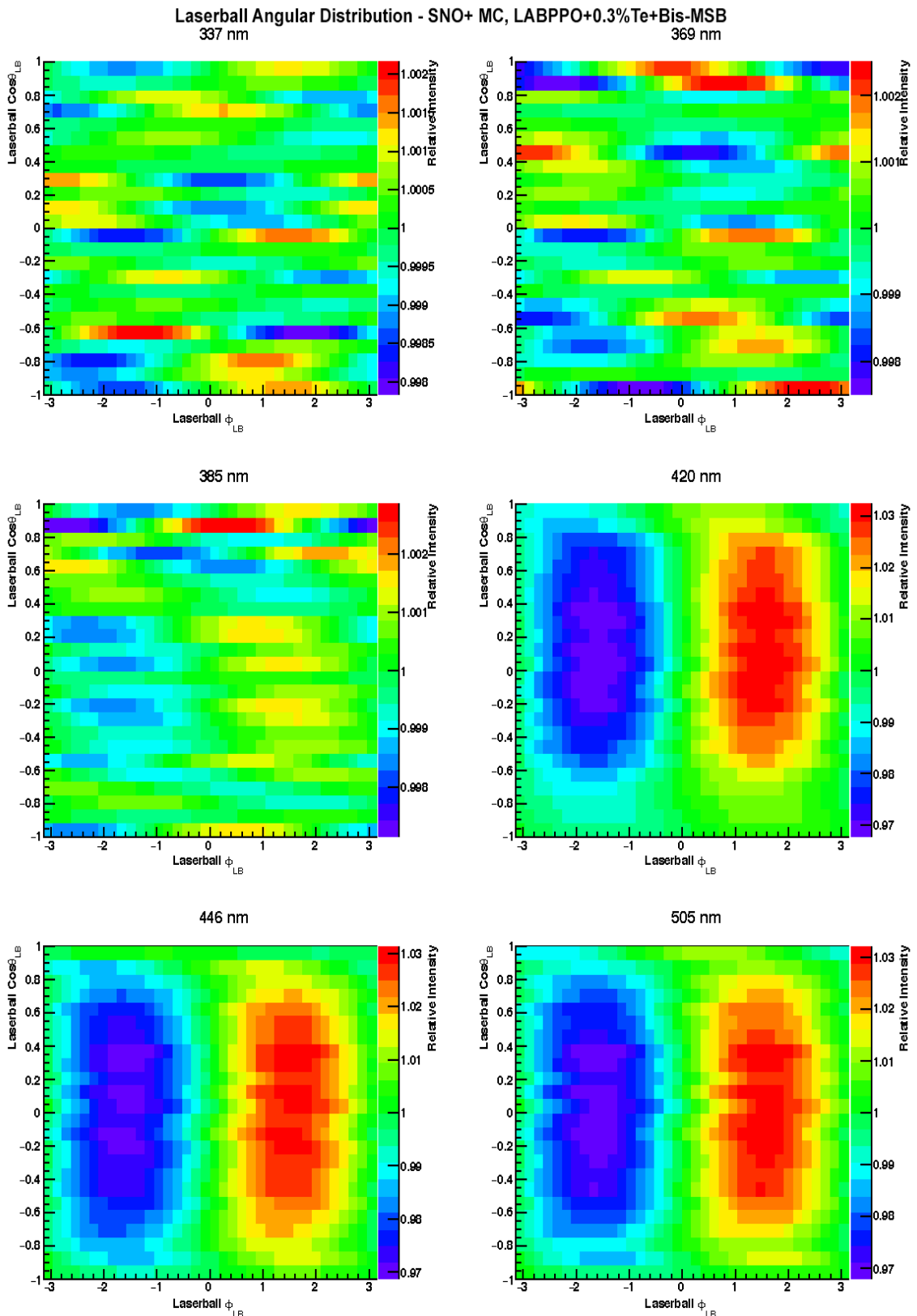


FIGURE 7.12: The fitted laserball angular distributions from the bis-MSB data set. Distributions were fitted using a sinusoidal model composed of 24 $\cos \theta_{LB}$ slices. At 337, 369 and 385 nm the angular distribution is reduced to being relatively flat as a result of absorption and reemission.

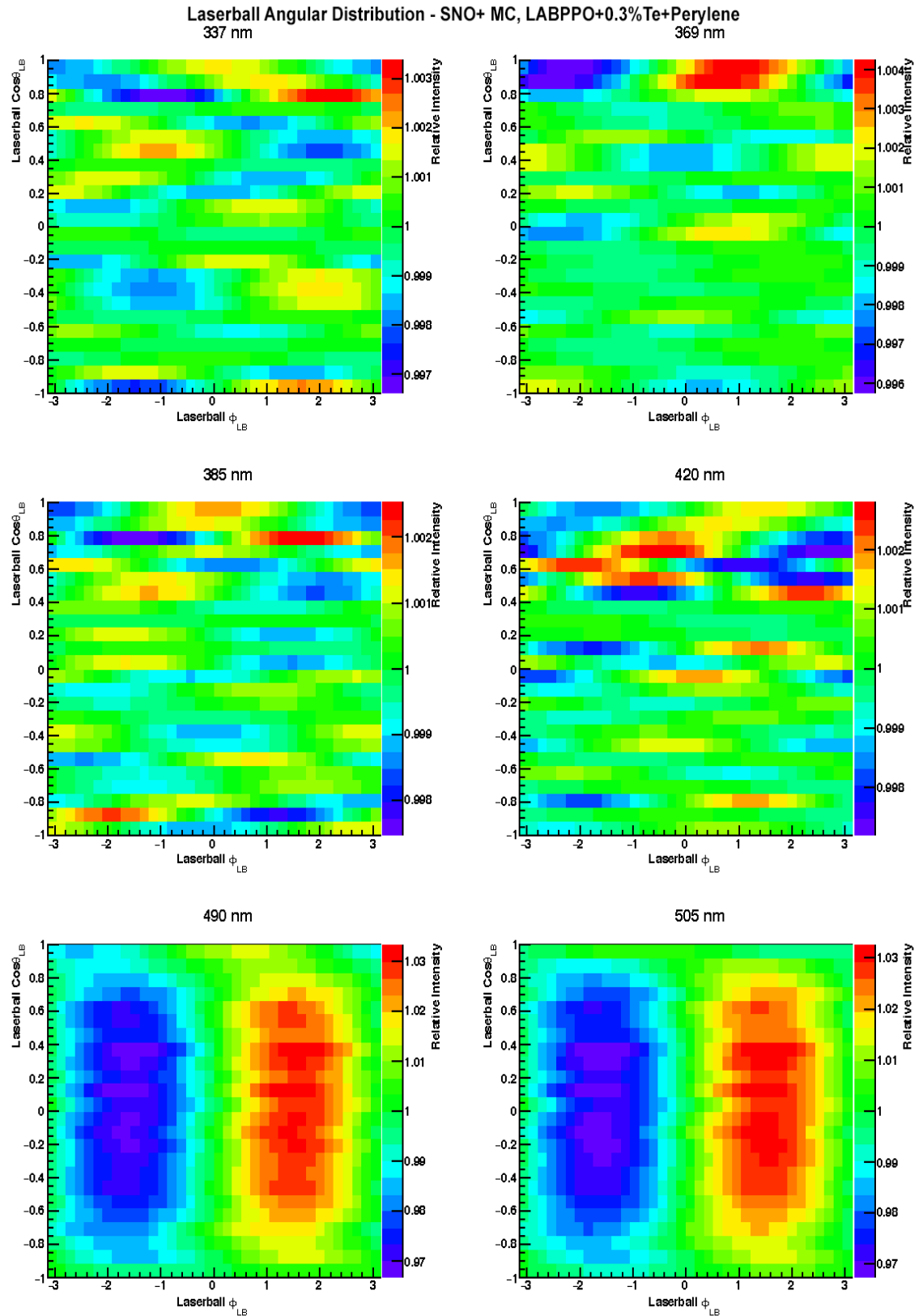


FIGURE 7.13: The fitted laserball angular distributions from the perylene data set. Distributions were fitted using a sinusoidal model composed of 24 $\cos\theta_{LB}$ slices. At 337, 369, 385 and 420 nm the angular distribution is reduced to being relatively flat as a result of absorption and reemission.

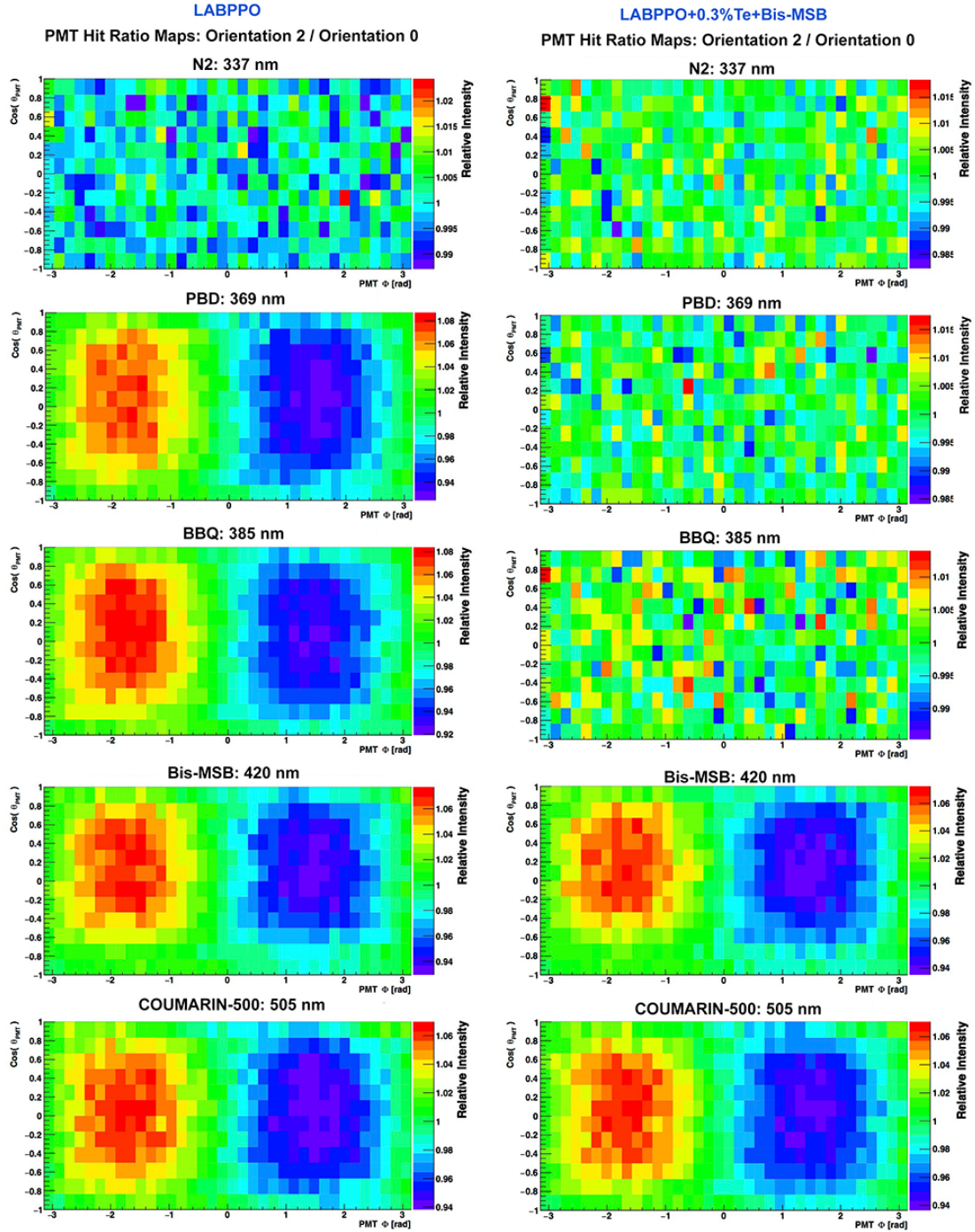


FIGURE 7.14: The distribution of the N_{Hit} ratios for the PPO and bis-MSB data sets at 337, 369, 385, 420 and 505 nm from central runs at two different orientations: orientation-0: $\phi_{\text{LB}} = 0$ and orientation-2: $\phi_{\text{LB}} = \pi$.

7.1.4 Covariance Matrix & Parameter Correlations

The optical model does not directly account for the action of absorption and reemission on the detector response; these effects are only interpreted through the parameter values and not the physics they describe. Therefore, the same calculations of the optical model in scintillator as in water leave the correlations largely the same. In the transparent regions of the scintillator they are no different to water; an example of the correlations in the bis-MSB data set at 420 nm is shown in Figure 7.15.

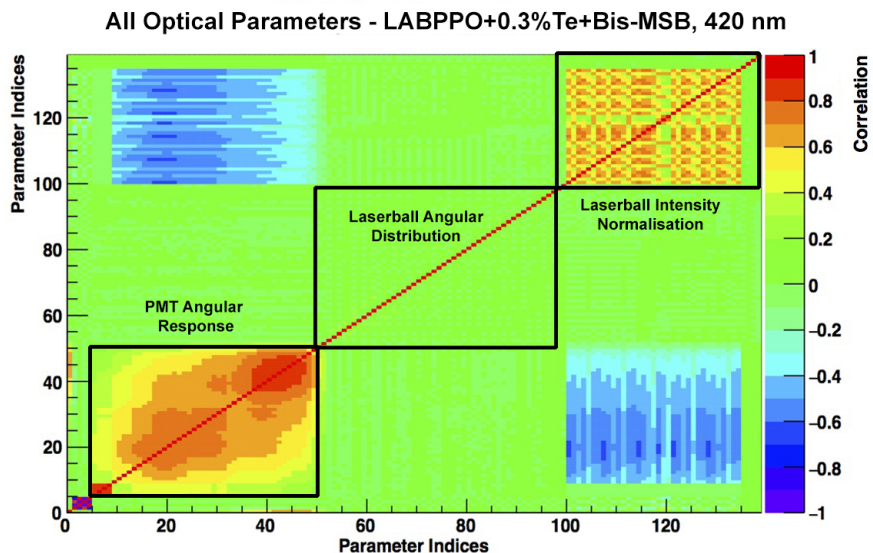


FIGURE 7.15: The global correlation space for the varying parameters from the bis-MSB data set at 420 nm. Shown are the three main composite parameter subsets; the relative PMT angular response, the laserball angular distribution and the laserball intensity normalisations. In the case of the PMT angular response, only the correlations for the parameters in the range $\theta_{\text{PMT}} \in (0^\circ, 50^\circ)$ are shown.

Similarly, absorption of the light does not affect the known correlation between the outer AV water attenuation coefficient, $\alpha_{\text{H}_2\text{O}}$ and the PMT angular response. An example is shown in Figure 7.16 for the 369 nm scan (a short wavelength which is absorbed and reemitted) from the perylene data set.

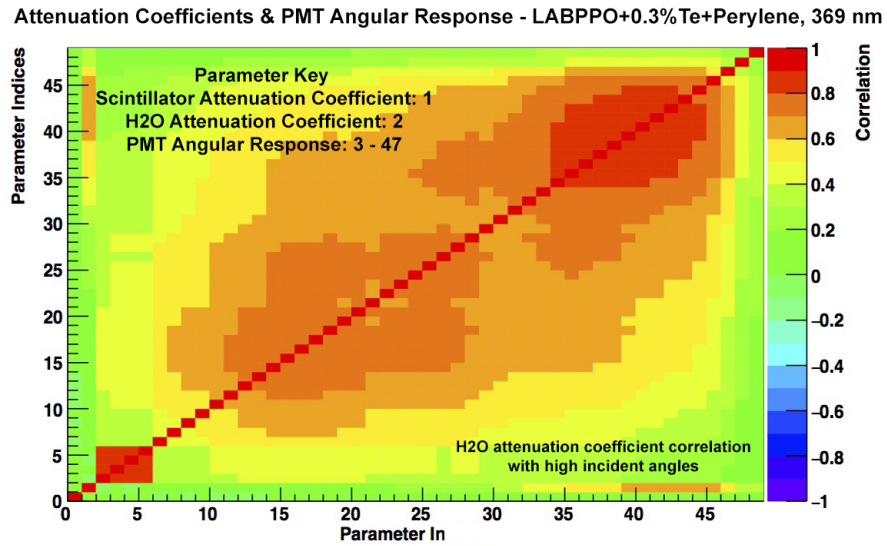


FIGURE 7.16: The correlation matrix for the fitted attenuation coefficients, $\alpha_{\text{scint}}^{\text{pery}}$ and $\alpha_{\text{H}_2\text{O}}^{\text{pery}}$, with the relative PMT angular response for the perylene data set at 369 nm. The angular response is shown for values $\theta_{\text{PMT}} \in (0^\circ, 45^\circ)$. A strong correlation arises between $\alpha_{\text{H}_2\text{O}}$ and the angular response in the $\theta_{\text{PMT}} \in (30^\circ, 45^\circ)$ region.

7.1.5 Systematic Errors

The systematic uncertainties applied are the same as those applied to the SNO+ MC water data in Section 6.2.6. The uncertainties that each systematic contributes to the attenuation coefficient values are shown in Table 7.2. The range shown for the outer AV water region attenuation is representative of all three data sets. Table 7.3 provides a summary of the reduced χ^2 ranges for each systematic.

Overall, the impact of the systematic uncertainties on the optical model and the attenuation coefficients is smaller in scintillator than in water. The uncertainty on the scintillator attenuation varies between 1-10% in the PPO data set, and is smaller for the bis-MSB and perylene data sets, 1-4%. The action of absorption and reemission affects the model to a greater extent as it readjusts the transit of light more so than any small changes in the laserball position. Therefore, this effectively reduces the systematic impact of the uncertainties related to the laserball position. The systematic uncertainties are most pronounced in the transparent wavelength regions of each mixture where the data is subject to systematic changes in a similar fashion to measurements in water. The increased uncertainty at longer wavelengths is evident by comparing the systematic contributions between short

(absorbed) and long (not absorbed) wavelengths. Examples are shown in tables 7.4 and 7.5 for PPO at 337 and 420 nm, tables 7.6 and 7.7 for bis-MSB at 337 and 420 nm and tables 7.8 and 7.9 for perylene at 385 and 505 nm. The tables for each wavelength scan of each data set can be found in Appendix C.2.

Attenuation Coefficient Uncertainties by Systematic

Systematic	PPO	Bis-MSB	Perylene	Water
	$\alpha_{\text{scint}}^{\text{ppo}}$	$\alpha_{\text{scint}}^{\text{bis.}}$	$\alpha_{\text{scint}}^{\text{pery.}}$	$\alpha_{\text{H}_2\text{O}}^{\text{ppo/bis/pery}}$
$ r_{\text{LB}} \times 1.01$	0.33-0.67%	0.30-0.49%	0.35-0.50%	2.21-6.9%
$r_{x,y,z} \pm 50.0 \text{ mm}$	0-4.24%	0-1.70%	0-1.64%	0-26.17%
$\lambda \pm \lambda_{\text{RMS}} \text{ nm}$	0.53-1.17%	0.11-0.28%	0.17-0.75%	0.12-4.50%
$H^2(\cos \theta_{\text{LB}}, \phi_{\text{LB}})$	< 0.01%	< 0.01%	< 0.01%	0-0.02%
$H(\cos \theta_{\text{LB}}, \phi_{\text{LB}}) = 1.0$	1.17-8.07%	0.55-3.24%	1.42-3.10%	1.66-5.16%
$\chi_{\text{lim,f}}^2 = 16$	0.01-0.51%	0.06-0.29%	0.01-0.26%	7.18-17.70%
$\chi_{\text{lim,f}}^2 = 9$	0-0.23%	0.01-0.12%	0-0.15%	0.15-4.36%
Total	1.69-9.97%	0.70-3.95%	1.73-3.80%	12.52-35.97%

TABLE 7.2: Shown is the range of systematic uncertainties across all wavelength scans in the three different scintillator mixtures for their respective fitted attenuation coefficients; $\alpha_{\text{scint}}^{\text{ppo}}$, $\alpha_{\text{scint}}^{\text{bis.}}$ and $\alpha_{\text{scint}}^{\text{pery.}}$. Alongside this is the range of uncertainty associated with the water region attenuation coefficient across all data sets, $\alpha_{\text{H}_2\text{O}}^{\text{ppo/bis./pery}}$.

Reduced Chi-Square by Systematic

Systematic	Reduced Chi-Square, $\chi^2/\text{No.Dof}$		
	PPO	Bis-MSB	Perylene
$ r_{\text{LB}} \times 1.01$	0.99-1.06	1-1.19	1-1.11
$r_{x,y,z} \pm 50.0 \text{ mm}$	0.97-1.05	0.97-1.18	0.97-1.10
$\lambda \pm \lambda_{\text{RMS}} \text{ nm}$	0.97-1.03	0.98-1.17	0.98-1.08
$H^2(\cos \theta_{\text{LB}}, \phi_{\text{LB}})$	0.98-1.02	0.98-1.16	0.98-1.08
$H(\cos \theta_{\text{LB}}, \phi_{\text{LB}}) = 1.0$	1.40-1.43	1.41-1.48	1.41-1.45
$\chi_{\text{lim,f}}^2 = 16$	1.15-1.24	1.16-1.48	1.15-1.34
$\chi_{\text{lim,f}}^2 = 9$	1.04-1.10	1.05-1.26	1.04-1.17

TABLE 7.3: Shown is the range of reduced χ^2 values across all wavelength scans in the PPO, bis-MSB and perylene data sets.

Attenuation Systematics - SNO+ MC, LABPPO, 337 nm

Systematic	$\alpha_{\text{Scint}}^{\text{ppo}}$ 10^{-5} mm^{-1}	$s_i \times \Delta\alpha/\alpha$	$\alpha_{\text{H}_2\text{O}}^{\text{ppo}}$ 10^{-5} mm^{-1}	$s_i \times \Delta\alpha/\alpha$	$\chi^2/\text{No.Dof}$
Nominal	10.67	0.00%	9.21	0.00%	1.02
$ r_{\text{LB}} \times 1.01$	10.40	-0.50%	7.02	-4.75%	1.05
$r_x - 50.0 \text{ mm}$	10.66	-0.01%	8.57	-1.38%	1.03
$r_x + 50.0 \text{ mm}$	10.66	-0.01%	8.53	-1.47%	1.03
$r_y - 50.0 \text{ mm}$	10.65	-0.04%	8.50	-1.54%	1.03
$r_y + 50.0 \text{ mm}$	10.69	0.03%	8.72	-1.06%	1.03
$r_z - 50.0 \text{ mm}$	10.75	0.37%	7.95	-6.85%	1.05
$r_z + 50.0 \text{ mm}$	10.53	-0.64%	7.21	-10.84%	1.00
$\lambda - \lambda_{\text{RMS}} \text{ nm}$	10.74	0.66%	8.80	-4.44%	1.03
$\lambda + \lambda_{\text{RMS}} \text{ nm}$	10.60	-0.63%	8.20	-10.91%	1.01
H^2	10.67	0.00%	9.20	-0.00%	1.02
$H = 1.0$	7.23	-1.61%	4.30	-2.66%	1.43
$\chi^2_{\text{lim,f}} = 16$	10.66	-0.07%	10.25	11.29%	1.24
$\chi^2_{\text{lim,f}} = 9$	10.67	0.04%	9.57	3.98%	1.10
Total		2.05%		21.99%	

TABLE 7.4: Systematic contributions to $\alpha_{\text{Scint}}^{\text{ppo}}$ and $\alpha_{\text{H}_2\text{O}}^{\text{ppo}}$ from the SNO+ MC data set with PPO at 337 nm.**Attenuation Systematics - SNO+ MC, LABPPO, 420 nm**

Systematic	$\alpha_{\text{Scint}}^{\text{ppo}}$ 10^{-5} mm^{-1}	$s_i \times \Delta\alpha/\alpha$	$\alpha_{\text{H}_2\text{O}}^{\text{ppo}}$ 10^{-5} mm^{-1}	$s_i \times \Delta\alpha/\alpha$	$\chi^2/\text{No.Dof}$
Nominal	5.07	0.00%	4.86	0.00%	1.00
$ r_{\text{LB}} \times 1.01$	4.96	-0.41%	3.18	-6.90%	1.01
$r_x - 50.0 \text{ mm}$	5.07	0.03%	4.67	-0.75%	1.02
$r_x + 50.0 \text{ mm}$	5.06	-0.02%	4.50	-1.48%	1.01
$r_y - 50.0 \text{ mm}$	5.05	-0.05%	4.40	-1.89%	1.01
$r_y + 50.0 \text{ mm}$	5.09	0.10%	4.48	-1.57%	1.01
$r_z - 50.0 \text{ mm}$	5.25	1.80%	4.11	-7.69%	1.02
$r_z + 50.0 \text{ mm}$	4.85	-2.11%	2.43	-25.01%	1.00
$\lambda - \lambda_{\text{RMS}} \text{ nm}$	5.10	0.61%	4.90	0.94%	1.00
$\lambda + \lambda_{\text{RMS}} \text{ nm}$	5.04	-0.53%	4.85	-0.18%	1.00
H^2	5.07	0.00%	4.86	0.01%	1.00
$H = 1.0$	1.25	-3.77%	0.35	-4.64%	1.41
$\chi^2_{\text{lim,f}} = 16$	5.06	-0.02%	5.64	16.18%	1.18
$\chi^2_{\text{lim,f}} = 9$	5.06	-0.06%	5.00	3.01%	1.07
Total		4.76%		32.16%	

TABLE 7.5: Systematic contributions to $\alpha_{\text{Scint}}^{\text{ppo}}$ and $\alpha_{\text{H}_2\text{O}}^{\text{ppo}}$ from the SNO+ MC data set with PPO at 420 nm.

**Attenuation Systematics - SNO+ MC
LABPPO + 0.3%Te + Bis-MSB, 337 nm**

Systematic	$\alpha_{\text{Scint}}^{\text{bis.}}$ 10^{-5} mm^{-1}	$s_i \times \Delta\alpha/\alpha$	$\alpha_{\text{H}_2\text{O}}^{\text{bis.}}$ 10^{-5} mm^{-1}	$s_i \times \Delta\alpha/\alpha$	$\chi^2/\text{No.Dof}$
Nominal	20.23	0.00%	14.03	0.00%	1.16
$ r_{\text{LB}} \times 1.01$	19.81	-0.41%	11.84	-3.13%	1.19
$r_x - 50.0 \text{ mm}$	20.23	-0.00%	13.58	-0.63%	1.16
$r_x + 50.0 \text{ mm}$	20.22	-0.01%	13.41	-0.88%	1.16
$r_y - 50.0 \text{ mm}$	20.20	-0.02%	13.66	-0.53%	1.16
$r_y + 50.0 \text{ mm}$	20.25	0.02%	13.87	-0.23%	1.16
$r_z - 50.0 \text{ mm}$	20.25	0.05%	12.74	-4.60%	1.18
$r_z + 50.0 \text{ mm}$	20.15	-0.20%	12.88	-4.11%	1.12
$\lambda - \lambda_{\text{RMS}} \text{ nm}$	20.27	0.19%	13.40	-4.50%	1.16
$\lambda + \lambda_{\text{RMS}} \text{ nm}$	20.21	-0.12%	14.00	-0.19%	1.15
H^2	20.23	0.00%	14.01	-0.01%	1.16
$H = 1.0$	16.90	-0.82%	9.03	-1.78%	1.47
$\chi^2_{\text{lim,f}} = 16$	20.28	0.27%	15.04	7.18%	1.48
$\chi^2_{\text{lim,f}} = 9$	20.25	0.12%	14.01	-0.15%	1.26
Total		1.02%		11.15%	

TABLE 7.6: Systematic contributions to $\alpha_{\text{Scint}}^{\text{bis.}}$ and $\alpha_{\text{H}_2\text{O}}^{\text{bis.}}$ from the SNO+ MC data set with bis-MSB at 337 nm.

**Attenuation Systematics - SNO+ MC
LABPPO + 0.3%Te + Bis-MSB, 420 nm**

Systematic	$\alpha_{\text{Scint}}^{\text{bis.}}$ 10^{-5} mm^{-1}	$s_i \times \Delta\alpha/\alpha$	$\alpha_{\text{H}_2\text{O}}^{\text{bis.}}$ 10^{-5} mm^{-1}	$s_i \times \Delta\alpha/\alpha$	$\chi^2/\text{No.Dof}$
Nominal	31.96	0.00%	7.39	0.00%	1.04
$ r_{\text{LB}} \times 1.01$	31.48	-0.30%	6.57	-2.21%	1.07
$r_x - 50.0 \text{ mm}$	31.96	0.00%	7.27	-0.33%	1.05
$r_x + 50.0 \text{ mm}$	31.95	-0.00%	7.03	-0.96%	1.05
$r_y - 50.0 \text{ mm}$	31.93	-0.01%	7.23	-0.43%	1.05
$r_y + 50.0 \text{ mm}$	31.98	0.02%	7.49	0.29%	1.05
$r_z - 50.0 \text{ mm}$	32.04	0.13%	7.41	0.15%	1.07
$r_z + 50.0 \text{ mm}$	31.82	-0.22%	5.20	-14.82%	1.01
$\lambda - \lambda_{\text{RMS}} \text{ nm}$	31.99	0.11%	7.35	-0.46%	1.04
$\lambda + \lambda_{\text{RMS}} \text{ nm}$	31.92	-0.12%	7.29	-1.39%	1.04
H^2	31.96	0.00%	7.37	-0.01%	1.04
$H = 1.0$	28.44	-0.55%	1.98	-3.66%	1.41
$\chi^2_{\text{lim,f}} = 16$	31.98	0.06%	8.34	12.86%	1.24
$\chi^2_{\text{lim,f}} = 9$	31.96	0.02%	7.64	3.44%	1.11
Total		0.70%		20.46%	

TABLE 7.7: Systematic contributions to $\alpha_{\text{Scint}}^{\text{bis.}}$ and $\alpha_{\text{H}_2\text{O}}^{\text{bis.}}$ from the SNO+ MC data set with bis-MSB at 420 nm.

**Attenuation Systematics - SNO+ MC
LABPPO + 0.3%Te + Perylene, 385 nm**

Systematic	$\alpha_{\text{Scint}}^{\text{pery.}}$ 10^{-5} mm^{-1}	$s_i \times \Delta\alpha/\alpha$	$\alpha_{\text{H}_2\text{O}}^{\text{pery.}}$ 10^{-5} mm^{-1}	$s_i \times \Delta\alpha/\alpha$	$\chi^2/\text{No.Dof}$
Nominal	10.92	0.00%	13.51	0.00%	1.07
$ r_{\text{LB}} \times 1.01$	10.64	-0.50%	10.69	-4.17%	1.09
$r_x - 50.0 \text{ mm}$	10.92	0.00%	13.32	-0.29%	1.07
$r_x + 50.0 \text{ mm}$	10.91	-0.02%	13.14	-0.56%	1.07
$r_y - 50.0 \text{ mm}$	10.90	-0.04%	13.22	-0.44%	1.07
$r_y + 50.0 \text{ mm}$	10.94	0.03%	13.44	-0.11%	1.07
$r_z - 50.0 \text{ mm}$	10.99	0.33%	11.80	-6.33%	1.09
$r_z + 50.0 \text{ mm}$	10.77	-0.69%	11.08	-9.01%	1.04
$\lambda - \lambda_{\text{RMS}} \text{ nm}$	10.94	0.17%	13.45	-0.45%	1.07
$\lambda + \lambda_{\text{RMS}} \text{ nm}$	10.90	-0.20%	13.54	0.19%	1.06
H^2	10.92	-0.00%	13.51	-0.00%	1.07
$H = 1.0$	7.80	-1.43%	8.71	-1.78%	1.45
$\chi^2_{\text{lim,f}} = 16$	10.93	0.11%	14.73	8.97%	1.32
$\chi^2_{\text{lim,f}} = 9$	10.93	0.13%	13.84	2.38%	1.15
Total		1.73%		15.13%	

TABLE 7.8: Systematic contributions to $\alpha_{\text{Scint}}^{\text{pery.}}$ and $\alpha_{\text{H}_2\text{O}}^{\text{pery.}}$ from the SNO+ MC data set with perylene at 385 nm.

**Attenuation Systematics - SNO+ MC
LABPPO + 0.3%Te + Perylene, 505 nm**

Systematic	$\alpha_{\text{Scint}}^{\text{pery.}}$ 10^{-5} mm^{-1}	$s_i \times \Delta\alpha/\alpha$	$\alpha_{\text{H}_2\text{O}}^{\text{pery.}}$ 10^{-5} mm^{-1}	$s_i \times \Delta\alpha/\alpha$	$\chi^2/\text{No.Dof}$
Nominal	5.98	0.00%	6.79	0.00%	0.99
$ r_{\text{LB}} \times 1.01$	5.85	-0.46%	5.19	-4.73%	1.01
$r_x - 50.0 \text{ mm}$	5.99	0.02%	6.83	0.12%	1.00
$r_x + 50.0 \text{ mm}$	5.98	-0.00%	6.60	-0.55%	1.00
$r_y - 50.0 \text{ mm}$	5.96	-0.07%	6.64	-0.43%	1.00
$r_y + 50.0 \text{ mm}$	6.01	0.09%	6.79	-0.01%	1.00
$r_z - 50.0 \text{ mm}$	6.14	1.33%	6.15	-4.70%	1.01
$r_z + 50.0 \text{ mm}$	5.79	-1.64%	4.81	-14.58%	0.98
$\lambda - \lambda_{\text{RMS}} \text{ nm}$	5.99	0.22%	6.82	0.44%	0.99
$\lambda + \lambda_{\text{RMS}} \text{ nm}$	5.97	-0.25%	6.82	0.41%	0.99
H^2	5.98	0.00%	6.78	-0.01%	0.99
$H = 1.0$	2.27	-3.10%	2.59	-3.09%	1.41
$\chi^2_{\text{lim,f}} = 16$	5.98	0.05%	7.82	15.13%	1.17
$\chi^2_{\text{lim,f}} = 9$	5.98	0.03%	7.09	4.36%	1.06
Total		3.80%		22.70%	

TABLE 7.9: Systematic contributions to $\alpha_{\text{Scint}}^{\text{pery.}}$ and $\alpha_{\text{H}_2\text{O}}^{\text{pery.}}$ from the SNO+ MC data set with perylene at 505 nm.

7.1.6 Conclusion on Optical Fit in Scintillator

Overall, the optical model performs well in identifying the attenuation coefficient of the candidate scintillator mixtures to a good degree of accuracy. The small systematic uncertainties on the coefficients is reflective of the fact that the scintillator is strongly attenuating, but also that the model does not explicitly account for absorption and reemission². This is evident by the overall larger reduced χ^2 at shorter wavelengths. However, it is clear that absorption and reemission affects the other parameters in the model. In the case of the laserball light distribution and the PMT angular response, the fitted values are not necessarily wrong, indeed, they are as expected and imply absorption and reemission. Rather it is that these processes are unquantified. This is because the model only describes the response of the detector to the effective intensity of laser/scintillation light emitted, whether or not it was absorbed. Better understanding of the absorption and reemission is obtained by studying its impact on the timing at PMTs; an aspect to which the optical model is not directly sensitive to. Using the scintillation time profile model presented in Section 4.5.2, an approach to quantify the absorption and reemission is discussed in the next.

Of the parameters in the model, the uncertainty on the water attenuation coefficient is of most concern and remains largely unaccounted for (see Figure 7.5). As demonstrated by Figure 7.6 it is clear that the larger and more attenuating medium of the scintillator region biases the overall attenuation of light in the detector. This makes an accurate measurement of the water attenuation with laserball data in scintillator very difficult. Combined with absorption and reemission at shorter wavelengths, the optical model ultimately loses all sensitivity to such a measurement. As discussed in Chapter 6 this reinforces the importance of a water phase prior to the deployment of scintillator in SNO+; it is the *only* phase in which an accurate characterisation of water in the detector can be made. In general, for physics events in scintillator the light will be shifted to longer wavelengths where water is more attenuating. This presents uncertainties related to the expected light yield of physics events if light is attenuated to an unknown extent once it escapes the AV region. This subsequently manifests as uncertainties in the reconstructed energy of all physics events.

²The only systematic to account for the absorption and reemission is the $\lambda \pm \lambda_{\text{RMS}}$ systematic which probes the change in wavelength due to reemission. However, its effect on the optical parameters is small $\sim 1\%$

Failing an accurate measurement of the water attenuation, this poses the question of how the water attenuation could be regularly monitored during the scintillator phases. In conclusion, it is clear that scintillator should not be deployed into the detector until the optical properties of the water region is fully understood.

7.2 Scintillator Timing

Thus far it has been shown that the action of absorption and reemission of the three scintillator mixtures can only be identified, not characterised, by studying its effect on the output parameters of the optical model. An understanding of absorption and reemission is instead developed through the timing information. The scintillator time profile model as presented in Section 4.5.2 is designed to characterise the effective absorption and reemission properties of the scintillator components at specific wavelengths in terms of two parameters; the photon walk, $\alpha_w(\lambda_{LB})$ and the scintillator emission time constant, τ_s .

The different wavelength shifting properties of PPO, bis-MSB and perylene is exhibited by the time residual distributions from the central laserball runs in each respective data set, see Figure 7.17. The most prominent feature of these plots is the shift in the central value of the prompt peaks. The central value of the prompt peak can be determined by the laserball position fit as described in Section 5.2.2; it is the global time offset and is an estimator of the trigger time of the laser, t_0 . However, in scintillator the value obtained from this fit is not the *true* trigger time because it contains information about the absorption and reemission of the initial laser light as shown. For example, at wavelengths that are absorbed and reemitted in perylene; 337, 369, 385 and 420 nm the peak is shifted by ~ 5 ns. At larger residual values in the 410-440 ns region, any evidence of AV, PMT or PSUP reflections is smeared completely. Evidence for absorption and reemission is also evident in the PPO and bis-MSB data sets, but these effects are less pronounced than in perylene.

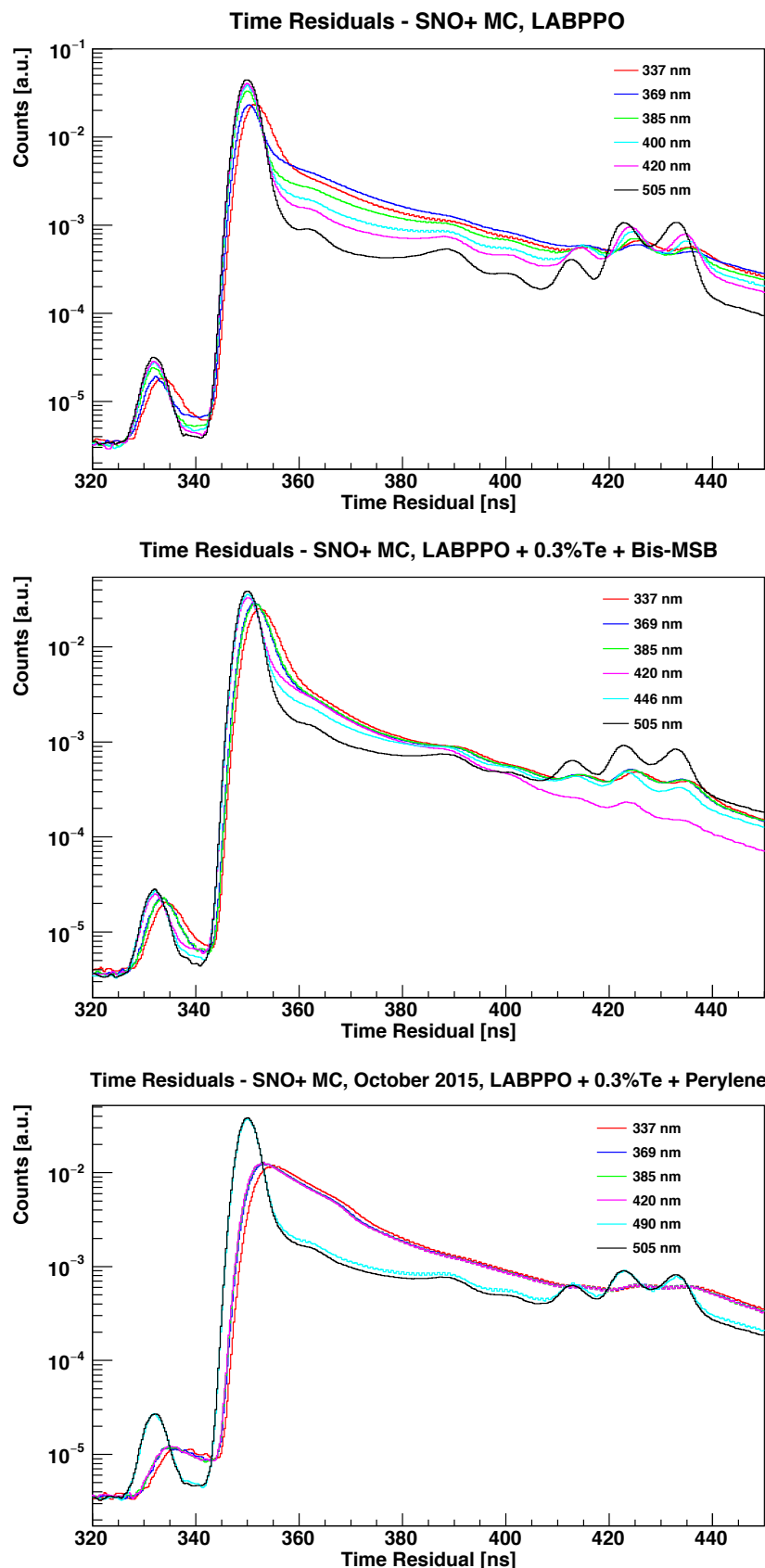


FIGURE 7.17: Shown are the time residual distributions from central laserball runs at different wavelengths for each of the PPO (top), bis-MSB (middle) and perylene (bottom) data sets.

The time profile model was implemented according to the time residual expression in Equation 4.43;

$$t_0 + t_{\text{res}} = t_{\text{PMT}}(\alpha_w(\lambda_{\text{LB}}), \tau_s) - \sum_k \frac{d_k(\vec{r}_{\text{LB}})}{v_{g,k}(\lambda_{\text{emit}})} - t_{\text{bucket}}(\theta_\gamma), \quad (7.2)$$

where $t_{\text{PMT}}(\alpha_w, \tau_s)$ is the arrival time of the light at the PMT, as generated iteratively through MC according to Equation 4.40. It is the MC generated distribution of $t_0 + t_{\text{res}}$ that is used as the model prediction to the observed time residual distribution over which the minimisation of the log-likelihood (see Equation 4.48) is performed. Here, t_0 is the true time in the event window when the laserball was triggered; it is a constant. This is known precisely in MC data as presented here, with a nominal value of $t_0 = 350.0$ ns. However, it may not be precisely known in data and can be considered as a third parameter in addition to $\alpha_w(\lambda_{\text{LB}})$ and τ_s . As will be discussed, this offset ultimately impacts the value of $\alpha_w(\lambda_{\text{LB}})$ as both parameters characterise a shift in the central value of the prompt peak. Two fits are therefore considered;

- **t_0 -Fixed:** The trigger time is set to the MC value, $t_0 = 350.0$ ns and is considered a systematic of the floating parameters $\alpha_w(\lambda_{\text{LB}})$ and τ_s .
- **t_0 -Float:** The trigger time is allowed to float and the fit is performed over three parameters; $\alpha_w(\lambda_{\text{LB}})$, τ_s and t_0 .

Henceforth these fits will be referred to as *t_0 -fixed* and *t_0 -float* respectively.

7.2.1 Scintillator Time Model Results

The fits are performed using the central laserball runs at absorbed and reemitted wavelengths as discussed in Section 7.1.1; these include PPO : {337 nm}, bis-MSB : {337, 369, 385 nm} and perylene : {337, 369, 385, 420 nm}. Based on the distributions in Figure 7.17, for the PPO and bis-MSB runs the time residual distribution is restricted to a range of (345, 360) ns about the prompt peak. Due to the larger offset of the prompt peak in the perylene data set, a wider range of (345, 370) ns is selected. The choice of these time windows are made such that the peak information, characterised by α_w , and the immediate tail, characterised by τ_s are both included in the fit. Beyond this, the true distributions begin to include

reflection and PMT pulsing effects that are not included in the model. Both the model predicted and observed time residual distributions use 0.25 ns binning.

The obtained values of $\alpha_w(\lambda_{LB})$ and τ_s for the t_0 -fixed fit are shown in Table 7.10. The values of $\alpha_w(\lambda_{LB})$, τ_s and t_0 from the t_0 -float fit are shown in Table 7.11. Both parameter sets are presented alongside their respective statistical and systematic uncertainties. The calculation of these uncertainties is discussed in Section 7.2.3.

 t_0 -Fixed Parameters \pm stat. \pm sys.

Data : λ_{LB} [nm]	$\alpha_w(\lambda_{LB})$ [mm]	τ_s [ns]
PPO : 337	$1.00 \pm 0.71 \pm 144.46$	$1.47 \pm_{< 0.01} \pm 0.29$
Bis. : 337	$454.71 \pm 0.35 \pm 164.97$	$2.11 \pm_{< 0.01} \pm 0.32$
Bis. : 369	$125.10 \pm 2.84 \pm 115.58$	$1.15 \pm_{< 0.01} \pm 0.23$
Bis. : 385	$285.24 \pm 1.90 \pm 107.67$	$1.15 \pm_{< 0.01} \pm 0.27$
Pery. : 337	$875.07 \pm 0.79 \pm 221.60$	$9.88 \pm 0.01 \pm 1.07$
Pery. : 369	$187.59 \pm 9.37 \pm 736.31$	$8.11 \pm_{< 0.01} \pm 0.74$
Pery. : 385	$18.45 \pm 0.86 \pm 854.08$	$7.75 \pm 0.01 \pm 0.62$
Pery. : 420	$35.95 \pm 1.06 \pm 887.60$	$7.39 \pm_{< 0.01} \pm 0.61$

TABLE 7.10: Fitted values of the photon walk, $\alpha_w(\lambda_{LB})$ and the emission time constant, τ_s for absorbed wavelengths in the PPO, bis-MSB and perylene data sets. Errors less than 2 d.p. are quoted as $\pm_{< 0.01}$. t_0 -Float Parameters \pm stat. \pm sys.

Data : λ_{LB} [nm]	$\alpha_w(\lambda_{LB})$ [mm]	τ_s [ns]	t_0 [ns]
PPO : 337	$1.00 \pm 9.09 \pm 9.00$	$1.47 \pm_{< 0.01} \pm_{< 0.01}$	$350.05 \pm_{< 0.01} \pm 0.02$
Bis. : 337	$105.85 \pm 1.02 \pm 24.71$	$2.01 \pm_{< 0.01} \pm_{< 0.01}$	$350.42 \pm_{< 0.01} \pm 0.02$
Bis. : 369	$123.32 \pm 7.41 \pm 150.33$	$1.15 \pm_{< 0.01} \pm_{< 0.01}$	$350.03 \pm_{< 0.01} \pm 0.13$
Bis. : 385	$62.60 \pm 0.94 \pm 9.17$	$1.15 \pm_{< 0.01} \pm_{< 0.01}$	$350.22 \pm 0.01 \pm 0.25$
Pery. : 337	$88.34 \pm 2.82 \pm 36.45$	$8.96 \pm 0.01 \pm 0.04$	$350.95 \pm_{< 0.01} \pm 0.05$
Pery. : 369	$1.00 \pm 2.62 \pm 104.85$	$7.91 \pm_{< 0.01} \pm 0.19$	$350.2 \pm_{< 0.01} \pm 0.10$
Pery. : 385	$1.00 \pm 1.54 \pm 52.42$	$7.75 \pm 0.04 \pm 0.20$	$350.00 \pm_{< 0.01} \pm 0.05$
Pery. : 420	$1.00 \pm 1.70 \pm 17.47$	$7.58 \pm 0.02 \pm 0.11$	$350.1 \pm_{< 0.01} \pm 0.01$

TABLE 7.11: Fitted values of the photon walk, $\alpha_w(\lambda_{LB})$ emission time constant, τ_s and the laser trigger time, t_0 for absorbed wavelengths in the PPO, bis-MSB and perylene data sets. Errors less than 2 d.p. are quoted as $\pm_{< 0.01}$.

Examples of the generated time residuals using the fitted values are shown in comparison to the observed distributions in Figure 7.18. Shown are the distributions for the 337 nm runs in PPO, bis-MSB and perylene.

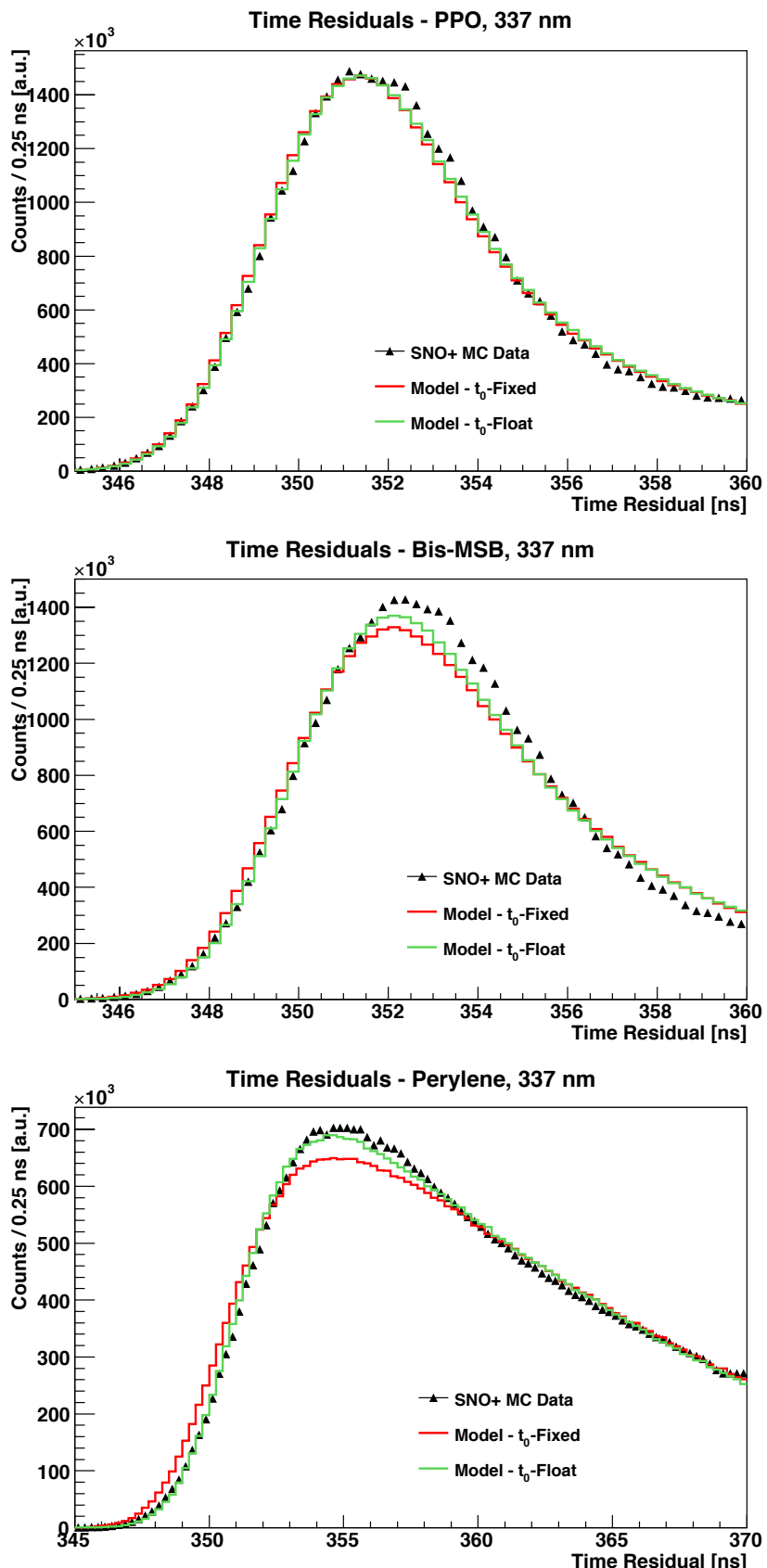


FIGURE 7.18: Shown are the fitted model time residual distributions for the 337 nm runs in PPO (top), bis-MSB (middle) and perylene (bottom). The observed residual distribution from the MC data is shown in black. The t_0 -fixed and t_0 -float results are shown in red and green respectively

The obtained values of $\alpha_w(\lambda_{LB})$ from the t_0 -fixed fit are generally larger in comparison to those obtained in the t_0 -float fit, for which values of t_0 reside up to 0.95 ns above the true MC value of $t_0 = 350.0$ ns. This slight shift in t_0 is largest at 337 nm in the bis-MSB and perylene run. By allowing t_0 to float, and increase, it constrains $\alpha_w(\lambda_{LB})$ to be small $\lesssim 125.0$ mm; t_0 and $\alpha_w(\lambda_{LB})$ are negatively correlated. As the constraint on $\alpha_w(\lambda_{LB})$ is not present in the t_0 -fixed fit, it has more resolving power to characterise shifts in the prompt peak and hence values of $\alpha_w(\lambda_{LB})$ are larger. However, by including variations in t_0 as a systematic, these values of $\alpha_w(\lambda_{LB})$ carry a large uncertainty, and at the lower limits are close to, if not consistent with, those obtained in the t_0 -float fit. For PPO at 337 nm and perylene at 369, 385 and 420 nm these large uncertainties in $\alpha_w(\lambda_{LB})$ exceed the parameter values, forcing the respective values of $\alpha_w(\lambda_{LB})$ to be consistent with zero. The systematic uncertainties in the t_0 -float fit are smaller, but similarly the values of $\alpha_w(\lambda_{LB})$ are consistent with zero across the same set of runs. As shown in Figure 7.18 the large value of $\alpha_w(\lambda_{LB})$ in the t_0 -fixed fit slightly suppresses the prompt peak in comparison to the small values in the t_0 -float fit.

The values of τ_s are more robust to changes in t_0 , and hence the values between the two fits are relatively consistent, particularly at longer wavelengths in bis-MSB and perylene. In both fits, these values of the time constant vary as the wavelength probes different components in the scintillator. The complexity of this is compounded for the bis-MSB and perylene runs, where the initial laser light is absorbed by a first component, for which the reemitted light is then absorbed by a second i.e. $\lambda_{LB} \rightarrow$ PPO \rightarrow perylene/bis-MSB. The values of the time constant obtained are therefore effective values that encapsulate the total action of successive absorptions and reemissions between different components. It was discussed in Section 7.1.1 that at absorbed wavelengths, the attenuation coefficient of the scintillator is geometrically constrained by the dimensions of the detector, with values of the attenuation coefficients $\sim 10^{-4}$ mm $^{-1}$. It was shown that these values coincided in the region where the absorption length of the active wavelength shifting component is ~ 10 m. In absorption regions below this length, the size of the detector gives the wavelength shifter enough *space* to reabsorb again. Subsequently, the time profile also contains information about the elastic behaviour of the wavelength shifters that self-absorb their own, or another component's emission spectrum. Using a value of 10 m as a threshold value for the absorption length, the percentage of the reemission spectrum that is subject to elastic scattering can be estimated, see Figure 7.19.

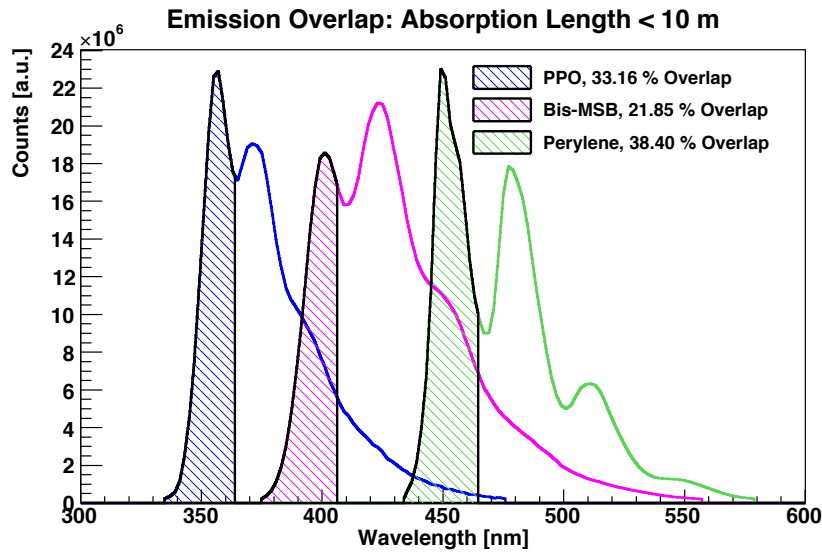


FIGURE 7.19: Shown are the overlap regions for the PPO, bis-MSB and perylene emission spectra when the absorption length of the respective wavelength shifter is < 10 m, the approximate value of the absorption length beyond which light is able to escape the inner AV region.

Given this behaviour, in order to interpret these effective time constants, τ_s it is useful to discuss them relative to the individual time constants of the components used in the MC; LAB, PPO, bis-MSB and perylene. These are shown in Table 7.12.

SNO+ MC Time Constant Values	
Component	τ_s^{MC} [ns]
LAB	5.80
PPO	1.60
Bis-MSB	1.40
Perylene	6.40

TABLE 7.12: The individual reemission time constant values for LAB, PPO, bis-MSB and perylene. These are used in the MC scintillator mixtures in RAT.

The simplest of the values to interpret is that from the PPO data set, where there is only one wavelength shifter. In both fits, the obtained value of $\tau_s = 1.47$ ns for the PPO run at 337 nm is within 10% of the true MC input, $\tau_s^{\text{MC}} = 1.60$ ns. For the t_0 -fixed fit it is within systematic uncertainty; $\tau_s = 1.47 \pm_{< 0.01} \pm 0.29$ ns.

For the ternary mixtures, it is useful to define the fraction of the total absorption coefficient of the two wavelength shifting components at a given wavelength;

$$f_i^{\text{abs}} = \alpha_i^{\text{abs}} / \sum_i^{N_{\text{comp}}} \alpha_i^{\text{abs}}, \quad (7.3)$$

where α_i^{abs} is the absorption coefficient for the i -th component. For the bis-MSB and perylene mixtures considered here, $N_{\text{comp.}} = 2$.³ The values of f_i^{abs} are shown for these mixtures in Figure 7.20 as fractional percentages. These provide a visual illustration to the competing nature of the wavelength shifters across different wavelengths. For example, in the 337 nm run in perylene, the PPO absorbs the initial laser light and reemits according to its emission spectrum; this is then absorbed by the perylene. From Figure 7.20, at 337 nm the two successive absorptions are equally separated between where the PPO is highly absorbing, and where the perylene is highly absorbing. Therefore, the emission distribution in time should be distributed as the equal sum of the PPO and perylene components i.e.

$$e^{-t/\tau_s} \sim \left(e^{-t/\tau_s^{\text{MC, ppo}}} + e^{-t/\tau_s^{\text{MC, pery.}}} \right). \quad (7.4)$$

Using the values from Table 7.12, one can calculate the mean of this distribution over the reemission time window ($\tau_s^{\text{MC, pery.}}, 3\tau_s^{\text{MC, pery.}}$) (as discussed in Section 4.5.2, Equation 4.45);

$$\langle t \rangle = \int_{\tau_s^{\text{MC, pery.}}}^{3\tau_s^{\text{MC, pery.}}} t (e^{-t/1.60} + e^{-t/6.40}) dt = 10.76 \text{ ns}. \quad (7.5)$$

This is within uncertainty of the fitted values of τ_s at this wavelength in perylene for the t_0 -fixed fit; $\tau_s = 9.88 \pm 0.01 \pm 1.07$ ns. The value obtained by the t_0 -float fit generally underestimates this value; $\tau_s = 8.96 \pm 0.01 \pm 0.04$ ns. This calculation can be similarly be applied to the 337 nm run in bis-MSB;

$$\langle t \rangle = \int_{\tau_s^{\text{MC, bis.}}}^{3\tau_s^{\text{MC, bis.}}} t (e^{-t/1.60} + e^{-t/1.40}) dt = 2.39 \text{ ns}, \quad (7.6)$$

³Technically the LAB does have its own emission spectrum, however, it is has a small emission probability, $\epsilon_p \sim 0.5$. In addition, in the MC the LAB emission spectrum is set to match that of PPO.

which is consistent with the obtained value, $\tau_s = 2.11 \pm_{<} 0.01 \pm_{<} 0.32$ ns from the t_0 -fixed fit. Similarly to perylene, the t_0 -float fit underestimates the value with bis-MSB; $\tau_s = 2.01 \pm_{<} 0.01 \pm_{<} 0.01$. Therefore, whilst the time constant is generally robust to changes in t_0 , at smaller wavelengths it shares a slight negative correlation with t_0 .

At longer wavelengths e.g. 369 and 385 nm the picture becomes more complicated. The laser light is emitted over a broader wavelength spectrum (see Figure 5.1) because it is produced by a chemical compound in the laser-dye. In comparison, the intrinsic spectrum of the N₂ laser at 337 nm is near-monochromatic. As a result, in both bis-MSB and perylene, the initial laser-dye spectrum overlaps the transition between regions of absorption dominated by PPO and bis-MSB/perylene, 350-370 nm. This region is shown in Figure 7.20. Consequently, some of the light is directly absorbed by the secondary wavelength shifter and hence the values of τ_s are smaller.

7.2.2 Shape Comparison

Beyond visual inspection, a quantifiable shape comparison between the model predicted and observed time residual distributions is done by computing the Bhattacharyya distance measure (BDM) [149]. The BDM between two histograms, u and v is computed as follows;

$$T_{\text{BDM}} = \sqrt{\frac{\vec{u}}{N_u} \cdot \frac{\vec{v}}{N_v}} = \left(\sum_{i=1}^k \frac{u_i v_i}{N_u N_v} \right)^{1/2}, \quad (7.7)$$

where k is the number of histogram bins and \vec{u} and \vec{v} are vectors of the normalised histogram bin entries;

$$\vec{u} = \left(\frac{u_1}{N_u}, \frac{u_1}{N_u}, \dots, \frac{u_k}{N_u} \right), \quad N_u = \sum_{i=1}^k u_i, \quad (7.8)$$

$$\vec{v} = \left(\frac{v_1}{N_v}, \frac{v_1}{N_v}, \dots, \frac{v_k}{N_v} \right), \quad N_v = \sum_{i=1}^k v_i. \quad (7.9)$$

The BDM is analogous to the dot product of two vectors; if identical, the two vectors *point* in the same direction i.e. if the shapes of the histograms are identical

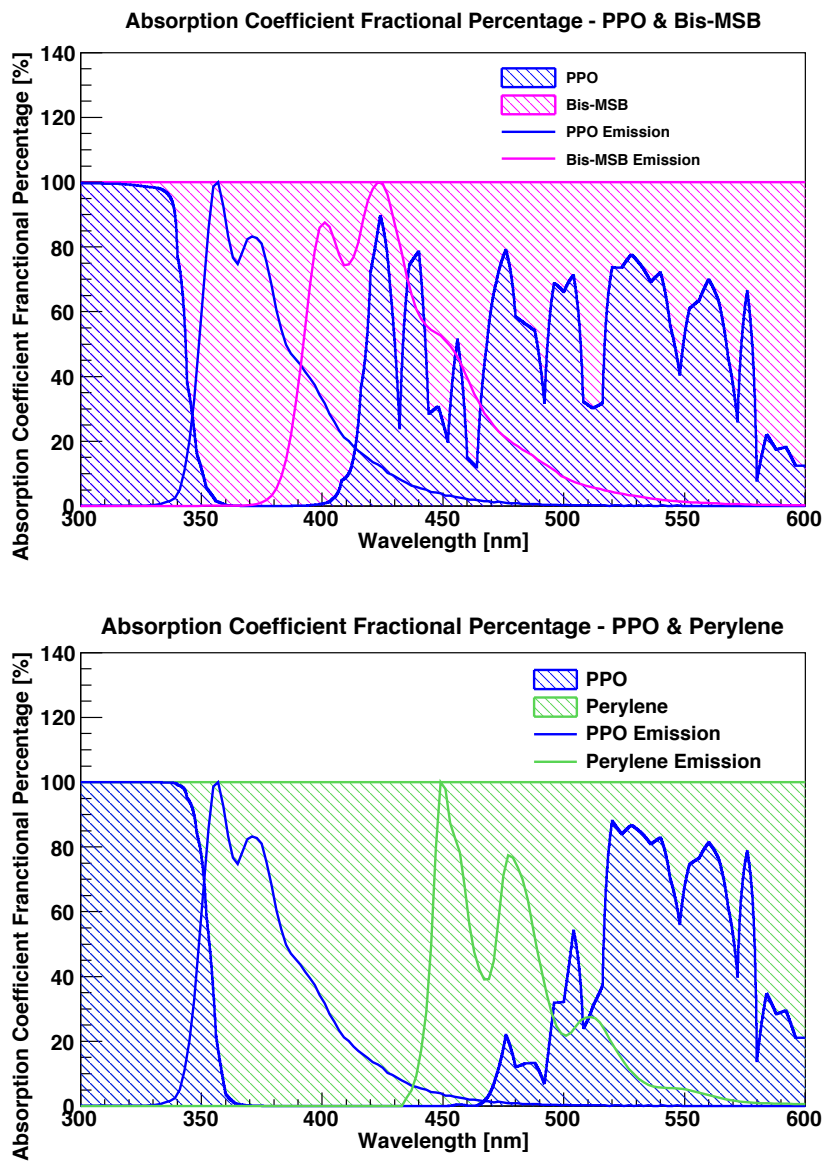


FIGURE 7.20: Shown are the fractional percentages of the total absorption coefficients for each of the wavelength shifting components; PPO and bis-MSB (top) and PPO and perylene (bottom). The fractional percentages are calculated using Equation 7.3. The emission spectra of each component is also shown.

$T_{\text{BDM}} = 1$. The BDM was computed between each fitted model distribution and the observed distribution; the values are shown in Table 7.13. Overall, the values are small, which is due to discrepancies about the peak or in the tail of the distribution as evident in Figure 7.18. In addition, the variation in the BDM measure between t_0 -fixed and t_0 -float distributions is itself small, with the shape of the t_0 -float distributions marginally favoured. This is consistent with a visual inspection

of the distributions in Figure 7.18 which suggests that the t_0 -float distributions are in better agreement with observations over the t_0 -fixed model. Ultimately, the BDM values suggest that there are discrepancies in the model, especially for bis-MSB which appear inconsistent both in the peak and tail shape.

BDM Measure Comparison

Data : λ [nm]	t_0 -Fixed BDM	t_0 -Float BDM
PPO : 337	0.15888	0.15896
Bis. : 337	0.15694	0.15799
Bis. : 369	0.16258	0.16258
Bis. : 385	0.16223	0.16241
Pery. : 337	0.11324	0.11427
Pery. : 369	0.11335	0.11341
Pery. : 385	0.11333	0.11329
Pery. : 420	0.11357	0.11345

TABLE 7.13: BDM measure for shape comparison for each run. The BDM measure is computed for each model predicted distribution from each fit type against the observed distribution.

7.2.3 Statistical and Systematic Uncertainties

Globally, the log-likelihood in each of the parameter directions has a well defined form such that the minimum can be identified. An example of this is given in the form of the log-likelihood (α_w, τ_s) -plane in bis-MSB at 369 nm, and perylene at 337 nm as shown in Figure 7.21 for the t_0 -fixed fits. Shown also are the t_0 -float slices in the t_0 -direction. However, given that the PDFs are generated through binned MC distributions, not analytically, the log-likelihood is not locally smooth and is limited by statistical fluctuations, 0.3-0.7% per bin. Although this fluctuation is small, for a given parameter, p_i it makes the log-likelihood difficult to double-differentiate in order to estimate the parameter error, $\delta p_i = \partial^2 \mathcal{L} / \partial^2 p_i$ ⁴. Instead, as discussed in [150], it is appropriate to approximate the error as the change in p_i such that the difference in the log-likelihood changes by 0.5;

$$\delta p_i = |p_{i,\min} - p_i^*| \quad \text{s.t.} \quad \mathcal{L}(p_{i,\min} \pm p_i^*) - \mathcal{L}(p_{i,\min}) = 0.5, \quad (7.10)$$

⁴This is the classical approximation to an error that is Gaussian about the minimum, which is not guaranteed for the scenario considered here. Most textbooks quote the error as $\delta p_i = -\partial^2 \mathcal{L} / \partial^2 p_i$ where the negative sign is due to the fact that it is most often a maximum of the log-likelihood which is discussed. Here, the negative sign is implicit to the definition of \mathcal{L} as defined in chapter 4.

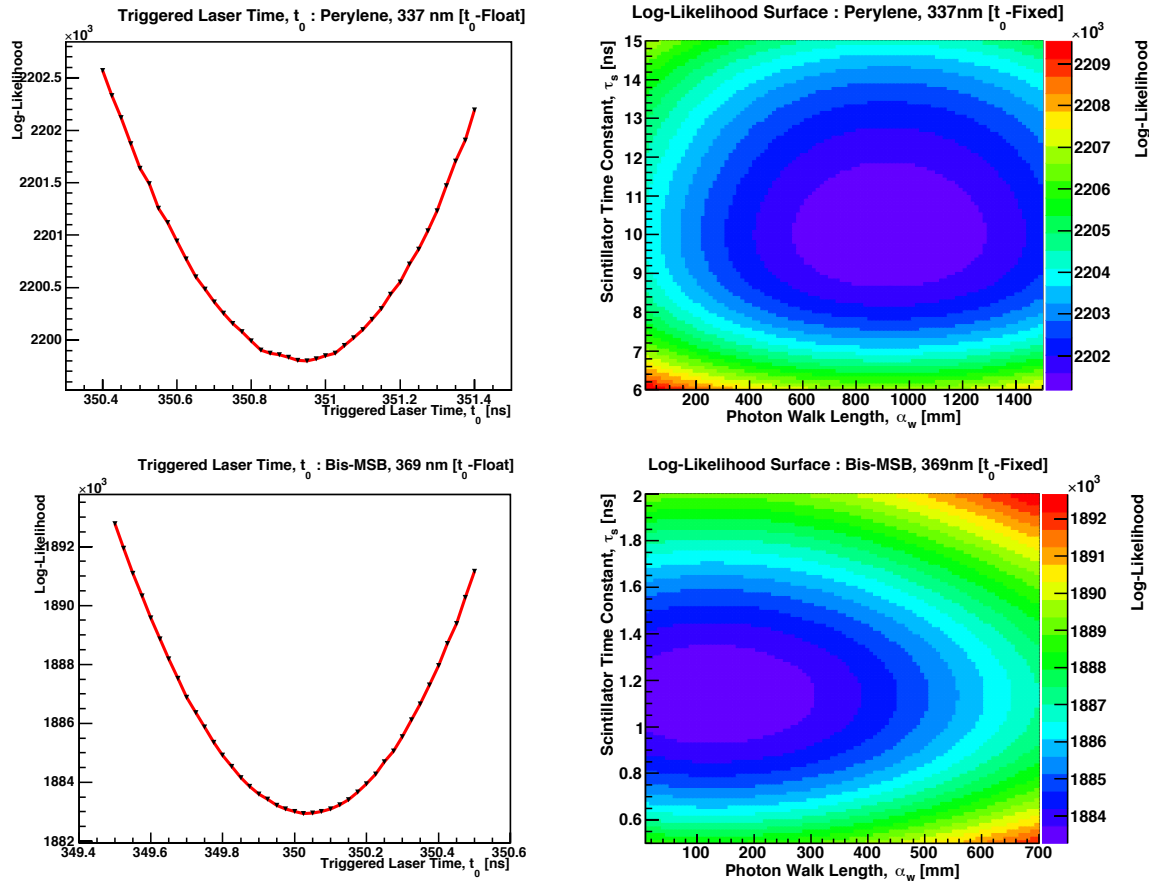


FIGURE 7.21: Shown top-left and bottom-left are the log-likelihood scans for the triggered laser time, t_0 in perylene at 337 nm and bis-MSB at 369 nm for the t_0 -float fit. Shown top-right and bottom-right are the log-likelihood (α_w, τ_s)-planes from the t_0 -fixed fits in perylene at 337 nm and bis-MSB at 369 nm.

where $p_{i,\min}$ is the parameter value at the minimum. For the evaluation of the error in each parameter direction, the re-minimised values of the other remaining parameters is calculated. As presented in Table 7.10 and 7.11, the statistical uncertainties are small, $\lesssim 1\%$ across all parameters in both fits.

The largest contributions to the uncertainty on the parameters come from the systematic uncertainties. As described, one systematic is applied to both fits, and a second to the t_0 -fixed fit:

- **Reemitted attenuation length α ($\bar{\lambda}_{\text{emit}}$) $\pm 2\delta\alpha$:** In generating the MC distribution, once the light is absorbed and reemitted for a first time, the path samples distances based on the attenuation length of the mean emitted wavelength as described in Section 4.5.2 (see Equation 4.46). The values of

$\alpha(\bar{\lambda}_{\text{emit}})$ used are the attenuation lengths obtained from the optical model fit in Section 7.1.1. The fit is performed using values $\alpha(\bar{\lambda}_{\text{emit}}) \pm 2\delta\alpha$ where $\delta\alpha$ is the systematic error. Twice the error value is used to exaggerate the effect of changing the attenuation length to $\pm 10\text{-}20\%$ of the original value. The error in the fitted parameter is then rescaled by a factor of $s_1 = 0.5$.

- **Triggered laser time, $t_0 \pm 1.0$ ns:** The triggered laser time in the t_0 -float fit is varied by 1.0 ns either side of the MC time, $t_0 = 350.0$ ns. The error is scaled by a factor of $s_2 = 0.25$, such that it is equivalent to the 0.25 ns bin width.

Scintillator Time Profile Model - Systematic Uncertainties

Data : λ [nm]	Parameter	t_0 -Fixed		t_0 -Float
		$\alpha_w(\bar{\lambda}_{\text{emit}}) \pm 2\delta\alpha$	$t_0 \pm 1.0$ ns	$\alpha(\bar{\lambda}_{\text{emit}}) \pm 2\delta\alpha$
PPO : 337	$\alpha_w(\lambda_{\text{LB}})$	1746%	14381%	899.33%
	τ_s	< 0.01%	19.74%	< 0.01%
	t_0	-	-	< 0.01%
Bis. : 337	$\alpha_w(\lambda_{\text{LB}})$	13.68%	33.60%	23.35%
	τ_s	< 0.01%	15.04%	< 0.01%
	t_0	-	-	< 0.01%
Bis. : 369	$\alpha_w(\lambda_{\text{LB}})$	1.41%	92.38%	121.90%
	τ_s	< 0.01%	19.98%	< 0.01%
	t_0	-	-	0.04%
Bis. : 385	$\alpha_w(\lambda_{\text{LB}})$	12.32%	35.68%	14.65%
	τ_s	< 0.01%	23.48%	< 0.01%
	t_0	-	-	0.01%
Pery. : 337	$\alpha_w(\lambda_{\text{LB}})$	2.23%	25.22%	41.25%
	τ_s	2.61%	10.52%	0.42%
	t_0	-	-	0.01%
Pery. : 369	$\alpha_w(\lambda_{\text{LB}})$	25.73%	391.66%	10447.9%
	τ_s	1.23%	9.04%	2.41%
	t_0	-	-	0.02%
Pery. : 385	$\alpha_w(\lambda_{\text{LB}})$	299.11%	4613.19%	5238.9%
	τ_s	2.58%	7.55%	2.58%
	t_0	-	-	0.01%
Pery. : 420	$\alpha_w(\lambda_{\text{LB}})$	68.74%	2468.02%	1746.27%
	τ_s	2.20%	8.02%	1.41%
	t_0	-	-	0.0%

TABLE 7.14: Shown are the systematic uncertainties as percentages of the parameter values obtained for the t_0 -fixed and t_0 -float fits.

The systematic contributions to each parameter are shown in Table 7.14. Overall, the parameters in the t_0 -fixed fit are subject to large uncertainties due to the inclusion of t_0 as a systematic, producing variations of 25-35% in $\alpha_w(\lambda_{LB})$ for values inconsistent with zero. In cases where the fitted value $\alpha_w(\lambda_{LB})$ is small or consistent with zero, the systematic uncertainties, $\geq 100\%$ are redundant. The variations in t_0 for the t_0 -fixed fit induce a 7-25% uncertainty in τ_s . In comparison, the systematic uncertainty in $\alpha(\bar{\lambda}_{emit})$ give rise to small uncertainties, $< 2.6\%$ in both fits.

7.2.4 Conclusion on Scintillator Time Profile Model

The time profile model provides sensitivity to the absorbing and reemitting action of the scintillator. However, the model is largely dominated by uncertainties associated with the trigger time of the laser, t_0 . In practice, the trigger time cannot be guaranteed to a sufficient degree of accuracy. One idea to partially resolve this could be to calculate the global time offset as an estimator for t_0 for a run close to the reemitted wavelength i.e. PPO: 400 nm, bis-MSB: 446 nm and perylene: 490 nm, and use this value as the fixed trigger time at shorter wavelengths in the model. However, again, this would require performing two successive laserball runs in which only the dye is changed; even then it cannot be guaranteed that the detector state would otherwise remain unchanged between these two runs.

A further problem is that the model assumes characteristics of the laser emission, ($\sigma_{LB} = 0.7$ ns) and the PMT time response ($\sigma_{PMT} = 1.7$ ns). Again, in practice these values cannot be assumed. In principle these could be added as additional parameters into the fit, although this would ultimately over constrain the model as presented here; a model that uses only one central run per wavelength, of which a relatively small time residual window of 15-20 ns is used.

Despite these issues, the most interesting result from studying this model comes from the emission time value, τ_s which is sensitive to the multi-component nature of the ternary mixtures, identifying the variation in absorption strengths of the different wavelength shifters across short wavelengths. Furthermore, the sensitivity of τ_s is reasonably robust to changes in the trigger time depending on whether it varies (or is fixed) in the fit with uncertainties ranging from 0.01-2.6% (8.0-23.5%). To this extent, the model is in principle able to quantify the micro-physical processes within the bulk liquid scintillator.

The photon walk ultimately appears to be a minor effect in the model whose systematic uncertainties ($> 1000\%$ in perylene) are dominated by variations t_0 . A re-parameterisation of the model could replace $\alpha_w(\lambda_{LB})$ with the rise-time of the scintillator, τ_r as in Equation 3.6. Although the sensitivity to time would remain; the rise time of most scintillators is typically no larger than 1 ns. The value would therefore be minor in comparison to variations in t_0 and the combined uncertainties in the laser emission time and the PMT timing.

8

Conclusions

*It's a great thing when you realise you still have the ability to surprise yourself.
Makes you wonder what else you can do that you've forgotten about.*

Lester Burnham (American Beauty), Alan Ball

The SNO+ experiment is a liquid scintillator based neutrino experiment. It is a re-purposing of the original Cherenkov detector used to study solar neutrinos in the SNO experiment. The experiment is sensitive to a variety of interesting physics that include; invisible nucleon decay modes, *pep*-chain and CNO-cycle solar neutrinos, geo-neutrinos, reactor anti-neutrinos, supernova neutrinos and $0\nu\beta\beta$ -decay. To study these processes the experiment will operate over three phases; water, scintillator and tellurium (loading of the scintillator with tellurium). The primary objective is during the tellurium phase, in which SNO+ will search for the $0\nu\beta\beta$ -decay of ^{130}Te . This phase will begin by loading 780 tonnes of liquid scintillator with 0.3% natural tellurium that has an abundance of \sim 34% ^{130}Te . At 0.3% loading this is equivalent to \sim 800 kg of ^{130}Te . Several upgrades have been made to the detector to ensure it is compatible with scintillator. This includes the installation of AV hold-down ropes and a variety of electronics upgrades to handle the increased light yield, a factor of 50 times larger than that of the D₂O used in SNO.

The base scintillator mixture used is LABPPO, which consists of an LAB solvent containing a PPO fluor. As part of the loading procedure for the tellurium phase, a surfactant, PRS is added to the LABPPO to keep the tellurium in suspension. PRS

is highly absorbing over the PPO emission spectrum and therefore a secondary wavelength shifter is required. There are currently two candidates, bis-MSB and perylene;

- Scintillator Phase: LABPPO
- Tellurium Phase - Candidate A: LABPPO+0.3%Te+Bis-MSB
- Tellurium Phase - Candidate B: LABPPO+0.3%Te+Perylene

The use of scintillator increases sensitivity to physics in a 1-3 MeV ROI. A variety of internal and external backgrounds coincide with this ROI, contaminating the signal region with unwanted physics events. The source of these backgrounds is predominately from the radioactive decay of daughter nuclei from the ^{238}U and ^{232}Th chains. SNO+ has therefore imposed stringent radiopurity levels throughout its commissioning which has included the construction of a scintillator plant. The plant must be sealed from contaminants in the lab atmosphere such as radon that emanates from the surrounding mine rock. To prevent such contaminants entering the detector, the facility has been constructed with a per-component leak rate $\leq 10^{-9}$ mBar L s $^{-1}$.

Prior to collecting physics data in each of the three phases, a full detector calibration is required. This is further warranted by the fact that the original components of the SNO detector, including the PMTs, are now \sim 20 years old. The calibration can be divided up into four procedures;

- Calibration of the electronic systems.
- Calibration of the PMTs.
- Calibration of the detector optical response.
- Calibration of the detector energy response.

The optical calibration aims to characterise optical effects in the detector such as reflections, refraction and attenuation; the combined effect of scattering and absorption. In addition, the optical calibration determines both the angular and timing response of the \sim 9000 PMTs in the detector. The overall objective of such a calibration is to minimise the uncertainties associated with the PMT response

such that the meaningful behaviour of physical interactions inside the detector can be resolved i.e. the scintillation time profile.

Optical calibration is sought through two hardware systems, a fibre based laser/LED injection system installed into the PSUP [107] and the laserball, a light diffusing sphere [110]. The laserball, as discussed in this thesis can be used to collect data over which a parameterisation of the detector optical response can be modelled. This model characterises the PMT angular response and the attenuation of the three main detector media; the inner AV region, the acrylic of the AV itself, and the outer AV water region. The model can be applied to data collected in all three detector phases.

In the water phase, a comparison between original SNO data and SNO+ MC highlights differences between the ideal scenario as assumed in MC, and the reality of the true detector state as in SNO. Most notably, the reflectors which surround each PMT are not perfectly reflecting, and have been subject to degradation over time. This introduces an additional systematic to the optical model known as the PMT variability. The degradation of the PMT reflectors is important to monitor, as it affects the overall optical response and the energy response that it underpins.

The water phase will be the first time that the inner AV and outer AV regions have been occupied by the same material. This provides a good opportunity to break the correlation between the attenuation coefficients of the AV acrylic and the water of the outer AV region as observed in SNO. In doing so, the systematic uncertainties on the water attenuation coefficient can be significantly reduced from $> 100\%$ to $< 12\%$. In addition, the broken correlation between the acrylic and the water regions allows for an in-situ measurement of the acrylic attenuation coefficient. However, given the thin 55.0 mm nature of the acrylic, these values of the attenuation coefficient are subject to large systematic variations in the region of 10-140%.

The scintillator phase presents a new phenomena which is observed in the detector; absorption and reemission. This impacts the optical response of the detector as light that is emitted inside the detector at short wavelengths is absorbed and reemitted at longer wavelengths. At these longer wavelengths the scintillator is relatively transparent. The wavelength regions in which the scintillator is absorbing varies based on the composition of the scintillator mixture; $\lambda \lesssim 360$ nm (PPO), $\lesssim 400$ nm (bis-MSB) and $\lesssim 450$ nm (perylene). The attenuation of the scintillator

has a strong resolving power in the fit of the optical model, and values are obtained with relatively small systematic uncertainties, 1-10% for PPO, and < 4% for the mixtures containing either bis-MSB or perylene. It is found that the values of the attenuation coefficients at absorbing regions is constrained by the dimensions of the detector; the inner AV radius. In cases where light is absorbed and reemitted, the obtained attenuation coefficient coincides in the region where the absorption length of the active wavelength shifting component is ~ 10 m.

A scintillator time profile model can be used on central runs in scintillator to quantify the multi-component nature of the scintillator. This is particularly interesting for the ternary mixtures proposed for the tellurium phase. Through timing information the model is able to quantify the different wavelength regions in which the different components are most absorbing. However, the model is subject to non-negligible systematic errors associated with the timing of the laserball trigger time.

The laserball data presented in scintillator use five of the laser/dye profiles from SNO; 337 nm (N_2), 369 nm (PBD), 385 nm (BBQ), 420 nm (bis-MSB) and 505 nm (COUMARIN-500). In addition, MC studies of the scintillator mixtures can be used to inform the wavelength of an additional laser-dye whose peak emission value coincides with the average reemitted wavelength of the scintillator. For the three mixtures considered here, these are as follows:

- LABPPO:
 - α -NPO, $\lambda \in (391\text{-}425)$ nm, $\lambda_{\text{peak}} = 400$ nm
- LABPPO+0.3%Te+Bis-MSB:
 - COUMARIN-440, $\lambda \in (420\text{-}475)$ nm, $\lambda_{\text{peak}} = 446$ nm
- LABPPO+0.3%Te+Perylene:
 - COUMARIN-481, $\lambda \in (461\text{-}549)$ nm, $\lambda_{\text{peak}} = 490$ nm

Probing the optical response at these wavelengths is of interest as they are located at the transition boundary between the absorbing and transparent regimes of the scintillator in the detector. It would be interesting to further probe this transition region either side of the boundary at different wavelengths. However, this would require near-monochromatic light sources; the distributions for the proposed dyes

above are broad. This may be resolved through using an LED source, either as a modification to the laserball or as part of the fibre based light injection system.

At time of writing, no final decision has been made for the scintillator mixture to be used in the tellurium phase. However, the current consensus amongst the SNO+ collaboration favours bis-MSB over perylene due to its short mean emission time (1.4 ns: bis-MSB, 6.4 ns: perylene) and an emission profile that coincides more so with the optimal quantum efficiency of the PMTs than perylene. Most notably, the shorter emission time is conducive to more accurate position reconstruction and efficient background rejection through α - β discrimination. However, as discussed here the bis-MSB emission competes with the PRS absorption around 420 nm. Therefore further developments have been made recently to investigate the use of an alternative loading technique that makes use 1,2 butanediol to molecularly suspend the tellurium, forming an organometallic complex, in the liquid scintillator [151]. Early indications are promising, but a final decision to implement this technique is subject to tests of the complex stability over 6-12 months.

Given the above, deployment of the laserball is critical in SNO+. It is an important component of the detector calibration, and alongside data collected with a complementary fibre-based LED system characterises the detector optical response. This is required to interpret physics events, specifically the expected light detected from candidate $0\nu\beta\beta$ -decay events and associated backgrounds in the tellurium phase. However, given that these *levels* of detection, such as the PMT response or attenuation of the detector regions may change over time, the optical response will also change. Repeated deployment of the laserball therefore allows for regular monitoring of the optical response ensuring data sets collected over time are consistent with one another. Although the scintillator mixtures discussed here are not finalised, the approach and analysis of laserball data presented here outline the principle technique for which regular monitoring of the optical response can be achieved.

Appendix A

Optical Response Calculations

A.1 Light Path Derivation

Suppose there is a light path with a starting position inside the AV, \vec{r}_i and a finishing position at PMT j , \vec{r}_j . In a coordinate frame whose origin is at the centre of the AV, and using a combination of Snell's law of refraction and sine and cosine rules, one may derive the values of $\cos \theta_1$, $\cos \theta_2$ and $\cos \theta_3$ as illustrated in figure (4.2). The vectors \vec{r}_1 and \vec{r}_2 are the intersection points of the path between the inner AV/AV and AV/outer AV regions respectively.

$\cos \theta_1$: With reference to figure (4.2) and by using the cosine rule, a formula for the distance through the scintillator region, d_{Scint} is obtained;

$$d_{\text{Scint}}^2 = |\vec{r}_i|^2 + |\vec{r}_1|^2 - 2|\vec{r}_i||\vec{r}_1| \cos \theta_1. \quad (\text{A.1})$$

Using the sine rule;

$$\frac{d_{\text{Scint}}}{\sin \theta_1} = \frac{|\vec{r}_1|}{\sin(\pi - \theta_\gamma)} = \frac{|\vec{r}_1|}{\sin \theta_\gamma}. \quad (\text{A.2})$$

Rearranging for d_{Scint} in the above expression and substituting into equation (A.1), with some trigonometric manipulation, the following expression is obtained;

$$\cos^2 \theta_1 - 2 \frac{|\vec{r}_i|}{|\vec{r}_1|} \sin^2 \theta_\gamma \cos \theta_1 + \sin^2 \theta_\gamma \left(\left(\frac{|\vec{r}_i|}{|\vec{r}_1|} \right)^2 + 1 \right) - 1 = 0, \quad (\text{A.3})$$

where the identity $\sin^2 \theta_1 + \cos^2 \theta_1 = 1$ has been used. Equation (A.3) is a quadratic in $\cos \theta_1$ and can therefore be solved using the standard quadratic formula;

$$\cos \theta_1 = -\frac{b}{2a} \pm \frac{1}{2a} \sqrt{b^2 - 4ac}, \quad (\text{A.4})$$

where

$$a = 1, \quad b = -2 \frac{|\vec{r}_i|}{|\vec{r}_1|} \sin^2 \theta_\gamma \quad \text{and} \quad c = \sin^2 \theta_\gamma \left(\left(\frac{|\vec{r}_i|}{|\vec{r}_1|} \right)^2 + 1 \right) - 1. \quad (\text{A.5})$$

Thus the expression for $\cos \theta_1$ follows;

$$\begin{aligned} \Rightarrow \cos \theta_1 &= \frac{|\vec{r}_i|}{|\vec{r}_1|} \sin^2 \theta_\gamma \\ &\quad \pm \frac{1}{2} \sqrt{4 \left(\frac{|\vec{r}_i|}{|\vec{r}_1|} \right)^2 \sin^4 \theta_\gamma - 4 \left(\frac{|\vec{r}_i|}{|\vec{r}_1|} \right)^2 \sin^2 \theta_\gamma - 4 \sin^2 \theta_\gamma + 4}, \\ &= \frac{|\vec{r}_i|}{|\vec{r}_1|} \sin^2 \theta_\gamma \\ &\quad \pm \sqrt{\left(\frac{|\vec{r}_i|}{|\vec{r}_1|} \right)^2 \sin^2 \theta_\gamma (\sin^2 \theta_\gamma - 1) + \cos^2 \theta_\gamma}, \\ &= \frac{|\vec{r}_i|}{|\vec{r}_1|} \sin^2 \theta_\gamma \pm \cos \theta_\gamma \sqrt{1 - \left(\frac{|\vec{r}_i|}{|\vec{r}_1|} \sin \theta_\gamma \right)^2}. \end{aligned} \quad (\text{A.6})$$

Similarly, an expression for $\cos \theta_2$ can be obtained by transforming the points which define the triangle for $\cos \theta_1$ to those which define that for $\cos \theta_2$ i.e.

$$\vec{r}_i \rightarrow \vec{r}_1, \quad \vec{r}_1 \rightarrow \vec{r}_2, \quad \text{and} \quad \theta_\gamma \rightarrow \theta_b. \quad (\text{A.7})$$

This gives an expression for $\cos \theta_2$;

$$\cos \theta_2 = \frac{|\vec{r}_1|}{|\vec{r}_2|} \sin^2 \theta_b \pm \cos \theta_b \sqrt{1 - \left(\frac{|\vec{r}_1|}{|\vec{r}_2|} \sin \theta_b \right)^2}. \quad (\text{A.8})$$

Using Snell's law of refraction for light passing from material a to material b with respective refractive indices of n_a and n_b (in this case from the scintillator region

to the acrylic of the AV), $\sin \theta_b$ can be expressed as follows;

$$\begin{aligned} \frac{\sin \theta_a}{\sin \theta_b} &= \frac{n_b}{n_a} \quad (\text{Snell's Law}) \\ \Rightarrow \sin \theta_b &= \frac{n_a}{n_b} \sin \theta_a. \end{aligned} \quad (\text{A.9})$$

$\sin \theta_b$ can subsequently be expressed in terms of θ_γ by use of the sine rule and again, Snell's law;

$$\begin{aligned} \frac{|\vec{r}_i|}{\sin \theta_a} &= \frac{|\vec{r}_1|}{\sin(\pi - \theta_\gamma)} = \frac{|\vec{r}_1|}{\sin \theta_\gamma} \\ \Rightarrow \sin \theta_a &= \frac{|\vec{r}_i|}{|\vec{r}_1|} \sin \theta_\gamma, \\ \frac{|\vec{r}_2|}{\sin(\pi - \theta_b)} &= \frac{|\vec{r}_2|}{\sin \theta_b} = \frac{n_b}{n_a} \frac{|\vec{r}_2|}{\sin \theta_a} \\ \Rightarrow \sin \theta_b &= \frac{n_a}{n_b} \sin \theta_a = \frac{n_a}{n_b} \frac{|\vec{r}_i|}{|\vec{r}_1|} \sin \theta_\gamma. \end{aligned} \quad (\text{A.10})$$

Using the above result and the transformations as in expression (A.7) one obtains the final result for $\cos \theta_2$;

$$\begin{aligned} \cos \theta_2 &= \frac{1}{|\vec{r}_1| |\vec{r}_2|} \left(\frac{n_a}{n_b} |\vec{r}_i| \sin \theta_\gamma \right)^2 \\ &\pm \left[\sqrt{1 - \left(\frac{n_a}{n_b} \frac{|\vec{r}_i|}{|\vec{r}_1|} \sin \theta_\gamma \right)^2} \right. \\ &\quad \left. \times \sqrt{1 - \left(\frac{n_a}{n_b} \frac{|\vec{r}_i|}{|\vec{r}_2|} \sin \theta_\gamma \right)^2} \right]. \end{aligned} \quad (\text{A.11})$$

Finally, an expression for $\cos \theta_3$ can be obtained using the same principle by a transformation of variables;

$$\vec{r}_i \rightarrow \vec{r}_2, \quad \vec{r}_1 \rightarrow \vec{r}_j, \quad \text{and} \quad \theta_\gamma \rightarrow \theta_d. \quad (\text{A.12})$$

This gives an expression for $\cos \theta_3$;

$$\cos \theta_3 = \frac{|\vec{r}_2|}{|\vec{r}_j|} \sin^2 \theta_d \pm \cos \theta_d \sqrt{1 - \left(\frac{|\vec{r}_2|}{|\vec{r}_j|} \sin \theta_d \right)^2}. \quad (\text{A.13})$$

Using Snell's law $\sin \theta_d$ can be expressed as follows;

$$\sin \theta_d = \frac{n_b}{n_c} \sin \theta_c. \quad (\text{A.14})$$

By applying the sine rule, a relation between $\sin \theta_c$ and $\sin \theta_b$ can be obtained;

$$\sin \theta_c = \frac{|\vec{r}_1|}{|\vec{r}_2|} \sin \theta_b. \quad (\text{A.15})$$

Finally, using this and equation (A.10), $\sin \theta_d$ can be expressed in terms of $\sin \theta_\gamma$ as follows;

$$\sin \theta_d = \frac{n_b}{n_c} \frac{|\vec{r}_1|}{|\vec{r}_2|} \sin \theta_b = \frac{n_a}{n_b} \frac{n_b}{n_c} \frac{|\vec{r}_1|}{|\vec{r}_2|} \frac{|\vec{r}_i|}{|\vec{r}_1|} \sin \theta_\gamma = \frac{n_a}{n_c} \frac{|\vec{r}_i|}{|\vec{r}_2|} \sin \theta_\gamma. \quad (\text{A.16})$$

$\cos \theta_3$ in terms of θ_γ is thus;

$$\begin{aligned} \cos \theta_3 &= \frac{1}{|\vec{r}_2| |\vec{r}_j|} \left(\frac{n_a}{n_c} |\vec{r}_i| \sin \theta_\gamma \right)^2 \\ &+ \left[\sqrt{1 - \left(\frac{|\vec{r}_i|}{|\vec{r}_2|} \frac{n_a}{n_c} \sin \theta_\gamma \right)^2} \right. \\ &\quad \times \left. \sqrt{1 - \left(\frac{|\vec{r}_i|}{|\vec{r}_j|} \frac{n_a}{n_c} \sin \theta_\gamma \right)^2} \right]. \end{aligned} \quad (\text{A.17})$$

A.2 PMT Bucket Time

As discussed in section (4.2.2), the light path calculation is calculated up to the entrance of the PMT bucket. The time spent inside the bucket prior to the creation of the photoelectron, $t_{\text{bucket}}(\theta_\gamma)$ is an additional time discussed by the author here [136]. Overall, the bucket time is a 0.45-0.7 ns correction, which can be assumed wavelength independent given its size. The time is related to the incident angle of the light entering the PMT bucket as shown in figure (A.1). It is calculated using MC simulations.

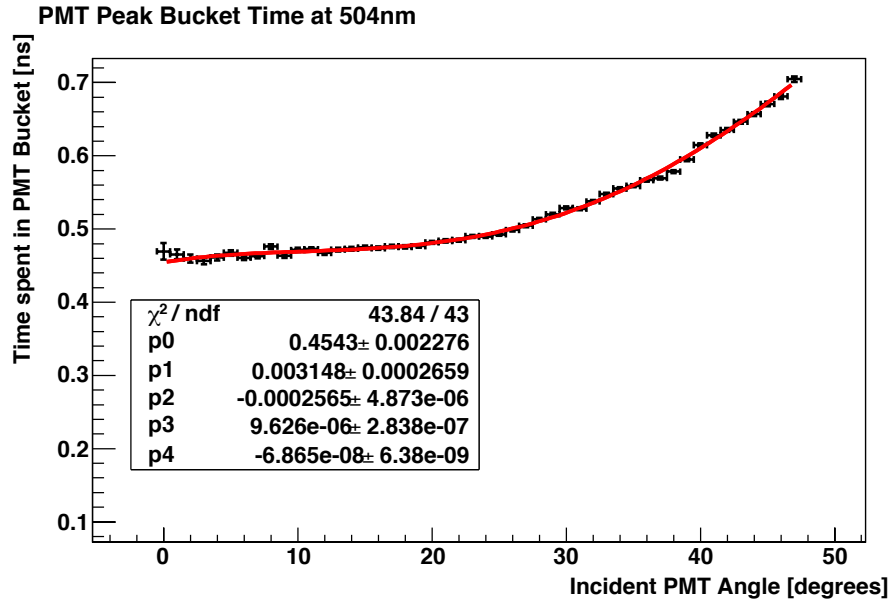


FIGURE A.1: The time spent inside the PMT bucket. This is measured as the time spent between the photon entering the PMT bucket, and the creation of the photoelectron at the PMT photocathode. The example above is shown for 504 nm, and is consistent with that observed for all wavelengths.

A.3 Fresnel Transmission Coefficient Calculation

The calculation of the Fresnel transmission coefficient assumes equal polarisation of the laserlight; half perpendicular to the plane of incidence and half parallel. The coefficient is calculated for both these components - perpendicular, T_{\perp} and parallel, T_{\parallel} - at each material interface of the path between the laserball position and the PMT; the inner AV/AV and AV/outer AV regions. For a light path passing from material A to material B with refractive indices n_A and n_B at an incident angle, θ_{inc} , the perpendicular and parallel components are calculated as follows;

$$T_{\perp} = \frac{4n_A \cos \theta_{\text{inc}} R(n_A, n_B, \theta_{\text{inc}})}{(n_A \cos \theta_{\text{inc}} + R(n_A, n_B, \theta_{\text{inc}}))^2}, \quad (\text{A.18})$$

$$T_{\parallel} = \frac{4n_A n_B^2 \cos \theta_{\text{inc}} R(n_A, n_B, \theta_{\text{inc}})}{(n_B^2 \cos \theta_{\text{inc}} + n_A R(n_A, n_B, \theta_{\text{inc}}))^2}, \quad (\text{A.19})$$

where,

$$R(n_A, n_B, \theta_{\text{inc}}) = \begin{cases} \sqrt{n_B^2 - n_A^2 \sin^2 \theta_{\text{inc}}} & \text{if } n_B > n_A \sin \theta_{\text{inc}} \\ 0 & \text{if } n_B < n_A \sin \theta_{\text{inc}} \end{cases}. \quad (\text{A.20})$$

In the case of $R(n_A, n_B, \theta_{\text{inc}}) = 0$, this is equivalent to total internal reflection. For the light path as described in section (A.1), from position \vec{r}_i to PMT j with position, \vec{r}_j the total transmission coefficient, T_{ij} is the product of these terms;

$$T_{ij} = \frac{1}{2} (T_{\perp}^{\text{IA}} T_{\perp}^{\text{OA}} + T_{\parallel}^{\text{IA}} T_{\parallel}^{\text{OA}}), \quad (\text{A.21})$$

where $\{T_{\perp}^{\text{IA}}, T_{\perp}^{\text{OA}}\}$ and $\{T_{\parallel}^{\text{IA}}, T_{\parallel}^{\text{OA}}\}$ are the respective transmission coefficients from the inner AV/AV (IA) and AV/outer AV (OA) material interfaces for the perpendicular and parallel components. The factor of 1/2 is due to the equal polarisation in both components as assumed. The value of θ_{inc} used in the calculations of the coefficients is obtained from the vector description of the light path;

$$\theta_{\text{inc}}^{\text{IA}} = \cos^{-1} \left(\hat{\vec{r}}_1 \cdot \hat{\vec{r}}_{\gamma} \right), \quad \theta_{\text{inc}}^{\text{OA}} = \cos^{-1} \left(\frac{(\hat{\vec{r}}_2 - \hat{\vec{r}}_1)}{\sqrt{2}} \cdot \hat{\vec{r}}_2 \right), \quad (\text{A.22})$$

where \vec{r}_{γ} is the initial photon direction from the laserball, \vec{r}_1 is the intersection point on the inner AV surface and \vec{r}_2 is the intersection point on the outer AV surface. The refractive indices are functions of the wavelength i.e. $n_A(\lambda), n_B(\lambda)$, whose values are obtained from the forms given in figure (4.3).

A.4 Scintillator Time Profile Model Timings

The scintillator time profile model as described in section (4.5.3) (see expression (4.47)) samples times according to the laserball pulse and PMT timing widths; $t_{\sigma, \text{LB}} = 0.7$ ns and $t_{\sigma, \text{PMT}} = 1.7$ ns. These distributions are shown in figure (A.2), and are the same time distributions implemented into RAT for the generation of MC data.

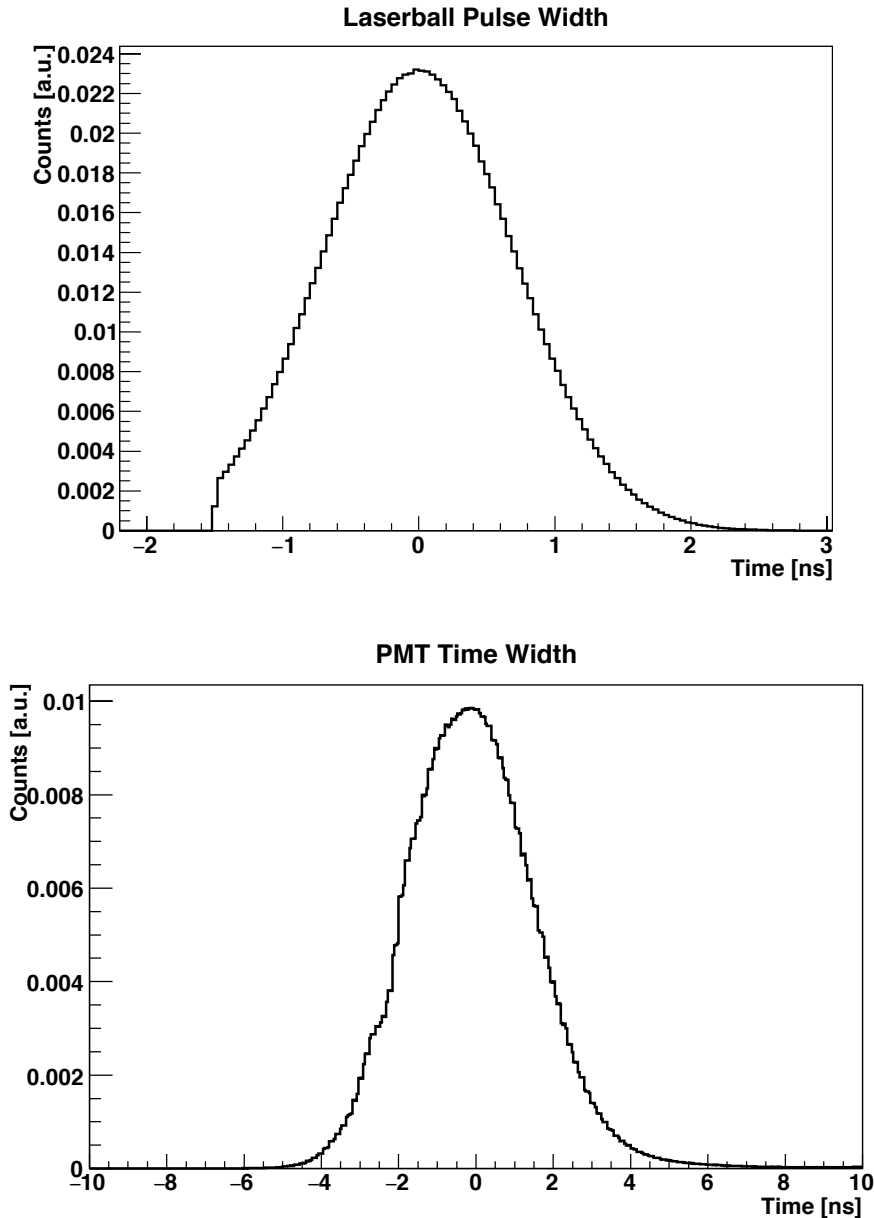


FIGURE A.2: Top: The laserball emission time. The distribution is truncated at -1.5 ns. The width of the distribution ($\sigma = 0.7$ ns) is due to the light dispersion in the ~ 40 m optical fibres from the laser system on the upper deck above the cavity to the laserball. Bottom: The time transit spread of the PMTs. The time transit spread is the distribution in times over which a photoelectron is accelerated through the PMT dynode stack. The spread of this distribution is $\sigma \simeq 1.7$ ns.

Appendix B

Monte-Carlo Data Production: Extended

B.1 KITON-RED Laser-Dye for Monte-Carlo Production

As stated in section (5.1.1), the KITON-RED laser-dye is omitted from the SNO+ MC data production. This is due to a combination of high attenuation in water at long wavelengths, $\alpha \sim 3 \times 10^{-4} \text{ mm}^{-1}$ (see table (6.2)) and low PMT efficiency, $< 2.5\%$ (see figure (3.13)). Shown in figure (B.1) are the average detector occupancies with varying intensities at 620 nm in water. Even at high intensities, the occupancy is small, $\leq 0.2\%$. Extrapolating the linear response as shown, a target occupancy of 3% would require $1236 \times 10^3 \text{ photons pulse}^{-1}$. This is computer intensive. In principle, the PMT efficiencies could be scaled up, or the attenuation coefficient could be scaled down. However, this is undesired given the aim of the optical model is to directly probe the expected value of these properties across all wavelengths.

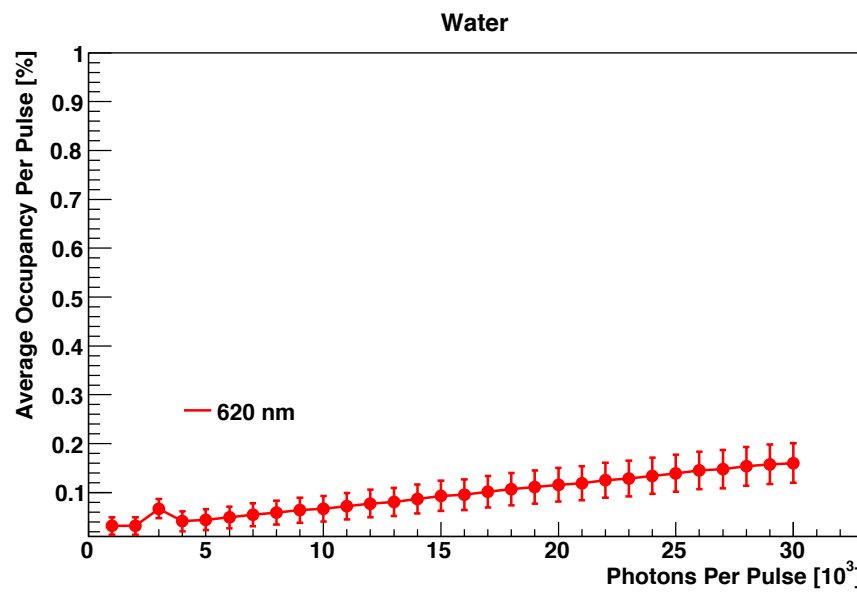


FIGURE B.1: Values for the average occupancy per pulse for the laserball at 620 nm in water. Here, the average occupancy is the ratio of the mean number of hits, \bar{N}_{Hits} to the total number of PMTs, $n_{\text{PMT}} = 9728$. Errors are statistical, $\pm \sqrt{\bar{N}_{\text{Hits}}}$. Photon units are in photons $\times 10^3$ as simulated in RAT.

Appendix C

Optical Model Fits: Extended Results

C.1 Attenuation Coefficient Systematics: Water & D₂O

The following are the full systematic contributions to the attenuation coefficients for each of the wavelengths scans from the SNO October 2003 (D₂O) and SNO+ MC data sets (H₂O). The SNO data set used a fixed value of the AV acrylic, α_{AV} based on ex-situ measurements from SNO. The SNO+ MC data combined the inner and outer AV water regions to fit for $\alpha_{H_2O}^{comb.}$ and α_{AV} .

Attenuation Systematics - SNO October 2003, D₂O, 337 nm

Systematic	$\alpha_{\text{D}_2\text{O}}$ 10^{-5} mm^{-1}	$s_i \times \Delta\alpha/\alpha$	$\alpha_{\text{H}_2\text{O}}$ 10^{-5} mm^{-1}	$s_i \times \Delta\alpha/\alpha$	$\chi^2/\text{No.Dof}$
Nominal	1.44	0.00%	3.89	0.00%	1.20
$ r_{\text{LB}} \times 1.01$	1.18	-3.58%	0.71	-16.38%	1.20
$r_x - 50.0 \text{ mm}$	1.43	-0.12%	3.55	-1.79%	1.21
$r_x + 50.0 \text{ mm}$	1.44	-0.04%	3.94	0.26%	1.21
$r_y - 50.0 \text{ mm}$	1.41	-0.45%	4.24	1.77%	1.20
$r_y + 50.0 \text{ mm}$	1.47	0.36%	3.47	-2.20%	1.21
$r_z - 50.0 \text{ mm}$	1.50	2.18%	2.89	-12.89%	1.20
$r_z + 50.0 \text{ mm}$	1.37	-2.49%	5.12	15.78%	1.20
$\lambda - \lambda_{\text{RMS}} \text{ nm}$	1.44	0.02%	3.92	0.81%	1.20
$\lambda + \lambda_{\text{RMS}} \text{ nm}$	1.45	0.24%	4.00	2.62%	1.20
H^2	1.44	-0.00%	4.02	0.16%	1.21
$H = 1.0$	1.43	-0.04%	4.31	0.53%	1.24
$\chi^2_{\text{lim,f}} = 16$	1.40	-2.57%	5.59	43.53%	1.47
$\sigma_{\text{PMT}} = 0$	1.48	2.79%	2.22	-43.09%	1.84
$d_{\text{innerAV}}^{50.0\text{mm}}$	1.44	0.19%	3.95	1.50%	1.20
Total		6.21%		66.76%	

TABLE C.1: Systematic contributions to $\alpha_{\text{D}_2\text{O}}$ and $\alpha_{\text{H}_2\text{O}}$ from the SNO October 2003 data set with heavywater at 337 nm.**Attenuation Systematics - SNO October 2003, D₂O, 369 nm**

Systematic	$\alpha_{\text{D}_2\text{O}}$ 10^{-5} mm^{-1}	$s_i \times \Delta\alpha/\alpha$	$\alpha_{\text{H}_2\text{O}}$ 10^{-5} mm^{-1}	$s_i \times \Delta\alpha/\alpha$	$\chi^2/\text{No.Dof}$
Nominal	0.93	0.00%	2.78	0.00%	0.98
$ r_{\text{LB}} \times 1.01$	0.67	-5.58%	-0.30	-22.16%	0.98
$r_x - 50.0 \text{ mm}$	0.93	0.14%	2.73	-0.40%	0.99
$r_x + 50.0 \text{ mm}$	0.91	-0.32%	2.71	-0.53%	0.99
$r_y - 50.0 \text{ mm}$	0.91	-0.40%	2.58	-1.49%	0.98
$r_y + 50.0 \text{ mm}$	0.94	0.30%	2.64	-1.00%	0.99
$r_z - 50.0 \text{ mm}$	0.98	2.89%	1.59	-21.44%	0.98
$r_z + 50.0 \text{ mm}$	0.87	-3.13%	3.79	17.97%	0.98
$\lambda - \lambda_{\text{RMS}} \text{ nm}$	0.92	-0.34%	2.74	-1.62%	0.98
$\lambda + \lambda_{\text{RMS}} \text{ nm}$	0.93	0.33%	2.83	1.71%	0.98
H^2	0.93	0.01%	2.78	-0.01%	0.98
$H = 1.0$	0.99	0.34%	3.16	0.68%	1.02
$\chi^2_{\text{lim,f}} = 16$	0.90	-2.62%	3.64	30.79%	1.16
$\sigma_{\text{PMT}} = 0$	1.03	10.76%	2.09	-24.93%	1.63
$d_{\text{innerAV}}^{50.0\text{mm}}$	0.93	0.04%	2.80	0.40%	0.98
Total		13.14%		53.41%	

TABLE C.2: Systematic contributions to $\alpha_{\text{D}_2\text{O}}$ and $\alpha_{\text{H}_2\text{O}}$ from the SNO October 2003 data set with heavywater at 369 nm.

Attenuation Systematics - SNO October 2003, D₂O, 385 nm

Systematic	α_{D_2O} 10^{-5} mm^{-1}	$s_i \times \Delta\alpha/\alpha$	α_{H_2O} 10^{-5} mm^{-1}	$s_i \times \Delta\alpha/\alpha$	$\chi^2/\text{No.Dof}$
Nominal	0.80	0.00%	3.90	0.00%	0.98
$ r_{LB} \times 1.01$	0.54	-6.55%	0.55	-17.17%	0.97
$r_x - 50.0 \text{ mm}$	0.80	0.00%	3.87	-0.14%	0.98
$r_x + 50.0 \text{ mm}$	0.80	-0.22%	3.73	-0.87%	0.98
$r_y - 50.0 \text{ mm}$	0.78	-0.71%	3.67	-1.18%	0.97
$r_y + 50.0 \text{ mm}$	0.83	0.59%	3.70	-1.03%	0.98
$r_z - 50.0 \text{ mm}$	0.86	3.29%	2.57	-17.01%	0.98
$r_z + 50.0 \text{ mm}$	0.75	-3.48%	4.84	12.00%	0.97
$\lambda - \lambda_{\text{RMS}} \text{ nm}$	0.80	-0.21%	3.87	-0.78%	0.98
$\lambda + \lambda_{\text{RMS}} \text{ nm}$	0.81	0.20%	3.91	0.18%	0.98
H^2	0.81	0.00%	3.89	-0.01%	0.98
$H = 1.0$	0.89	0.52%	4.27	0.48%	1.01
$\chi^2_{\text{lim,f}} = 16$	0.78	-3.27%	4.74	21.38%	1.15
$\sigma_{\text{PMT}} = 0$	0.91	12.54%	2.58	-33.81%	1.63
$d_{\text{innerAV}}^{50.0\text{mm}}$	0.80	-0.01%	3.90	-0.14%	0.98
Total		15.33%		48.30%	

TABLE C.3: Systematic contributions to α_{D_2O} and α_{H_2O} from the SNO October 2003 data set with heavywater at 385 nm.**Attenuation Systematics - SNO October 2003, D₂O, 420 nm**

Systematic	α_{D_2O} 10^{-5} mm^{-1}	$s_i \times \Delta\alpha/\alpha$	α_{H_2O} 10^{-5} mm^{-1}	$s_i \times \Delta\alpha/\alpha$	$\chi^2/\text{No.Dof}$
Nominal	0.60	0.00%	1.78	0.00%	1.02
$ r_{LB} \times 1.01$	0.35	-8.34%	-1.10	-32.41%	1.01
$r_x - 50.0 \text{ mm}$	0.60	0.04%	1.82	0.55%	1.02
$r_x + 50.0 \text{ mm}$	0.59	-0.24%	1.76	-0.21%	1.02
$r_y - 50.0 \text{ mm}$	0.56	-1.35%	1.55	-2.52%	1.02
$r_y + 50.0 \text{ mm}$	0.63	1.15%	1.68	-1.09%	1.03
$r_z - 50.0 \text{ mm}$	0.66	5.27%	0.65	-31.67%	1.02
$r_z + 50.0 \text{ mm}$	0.53	-5.41%	2.86	30.57%	1.02
$\lambda - \lambda_{\text{RMS}} \text{ nm}$	0.59	-0.61%	1.74	-2.06%	1.02
$\lambda + \lambda_{\text{RMS}} \text{ nm}$	0.60	0.18%	1.79	1.08%	1.02
H^2	0.59	-0.03%	1.78	0.00%	1.02
$H = 1.0$	0.67	0.65%	2.09	0.89%	1.06
$\chi^2_{\text{lim,f}} = 16$	0.53	-11.50%	3.10	74.52%	1.23
$\sigma_{\text{PMT}} = 0$	0.69	16.03%	0.38	-78.34%	1.63
$d_{\text{innerAV}}^{50.0\text{mm}}$	0.60	-0.00%	1.78	0.01%	1.02
Total		22.80%		121.21%	

TABLE C.4: Systematic contributions to α_{D_2O} and α_{H_2O} from the SNO October 2003 data set with heavywater at 420 nm.

Attenuation Systematics - SNO October 2003, D₂O, 505 nm

Systematic	α_{D_2O} 10^{-5} mm^{-1}	$s_i \times \Delta\alpha/\alpha$	α_{H_2O} 10^{-5} mm^{-1}	$s_i \times \Delta\alpha/\alpha$	$\chi^2/\text{No.Dof}$
Nominal	0.31	0.00%	4.87	0.00%	1.02
$ r_{LB} \times 1.01$	0.05	-16.85%	1.86	-12.36%	1.02
$r_x - 50.0 \text{ mm}$	0.31	-0.22%	4.71	-0.65%	1.03
$r_x + 50.0 \text{ mm}$	0.31	-0.13%	5.01	0.56%	1.03
$r_y - 50.0 \text{ mm}$	0.28	-2.03%	4.67	-0.81%	1.02
$r_y + 50.0 \text{ mm}$	0.34	1.97%	4.73	-0.58%	1.03
$r_z - 50.0 \text{ mm}$	0.35	6.67%	3.64	-12.61%	1.02
$r_z + 50.0 \text{ mm}$	0.26	-7.69%	6.14	13.03%	1.02
$\lambda - \lambda_{\text{RMS}} \text{ nm}$	0.31	-1.11%	4.80	-1.57%	1.02
$\lambda + \lambda_{\text{RMS}} \text{ nm}$	0.31	0.71%	5.08	4.23%	1.02
H^2	0.31	-0.01%	4.89	0.02%	1.03
$H = 1.0$	0.35	0.68%	4.96	0.09%	1.08
$\chi^2_{\text{lim,f}} = 16$	0.28	-10.07%	5.78	18.72%	1.24
$\sigma_{\text{PMT}} = 0$	0.37	18.86%	3.59	-26.41%	1.65
$d_{\text{innerAV}}^{50.0\text{mm}}$	0.31	-0.01%	4.87	0.02%	1.02
Total		29.24%		39.39%	

TABLE C.5: Systematic contributions to α_{D_2O} and α_{H_2O} from the SNO October 2003 data set with heavywater at 505 nm.**Attenuation Systematics - SNO October 2003, D₂O, 620 nm**

Systematic	α_{D_2O} 10^{-5} mm^{-1}	$s_i \times \Delta\alpha/\alpha$	α_{H_2O} 10^{-5} mm^{-1}	$s_i \times \Delta\alpha/\alpha$	$\chi^2/\text{No.Dof}$
Nominal	0.37	0.00%	32.68	0.00%	0.98
$ r_{LB} \times 1.01$	0.10	-14.44%	28.59	-2.51%	0.98
$r_x - 50.0 \text{ mm}$	0.37	-0.28%	32.57	-0.07%	0.99
$r_x + 50.0 \text{ mm}$	0.37	0.02%	32.74	0.04%	0.99
$r_y - 50.0 \text{ mm}$	0.34	-1.52%	32.98	0.18%	0.99
$r_y + 50.0 \text{ mm}$	0.40	1.44%	32.39	-0.18%	0.99
$r_z - 50.0 \text{ mm}$	0.38	1.57%	31.04	-2.51%	0.98
$r_z + 50.0 \text{ mm}$	0.36	-2.31%	34.43	2.67%	0.98
$\lambda - \lambda_{\text{RMS}} \text{ nm}$	0.37	-0.63%	32.65	-0.09%	0.99
$\lambda + \lambda_{\text{RMS}} \text{ nm}$	0.37	0.25%	32.69	0.04%	0.99
H^2	0.37	0.00%	32.75	0.01%	0.99
$H = 1.0$	0.42	0.58%	33.42	0.11%	1.02
$\chi^2_{\text{lim,f}} = 16$	0.37	0.02%	33.09	1.24%	1.16
$\sigma_{\text{PMT}} = 0$	0.39	5.57%	32.26	-1.29%	1.67
$d_{\text{innerAV}}^{50.0\text{mm}}$	0.37	-0.11%	32.69	0.01%	0.99
Total		15.90%		4.80%	

TABLE C.6: Systematic contributions to α_{D_2O} and α_{H_2O} from the SNO October 2003 data set with heavywater at 620 nm.

Attenuation Systematics - SNO+ MC, H₂O, 337 nm

Systematic	$\alpha_{\text{H}_2\text{O}}^{\text{comb.}}$ 10^{-5} mm^{-1}	$s_i \times \Delta\alpha/\alpha$	α_{AV} 10^{-3} mm^{-1}	$s_i \times \Delta\alpha/\alpha$	$\chi^2/\text{No.Dof}$
Nominal	2.70	0.00%	4.82	0.00%	1.00
$ r_{\text{LB}} \times 1.01$	2.44	-1.95%	3.65	-4.85%	1.00
$r_x - 50.0 \text{ mm}$	2.70	0.02%	4.87	0.23%	1.02
$r_x + 50.0 \text{ mm}$	2.70	-0.03%	4.90	0.36%	1.02
$r_y - 50.0 \text{ mm}$	2.66	-0.29%	4.68	-0.56%	1.02
$r_y + 50.0 \text{ mm}$	2.74	0.29%	5.00	0.76%	1.02
$r_z - 50.0 \text{ mm}$	2.75	0.85%	4.29	-5.46%	1.01
$r_z + 50.0 \text{ mm}$	2.65	-0.90%	5.33	5.34%	1.00
$\lambda - \lambda_{\text{RMS}} \text{ nm}$	2.70	0.00%	4.81	-0.01%	1.00
$\lambda + \lambda_{\text{RMS}} \text{ nm}$	2.70	0.01%	4.81	-0.04%	1.00
H^2	2.70	0.01%	4.81	-0.01%	1.00
$H = 1.0$	-1.29	-7.38%	5.16	0.36%	1.46
$\chi^2_{\text{lim,f}} = 16$	2.68	-0.82%	5.04	4.66%	1.20
$\chi^2_{\text{lim,f}} = 9$	2.69	-0.29%	4.87	1.14%	1.07
Total		7.79%		10.30%	

TABLE C.7: Systematic contributions to $\alpha_{\text{H}_2\text{O}}$ and α_{AV} from the SNO+ MC data set with water at 337 nm.**Attenuation Systematics - SNO+ MC, H₂O, 369 nm**

Systematic	$\alpha_{\text{H}_2\text{O}}^{\text{comb.}}$ 10^{-5} mm^{-1}	$s_i \times \Delta\alpha/\alpha$	α_{AV} 10^{-3} mm^{-1}	$s_i \times \Delta\alpha/\alpha$	$\chi^2/\text{No.Dof}$
Nominal	2.05	0.00%	1.39	0.00%	1.00
$ r_{\text{LB}} \times 1.01$	1.78	-2.61%	0.35	-14.96%	1.00
$r_x - 50.0 \text{ mm}$	2.05	-0.05%	1.39	-0.09%	1.02
$r_x + 50.0 \text{ mm}$	2.05	-0.03%	1.43	0.53%	1.02
$r_y - 50.0 \text{ mm}$	2.01	-0.43%	1.23	-2.30%	1.02
$r_y + 50.0 \text{ mm}$	2.09	0.36%	1.55	2.31%	1.02
$r_z - 50.0 \text{ mm}$	2.09	0.91%	0.90	-17.65%	1.00
$r_z + 50.0 \text{ mm}$	2.01	-1.09%	1.82	15.36%	1.00
$\lambda - \lambda_{\text{RMS}} \text{ nm}$	2.05	-0.01%	1.39	-0.01%	1.00
$\lambda + \lambda_{\text{RMS}} \text{ nm}$	2.05	-0.01%	1.40	0.31%	1.00
H^2	2.05	0.01%	1.39	-0.03%	1.00
$H = 1.0$	-2.11	-10.13%	1.66	0.97%	1.44
$\chi^2_{\text{lim,f}} = 16$	2.05	-0.29%	1.52	9.28%	1.19
$\chi^2_{\text{lim,f}} = 9$	2.05	0.06%	1.43	2.40%	1.07
Total		10.58%		29.58%	

TABLE C.8: Systematic contributions to $\alpha_{\text{H}_2\text{O}}$ and α_{AV} from the SNO+ MC data set with water at 369 nm.

Attenuation Systematics - SNO+ MC, H₂O, 385 nm

Systematic	$\alpha_{\text{H}_2\text{O}}^{\text{comb.}}$ 10^{-5} mm^{-1}	$s_i \times \Delta\alpha/\alpha$	α_{AV} 10^{-3} mm^{-1}	$s_i \times \Delta\alpha/\alpha$	$\chi^2/\text{No.Dof}$
Nominal	1.88	0.00%	0.65	0.00%	1.00
$ r_{\text{LB}} \times 1.01$	1.61	-2.90%	-0.31	-29.67%	1.00
$r_x - 50.0 \text{ mm}$	1.88	-0.02%	0.69	1.25%	1.02
$r_x + 50.0 \text{ mm}$	1.88	-0.02%	0.68	1.00%	1.02
$r_y - 50.0 \text{ mm}$	1.84	-0.42%	0.52	-3.97%	1.02
$r_y + 50.0 \text{ mm}$	1.92	0.38%	0.83	5.46%	1.02
$r_z - 50.0 \text{ mm}$	1.91	0.80%	0.22	-32.85%	1.01
$r_z + 50.0 \text{ mm}$	1.85	-0.91%	1.04	30.35%	1.00
$\lambda - \lambda_{\text{RMS}} \text{ nm}$	1.88	-0.01%	0.65	-0.18%	1.00
$\lambda + \lambda_{\text{RMS}} \text{ nm}$	1.88	-0.01%	0.65	0.31%	1.00
H^2	1.88	0.00%	0.65	-0.01%	1.00
$H = 1.0$	-2.19	-10.82%	1.14	3.81%	1.46
$\chi^2_{\text{lim,f}} = 16$	1.85	-1.75%	0.85	30.32%	1.22
$\chi^2_{\text{lim,f}} = 9$	1.88	-0.28%	0.70	7.32%	1.07
Total		11.42%		62.58%	

TABLE C.9: Systematic contributions to $\alpha_{\text{H}_2\text{O}}$ and α_{AV} from the SNO+ MC data set with water at 385 nm.

Attenuation Systematics - SNO+ MC, H₂O, 420 nm

Systematic	$\alpha_{\text{H}_2\text{O}}^{\text{comb.}}$ 10^{-5} mm^{-1}	$s_i \times \Delta\alpha/\alpha$	α_{AV} 10^{-3} mm^{-1}	$s_i \times \Delta\alpha/\alpha$	$\chi^2/\text{No.Dof}$
Nominal	2.05	0.00%	0.29	0.00%	1.02
$ r_{\text{LB}} \times 1.01$	1.78	-2.63%	-0.69	-68.04%	1.02
$r_x - 50.0 \text{ mm}$	2.05	-0.02%	0.29	0.02%	1.04
$r_x + 50.0 \text{ mm}$	2.05	0.02%	0.34	3.49%	1.03
$r_y - 50.0 \text{ mm}$	2.01	-0.39%	0.16	-8.76%	1.03
$r_y + 50.0 \text{ mm}$	2.09	0.35%	0.39	7.11%	1.03
$r_z - 50.0 \text{ mm}$	2.08	0.81%	-0.15	-76.78%	1.02
$r_z + 50.0 \text{ mm}$	2.01	-0.95%	0.69	69.88%	1.01
$\lambda - \lambda_{\text{RMS}} \text{ nm}$	2.05	-0.01%	0.28	-1.31%	1.02
$\lambda + \lambda_{\text{RMS}} \text{ nm}$	2.05	-0.00%	0.29	-0.26%	1.02
H^2	2.05	0.00%	0.29	-0.04%	1.02
$H = 1.0$	-2.11	-10.15%	0.72	7.47%	1.45
$\chi^2_{\text{lim,f}} = 16$	2.03	-0.96%	0.48	66.74%	1.23
$\chi^2_{\text{lim,f}} = 9$	2.05	0.03%	0.31	7.81%	1.09
Total		10.62%		141.84%	

TABLE C.10: Systematic contributions to $\alpha_{\text{H}_2\text{O}}$ and α_{AV} from the SNO+ MC data set with water at 420 nm.

Attenuation Systematics - SNO+ MC, H₂O, 505 nm

Systematic	$\alpha_{\text{H}_2\text{O}}^{\text{comb.}}$ 10^{-5} mm^{-1}	$s_i \times \Delta\alpha/\alpha$	α_{AV} 10^{-3} mm^{-1}	$s_i \times \Delta\alpha/\alpha$	$\chi^2/\text{No.Dof}$
Nominal	4.31	0.00%	0.29	0.00%	1.01
$ r_{\text{LB}} \times 1.01$	4.01	-1.39%	-0.69	-68.03%	1.02
$r_x - 50.0 \text{ mm}$	4.31	0.01%	0.33	3.41%	1.04
$r_x + 50.0 \text{ mm}$	4.31	0.00%	0.35	4.37%	1.03
$r_y - 50.0 \text{ mm}$	4.27	-0.19%	0.14	-10.42%	1.03
$r_y + 50.0 \text{ mm}$	4.35	0.18%	0.45	11.47%	1.03
$r_z - 50.0 \text{ mm}$	4.34	0.34%	-0.13	-72.97%	1.02
$r_z + 50.0 \text{ mm}$	4.27	-0.41%	0.67	68.11%	1.01
$\lambda - \lambda_{\text{RMS}} \text{ nm}$	4.31	0.00%	0.28	-1.49%	1.01
$\lambda + \lambda_{\text{RMS}} \text{ nm}$	4.31	0.00%	0.29	1.03%	1.01
H^2	4.31	0.00%	0.28	-0.07%	1.01
$H = 1.0$	0.25	-4.71%	0.57	4.99%	1.46
$\chi^2_{\text{lim,f}} = 16$	4.27	-0.79%	0.47	64.05%	1.24
$\chi^2_{\text{lim,f}} = 9$	4.30	-0.20%	0.32	12.98%	1.09
Total		5.01%		138.43%	

TABLE C.11: Systematic contributions to $\alpha_{\text{H}_2\text{O}}$ and α_{AV} from the SNO+ MC data set with water at 505 nm.

C.2 Attenuation Coefficient Systematics: Scintillator

The following are the full systematic contributions to the attenuation coefficients for each of the wavelengths scans from the SNO+ MC data sets in LABPPO, LABPPO+0.3%Te+bis-MSB and LABPPO+0.3%Te+perylene.

Attenuation Systematics - SNO+ MC, LABPPO, 337 nm

Systematic	$\alpha_{\text{Scint}}^{\text{ppo}}$ 10^{-5} mm^{-1}	$s_i \times \Delta\alpha/\alpha$	$\alpha_{\text{H}_2\text{O}}^{\text{ppo}}$ 10^{-5} mm^{-1}	$s_i \times \Delta\alpha/\alpha$	$\chi^2/\text{No.Dof}$
Nominal	10.67	0.00%	9.21	0.00%	1.02
$ r_{\text{LB}} \times 1.01$	10.40	-0.50%	7.02	-4.75%	1.05
$r_x - 50.0 \text{ mm}$	10.66	-0.01%	8.57	-1.38%	1.03
$r_x + 50.0 \text{ mm}$	10.66	-0.01%	8.53	-1.47%	1.03
$r_y - 50.0 \text{ mm}$	10.65	-0.04%	8.50	-1.54%	1.03
$r_y + 50.0 \text{ mm}$	10.69	0.03%	8.72	-1.06%	1.03
$r_z - 50.0 \text{ mm}$	10.75	0.37%	7.95	-6.85%	1.05
$r_z + 50.0 \text{ mm}$	10.53	-0.64%	7.21	-10.84%	1.00
$\lambda - \lambda_{\text{RMS}} \text{ nm}$	10.74	0.66%	8.80	-4.44%	1.03
$\lambda + \lambda_{\text{RMS}} \text{ nm}$	10.60	-0.63%	8.20	-10.91%	1.01
H^2	10.67	0.00%	9.20	-0.00%	1.02
$H = 1.0$	7.23	-1.61%	4.30	-2.66%	1.43
$\chi^2_{\text{lim,f}} = 16$	10.66	-0.07%	10.25	11.29%	1.24
$\chi^2_{\text{lim,f}} = 9$	10.67	0.04%	9.57	3.98%	1.10
Total		2.05%		21.99%	

TABLE C.12: Systematic contributions to $\alpha_{\text{Scint}}^{\text{ppo}}$ and $\alpha_{\text{H}_2\text{O}}^{\text{ppo}}$ from the SNO+ MC data set with ppo at 337 nm.

Attenuation Systematics - SNO+ MC, LABPPO, 369 nm

Systematic	$\alpha_{\text{Scint}}^{\text{ppo}}$ 10^{-5} mm^{-1}	$s_i \times \Delta\alpha/\alpha$	$\alpha_{\text{H}_2\text{O}}^{\text{ppo}}$ 10^{-5} mm^{-1}	$s_i \times \Delta\alpha/\alpha$	$\chi^2/\text{No.Dof}$
Nominal	15.04	0.00%	9.81	0.00%	1.02
$ r_{\text{LB}} \times 1.01$	14.79	-0.33%	8.01	-3.68%	1.06
$r_x - 50.0 \text{ mm}$	15.04	-0.01%	9.31	-1.01%	1.03
$r_x + 50.0 \text{ mm}$	15.03	-0.02%	9.02	-1.62%	1.03
$r_y - 50.0 \text{ mm}$	15.01	-0.04%	9.21	-1.22%	1.03
$r_y + 50.0 \text{ mm}$	15.05	0.01%	9.35	-0.93%	1.03
$r_z - 50.0 \text{ mm}$	15.17	0.42%	8.67	-5.81%	1.05
$r_z + 50.0 \text{ mm}$	14.83	-0.72%	7.87	-9.91%	0.99
$\lambda - \lambda_{\text{RMS}} \text{ nm}$	15.13	0.56%	9.48	-3.41%	1.03
$\lambda + \lambda_{\text{RMS}} \text{ nm}$	14.95	-0.59%	8.70	-11.32%	1.01
H^2	15.04	0.00%	9.82	0.00%	1.02
$H = 1.0$	11.53	-1.17%	4.76	-2.57%	1.40
$\chi^2_{\text{lim,f}} = 16$	15.06	0.08%	10.82	10.25%	1.21
$\chi^2_{\text{lim,f}} = 9$	15.05	0.04%	10.05	2.48%	1.09
Total		1.69%		20.23%	

TABLE C.13: Systematic contributions to $\alpha_{\text{Scint}}^{\text{ppo}}$ and $\alpha_{\text{H}_2\text{O}}^{\text{ppo}}$ from the SNO+ MC data set with ppo at 369 nm.

Attenuation Systematics - SNO+ MC, LABPPO, 385 nm

Systematic	$\alpha_{\text{Scint}}^{\text{ppo}}$ 10^{-5} mm^{-1}	$s_i \times \Delta\alpha/\alpha$	$\alpha_{\text{H}_2\text{O}}^{\text{ppo}}$ 10^{-5} mm^{-1}	$s_i \times \Delta\alpha/\alpha$	$\chi^2/\text{No.Dof}$
Nominal	10.23	0.00%	5.06	0.00%	0.99
$ r_{\text{LB}} \times 1.01$	10.02	-0.41%	3.53	-6.02%	1.00
$r_x - 50.0 \text{ mm}$	10.23	0.00%	4.69	-1.45%	1.00
$r_x + 50.0 \text{ mm}$	10.22	-0.01%	4.40	-2.60%	1.00
$r_y - 50.0 \text{ mm}$	10.21	-0.03%	4.41	-2.57%	0.99
$r_y + 50.0 \text{ mm}$	10.24	0.04%	4.49	-2.24%	1.00
$r_z - 50.0 \text{ mm}$	10.35	0.62%	4.36	-6.91%	1.00
$r_z + 50.0 \text{ mm}$	10.06	-0.82%	2.41	-26.17%	0.98
$\lambda - \lambda_{\text{RMS}} \text{ nm}$	10.29	0.59%	5.15	1.78%	0.99
$\lambda + \lambda_{\text{RMS}} \text{ nm}$	10.17	-0.54%	4.33	-14.36%	0.98
H^2	10.23	0.00%	5.06	0.00%	0.99
$H = 1.0$	6.74	-1.71%	0.20	-4.80%	1.42
$\chi^2_{\text{lim,f}} = 16$	10.21	-0.18%	5.87	16.12%	1.17
$\chi^2_{\text{lim,f}} = 9$	10.22	-0.03%	5.23	3.49%	1.05
Total		2.19%		35.97%	

TABLE C.14: Systematic contributions to $\alpha_{\text{Scint}}^{\text{ppo}}$ and $\alpha_{\text{H}_2\text{O}}^{\text{ppo}}$ from the SNO+ MC data set with ppo at 385 nm.**Attenuation Systematics - SNO+ MC, LABPPO, 400 nm**

Systematic	$\alpha_{\text{Scint}}^{\text{ppo}}$ 10^{-5} mm^{-1}	$s_i \times \Delta\alpha/\alpha$	$\alpha_{\text{H}_2\text{O}}^{\text{ppo}}$ 10^{-5} mm^{-1}	$s_i \times \Delta\alpha/\alpha$	$\chi^2/\text{No.Dof}$
Nominal	6.88	0.00%	4.96	0.00%	0.98
$ r_{\text{LB}} \times 1.01$	6.77	-0.34%	3.40	-6.27%	0.99
$r_x - 50.0 \text{ mm}$	6.89	0.01%	4.67	-1.15%	0.99
$r_x + 50.0 \text{ mm}$	6.88	-0.01%	4.57	-1.57%	0.99
$r_y - 50.0 \text{ mm}$	6.87	-0.04%	4.51	-1.80%	0.99
$r_y + 50.0 \text{ mm}$	6.90	0.05%	4.66	-1.18%	0.99
$r_z - 50.0 \text{ mm}$	7.07	1.33%	4.30	-6.63%	1.00
$r_z + 50.0 \text{ mm}$	6.67	-1.58%	2.63	-23.48%	0.97
$\lambda - \lambda_{\text{RMS}} \text{ nm}$	6.96	1.17%	4.90	-1.15%	0.98
$\lambda + \lambda_{\text{RMS}} \text{ nm}$	6.82	-0.99%	4.54	-8.51%	0.97
H^2	6.88	0.00%	4.96	-0.00%	0.98
$H = 1.0$	3.07	-2.77%	-0.16	-5.16%	1.41
$\chi^2_{\text{lim,f}} = 16$	6.88	0.01%	5.55	11.91%	1.15
$\chi^2_{\text{lim,f}} = 9$	6.88	-0.00%	5.08	2.46%	1.04
Total		3.79%		29.86%	

TABLE C.15: Systematic contributions to $\alpha_{\text{Scint}}^{\text{ppo}}$ and $\alpha_{\text{H}_2\text{O}}^{\text{ppo}}$ from the SNO+ MC data set with ppo at 400 nm.

Attenuation Systematics - SNO+ MC, LABPPO, 420 nm

Systematic	$\alpha_{\text{Scint}}^{\text{ppo}}$ 10^{-5} mm^{-1}	$s_i \times \Delta\alpha/\alpha$	$\alpha_{\text{H}_2\text{O}}^{\text{ppo}}$ 10^{-5} mm^{-1}	$s_i \times \Delta\alpha/\alpha$	$\chi^2/\text{No.Dof}$
Nominal	5.07	0.00%	4.86	0.00%	1.00
$ r_{\text{LB}} \times 1.01$	4.96	-0.41%	3.18	-6.90%	1.01
$r_x - 50.0 \text{ mm}$	5.07	0.03%	4.67	-0.75%	1.02
$r_x + 50.0 \text{ mm}$	5.06	-0.02%	4.50	-1.48%	1.01
$r_y - 50.0 \text{ mm}$	5.05	-0.05%	4.40	-1.89%	1.01
$r_y + 50.0 \text{ mm}$	5.09	0.10%	4.48	-1.57%	1.01
$r_z - 50.0 \text{ mm}$	5.25	1.80%	4.11	-7.69%	1.02
$r_z + 50.0 \text{ mm}$	4.85	-2.11%	2.43	-25.01%	1.00
$\lambda - \lambda_{\text{RMS}} \text{ nm}$	5.10	0.61%	4.90	0.94%	1.00
$\lambda + \lambda_{\text{RMS}} \text{ nm}$	5.04	-0.53%	4.85	-0.18%	1.00
H^2	5.07	0.00%	4.86	0.01%	1.00
$H = 1.0$	1.25	-3.77%	0.35	-4.64%	1.41
$\chi^2_{\text{lim,f}} = 16$	5.06	-0.02%	5.64	16.18%	1.18
$\chi^2_{\text{lim,f}} = 9$	5.06	-0.06%	5.00	3.01%	1.07
Total		4.76%		32.16%	

TABLE C.16: Systematic contributions to $\alpha_{\text{Scint}}^{\text{ppo}}$ and $\alpha_{\text{H}_2\text{O}}^{\text{ppo}}$ from the SNO+ MC data set with ppo at 420 nm.**Attenuation Systematics - SNO+ MC, LABPPO, 505 nm**

Systematic	$\alpha_{\text{Scint}}^{\text{ppo}}$ 10^{-5} mm^{-1}	$s_i \times \Delta\alpha/\alpha$	$\alpha_{\text{H}_2\text{O}}^{\text{ppo}}$ 10^{-5} mm^{-1}	$s_i \times \Delta\alpha/\alpha$	$\chi^2/\text{No.Dof}$
Nominal	2.37	0.00%	6.65	0.00%	0.98
$ r_{\text{LB}} \times 1.01$	2.29	-0.67%	5.05	-4.81%	0.99
$r_x - 50.0 \text{ mm}$	2.37	0.03%	6.50	-0.44%	0.99
$r_x + 50.0 \text{ mm}$	2.37	0.00%	6.51	-0.42%	0.99
$r_y - 50.0 \text{ mm}$	2.36	-0.09%	6.38	-0.80%	0.99
$r_y + 50.0 \text{ mm}$	2.39	0.18%	6.49	-0.47%	0.99
$r_z - 50.0 \text{ mm}$	2.55	3.79%	6.06	-4.43%	0.99
$r_z + 50.0 \text{ mm}$	2.17	-4.24%	4.28	-17.79%	0.98
$\lambda - \lambda_{\text{RMS}} \text{ nm}$	2.39	0.75%	6.66	0.16%	0.98
$\lambda + \lambda_{\text{RMS}} \text{ nm}$	2.35	-0.69%	6.65	0.04%	0.98
H^2	2.37	0.00%	6.65	0.00%	0.98
$H = 1.0$	-1.45	-8.07%	2.31	-3.26%	1.41
$\chi^2_{\text{lim,f}} = 16$	2.36	-0.51%	7.48	12.54%	1.15
$\chi^2_{\text{lim,f}} = 9$	2.36	-0.23%	6.92	4.19%	1.04
Total		9.97%		23.37%	

TABLE C.17: Systematic contributions to $\alpha_{\text{Scint}}^{\text{ppo}}$ and $\alpha_{\text{H}_2\text{O}}^{\text{ppo}}$ from the SNO+ MC data set with ppo at 505 nm.

**Attenuation Systematics - SNO+ MC
LABPPO + 0.3%Te + Bis-MSB, 337 nm**

Systematic	$\alpha_{\text{Scint}}^{\text{bis.}}$ 10^{-5} mm^{-1}	$s_i \times \Delta\alpha/\alpha$	$\alpha_{\text{H}_2\text{O}}^{\text{bis.}}$ 10^{-5} mm^{-1}	$s_i \times \Delta\alpha/\alpha$	$\chi^2/\text{No.Dof}$
Nominal	20.23	0.00%	14.03	0.00%	1.16
$ r_{\text{LB}} \times 1.01$	19.81	-0.41%	11.84	-3.13%	1.19
$r_x - 50.0 \text{ mm}$	20.23	-0.00%	13.58	-0.63%	1.16
$r_x + 50.0 \text{ mm}$	20.22	-0.01%	13.41	-0.88%	1.16
$r_y - 50.0 \text{ mm}$	20.20	-0.02%	13.66	-0.53%	1.16
$r_y + 50.0 \text{ mm}$	20.25	0.02%	13.87	-0.23%	1.16
$r_z - 50.0 \text{ mm}$	20.25	0.05%	12.74	-4.60%	1.18
$r_z + 50.0 \text{ mm}$	20.15	-0.20%	12.88	-4.11%	1.12
$\lambda - \lambda_{\text{RMS}} \text{ nm}$	20.27	0.19%	13.40	-4.50%	1.16
$\lambda + \lambda_{\text{RMS}} \text{ nm}$	20.21	-0.12%	14.00	-0.19%	1.15
H^2	20.23	0.00%	14.01	-0.01%	1.16
$H = 1.0$	16.90	-0.82%	9.03	-1.78%	1.47
$\chi^2_{\text{lim,f}} = 16$	20.28	0.27%	15.04	7.18%	1.48
$\chi^2_{\text{lim,f}} = 9$	20.25	0.12%	14.01	-0.15%	1.26
Total		1.02%		11.15%	

TABLE C.18: Systematic contributions to $\alpha_{\text{Scint}}^{\text{bis.}}$ and $\alpha_{\text{H}_2\text{O}}^{\text{bis.}}$ from the SNO+ MC data set with bis-MSB at 337 nm.

**Attenuation Systematics - SNO+ MC
LABPPO + 0.3%Te + Bis-MSB, 369 nm**

Systematic	$\alpha_{\text{Scint}}^{\text{bis.}}$ 10^{-5} mm^{-1}	$s_i \times \Delta\alpha/\alpha$	$\alpha_{\text{H}_2\text{O}}^{\text{bis.}}$ 10^{-5} mm^{-1}	$s_i \times \Delta\alpha/\alpha$	$\chi^2/\text{No.Dof}$
Nominal	19.46	0.00%	13.02	0.00%	1.13
$ r_{\text{LB}} \times 1.01$	19.05	-0.42%	10.94	-3.20%	1.16
$r_x - 50.0 \text{ mm}$	19.46	-0.00%	12.85	-0.26%	1.13
$r_x + 50.0 \text{ mm}$	19.47	0.00%	12.65	-0.57%	1.13
$r_y - 50.0 \text{ mm}$	19.44	-0.02%	12.62	-0.63%	1.13
$r_y + 50.0 \text{ mm}$	19.49	0.03%	12.99	-0.05%	1.13
$r_z - 50.0 \text{ mm}$	19.48	0.05%	11.88	-4.38%	1.16
$r_z + 50.0 \text{ mm}$	19.39	-0.18%	11.39	-6.29%	1.09
$\lambda - \lambda_{\text{RMS}} \text{ nm}$	19.50	0.18%	12.48	-4.21%	1.14
$\lambda + \lambda_{\text{RMS}} \text{ nm}$	19.44	-0.13%	13.06	0.31%	1.12
H^2	19.46	0.00%	13.00	-0.01%	1.13
$H = 1.0$	16.02	-0.88%	7.20	-2.24%	1.46
$\chi^2_{\text{lim,f}} = 16$	19.52	0.29%	14.09	8.20%	1.41
$\chi^2_{\text{lim,f}} = 9$	19.49	0.11%	13.41	2.97%	1.23
Total		1.07%		12.99%	

TABLE C.19: Systematic contributions to $\alpha_{\text{Scint}}^{\text{bis.}}$ and $\alpha_{\text{H}_2\text{O}}^{\text{bis.}}$ from the SNO+ MC data set with bis-MSB at 369 nm.

**Attenuation Systematics - SNO+ MC
LABPPO + 0.3%Te + Bis-MSB, 385 nm**

Systematic	$\alpha_{\text{Scint}}^{\text{bis.}}$ 10^{-5} mm^{-1}	$s_i \times \Delta\alpha/\alpha$	$\alpha_{\text{H}_2\text{O}}^{\text{bis.}}$ 10^{-5} mm^{-1}	$s_i \times \Delta\alpha/\alpha$	$\chi^2/\text{No.Dof}$
Nominal	19.73	0.00%	14.22	0.00%	1.14
$ r_{\text{LB}} \times 1.01$	19.31	-0.43%	12.06	-3.05%	1.17
$r_x - 50.0 \text{ mm}$	19.72	-0.01%	14.23	0.00%	1.14
$r_x + 50.0 \text{ mm}$	19.73	-0.00%	13.91	-0.45%	1.14
$r_y - 50.0 \text{ mm}$	19.70	-0.03%	13.98	-0.34%	1.14
$r_y + 50.0 \text{ mm}$	19.75	0.02%	14.02	-0.29%	1.14
$r_z - 50.0 \text{ mm}$	19.74	0.03%	12.99	-4.35%	1.17
$r_z + 50.0 \text{ mm}$	19.65	-0.20%	12.24	-6.99%	1.10
$\lambda - \lambda_{\text{RMS}} \text{ nm}$	19.76	0.16%	13.93	-2.09%	1.15
$\lambda + \lambda_{\text{RMS}} \text{ nm}$	19.70	-0.13%	14.14	-0.62%	1.13
H^2	19.73	0.00%	14.22	-0.00%	1.14
$H = 1.0$	16.35	-0.86%	8.58	-1.98%	1.48
$\chi_{\text{lim,f}}^2 = 16$	19.78	0.28%	15.26	7.26%	1.42
$\chi_{\text{lim,f}}^2 = 9$	19.75	0.10%	14.52	2.05%	1.24
Total		1.04%		11.96%	

TABLE C.20: Systematic contributions to $\alpha_{\text{Scint}}^{\text{bis.}}$ and $\alpha_{\text{H}_2\text{O}}^{\text{bis.}}$ from the SNO+ MC data set with bis-MSB at 385 nm.

**Attenuation Systematics - SNO+ MC
LABPPO + 0.3%Te + Bis-MSB, 420 nm**

Systematic	$\alpha_{\text{Scint}}^{\text{bis.}}$ 10^{-5} mm^{-1}	$s_i \times \Delta\alpha/\alpha$	$\alpha_{\text{H}_2\text{O}}^{\text{bis.}}$ 10^{-5} mm^{-1}	$s_i \times \Delta\alpha/\alpha$	$\chi^2/\text{No.Dof}$
Nominal	31.96	0.00%	7.39	0.00%	1.04
$ r_{\text{LB}} \times 1.01$	31.48	-0.30%	6.57	-2.21%	1.07
$r_x - 50.0 \text{ mm}$	31.96	0.00%	7.27	-0.33%	1.05
$r_x + 50.0 \text{ mm}$	31.95	-0.00%	7.03	-0.96%	1.05
$r_y - 50.0 \text{ mm}$	31.93	-0.01%	7.23	-0.43%	1.05
$r_y + 50.0 \text{ mm}$	31.98	0.02%	7.49	0.29%	1.05
$r_z - 50.0 \text{ mm}$	32.04	0.13%	7.41	0.15%	1.07
$r_z + 50.0 \text{ mm}$	31.82	-0.22%	5.20	-14.82%	1.01
$\lambda - \lambda_{\text{RMS}} \text{ nm}$	31.99	0.11%	7.35	-0.46%	1.04
$\lambda + \lambda_{\text{RMS}} \text{ nm}$	31.92	-0.12%	7.29	-1.39%	1.04
H^2	31.96	0.00%	7.37	-0.01%	1.04
$H = 1.0$	28.44	-0.55%	1.98	-3.66%	1.41
$\chi_{\text{lim,f}}^2 = 16$	31.98	0.06%	8.34	12.86%	1.24
$\chi_{\text{lim,f}}^2 = 9$	31.96	0.02%	7.64	3.44%	1.11
Total		0.70%		20.46%	

TABLE C.21: Systematic contributions to $\alpha_{\text{Scint}}^{\text{bis.}}$ and $\alpha_{\text{H}_2\text{O}}^{\text{bis.}}$ from the SNO+ MC data set with bis-MSB at 420 nm.

**Attenuation Systematics - SNO+ MC
LABPPO + 0.3%Te + Bis-MSB, 446 nm**

Systematic	$\alpha_{\text{Scint}}^{\text{bis.}}$ 10^{-5} mm^{-1}	$s_i \times \Delta\alpha/\alpha$	$\alpha_{\text{H}_2\text{O}}^{\text{bis.}}$ 10^{-5} mm^{-1}	$s_i \times \Delta\alpha/\alpha$	$\chi^2/\text{No.Dof}$
Nominal	17.68	0.00%	5.31	0.00%	1.00
$ r_{\text{LB}} \times 1.01$	17.41	-0.31%	4.07	-4.66%	1.01
$r_x - 50.0 \text{ mm}$	17.69	0.00%	5.14	-0.65%	1.01
$r_x + 50.0 \text{ mm}$	17.69	0.01%	5.29	-0.07%	1.01
$r_y - 50.0 \text{ mm}$	17.67	-0.01%	5.06	-0.96%	1.01
$r_y + 50.0 \text{ mm}$	17.71	0.03%	5.57	0.99%	1.01
$r_z - 50.0 \text{ mm}$	17.83	0.41%	5.00	-2.93%	1.01
$r_z + 50.0 \text{ mm}$	17.51	-0.48%	2.71	-24.45%	0.98
$\lambda - \lambda_{\text{RMS}} \text{ nm}$	17.73	0.27%	5.40	1.64%	1.00
$\lambda + \lambda_{\text{RMS}} \text{ nm}$	17.64	-0.22%	5.25	-1.18%	1.00
H^2	17.68	0.00%	5.31	-0.00%	1.00
$H = 1.0$	14.06	-1.02%	0.71	-4.33%	1.41
$\chi^2_{\text{lim,f}} = 16$	17.70	0.07%	6.25	17.70%	1.18
$\chi^2_{\text{lim,f}} = 9$	17.69	0.04%	5.54	4.27%	1.06
Total		1.29%		31.38%	

TABLE C.22: Systematic contributions to $\alpha_{\text{Scint}}^{\text{bis.}}$ and $\alpha_{\text{H}_2\text{O}}^{\text{bis.}}$ from the SNO+ MC data set with bis-MSB at 446 nm.

**Attenuation Systematics - SNO+ MC
LABPPO + 0.3%Te + Bis-MSB, 505 nm**

Systematic	$\alpha_{\text{Scint}}^{\text{bis.}}$ 10^{-5} mm^{-1}	$s_i \times \Delta\alpha/\alpha$	$\alpha_{\text{H}_2\text{O}}^{\text{bis.}}$ 10^{-5} mm^{-1}	$s_i \times \Delta\alpha/\alpha$	$\chi^2/\text{No.Dof}$
Nominal	5.65	0.00%	6.58	0.00%	0.98
$ r_{\text{LB}} \times 1.01$	5.51	-0.49%	4.83	-5.32%	1.00
$r_x - 50.0 \text{ mm}$	5.65	-0.00%	6.38	-0.60%	1.00
$r_x + 50.0 \text{ mm}$	5.64	-0.02%	6.34	-0.72%	1.00
$r_y - 50.0 \text{ mm}$	5.63	-0.07%	6.25	-0.98%	1.00
$r_y + 50.0 \text{ mm}$	5.66	0.06%	6.51	-0.19%	1.00
$r_z - 50.0 \text{ mm}$	5.80	1.34%	5.80	-5.88%	1.00
$r_z + 50.0 \text{ mm}$	5.45	-1.70%	4.37	-16.80%	0.97
$\lambda - \lambda_{\text{RMS}} \text{ nm}$	5.66	0.29%	6.59	0.27%	0.99
$\lambda + \lambda_{\text{RMS}} \text{ nm}$	5.63	-0.28%	6.51	-0.97%	0.98
H^2	5.65	0.00%	6.57	-0.00%	0.98
$H = 1.0$	1.98	-3.24%	2.31	-3.24%	1.42
$\chi^2_{\text{lim,f}} = 16$	5.65	0.09%	7.50	14.02%	1.16
$\chi^2_{\text{lim,f}} = 9$	5.65	0.01%	6.82	3.76%	1.05
Total		3.95%		23.85%	

TABLE C.23: Systematic contributions to $\alpha_{\text{Scint}}^{\text{bis.}}$ and $\alpha_{\text{H}_2\text{O}}^{\text{bis.}}$ from the SNO+ MC data set with bis-MSB at 505 nm.

**Attenuation Systematics - SNO+ MC
LABPPO + 0.3%Te + Perylene, 337 nm**

Systematic	$\alpha_{\text{Scint}}^{\text{pery.}}$ 10^{-5} mm^{-1}	$s_i \times \Delta\alpha/\alpha$	$\alpha_{\text{H}_2\text{O}}^{\text{pery.}}$ 10^{-5} mm^{-1}	$s_i \times \Delta\alpha/\alpha$	$\chi^2/\text{No.Dof}$
Nominal	10.94	0.00%	13.02	0.00%	1.07
$ r_{\text{LB}} \times 1.01$	10.69	-0.46%	10.41	-4.02%	1.09
$r_x - 50.0 \text{ mm}$	10.94	0.00%	13.06	0.06%	1.07
$r_x + 50.0 \text{ mm}$	10.93	-0.01%	12.64	-0.59%	1.07
$r_y - 50.0 \text{ mm}$	10.92	-0.04%	12.81	-0.33%	1.07
$r_y + 50.0 \text{ mm}$	10.96	0.04%	12.97	-0.09%	1.07
$r_z - 50.0 \text{ mm}$	11.03	0.43%	11.57	-5.60%	1.09
$r_z + 50.0 \text{ mm}$	10.77	-0.78%	11.17	-7.10%	1.03
$\lambda - \lambda_{\text{RMS}} \text{ nm}$	10.96	0.18%	12.92	-0.82%	1.07
$\lambda + \lambda_{\text{RMS}} \text{ nm}$	10.92	-0.19%	13.04	0.12%	1.06
H^2	10.94	0.00%	13.02	-0.00%	1.07
$H = 1.0$	7.81	-1.43%	8.15	-1.87%	1.45
$\chi^2_{\text{lim,f}} = 16$	10.95	0.09%	14.57	11.86%	1.32
$\chi^2_{\text{lim,f}} = 9$	10.94	0.05%	13.52	3.85%	1.15
Total		1.77%		16.06%	

TABLE C.24: Systematic contributions to $\alpha_{\text{Scint}}^{\text{pery.}}$ and $\alpha_{\text{H}_2\text{O}}^{\text{pery.}}$ from the SNO+ MC data set with perylene at 337 nm.

**Attenuation Systematics - SNO+ MC
LABPPO + 0.3%Te + Perylene, 369 nm**

Systematic	$\alpha_{\text{Scint}}^{\text{pery.}}$ 10^{-5} mm^{-1}	$s_i \times \Delta\alpha/\alpha$	$\alpha_{\text{H}_2\text{O}}^{\text{pery.}}$ 10^{-5} mm^{-1}	$s_i \times \Delta\alpha/\alpha$	$\chi^2/\text{No.Dof}$
Nominal	10.91	0.00%	13.67	0.00%	1.08
$ r_{\text{LB}} \times 1.01$	10.65	-0.48%	11.10	-3.76%	1.10
$r_x - 50.0 \text{ mm}$	10.91	-0.00%	13.47	-0.30%	1.08
$r_x + 50.0 \text{ mm}$	10.91	0.00%	13.26	-0.61%	1.08
$r_y - 50.0 \text{ mm}$	10.90	-0.03%	13.31	-0.53%	1.08
$r_y + 50.0 \text{ mm}$	10.93	0.03%	13.60	-0.11%	1.08
$r_z - 50.0 \text{ mm}$	10.99	0.38%	12.16	-5.54%	1.10
$r_z + 50.0 \text{ mm}$	10.75	-0.72%	11.83	-6.74%	1.05
$\lambda - \lambda_{\text{RMS}} \text{ nm}$	10.93	0.19%	13.60	-0.52%	1.08
$\lambda + \lambda_{\text{RMS}} \text{ nm}$	10.89	-0.20%	13.51	-1.17%	1.07
H^2	10.91	-0.00%	13.64	-0.01%	1.08
$H = 1.0$	7.82	-1.42%	9.13	-1.66%	1.45
$\chi^2_{\text{lim,f}} = 16$	10.91	0.01%	14.70	7.56%	1.32
$\chi^2_{\text{lim,f}} = 9$	10.91	0.00%	13.95	2.03%	1.16
Total		1.73%		12.52%	

TABLE C.25: Systematic contributions to $\alpha_{\text{Scint}}^{\text{pery.}}$ and $\alpha_{\text{H}_2\text{O}}^{\text{pery.}}$ from the SNO+ MC data set with perylene at 369 nm.

**Attenuation Systematics - SNO+ MC
LABPPO + 0.3%Te + Perylene, 385 nm**

Systematic	$\alpha_{\text{Scint}}^{\text{pery.}}$ 10^{-5} mm^{-1}	$s_i \times \Delta\alpha/\alpha$	$\alpha_{\text{H}_2\text{O}}^{\text{pery.}}$ 10^{-5} mm^{-1}	$s_i \times \Delta\alpha/\alpha$	$\chi^2/\text{No.Dof}$
Nominal	10.92	0.00%	13.51	0.00%	1.07
$ r_{\text{LB}} \times 1.01$	10.64	-0.50%	10.69	-4.17%	1.09
$r_x - 50.0 \text{ mm}$	10.92	0.00%	13.32	-0.29%	1.07
$r_x + 50.0 \text{ mm}$	10.91	-0.02%	13.14	-0.56%	1.07
$r_y - 50.0 \text{ mm}$	10.90	-0.04%	13.22	-0.44%	1.07
$r_y + 50.0 \text{ mm}$	10.94	0.03%	13.44	-0.11%	1.07
$r_z - 50.0 \text{ mm}$	10.99	0.33%	11.80	-6.33%	1.09
$r_z + 50.0 \text{ mm}$	10.77	-0.69%	11.08	-9.01%	1.04
$\lambda - \lambda_{\text{RMS}} \text{ nm}$	10.94	0.17%	13.45	-0.45%	1.07
$\lambda + \lambda_{\text{RMS}} \text{ nm}$	10.90	-0.20%	13.54	0.19%	1.06
H^2	10.92	-0.00%	13.51	-0.00%	1.07
$H = 1.0$	7.80	-1.43%	8.71	-1.78%	1.45
$\chi^2_{\text{lim,f}} = 16$	10.93	0.11%	14.73	8.97%	1.32
$\chi^2_{\text{lim,f}} = 9$	10.93	0.13%	13.84	2.38%	1.15
Total		1.73%		15.13%	

TABLE C.26: Systematic contributions to $\alpha_{\text{Scint}}^{\text{pery.}}$ and $\alpha_{\text{H}_2\text{O}}^{\text{pery.}}$ from the SNO+ MC data set with perylene at 385 nm.

**Attenuation Systematics - SNO+ MC
LABPPO + 0.3%Te + Perylene, 420 nm**

Systematic	$\alpha_{\text{Scint}}^{\text{pery.}}$ 10^{-5} mm^{-1}	$s_i \times \Delta\alpha/\alpha$	$\alpha_{\text{H}_2\text{O}}^{\text{pery.}}$ 10^{-5} mm^{-1}	$s_i \times \Delta\alpha/\alpha$	$\chi^2/\text{No.Dof}$
Nominal	10.93	0.00%	13.45	0.00%	1.08
$ r_{\text{LB}} \times 1.01$	10.65	-0.50%	10.66	-4.15%	1.11
$r_x - 50.0 \text{ mm}$	10.92	-0.01%	13.37	-0.12%	1.09
$r_x + 50.0 \text{ mm}$	10.92	-0.01%	13.25	-0.30%	1.09
$r_y - 50.0 \text{ mm}$	10.90	-0.04%	13.28	-0.26%	1.08
$r_y + 50.0 \text{ mm}$	10.94	0.03%	13.45	0.00%	1.09
$r_z - 50.0 \text{ mm}$	11.00	0.32%	11.88	-5.82%	1.11
$r_z + 50.0 \text{ mm}$	10.78	-0.67%	11.60	-6.86%	1.05
$\lambda - \lambda_{\text{RMS}} \text{ nm}$	10.95	0.19%	13.32	-0.95%	1.09
$\lambda + \lambda_{\text{RMS}} \text{ nm}$	10.90	-0.19%	13.60	1.11%	1.08
H^2	10.92	-0.00%	13.47	0.01%	1.08
$H = 1.0$	7.79	-1.43%	8.62	-1.80%	1.44
$\chi^2_{\text{lim,f}} = 16$	10.95	0.26%	14.95	11.18%	1.34
$\chi^2_{\text{lim,f}} = 9$	10.94	0.15%	13.89	3.24%	1.17
Total		1.74%		15.47%	

TABLE C.27: Systematic contributions to $\alpha_{\text{Scint}}^{\text{pery.}}$ and $\alpha_{\text{H}_2\text{O}}^{\text{pery.}}$ from the SNO+ MC data set with perylene at 420 nm.

**Attenuation Systematics - SNO+ MC
LABPPO + 0.3%Te + Perylene, 490 nm**

Systematic	$\alpha_{\text{Scint}}^{\text{pery.}}$ 10^{-5} mm^{-1}	$s_i \times \Delta\alpha/\alpha$	$\alpha_{\text{H}_2\text{O}}^{\text{pery.}}$ 10^{-5} mm^{-1}	$s_i \times \Delta\alpha/\alpha$	$\chi^2/\text{No.Dof}$
Nominal	7.21	0.00%	5.90	0.00%	0.98
$ r_{\text{LB}} \times 1.01$	7.08	-0.35%	4.10	-6.10%	1.00
$r_x - 50.0 \text{ mm}$	7.21	0.02%	5.74	-0.54%	0.99
$r_x + 50.0 \text{ mm}$	7.20	-0.02%	5.46	-1.48%	0.99
$r_y - 50.0 \text{ mm}$	7.19	-0.05%	5.51	-1.31%	0.99
$r_y + 50.0 \text{ mm}$	7.23	0.07%	5.82	-0.25%	0.99
$r_z - 50.0 \text{ mm}$	7.38	1.22%	5.09	-6.83%	1.00
$r_z + 50.0 \text{ mm}$	6.99	-1.47%	3.58	-19.67%	0.97
$\lambda - \lambda_{\text{RMS}} \text{ nm}$	7.26	0.75%	6.03	2.28%	0.98
$\lambda + \lambda_{\text{RMS}} \text{ nm}$	7.16	-0.58%	5.92	0.46%	0.98
H^2	7.20	-0.00%	5.88	-0.02%	0.98
$H = 1.0$	3.46	-2.60%	1.09	-4.08%	1.41
$\chi^2_{\text{lim,f}} = 16$	7.21	0.09%	6.80	15.28%	1.15
$\chi^2_{\text{lim,f}} = 9$	7.21	0.02%	6.11	3.54%	1.04
Total		3.38%		27.26%	

TABLE C.28: Systematic contributions to $\alpha_{\text{Scint}}^{\text{pery.}}$ and $\alpha_{\text{H}_2\text{O}}^{\text{pery.}}$ from the SNO+ MC data set with perylene at 490 nm.

**Attenuation Systematics - SNO+ MC
LABPPO + 0.3%Te + Perylene, 505 nm**

Systematic	$\alpha_{\text{Scint}}^{\text{pery.}}$ 10^{-5} mm^{-1}	$s_i \times \Delta\alpha/\alpha$	$\alpha_{\text{H}_2\text{O}}^{\text{pery.}}$ 10^{-5} mm^{-1}	$s_i \times \Delta\alpha/\alpha$	$\chi^2/\text{No.Dof}$
Nominal	5.98	0.00%	6.79	0.00%	0.99
$ r_{\text{LB}} \times 1.01$	5.85	-0.46%	5.19	-4.73%	1.01
$r_x - 50.0 \text{ mm}$	5.99	0.02%	6.83	0.12%	1.00
$r_x + 50.0 \text{ mm}$	5.98	-0.00%	6.60	-0.55%	1.00
$r_y - 50.0 \text{ mm}$	5.96	-0.07%	6.64	-0.43%	1.00
$r_y + 50.0 \text{ mm}$	6.01	0.09%	6.79	-0.01%	1.00
$r_z - 50.0 \text{ mm}$	6.14	1.33%	6.15	-4.70%	1.01
$r_z + 50.0 \text{ mm}$	5.79	-1.64%	4.81	-14.58%	0.98
$\lambda - \lambda_{\text{RMS}} \text{ nm}$	5.99	0.22%	6.82	0.44%	0.99
$\lambda + \lambda_{\text{RMS}} \text{ nm}$	5.97	-0.25%	6.82	0.41%	0.99
H^2	5.98	0.00%	6.78	-0.01%	0.99
$H = 1.0$	2.27	-3.10%	2.59	-3.09%	1.41
$\chi^2_{\text{lim,f}} = 16$	5.98	0.05%	7.82	15.13%	1.17
$\chi^2_{\text{lim,f}} = 9$	5.98	0.03%	7.09	4.36%	1.06
Total		3.80%		22.70%	

TABLE C.29: Systematic contributions to $\alpha_{\text{Scint}}^{\text{pery.}}$ and $\alpha_{\text{H}_2\text{O}}^{\text{pery.}}$ from the SNO+ MC data set with perylene at 505 nm.

Bibliography

- [1] W. Pauli. Open Letter to the Group of Radioactive People at the Gauverein meeting in Tübingen. Letter, December 1930.
- [2] C. Cowan et al. Detection of the Free Neutrino: A Confirmation. *Science*, 124:103–104, July 1956.
- [3] NobelPrize.org. The Nobel Prize in Physics 1995. Press Release, October 1995. URL http://www.nobelprize.org/nobel_prizes/physics/laureates/1995/.
- [4] T. Lee and C. Yang. Parity Nonconservation and a Two-Component Theory of the Neutrino. *Phys. Rev.*, 105:1671–1675, March 1957.
- [5] C. Wu et al. Experimental Test of Parity Conservation in Beta Decay. *Phys. Rev. Lett.*, 105:1413–1415, February 1957.
- [6] K. Monig. Recent Results from LEP at the Z^0 on Electroweak and Heavy Flavour Physics. CERN, URL: <http://www.slac.stanford.edu/cgi-wrap/getdoc/ssi96-020.pdf>, 5-6, 1990-1995.
- [7] J. Lesgourges et al. Neutrino Cosmology and Planck. *New J. Phys.*, 16, June 2014.
- [8] R. Davis. A Review of the Homestake Solar Neutrino Experiment. *Prog. Part. Nucl. Phys.*, 32:13–32, January 1994.
- [9] R. Davis et al. Measurement of the Solar Electron Neutrino Flux with the Homestake Chlorine Detector. *The Astrophysical Journal*, (496), March 1998.
- [10] J. Bachall et al. Present Status of the Theoretical Predictions for the Cl-37 Solar-Neutrino Experiment. *Phys. Rev. Lett.*, 20(1209), May 1968.

- [11] R. Davis et al. Search for Neutrinos from the Sun. *Phys. Rev. Lett.*, 20(1205), May 1968.
- [12] C. Giunti and C. Kim. *Fundamentals of Neutrino Physics and Astrophysics*. Oxford University Press, 2007.
- [13] J. Bachall et al. Standard neutrino spectrum from ${}^8\text{B}$ decay. *Phys. Rev. C*, 54(411), July 1996.
- [14] J. Abdurashitov et al. Results from SAGE (The Russian-American gallium solar neutrino experiment. *Phys. Lett. B*, 328(1-2):234–248, May 1994.
- [15] P. Anselmann et al. Solar Neutrinos observed by GALLEX at Gran Sasso. *Phys. Lett. B*, 285(4):376–389, July 1992.
- [16] M. Altmann et al. Complete results for five years of GNO solar neutrino observations. *Phys. Lett. B*, 618(3-4):174–190, June 2005.
- [17] J. Abdurashitov et al. Measurement of the solar neutrino capture rate with gallium metal. III. Results for the 2002-2007 data-taking period. *Phys. Rev. C*, 80(1), July 2009.
- [18] P. Čerenkov. Visible Radiation Produced by Electrons Moving in a Medium with Velocities Exceeding that of Light. *Phys. Rev.*, 52:378, June 1937.
- [19] S. Davini. *Measurement of the pep and CNO Solar Neutrino Interaction rates in Borexino*. PhD thesis, Universita Degli Studi di Genova, 2012.
- [20] I. Tamm. Radiation Emitted by Uniformly Moving Electrons. *J. Phys. (USSR)*, 1, 1939.
- [21] L. Radel and C. Wiebusch. Calculation of the Čerenkov light yield from low energetic secondary particles accompanying high-energy muons in ice and water with Geant4 simulations. *Astrophys.J.*, 38:53–67, June 2012.
- [22] K. Hirata et al. Observation of ${}^8\text{B}$ solar neutrinos in the Kamiokande-II detector. *Phys. Rev. Lett.*, 63(1), July 1989.
- [23] J. Bachall and A. Serenelli. New Solar Opacities, Abundances, Helioseismology, and Neutrino Fluxes. *Astrophys.J.*, (621), January 2005.
- [24] J. Bachall and R. Ulrich. Solar Models, Neutrino Experiments, and Helioseismology. *Rev. Mod. Phys.*, 60(2):297, April 1988.

- [25] Y. Fukuda et. al. Measurements of the Solar Neutrino Flux from Super-Kamiokande's First 300 Days. *Phys. Rev. Lett.*, 81(1):1158–1162, May 1998.
- [26] Q. Ahmad et al. The Sudbury Neutrino Observatory. *Nuclear Instruments and Methods in Physics Research A*, 449:172–207, 2000.
- [27] Q. Ahmad et al. Direct Evidence for Neutrino Flavour Transformation from Neutral-Current Interactions in the Sudbury Neutrino Observatory. *Phys. Rev. Lett.*, 89(1), July 2002.
- [28] B. Aharmin et al. Electron energy spectra, fluxes, and day-night asymmetries of ${}^8\text{B}$ solar neutrinos from measurements with NaCl dissolved in the heavy-water detector at the Sudbury Neutrino Observatory. *Phys. Rev. C*, 72(5), November 2005.
- [29] B. Aharmin et al. Independent Measurement of the Total Active ${}^8\text{B}$ Solar Neutrino Flux Using an Array of ${}^3\text{He}$ Proportional Counters at the Sudbury Neutrino Observatory. *Phys. Rev. Lett.*, 101(11-12), September 2008.
- [30] A. Bandyopadhyay et al. On the measurement of solar neutrino oscillation parameters with KamLAND. *Phys. Lett. B*, 581(1-2):62–74, February 2004.
- [31] F. Suekane et al. An Overview of the KamLAND 1-kiloton Liquid Scintillator. *arXiv:physics/0404071 [physics.ins-det]*, 2004.
- [32] K. Eguchi et al. First Results from KamLAND: Evidence for Reactor Antineutrino Disappearance. *Phys. Rev. Lett.*, 90(2):021802, January 2003.
- [33] T. Araki et al. Measurement of Neutrino Oscillation with KamLAND: Evidence of Spectral Distortion. *Phys. Rev. Lett.*, 94(081801), March 2005.
- [34] K. Hirata et al. Experimental study of the atmospheric neutrino flux. *Phys. Lett. B*, 205(2-3):416–420, April 1988.
- [35] K. Hidaka et al. Neutrino Oscillations and the Anomalous Atmospheric Neutrino Flux. *Phys. Rev. Lett.*, 61(14):1537–1540, October 1988.
- [36] K. Hirata et al. Observation of a small atmospheric ν_μ/ν_e ratio in Kamiokande. *Phys. Lett. B*, 280(1-2):146–152, April 1992.
- [37] Y. Fukuda et al. Evidence for Oscillation of Atmospheric Neutrinos. *Phys. Rev. Lett.*, 81:1562–1567, August 1998.

- [38] B. Pontecorvo. Mesonium and Anti-Mesonium. *J. Exptl. Theoret. Phys. (U.S.S.R.)*, 33:549–551, August 1957.
- [39] W. Rodejohann. The See-Saw Mechanism: Neutrino Mixing, Leptogenesis and Lepton Flavour Violation. *Pramana - J. Phys.*, 72:217–227, January 2009.
- [40] L. Wolfenstein. Neutrino Oscillations in Matter. *Phys. Rev. D*, 17(9):2369–2374, May 1978.
- [41] M. Thompson. Future Neutrino Facilities. In *SLAC Summer Institute: The Universe of Neutrinos*, page 16, August 2015.
- [42] K. Kimura et al. Exact formulas and simple CP dependence of Neutrino Oscillation Probabilities in Matter with Constant Density. *Phys. Rev. D*, 66(7), October 2002.
- [43] M. Goodman. The Deep Underground Neutrino Experiment. *Advances in High Energy Physics*, (256351), 2015.
- [44] M. Nakahata. Future Prospects of Super-kamiokande and Hyper-kamiokande. *Physics Procedia*, 61:568–575, 2015.
- [45] P. Adamson et al. Combined Analysis of ν_μ Disappearance and $\nu_\mu \rightarrow \nu_e$ Appearance in MINOS Using Accelerator and Atmospheric Neutrinos. *Phys. Rev. Lett.*, 112(19), May 2014.
- [46] K. Abe et al. Evidence of electron neutrino appearance in a muon neutrino beam. *Phys. Rev. D*, 88:032002, August 2013.
- [47] K. Abe et al. Measurements of Neutrino Oscillations in Appearance and Disappearance Channels by the T2K Experiment with 6.6×10^{20} Protons on Target. *Phys. Rev. D*, 91(7), April 2015.
- [48] P. Harrison et al. Tri-Bimaximal Mixing and the Neutrino Oscillation Data. *Phys. Lett. B*, 530(1-4):167–173, March 2002.
- [49] K. Abe et al. Indication fo Electron Neutrino Appearance from an Accelerator Produced Off-Axis Muon Neutrino Beam. *Phys. Rev. Lett.*, 107(041801), July 2011.
- [50] M. Gonzalez-Garcia et al. Updated Fit to Three Neutrino Mixing: Status of Leptonic CP Violation. *J. HEP*, 52, November 2014.

- [51] P. Huber. Determination of Antineutrino Spectra from Nuclear Reactors. *Phys. Rev. C*, 84(2), August 2011.
- [52] NobelPrize.org. The Nobel Prize in Physics 2002. Press Release, October 2002. URL http://www.nobelprize.org/nobel_prizes/physics/laureates/2002/.
- [53] E. Otten et al. Neutrino Mass Limit from Tritium Beta Decay. *Reports on Progress in Physics*, 71(8), July 2008.
- [54] E. Majorana. A Symmetric Theory of Electrons and Positrons. *Il Nuovo Cimento*, 14:171–184, 1937.
- [55] G. Altarelli. The Mystery of Neutrino Mixings. arXiv:1111.6421 [hep-ph]:2, November 2011.
- [56] W. Rodejohann. Neutrino-less Double Beta Decay and Particle Physics. *J. Modern Physics E*, October 2011.
- [57] W. Buchmuller. Leptogenesis: Theory & Neutrino Masses. *Nuclear Physics B*, 235-236:329–335, March 2012.
- [58] J. Lesgourgues et al. Neutrino Mass from Cosmology. *Advances in High Energy Physics*, 2012(608515), October 2012.
- [59] S. Betts et al. Development of a Relic Neutrino Detection Experiment at PTOLEMY: Princeton Tritium Observatory for Light, Early-Universe, Massive-Neutrino Yield. arXiv:1307.4738v2 [astro-ph.IM], July 2013.
- [60] E. Fermi. *Nuovo Cim.*, 11:1–19, 1934.
- [61] R. Robertson. KATRIN: An experiment to Determine the Neutrino Mass. *Journal of Physics: Conference Series*, 120(5), 2008.
- [62] C. Weinheimer. Neutrino Masses. *Annalen der Physik*, 525:565–575, September 2013.
- [63] W. Rodejohann. Neutrinoless Double Beta Decay: Theory. In *SLAC Summer Institute: The Universe of Neutrinos*, page 104, 2015.
- [64] H. Klapdor-Kleingrothaus et al. Evidence for Neutrinoless Double Beta Decay. *Mod. Phys. Lett. A*, 16:2409–2420, December 2001.

- [65] L. Kaufman. Neutrinoless Double Beta Decay: Experiments. In *SLAC Summer Institute: The Universe of Neutrinos*, page 50, 2015.
- [66] J. Gomez-Cadenas et al. Sense and sensitivity of double beta decay experiments. *JCAP*, 1106(007), 2011.
- [67] T. Iida et al. Search for Neutrino-less Double Beta Decay with CANDLES. *Physics Procedia*, 61(1-3):283–288, 2015.
- [68] R. Arnold et al. Probing New Physics Models of Neutrinoless Double Beta Decay with SuperNEMO. *Eur. Phys. J. C.*, 70:927–943, May 2010.
- [69] GERDA Collaboration. $2\nu\beta\beta$ decay of ^{76}Ge into excited states with GERDA Phase I. *J. Phys. G: Nucl. Part. Phys.*, 24(115201), 2015.
- [70] N. Abgrall et al. The MAJORANA DEMONSTRATOR Neutrinoless Double-Beta Decay Experiment. *Advances in High Energy Physics*, (365432), 2014.
- [71] A. Barabash. NEMO 3 double beta decay experiment: latest results. *J. Phys. Conf. Ser.*, 173(1), 2009.
- [72] J. Argyriades et al. Measurement of the two neutrino double beta decay half-life of Zr-96 with the NEMO-3 detector. *Nuclear Physics A*, 847(3-4): 168–179, December 2010.
- [73] R. Arnold et al. Result of the search for neutrinoless double- β decay in ^{100}Mo with the NEMO-3 experiment. *Phys. Rev. D*, 92(072011), 2015.
- [74] V. Lozza et al. Current Status and Future Prospects of the SNO+ Experiment. *Advances in High Energy Physics*, Neutrino Masses and Oscillations, Special Issue 2015.
- [75] C. Arnaboldi et al. Results from a search for the $0\nu\beta\beta$ -decay of ^{130}Te . *Phys. Rev. C*, 78(035502), 2008.
- [76] The EXO-200 Collaboration. Search for Majorana neutrinos with the first two years of EXO-200 data. *Nature*, 510, June 2014.
- [77] The KamLAND-Zen Collaboration. Results from KamLAND-Zen. In *Neutrino 2014 Proceedings*, 2014.

- [78] J. Argyriades et al. Measurement of the Double Beta Decay Half-life of ^{150}Nd and Search for Neutrinoless Decay Modes with the NEMO-3 Detector. *Phys. Rev. C*, 80(032501), 2009.
- [79] M. Agostini et al. Results on Neutrinoless Double- β Decay of ^{76}Ge from Phase I of the GERDA Experiment. *Phys. Rev. Lett.*, 111(122503), September 2013.
- [80] M. Bongrand et al. Results of the NEMO-3 Double Beta Decay Experiment. In *22nd Rencontres de Blois*, 2010.
- [81] C. Bucci et al. Final results of CUORICINO and status of CUORE. *Nuclear Physics B*, 217(1):41–43, August 2011.
- [82] A. Kirsch. *Search for Neutrinoless Double β -decay in GERDA Phase I using a Pulse Shape Discrimination technique*. PhD thesis, Ruperto-Carola University of Heidelberg, July 2014.
- [83] K. Ackermann et al. The GERDA experiment for the search of $0\nu\beta\beta$ -decay in ^{76}Ge . *Eur. Phys. J. C.*, 73(2330), March 2013.
- [84] C. O’Shaughnessy. The MAJORANA DEMONSTRATOR search for neutrinoless double beta decay. In *Invisibles Conf.*, June 2015.
- [85] C. Alduino et al. Analysis Techniques for the Evaluation of the Neutrinoless Double-Beta Decay Lifetime in ^{130}Te with CUORE-0. *PRC*, January 2016.
- [86] C. Rubbia et al. Underground operation of the ICARUS T600 LAr-TPC: first results. *J. INST*, 6, July 2011.
- [87] N. Abgrall et al. Time projection chambers for the T2K near detectors. *Nuclear Instruments and Methods in Physics Research A*, 637(1):25–46, May 2011.
- [88] M. Auger et al. The EXO-200 detector, part I: Detector Design and Construction. *J. INST*, 7, May 2012.
- [89] nEXO Collaboration. nEXO Proposal - Position Paper. *Fundamental Symmetries and Neutrinos 2014 Town Meeting*, 2014.
- [90] J. Argyriades et al. Spectral modelling of scintillator for the NEMO-3 and SuperNEMO detectors. *Phys. Res. A*, 625(1):20–28, January 2011.

- [91] G. Alimonti et al. The Borexino detector at the Laboratori Nazionali del Gran Sasso. *Nuclear Instruments and Methods in Physics Research A*, 600 (3):568–593, March 2009.
- [92] A. Aguilar et al. Evidence for Neutrino Oscillations from the Observation of Electron Anti-neutrinos in a Muon Anti-Neutrino Beam. *Phys. Rev. D*, 64(112007), November 2001.
- [93] A. Aguilar et al. Improved Search for $\bar{\nu}_\mu \rightarrow \bar{\nu}_e$ Oscillation in the MiniBooNE Experiment. *Phys. Rev. Lett.*, 110(161801), April 2013.
- [94] X. Guo et al. A Precision measurement of the neutrino mixing angle θ_{13} using reactor anti-neutrinos at Daya-Bay. *BNL-77369-2006-IR, LBNL-62137, TUHEP-EX-06-003*, October 2007.
- [95] SNOLAB. SNOLAB User’s Handbook Rev 2. June 2008.
- [96] D. Hallman. Liners & Seals: The SNO(+) Experience. Advances in Neutrino Technology 2011, October 2011.
- [97] R. Ford. SNO+ Scintillator Operating Modes and Liquid Handling System Specifications and Process Descriptions. Internal document: SLDO-SNP-TR-5003_Rev_1, March 2013.
- [98] K. Singh et al. The Expected Performance and Motion of the Upward and Downward Ropes in the SNO+ Rope Net. SNO+ Document 1872-v1, April 2013.
- [99] J. Klein et al. The SNO Trigger System. SNO+ Document 827-v1, February 2011.
- [100] I. Coulter. *Modelling and reconstruction of events in SNO+ related to future searches for lepton and baryon number violation*. PhD Thesis, University of Oxford, Denys Wilkinson Building, Keble Rd, Oxford, May 2013.
- [101] H. O’Keeffe. *Low Energy Background in the NCD Phase of the Sudbury Neutrino Observatory*. PhD Thesis, University of Oxford, Denys Wilkinson Building, Keble Rd, Oxford, 2008.
- [102] V. Lozza. Background Table. SNO+ Document 1981-v18, August 2015.

- [103] N. McCauley. *Producing a Background Free Data Set for Measurement of the Charge Current Flux and Day-Night Asymmetry at the Sudbury Neutrino Observatory*. PhD thesis, University of Oxford, October 2001.
- [104] K. Kamdin. Understanding the SNO+ Detector. SNO+ Document 2504-v2, April 2014.
- [105] F. Deschamps. PCA Calibration. SNO+ Document 1081-v3, January 2016.
- [106] M. Mottram. Deployed Calibration Sources in SNO+. SNO+ Document 1832-v3, April 2013.
- [107] R. Alves et al. The calibration system for the photomultiplier array of the SNO+ experiment. *J. INST*, 10, March 2015.
- [108] R. Ford. SNO N₂/Dye Laser System Manual. SNO-STR-96-056, January 1998.
- [109] J. Sinclair. Scintillator Phase Laserball hardware Status. SNO+ Document 2901-v1, January 2015.
- [110] B. A. Moffat et al. Optical calibration hardware for the Sudbury Neutrino Observatory. *Nuclear Instruments and Methods in Physics Research A*, 554 (1-3):255–265, December 2005.
- [111] J. Maneira et al. URM Status. SNO+ Document 2740-v1, August 2014.
- [112] S. Manecki et al. Umbilical Log. SNO+ Document 2820-v2, August 2015.
- [113] S. Steibert et al. RAT: Reactor Analysis Tools, 2014. URL <http://rat.readthedocs.org/en/latest/index.html>.
- [114] S. Agostinelli et al. GEAT4: A Simulation toolkit. *Nuclear Instruments and Methods in Physics Research A*, 506:250–303, 2003.
- [115] G. Horton-Smith et al. GLG4Sim - An adaptation of KamLAND’s KGL4Sim, 2005. URL <http://neutrino.phys.ksu.edu/~GLG4sim/>.
- [116] R. Brun et al. ROOT - An Object Orientated Data Analysis Framework. *Nuclear Instruments and Methods in Physics Research A*, 389:81–86, 1997.
- [117] The KamLAND Collaboration. A high sensitivity search for electron anti-neutrinos from the Sun and other sources at KamLAND. *Phys. Rev. Lett.*, 92(071301), 2004.

- [118] Y. Abe et al. Indication for the disappearance of reactor electron anti-neutrinos in the Double Chooz experiment. *Phys. Rev. Lett.*, 108(131801), March 2012.
- [119] G. Bellini et al. Measurement of geo-neutrinos from 1353 days of Borexino. *Phys. Lett. B*, 722:295–300, 2013.
- [120] J. Birks. *The Theory and Practice of Scintillation Counting*. Pergamon Press, Second edition, 1967.
- [121] S. Maguire (SNOLAB Chemist). Discussion of tellurium in scintillator. Private correspondence, October 2014.
- [122] L. Segui. Scintillator Model: Comparison between new data and old model. SNO+ Document 2774-v3, February 2015.
- [123] J. Morse. The Structure and Dimensions of the Benzene Ring. *Proc. Natl Acad Sci U.S.A.*, 12:789–793, December 1927.
- [124] G. Knoll. Introduction to Radiation Detectors and Electronics - III Scintillation Detectors. page 4, 1998.
- [125] M. Moorhead. *Reflectors in Cerenkov Detectors*. PhD thesis, University of Oxford, February 1992.
- [126] S. Grullon et al. Time Profiles and Scintillation Decay Times for Tellurium-loaded LAB. SNO+ Document 2249-v2, January 2014.
- [127] H. O’Keeffe et al. Scintillation Decay Time and Pulse Shape Discrimination in Oxygenated and Deoxygenated Solutions of Linear Alkylbenzene for the SNO+ Experiment. *Nuclear Instruments and Methods in Physics Research A*, 640(1), June 2011.
- [128] B. von Krosigk et al. Measurement of α -particle quenching in LAB based scintillator in independent small-scale experiments. *Eur. Phys. J. C.*, 76(109), March 2016.
- [129] R. Ford et al. SNO+ Scintillator Purification and Assay. In *LRT2010 Sudbury*, August 2010.
- [130] Edwards. Instruction Manual. nXDS6i Scroll Pump, July 2013.

- [131] Leybold Inficon. Technical Handbook. UL 200 Helium Leak Detector, December 1997.
- [132] A. Bialek. He-leak Check Documentation Package. SNO+ Document 2799-v1, October 2014.
- [133] B. Moffat. *The Optical Calibration of the Sudbury Neutrino Observatory*. PhD thesis, Queen's University, Kingston, Ontario, Canada, July 2001.
- [134] N. Baros. *Precision Measurements of Neutrino Oscillation Parameters: Combined Three-Phase Results of the Sudbury Neutrino Observatory*. PhD thesis, Universidade de Lisboa, December 2011.
- [135] R.P. Stainforth. LightPathCalculator Documentation. SNO+ Document 1700-v8, February 2015.
- [136] R. Stainforth. PMT Bucket Time. SNO+ Document 3138-v6, May 2015.
- [137] O. Simard. *Measurement of the Survival Probability and Determination of the Three-Flavour Neutrino Oscillation Parameters at the Sudbury Neutrino Observatory*. PhD thesis, Ottawa-Carleton Institute for Physics, Carleton University, Ottawa, Ontario, Canada, September 2009.
- [138] C. Jackson. Photographs of aged concentrators. SNO+ Document 3518-v1, January 2016.
- [139] O. Simard. A New Laserball Model for the Optics in the NCD Phase. Internal SNO Optics Note, July 2008.
- [140] H. Gavin. The Levenberg-Marquardt method for nonlinear least squares curve-fitting problems. September 2015.
- [141] J. Maneira. Measurement of the Wavelength Spectra of the SNO Laser Dyes. Internal SNO+ Document, March 2004.
- [142] Exciton. α -NPO Dye, COUMARIN-400, COUMARIN-481. Laser Dye Sheet, Accessed: January 2015 .
- [143] W. Press et al. *Numerical Recipes: The Art of Scientific Computing*. Cambridge University Press, Third Edition edition, 2007.

- [144] L. Boivin et al. Determination of the attenuation coefficients of visible and ultraviolet radiation in heavy water. *Applied Optics*, 25(6):877–882, March 1986.
- [145] R. Pope et al. Absorption spectrum (380-700 nm) of pure water II: Integrating cavity measurements. *Applied Optics*, 36(33):8710–8723, November 1997.
- [146] SNO E&O Working Group. Tech. Rep. MANN-5M6QZ3. Energy and Optics Measurements for the Salt Phase of SNO, 2003.
- [147] S. Grullon. Optical Properties Task Force Investigative Summary. SNO+ Document 1531-v3, February 2013.
- [148] C Jackson. Angular Response and Concentrator Ageing. SNO+ Document 3130-v1, April 2015.
- [149] F. Porter. Testing Consistency of Two Histograms. Cal. Tech, March 2008.
- [150] L. Lyons. *Statistics for nuclear and particle physicists*. Cambridge University Press, 1999.
- [151] S. Biller et al. Tellurium Loading Downselect Background Information Document. SNO+ Document 3505-v1, December 2015.